Title
Unraveling the structure-property relationships in perovskite oxides

Author
Gao, Ran

Publication Date
2019

Peer reviewed|Thesis/dissertation

Unraveling the structure-property relationships in perovskite oxides

by

Ran Gao

A dissertation submitted in partial satisfaction of the

requirements for the degree of

Doctor of Philosophy

in

Materials Science and Engineering

in the

Graduate Division

of the

University of California, Berkeley

Committee in charge:

Professor Lane W. Martin, Chair
Professor Nitash Balsara
Associate Professor Kristin Persson

Spring 2019

Unraveling the structure-property relationships
in perovskite oxides

Abstract

Unraveling the structure-property relationships
in perovskite oxides

by

Ran Gao

Doctor of Philosophy in Materials Science and Engineering

University of California, Berkeley

Professor Lane W. Martin, Chair

This dissertation focuses on the manipulation of the lattice degree of freedom in perovskite oxide thin films, and explores the fundamental structure-property relationships. Epitaxial thin-film engineering and state-of-the-art thin-film characterization techniques are employed to achieve an effective and quantifiable control over a number of structural features including lattice expansion/compression, lattice tilting, octahedral rotations, and surface structures. Henceforth, the detailed correlation between structural features and corresponding physical properties are established and exemplified in several model perovskite systems. The key findings in this work include that, first, the interfacial structural coupling effect is explored and demonstrated in $SrRuO_3$ thin films where the lattice symmetry, magnetic anisotropy, and electrical transport can be readily controlled. Moreover, growth-mediated antisite defects are found to be responsible in determining the energy competition between the low-symmetry antiferroelectric and the high-symmetry ferroelectric phases in $PbZrO_3$ thin films, and the metastable ferroelectric phase can be stabilized. In addition, detailed relationships between ionic charge transport and lattice structure is explored in $La_{0.9}Sr_{0.1}Ga_{0.95}Mg_{0.05}O_{3-\delta}$, and in turn, an optimal design of perovskite structure for high ionic conduction is successfully demonstrated through epitaxial strain and interfacial engineering. And lastly, surface engineering via growth-orientation control is explored in $La_{0.8}Sr_{0.2}Co_{0.2}Fe_{0.8}O_{3-\delta}$ to establish the correlation between surface structure and electrochemical activities.

To my parents and my friends for their unconditional love and support

Contents

Contents **ii**

List of Figures **iv**

List of Tables **xiii**

List of Symbols and Abbreviations **xiv**

1 Structure-property coupling in perovskite oxides **1**
1.1 Introduction to perovskite oxides 2
1.2 Lattice degree of freedom and structural features 4
1.3 Motivation and opportunities 8
1.4 Statement and organization of the dissertation 10

2 The control and manipulation of perovskite structures **12**
2.1 An epitaxial thin-film approach 13
2.2 Control of lattice structures in perovksite thin films 21
2.3 Control of surface structures in perovskite thin films 29

3 Characterization of perovskite heterostructures **31**
3.1 Structural characterization of perovskite oxides 32
3.2 Physical properties and characterization 38

4 Structure control, magnetism, and transport in $SrRuO_3$ **45**
4.1 Introduction 46
4.2 Sample design and thin-film synthesis 47
4.3 Structural characterization 48
4.4 Octahedra rotational domains 52
4.5 Impact on physical properties of $SrRuO_3$ 55
4.6 Conclusions 56

5 Control of antiferro-/ferroelectricity in $PbZrO_3$ **58**
5.1 Introduction 59

5.2 $PbZrO_3$ thin-film growth dynamics . . . 61
5.3 Structural and chemistry characterization . . . 63
5.4 Electrical characterization . . . 64
5.5 Lattice symmetry determination . . . 67
5.6 Energy ground states in lead-excess $PbZrO_3$ . . . 71
5.7 Conclusions . . . 73

6 Designing optimal ion-conducting perovskite structure 74
6.1 Introduction . . . 75
6.2 Strain engineering and quantification of structural features . . . 76
6.3 Ion-transport measurement . . . 80
6.4 First-principle calculations . . . 84
6.5 Experimental realization of the optimal structure . . . 88
6.6 Conductivity measurement in superlattice structures . . . 92
6.7 Conclusions . . . 94

7 Correlating surface orientations and electrochemistry 95
7.1 Introduction . . . 96
7.2 Epitaxial all-perovskite, half-cell structures . . . 97
7.3 Heterostructure synthesis and characterization of the half-cells . . . 98
7.4 The fabrication of the epitaxial half cells . . . 101
7.5 Validating the epitaxial half cells . . . 104
7.6 Orientation-dependent gas-exchange kinetics . . . 105
7.7 Rate-limiting step in the gas exchange reactions . . . 107
7.8 Conclusions and future works . . . 110

8 Summary of findings and suggestions 112
8.1 Summary of findings . . . 113
8.2 Suggestions for future work . . . 115

References 119

A Pseudo-cubic lattice notation 138

B Characterization of thin-film chemistry 140
B.1 Rutherford backscattering spectrometry . . . 140
B.2 X-ray photoelectron spectroscopy . . . 141
B.3 Low-energy ion scattering spectroscopy . . . 143

C Electrochemical impedance spectroscopy 145
C.1 Ionic diffusion in mixed conductors . . . 147
C.2 Surface reaction at solid-gas interface . . . 149

List of Figures

1.1 Schematic of a cubic perovskite structure with formula ABO_3 2
1.2 Illustration of the parameters used in tolerance factor calculation. Note that atomic size is shown instead of realistic ionic size. 4
1.3 Energy levels of *B*-site cation 3*d* orbitals in a octahedral cage. A schematic of shifted energy levels in compressed and elongated octahedra are also given. . . 5
1.4 Schematics of the three structural features that can be engineered in thin-film perovskite oxides: lattice expansion&compression, lattice tilting, and octahedral rotations 6
1.5 Surface structure of perovskites at solid-gas interface can be effectively engineered by slicing the material along different lattice plane. 7

2.1 An illustration of homoepitaxy and heteroepitaxy in perovskite thin-films. Note that compressive strain is shown in the heteroepitaxy. 13
2.2 The setup of pulsed-laser deposition. 14
2.3 (a)The microscopic steps during the growth of perovskite oxides. (b)Schematic of atomic nucleation process during film growth. (c)Illustration of the three thin-film growth modes at near-equilibrium conditions 15
2.4 (a)Microscopic illustration of the growth kinetics under varied conditions. (b)The theoretical surface roughness as function of time (surface coverage) under three different growth kinetics (Figure adapted from [57]). 17
2.5 Schematic of reflection high-energy electron diffraction (Figure adapted from [61]). The inset gives an example of the intensity oscillation of the diffraction spot during the growth of one monolayer. 19
2.6 A collection of realistic RHEED patterns of Fe_3O_4 thin films grown under various growth modes (Figure adapted from [52]). 20
2.7 (a)Illustration of crystalline, polycrystalline, and amorphous materials. (b)A schematic of the structure of a crystalline material. The structure of a crystal material can be described by crystal lattice plus basis. 21
2.8 Tetragonal $SrTiO_3$ at low temperature. The crystal symmetry transition from $Pm\hat{3}m$ to $I4/mcm$ can be represented by a expansion of the *c*-axis in pseudo-cubic unit cell plus out-of-phase octahedral rotation along the *c*-axis. 22

2.9 Orthorhombic $DyScO_3$ belongs to space group $Pnma$. The pseudo-cubic lattice (indicated by yellow dashed line) possesses lattice tilting, anisotropic lattice parameters, and octahedral rotation with Glazer pattern $a^-a^+c^-$. 23
2.10 (a) Coherently strained film on substrate. (b) Partially relaxed film on substrate that has larger lattice mismatch. The strain is relaxed by forming dislocations at the interface (Figure adapted from [67]). 24
2.11 (a)Illustration of the accommodation of epitaxial strain by a change in the rotation magnitudes along three orthogonal directions. (b)The evolution of octahedral rotation patterns of $LaAlO_3$ under strain (Figure adapted from [33]). . . 25
2.12 (a)Cation size effect on the lattice and electronic structure of nicklates (Figure adapted from [71]). (b)Change in magnetic susceptibility and magnetoresistance in Sr_2FeMoO_6 induced by cation anti-site defects (Figure adapted from [72]). (c)Illustration of the breaking of inversion symmetry via cation ordering in perovskite structure (Figure adapted from [73]). 26
2.13 Illustration of interfacial structural coupling between a high-symmetry film and low-symmetry substrate. The structural features such as octahedral rotation pattern from the substrate propagates into the epitaxial film. 27
2.14 The octahedral rotation pattern of $La_{0.7}Sr_{0.3}MnO_3$ thin film can be engineered by substrate surface symmetry and the magnetic easy axis is able to turn 90° depending on the thickness of the high-symmetry buffer layer (Figure adapted from [7]). 28
2.15 (a) Surface-orientation dependency of surface activity in RuO_2 (Figure adapted from [87]). (b) Correlation between surface stability and electrochemical activity in $SrRuO_3$ grown along (001), (110), and (111) (Figure adapted from [88]). 29

3.1 RSM scan in real space (a) and reciprocal space (b). (c)Schematic of lattice distortions in the real space while the corresponding changes in diffraction spots in reciprocal space are illustrated (d). 33
3.2 (a)Illustration of octahedral rotation in the perovskite lattice. (b)Once the octahedra rotate out-of-phase along one direction (*c*-axis as illustrated), the origin of half-order peak can be interpreted as the doubling of pseudo-cubic unit cell. . 34
3.3 (a)Schematic setup of the synchrotron-based crystal truncation rod measurements. (b)Representative truncation rod measurements data where the fine intensity variation in between the Bragg's rods contains necessary information for electron density map reconstruction. (c)3D electron density map (atomic position) of $CaTiO_3$ grown under various strain states (Figure adapted from [37]). 37
3.4 (a)The SQUID measurement unit and an illustration of the oscillating voltage under external magnetic flux. (b)The sample holder for thin film heterostructures. (c)Resistivity measurement on thin-film samples using van der Paul method 40

3.5 The electrical hysteresis loops of paraelectric (a), ferroelectric (b), and antiferroelectric (c) materials. The corresponding dipole alignment and domain structures are illustrated in the insets. (d)Microfabrication process of top circular electrodes using a MgO hard-mask (Figure adapted from [116]). 41
3.6 The schematic of the tube-furnace based measurement setup for temperature dependent and gas-pressure dependent studies for thin-film heterostructures . . 43

4.1 (a)Illustration of the two sample geometries used in this study (b)X-Ray θ-2θ scans about the 002-diffraction conditions for a 10 nm $SrRuO_3$ film grown on both a non-buffered and buffered $SrTiO_3$ substrate. Rocking curves are shown in the insets. 47
4.2 (a)Reciprocal space mapping about 103- and 013-diffraction conditions of the $SrRuO_3$ and $SrTiO_3$ for films grown on non-buffered and buffered substrates. (b)Four structural domains (D_X, D_Y, $D_{X'}$, and $D_{Y'}$) of $SrRuO_3$ on $SrTiO_3$ substrates. D_Y, $D_{X'}$, and $D_{Y'}$ domains can be thought of rotating domain D_X by 90°, 180°, and 270° about [001] direction. Note that [100] direction is aligned with in-phase (+) rotation axis. 49
4.3 Four representative half-order Bragg peak patterns for 10 nm thick $SrRuO_3$ films grown on (a) non-buffered and (b) buffered $SrTiO_3$. (c)Difference in l of corresponding *hkl* diffractions from $GdScO_3$ buffer layer and tetragonal $SrRuO_3$ films. Higher index gives bigger difference, which is indicating that $GdScO_3$ has a monoclinic structure. 50
4.4 Half-order Bragg peak analysis results of non-buffered $SrRuO_3$ films grown on non-buffered $SrTiO_3$ substrates (a) and $GdScO_3$-buffered $SrTiO_3$ substrates (b). Red data are acquired from experiments and blue data are calculated intensities. (c)The experimentally measure and extracted octahedral rotation angles and domain variant fractions as obtained from the half-order Bragg peaks analysis. 51
4.5 (a)Schematic illustration of the four "rotational" domains (R_X, R_Y, $R_{X'}$, and $R_{Y'}$) possible in the tetragonal variant of $SrRuO_3$ where the various rotational domains can be thought of rotating the octahedra within the lattice about the [001] by 0°, 90°, 180°, or 270°. (b) Illustration of the tendency of the $SrRuO_3$ to align its in-phase (+) rotation axis with the $GdScO_3$ (+) rotation axis during growth and the corresponding coupling between $GdScO_3$ structural domains and $SrRuO_3$ rotational domains. Arrows show the direction of in-phase (+) octahedral rotation axis. 53
4.6 Temperature-dependent electrical resistivity behavior for 10 nm $SrRuO_3$ films grown on non-buffered and buffered $SrTiO_3$. The inset shows $d\rho/dT$ vs. T curves and demarcates the T_C. 55
4.7 Magnetization-magnetic field and magnetization-temperature results for 10 nm $SrRuO_3$ films grown on (a),(b) non-buffered and (c),(d) buffered $SrTiO_3$. All sample are cooled at 1 T field from room temperature to 5 K prior to study. . . . 56

5.1 (a) A representative polarization hysteresis loop of antiferroelectrics. (b) Projection of atomic displacements associated with the Σ_2 mode at $q = \frac{2\pi}{a}(1/4, 1/4, 0)$ onto the *ab*-plane. Squares and circles indicate lead and oxygen ions, respectively. Filled and open circles show ions on the lead cation layer and ions on the zirconium cation layer, respectively [153]. 59
5.2 (a) Monitored main diffraction peak intensity in RHEED for $Pb_{1.2}ZrO_3$ heterostructure growth. The insets show 3D and 2D diffraction patterns under *S-K* growth mode at different growth stages. (b) Initial 2-3 unit cells of $Pb_{1.2}ZrO_3$ under layer-by-layer growth mode. (c) Layer-by-layer growth after surface reconstruction during laser-off time period. (d) Continuous layer-by-layer growth which can be sustained by intermittently stopping the laser to have film surface reconstructed. 62
5.3 (a) X-ray θ-2θ line scans reveal high-quality $(120)_O$-oriented 50 nm $Pb_{1+\delta}ZrO_3$ films on 10 nm $SrRuO_3$/$DyScO_3$ 220 grown with different (non)stoichiometric lead zirconate targets. (b)-(d) Reciprocal space mapping of three heterostructures confirms fully relaxed epitaxial $Pb_{1+\delta}ZrO_3$ films with similar lattice parameters. (e)-(g) Rocking curves of three $Pb_{1+\delta}ZrO_3$ heterostructures show consistent and high crystallinity as indicated by a film FWHM of 0.025° as compared with FWHM of 0.006° for $DyScO_3$ substrates. 64
5.4 Rutherford back-scattering spectrometry studies on three $Pb_{1+\delta}ZrO_3$ films reveal nominal chemistries of (a) $PbZrO_3$, (b) $Pb_{1.1}ZrO_3$, and (c) $Pb_{1.2}ZrO_3$. 65
5.5 Antiferroelectric double-hysteresis loops are observed for $PbZrO_3$ and $Pb_{1.1}ZrO_3$ variants (a) (b), while single hysteresis loops are shown in $Pb_{1.2}ZrO_3$ films (c). Temperature-dependent dielectric responses under various probed frequencies reveal sharp dielectric anomalies for antiferroelectric (d) $PbZrO_3$ and (e) $Pb_{1.1}ZrO_3$ films, while (f) a broader phase transition with no frequency-dispersion change across transition temperature is observed in ferroelectric $Pb_{1.2}ZrO_3$ heterostructures. 66
5.6 (a) I-V studies on three $Pb_{1+\delta}ZrO_3$ heterostructures show good insulation and low leakage currents as compared with ferroelectric PZT films. (b) Room temperature dielectric responses. (c) Hysteresis loops for $Pb_{1.2}ZrO_3$ taken at frequencies from 0.1 Hz to 100 kHz at room temperature reveals characteristic ferroelectric response in the sample. 67

5.7 Synchrotron-based X-ray reciprocal space mapping around $DyScO_3$ 332_O-diffraction conditions are taken for all three heterostructures. Data is plotted in reciprocal HKL vector space with respect to $DyScO_3$ orthorhombic lattice such that [0 0 L] is the in-plane axis and [H K 0] is the out-of-plane axis. Relaxed and strained peaks from $Pb_{1+\delta}ZrO_3$ are labeled as "R" and "S", respectively. Quarter-order Bragg peaks (450_O and 290_O in orthorhombic lattice) are labeled for (a) $PbZrO_3$ and (b) $Pb_{1.1}ZrO_3$ heterostructures, while diffused patterns along $[\bar{1}01]_{pc}$ are observed in (c) $Pb_{1.2}ZrO_3$. (d) Plotting normalized 450_O peak intensity with respect to substrate along *L*-direction reveals strong Bragg diffraction for antiferroelectric $PbZrO_3$ and $Pb_{1.1}ZrO_3$ heterostructures. However, antiferroelectric quarter-order peak intensity is two orders lower in magnitude for ferroelectric $Pb_{1.2}ZrO_3$ heterostructures. 69

5.8 (a) Diffused pattern observed around 450_O-diffraction condition in $Pb_{1.2}ZrO_3$ indicates weak antiferroelectric ordering along $[\bar{1}01]_{pc}$ axis while stronger antiferroelectric ordering along $[101]_{pc}$. (b) Fitted Lorentzian profiles along orange line ($[\bar{1}01]_{pc}$ and red line ($[101]_{pc}$) are given. 70

5.9 (a) Formation energies at T=0 K of stoichiometric $PbZrO_3$, zirconium vacancies ($V_{Zr}^{''''}$) and antisite defects ($Pb_{Zr}^{\times}$) in *Pbam* $PbZrO_3$ lattice are given. Stoichiometric $PbZrO_3$ is suggested to be metastable at low temperature while antisite defect formation in $PbZrO_3$ lattice is unavoidable. (b) The energy difference between *R*3*c* and *Pbam* phases in nonstoichiometric $Pb_{1+\delta}ZrO_3$ is small and remains <1 meV. (c) Antisite defects ($Pb_{Zr}^{\times}$) can both form in *Pbam* and *R*3*c* $Pb_{1+\delta}ZrO_3$ films, while it is more favored in *R*3*c* phase as suggested by the lower defect formation energy across whole doping range. 72

6.1 (a) X-ray line scans for all heterostructures reveal high quality, single phase, epitaxial LSGM thin films from biaxial compressive strain to tensile strain. (b) A representative RSM of LSGM/$DyScO_3$ heterostructure along two orthogonal directions is given, suggesting that the film is coherently strained onto the substrate. (c) RBS studies of LSGM thin films grown on sapphire substrate under the same growth conditions reveal nominal chemistry of $La_{0.9}Sr_{0.1}Ga_{0.95}Mg_{0.05}O_{3-\delta}$. 77

6.2 (a) The similar peak intensities of (1/2 1/2 3/2) scans at 25°C and 650°C suggest that the octahedral rotation pattern remains essentially the same within the measurement temperatures. Comparison of calculated half-order peak intensities and experimental values for all heterostructures (b) LSGM/$NdGaO_3$, (c) LSGM/$SrTiO_3$, and (d) LSGM/$DyScO_3$ are given. 78

6.3 (a) Structural parameters of LSGM under various strain states are given and schematics of these evolution are illustrated (b). Note that the oxygen positions are extracted from X-ray studies while the rotation magnitude indicator is exaggerated for better representation. 79

6.4 Impedance spectra for all heterostructures under both O_2 and N_2 environment (a) LSGM/$NdGaO_3$, (b) LSGM/$SrTiO_3$, and (c) LSGM/$DyScO_3$. 81

6.5 Impedance spectra for all bare substrates under both O_2 and N_2 environment (a) $NdGaO_3$, (b) $SrTiO_3$, and (c) $DyScO_3$. 81
6.6 (a) Transmission line model used for fitting mixed ionic and electronic conductors. (b) Extracted ionic charge transference numbers are in good agreement with bulk single crystal and further supports that the ionic conduction is given by LSGM films in all heterostructures. (c) Arrhenius plot of LSGM conductivity as function of strain and temperature. Activation energies of oxygen vacancy migration for all heterostructures are ∼0.65-0.75 eV. (d) Ionic conduction measurement at low temperature region. A clearer difference in activation energy is noted. 82
6.7 (a) Geometry of the $LaGaO_3$ unit cell relaxed from DFT. The La atoms are orange, Ga atoms are light purple and the O atoms are red. The O atoms in the Ga plane perpendicular to $[010]$ are *O1* and the ones in La plane are *O2*. The *O1-O1-O1* bond angle (Θ) and the *Ga-O2-Ga* bond angle (Φ) measure the in-plane octahedral rotation and out- of-plane octahedral tilt angle, respectively. The in-plane rotation $\theta = (90 - \Theta)/2$, and the out-of-plane tilt angle $\phi = (180 - \Phi)/2$. Comparison of experimental values are also given. (b) Strain effects on unit cell volume and octahedral rotation and tilt in $LaGaO_3$. (c) Oxygen vacancy migration energy versus strain. Tensile strain reduces migration energy barrier of all types of jumps. 84
6.8 (a) Illustration of the undoped $LaGaO_3$ crystal from the DFT calculations (top). Calculations further reveal six unique energy barriers for different oxygen vacancy jumps (each jump is labeled with different color, bottom). The values of migration barriers are given relative to the *O1* site and there are two *O1-O1-* and four *O1-O2*-type jumps. Schematic illustration of various fast ion-conducting oxygen vacancy migration pathways including ones based on (b) a series of *O1-O1*-type jumps (two equivalent pathways along different directions are shown) and one based on (c) a series of *O1-O1* and *O1-O2*-type jumps. (d) DFT calculated vacancy diffusivity as a function of strain for undoped $LaGaO_3$. e, Migration energies for oxygen vacancies when $LaGaO_3$ is doped with strontium at lanthanum-sites where, vacancies are found to either jump between bound sites (*i.e.*, circle around the strontium trap) through low-energy barrier jumps (0.20-0.45 eV) or jump towards unbound sites (*i.e.*, escape from the strontium trap) through high-energy barrier jumps (0.61-0.80 eV). 86
6.9 The binding energy of O vacancy at (a) *O1* and (b) *O2* sites with dopant atoms at sites within the first neighbor shell. The *O-Sr* pair has a strong attractive binding while *O-Mg* pair has a weakly repulsive binding. 87
6.10 Illustration of introduction of octahedral rotation via interfacial engineering. . . 88

6.11 (a) RHEED spectra of LSGM and $DyScO_3$ growth on $DyScO_3$ substrates. All films reveal layer-by-layer growth mode and the exact monolayer numbers can be deterministically controlled. Sharp electron diffraction patterns reveal high surface quality and crystallinity (figure insets). (b) X-ray line scans of all superlattice structures reveal clear Laue thickness fringes and superlattice peaks, indicating good crystallinity and sharp interfaces. (c) Synchrotron X-ray RSM show clear strained superlattice peaks. (d) X-ray line scans before and after high temperature measurement (24 hours at above 500°C under O_2 and N_2 environment) show now changes in line-scan profile, suggesting robustness of sample during measurement hours. 89
6.12 (a) Electron density map for a $(DyScO_3)_6/(LSGM)_6/DyScO_3$ heterostructure from the COBRA analysis. The map reveals large octahedral rotations extending from the $DyScO_3$ into the ultrathin LSGM. (b) Extracted octahedral rotation angles as a function of unit cell through the thickness of the heterostructure confirming the large octahedral rotation of both the bottom and top $DyScO_3$ layers and the formation of large in-plane rotations (α and β angles) in the LSGM that are markedly different from bulk values (solid and dashed lines). . . 90
6.13 (a) Representative impedance spectra for a superlattice sample at 500°C. (b) Same normalized impedance per LSGM layer of $(LSGM)_6/(DyScO_3)_6$ superlattices with different repetition (*i.e.*, 8 and 16 repetitions) suggests that all LSGM layers are effectively conducting. (c) Illustration of hypothesized conducting and non-conducting part of LSGM ultrathin films. The conductivity and thickness of non-conducting part of LSGM can be extracted via linear fitting of superlattice samples with different LSGM thickness (d), and the impedance of LSGM and number of non-conducting "dead layers" in LSGM are given (e) Note that for all superlattice geometries, there are consistently 5UC of LSGM that are not conducting. In other words, when calculating the conductivity of LSGM I use the thickness of conducting LSGM unit cells instead of the total thickness 91
6.14 LEIS studies on 5UC LSGM/$DyScO_3$ sample is subsequently performed to better understand the origin of "dead layer" in LSGM. The total yield reveals that 5UC LSGM has the same nominal chemistry compared with thicker films (a), while the depth profile of LSGM suggests that there is significant Sr redistribution along the out-of-plane direction of the film (b). The redistribution (segregation) of Sr is likely to be the cause of transport "dead layer" in ultrathin LSGM. 93
6.15 Conductivity of LSGM at 600°C as function of unit cell volume and octahedral rotation magnitudes. The optimal structure of LSGM achieves an enhancement of conductivity by a factor of 2.5 compared with non-optimal heterostructures at compressive strain state 94

7.1 (a) The schematic of a half cell for thin-film gas kinetic measurement. (b) The transport process involved in one voltage cycle and the hypothesized potential profile across the heterostructure if provided. 97

7.2 (a) X-ray line scan of the heterostructures grown on $SrTiO_3$ (001), (110), and (111) substrates. (b) RSM around 103-diffraction condition for the heterostructure on $SrTiO_3$ (001) substrates. (c) AFM image of LSCF surface. 99
7.3 (a) A representative XPS scan around strontium 3*d* peak. (b) The ratio between surface strontium to lattice strontium for as-grown LSCF films and LSCF annealed for 8 hours in air. 100
7.4 LEIS spectra on LSCF surfaces along different orientations. The outermost layer is purely *A*-cite terminated. The inset gives the ratio of strontium and lanthanum concentration, which reveals strontium segregation at the surface. . . . 101
7.5 (a) Side view of the half-cell heterostructure. (b) Detailed schematics of the device structure around LSCF working electrodes. (c) Device fabrication process flow involving ion-milling. 102
7.6 (a) Comparison of impedance spectra of LSCF electrode and LSCF electrode with platinum capping layer. (b) Comparison of impedance spectra of half cells with varied electrolyte (LSGM) thicknesses. (c) Examination of TPB contributions by varying the working-electrode diameters. 104
7.7 (a) Impedance spectra of the half cells grown along three orientations. (b) The extracted rate constant k^q for three LSCF surfaces. 106
7.8 (a) The sequence of a typical electrical conductivity relaxation measurement. (b) Relaxation curve for a pressure change from 380 torr to 200 torr in dry oxygen for LSCF/$SrTiO_3$ (001), (110), and (111). 106
7.9 Schematics of the reaction steps in a surface gas exchange process. 108
7.10 Sheet resistance of 30 nm LSCF films grown on $SrTiO_3$. 110
7.11 oxygen-partial-pressure dependent studies on three half-cell geometries grown along (a) (001), (b) (110), and (c) (111). 110

A.1 The epitaxial relation of $GdFeO_3$-type orthorhombic lattice on cubic substrate. The subscript "O" denotes orthorhombic lattice while "pc" denotes pesudo-cubic lattice. 138

B.1 (a) Schematic of the operation of RBS measurement. (b) An illustration of the elastic scattering of the incident ion by the immobile nuclei. 140
B.2 (a) The working principle of XPS and the relationship between different energy terms are illustrated. (b) A schematic of the setup of a laboratory-based XPS. . 142
B.3 Schematics of the scattering of incident ions by the outermost atomic layer in the LEIS measurement. 143

C.1 Chemical potential profile and Nyquist plot in a (a) surface-reaction-limited process and a (b) diffusion limited process (Figure adapted from [281]). 146

C.2 Equivalent circuit based on the derived charge flow response under small electrical perturbation (Figure adapted from [238]). Notice that the material is sliced into N slices. For a homogeneous material, position-independent material properties can be used. 148
C.3 (a) Equivalent circuit in half cells with large-area porous counter electrode (Figure adapted from [237]). (b) Equivalent circuit for thin-film epitaxial half cells with embedded counter electrode. 149

List of Tables

3.1 Correlation between the octahedral rotation tilting pattern and corresponding half-order peak conditions [65, 112] 35
3.2 A comparison of the crystal structure analysis techniques 38

6.1 Extracted structural parameters from X-ray diffraction studies for all heterostructures. Structural parameters for bulk LSGM are also included. 79

B.1 Summary of few surface sensitive thin-film chemistry characterization techniques144

C.1 Several commonly used passive electrical circuit element in EIS analysis 146

List of Symbols and Abbreviations

Symbols

ϵ_0	Vacuum permittivity
ϵ_r	Relative permittivity
$\epsilon_{\parallel}$	In-plane strain
$\epsilon_{\perp}$	Out-of-plane strain
γ_{fs}	Surface energy at the film-substrate interface
γ_{fv}	Surface energy at the film-vapor interface
γ_{sv}	Surface energy at the substrate-vapor interface
λ	Mean free path of the adatoms at the surface
μ_B	Bohr magneton
ν	Poisson's ratio
ν_0	Debye frequency
Φ_x	External magnetic flux
π	Archimedes' constant
ρ	Resistivity
σ	Conductivity
$\sigma_{\parallel}$	In-plane stress
$\sigma_{\perp}$	Out-of-plane stress
$\tan\delta$	Dielectric loss tangent
$\mathbf{a}^*$	Reciprocal lattice vector along x-direction

$\mathbf{a}_i$	Primitive lattice vector along i^{th} direction
$\mathbf{b}^*$	Reciprocal lattice vector along y-direction
$\mathbf{c}^*$	Reciprocal lattice vector along z-direction
G	Reciprocal lattice vector
$\mathbf{k}_i$	Wave-vector of the incident electromagnetic wave
$\mathbf{k}_o$	Wave-vector of the outgoing electromagnetic wave
R	Lattice vector in a crystal
a_f	Lattice constant of the epitaxial film
a_s	Lattice constant of the substrate
a_{hkl}	Lattice constant along *hkl*-direction
a_O	Orthorhombic lattice constant along x-direction
a_{pc}	Psudo-cubic lattice constant along x-direction
b_O	Orthorhombic lattice constant along y-direction
b_{pc}	Psudo-cubic lattice constant along y-direction
c_O	Orthorhombic lattice constant along z-direction
c_{pc}	Psudo-cubic lattice constant along z-direction
D	Diffusivity
d	Terrace width on a sngle crystal mis-cut substrate
E	Young's modulus
E_a	Activation energy
e_g	Doubly degenerated subgroup of *d*-orbitals
F	Faraday constant
f	Lattice mismatch between the epitaxial film and the substrate
f_O^{2-}	Atomic scattering factor of O^{2-}
F_{dep}	Deposition flux

F_{hkl} Structure factor at *hkl*-diffraction condition

j Current density

k^q Gas exchange rate constant extracted from electrical measurements

k^{chem} Gas exchange rate constant extracted from chemical-potential-driven measurements

k_B Boltzmann constant

n_x Density of nuclei

$Q_{\parallel}$ In-plane reciprocal lattice constant

$Q_{\perp}$ Out-of-plane reciprocal lattice constant

$r.l.u.$ Reciprocal lattice unit

T Temperature

t Tolerance factor of perovksite structure

t_{2g} Triply degenerated subgroup of *d*-orbitals

$T_{\eta,\zeta}$ Complex scattering factor along a specific Bragg rod

T_C Curie temperature

Abbreviations

AC Alternating current

AFM Atomic force microscopy

CDI Coherent diffraction imaging

CERDIP ceramic dual in-line package

COBRA Coherent Bragg rod analysis

CPE Constant-phase element

CTR Crystal truncation rod

CVD Chemical vapor deposition

DFT Density functional theory

ECR Electrical conductivity relaxation

EIS Electrochemical impedance spectroscopy

FWHM Full width at half maximum

LEIS Low-energy ion scattering spectroscopy

LSCF $La_{0.8}Sr_{0.2}Co_{0.2}Fe_{0.8}O_{3-\delta}$

LSGM $La_{0.9}Sr_{0.1}Ga_{0.95}Mg_{0.05}O_{3-\delta}$

LSMO $La_{0.7}Sr_{0.3}MnO_3$

PLD Pulsed-laser deposition

PVD Physical vapor deposition

RBS Rutherford backscattering spectrometry

RHEED Reflection high-energy electron diffraction

RSM Reciprocal space mapping

SQUID Superconducting quantum interference device

STEM Scanning transmission electron microscopy

TEM Transmission electron microscopy

TPB Triple phase boundary

UC Unit cell

XPS X-ray photoelectron spectroscopy

XRD X-ray diffraction

YSZ Yttria-stabilized zirconia

Acknowledgments

First and foremost, I would like to thank Prof. Lane Martin for the opportunity to work in this amazing laboratory and for carrying me through my graduate studies. Lane is a scientist and academic advisor with an essential combination of big-picture vision, encyclopedic knowledge, and attention to details. His emphasis on knowing everything of the experimental facilities, doing research in the right ways, and being a proactive learner has made the group an incomparable place to perform cutting-edge research. Again, thank you Lane for your continuous support and guidance in my research and the freedom you gave me to explore new ideas!

Brent was my first research mentor in Prometheus group, and he will continuously be the best in my mind. His enthusiasm, self-discipline, and rigorousness had really brought me on board as a researcher and a team player. Thank you for spending so much time in training me and bearing with me being a raw and stubborn student sometimes.

Zuhuang and Sungki had always been the go-to person whenever I encountered a problem in research. Their wide breadth of knowledge and modesty have taught me the essence of being a scientific researcher. Thank you for your kind advice and help, and I am sure we will grab lunch together again in the future.

Ruijuan is one of the most talented graduate students that I have ever met. Her passion, rigorousness, and consistency in research are merits that constitute the excellence in her career, and for me to learn for many years to come. Thank you for your inspiring advice in my research, and all the fun in our hot-pot parties.

Shishir has always been the most efficient person, and I hate to admit that this guy is one-step faster in everything. I feel lucky to have such a critical and intelligent mind around, and I have learnt a lot from you. You will always be one of my best friends and thank you for the good old jamming days!

Sahar is one of the few people who manages to have a perfect work-life balance, and will never hesitate to help with anything. Since we joint the group the same time, we have shared a very similar timeline, and been through many tough challenges together. Thank you for the good memories and best wishes for your new life in California!

Anoop, Eric, Josh, and Liv, you are the reasons that Champaign will always hold a special place in me. I have learnt a lot from you all and I gratefully thank you for all the help that made my research a lot more easier. And I would like to extend my thanks to all the current Prometheus group members, Jieun, Arvind, Eduardo, Gabe, Abel, Yizhe, Megha, Lei, David, Derek, Wenbo, for their help in my research, fruitful discussions, and being good friends and colleagues. Also, thank you Aileen for being a great team member in the PIRE program and I wish you all the best in your future graduate studies.

Moreover, I would like to thank my collaborators for their help and scientific inputs in many of my research projects. Thank Yongqi Dong and Dr. Hua Zhou for the analysis of X-ray diffraction data and it has been a fantastic experience working with you at the Advanced Photon Source. Thank Dr. Yakun Yuan and Prof. Venkatraman Gopalan for your help on the analysis of COBRA data and discussions on the experimental results. Thank

Dr. Sebastian E. Reyes-Lillo and Prof. Jeff Neaton for your insightful contributions in the theoretical understanding of antiferroelectric materials. Thank you Abhinav Jain and Prof. Dallas Trinkle for your expertise in vacancy diffusion calculation and it was a great time when we worked together on the ion-diffusion project. Thank Prof. Nicola Perry for your kind help and advice in understanding the electrochemistry, and thank Dr. Vincent Thoréton for the LEIS experiments and analysis.

In addition, I want to thank my dissertation committee members, Prof. Kristin Persson and Prof. Nitash Balsara, for their kind comments and guidance to keep me on track of my PhD studies. Thank Prof. Mark Asta and Prof. Junqiao Wu for serving in my qualify-exam committee and I will always cherish the advice you gave for my research. Thank you Prof. Elif Ertekin and Prof. Narayana R. Aluru for being great leaders in making the PIRE program a remarkable place to collaborate in research and to learn new things.

Finally, sincere thanks to my parents for their love and unconditional support for my graduate studies and decisions in life. I am glad that I have accomplished more than I would ever imagined five years ago.

Chapter 1

Structure-property coupling in perovskite oxides

This chapter provides the reader an introduction to the properties and applications of perovskite oxides and a detailed discussion on the central scientific question — How to control the properties of perovskite oxides by deterministically engineer the crystal structures. Driven by the potential applications in solid-state memory, low-energy logic circuits, and energy conversion, four representative perovskite systems — $SrRuO_3$ (magnetism/transport), $PbZrO_3$ (ferroelectricity), $La_{0.9}Sr_{0.1}Ga_{0.95}Mg_{0.05}O_{3-\delta}$ (ionic transport), $La_{0.8}Sr_{0.2}Co_{0.2}Fe_{0.8}O_{3-\delta}$ (electrochemistry) — are specifically chosen to reveal the correlation between crystal structure and the corresponding physical properties. I will first briefly recap the physical properties of perovskite oxides and introduce the detailed crystal structural features to be controlled and studied. I will then highlight the prior research work in understanding structure-property coupling in perovskite oxides and opportunities to be further explored. Finally, the goal, organization, and key findings of the dissertation are given.

1.1 Introduction to perovskite oxides

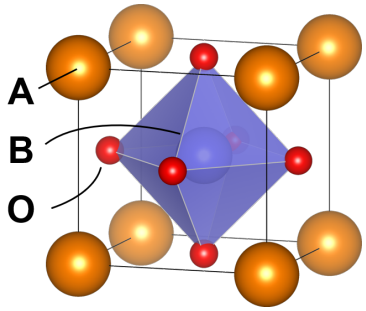

Figure 1.1: *Schematic of a cubic perovskite structure with formula ABO_3*

The term perovskite generally refers to the class of materials with ABO_3 chemistry as exemplified by the compound $CaTiO_3$. Later, the naming was extended to a more broaden description of chemical compounds that possess a chemical formula of ABO_3 and a similar crystal structure as compared to $CaTiO_3$.[1] A schematic structure of a cubic perovskite material is given by **Figure 1.1**, where the *A*-site cation sits at the corners of the cubic structure, the *B*-site cation is at the cubic body-center, and the oxygen anions are located at the face centers. The network of the oxygen anions forms a so-called oxygen octahedra of which the rotation and tilts are essential in determining the macroscopic physical properties. Over the past decades, there has been an increasing and extensive research interest in perovksite oxides due to the impressive variety of functionalities that are manifested therein. For instance, perovskite oxides have been demonstrated to exhibit ferroelectricity (*e.g.*, $BaTiO_3$) [1], magnetism (*e.g.*, $SrRuO_3$, $LaMnO_3$) [2, 3], multiferroicity (*e.g.*, $BiFeO_3$) [4], superconductivity (*e.g.*,$YBa_2Cu_3O_{7-\delta}$) [5], superior electrocatalytic activity (*e.g.*, $Ba_{0.6}Sr_{0.4}Co_{0.2}Fe_{0.8}O_3$) [6], *etc*.

Beyond the rich functionalities in such material systems, What makes perovskites more attractive for potential applications lies in the tunability of the physical properties via a range of structural engineering routes that are available in state-of-the-art thin-film synthesis technologies. In another word, novel structure distortions and emergent phenomena that do not present or difficult to achieve in either traditional material systems or bulk perovskite systems can be realized and well-controlled in thin-film heterostructures. For instance, in magnetic systems, the magnetic easy-axis of the ferromagnetic perovskite $La_{0.7}Sr_{0.3}MnO_3$ can be rotated by 90° if the oxygen octahedra are strongly coupled and modified by the underlying coupling layer or substrates [7]. In ferroic materials, in addition, saturated polarization [8], switching kinetics [9, 10], and domain structures [11, 12]

[1] In general, the formula of a family of perovskite structures can also be written as $A_{n+1}B_nO_{3n+1}$, where n is an integer number. One gets the conventional ABO_3 formula when n is infinity. If n is a finite number, the structure becomes so-called layered-perovskite-structure, or Ruddlesden-Popper structure where n indicates the number of repetition layers per unit cell

can be manipulated in a deterministic manner in thin-film heterostructures by properly engineering the symmetry and structure of the materials. Moreover, the charge transport in perovskites, *i.e.*, electrons/holes and ionic charges, are also found to be extremely sensitive to the lattice structure and local structural distortions. For example, the metal-insulator-transition temperature and magnitude in electronically conducting nicklates can be tuned by varying epitaxial strain [13], interfacial structural coupling [14], stoichiometry [15], *etc*. In ionically conducting perovskites, the diffusivity of oxygen vacancies in a range of materials are predicted and experimentally found to be largely dependent on the epitaxial strain [16, 17].

In general, perovskite structures possess short-range interaction between neighboring electron clouds such that the bonding between cations and anions has strong covalency. Such covalent bonding gives rise to marked sensitivity of electronic structures on the bonding length, bonding angle, local strain and chemistry, *etc*. In the archetypal ferroelectric $BaTiO_3$, for instance, the spontaneous polarization is a direct consequence of the strong hybridization between oxygen 2*p* orbitals and the empty titanium *d*-orbitals [18]. If one perturbs the covalent bonding by straining $BaTiO_3$ on a perovksite substrate, the saturated polarization can be enhanced by four-fold compared to bulk values, plus a significantly increased phase-transition temperature [8]. In transition metal perovskites, the situation can be a lot more interesting due to the transfer of *B*-site (transition metal) *s* electrons to the oxygen anions while the strongly correlated *d* electrons dictates the physical properties [19]. On the one hand, the localized electrons are interacting with the surrounding electrons and lattice atoms, which brings about a range of phenomena such as superconductivity, multiferroicity, magnetoresistance, metal-insulator transition, electrocatalytic activity, *etc*. On the other hand, the interaction between lattice degree of freedom and the charge, spin, orbital degrees of freedom indicates the potential of tuning material functionalities by perturbing one or few of the correlated degrees of freedom. In fact, emergent properties such as two-dimension electron gas, charge ordering, breaking of inversion-symmetry, *etc*. can be artificially created or engineered by controlling the lattice of perovskite materials.

Although the perovskite systems have demonstrated promising functionalities and high susceptibility to external engineering approaches, the exact relationships between various degrees of freedom in the system and the micro-/macroscopic properties are still to be thoroughly understood. Such knowledge, however, is truthfully needed to better consolidate the current theoretical modeling and provide new insights in better simulating complex structures. While from a material science standpoint, it is critical to utilize the advancing technologies and experimental designs to reveal the interrelationships among various material parameters and the potential routes to efficiently control the desired properties. The understanding, in turn, can be used as design guidance for novel material structures or chemistries with better functionalities. Thus, this dissertation will focus on the lattice degree of freedom in the perovskite systems and examine how the evolution of different structural features are impacting the overall physical properties. Here, I will first introduce the lattice degree of freedom in the perovskites and a range of specific distortions that can take place in the structure, which will then be further studied and characterized.

1.2 Lattice degree of freedom and structural features

Despite the fact that perovskite materials can be chemically described by a simple formula (*i.e.*, ABO_3), this family of compounds shows an enormous richness of structural flexibility and variants. Indeed, there are only a few perovskites that exhibit perfect cubic symmetry. One of the primary factors that determines the structure of a perovskite compound is the relative ionic size difference between *A*- and *B*-site cations. In 1926, Goldschmidt initiated the use of an empirical *tolerance factor* to determine if a specific chemical compound can form the perovskite structure, and if the structure will be distorted to lower crystal symmetry group compared to perfect cubic symmetry [20]. The Goldschmidt tolerance factor is the ratio of the ionic radii of both cations and anions that participate in the formation of perovskite structure, and the ratio is given by

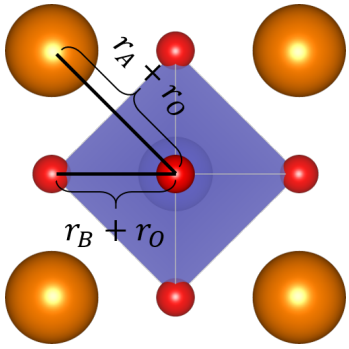

Figure 1.2: *Illustration of the parameters used in tolerance factor calculation. Note that atomic size is shown instead of realistic ionic size.*

$$t = \frac{r_A + r_O}{\sqrt{2}(r_B + r_O)} \tag{1.1}$$

where r_A, r_B, and r_O are the ionic radii of *A*-site, *B*-site, and oxygen ions, respectively. As one can see (**Figure 1.2**), the tolerance factor is a simple geometrical relationship between cation and anion ionic radii. If t is exactly 1, the inter-ionic distances follow the Pythagorean relationship. If $0.9 < t < 1$, the structure is typically cubic, namely, no structural distortion. While if $0.71 < t < 0.9$, the *A*-site cation is too small to fill the interstitial site, and thus the perovskite structure will distort (*i.e.*, systematic displacement of *A*-site cation and anions) and possess a lower symmetry group such as orthorhombic and rhombohedral. If $t < 0.71$, the perovskite structure will no longer be stable and other crystal structures start to form according to the stoichiometry of the compounds. This relationship between structure and ionic size further suggests that the crystal symmetry of perovskites can be purposely controlled by doping the *A*- or *B*-site with different cations.

Beyond the size-effect of cations on perovskite oxide structures, finer structural distortions are also related to the specific occupation of electrons at *B*-site cations. Such phenomena are especially significant in perovskites with an odd electron-occupancy in the *d*-orbitals. Briefly, given a perovskite system with the *B*-site cation being a transition metal with *d* electrons, the crystal field generated by a symmetric oxygen octahedra (*i.e.*, an octahedral cage with identical edge lengths) removes the five-fold degeneracy of the *d*-orbital and further split the orbitals into two sub-groups (**Figure 1.3**). The triply degenerated sub-group with lower energy is called t_{2g} orbitals while the doubly degenerated sub-group

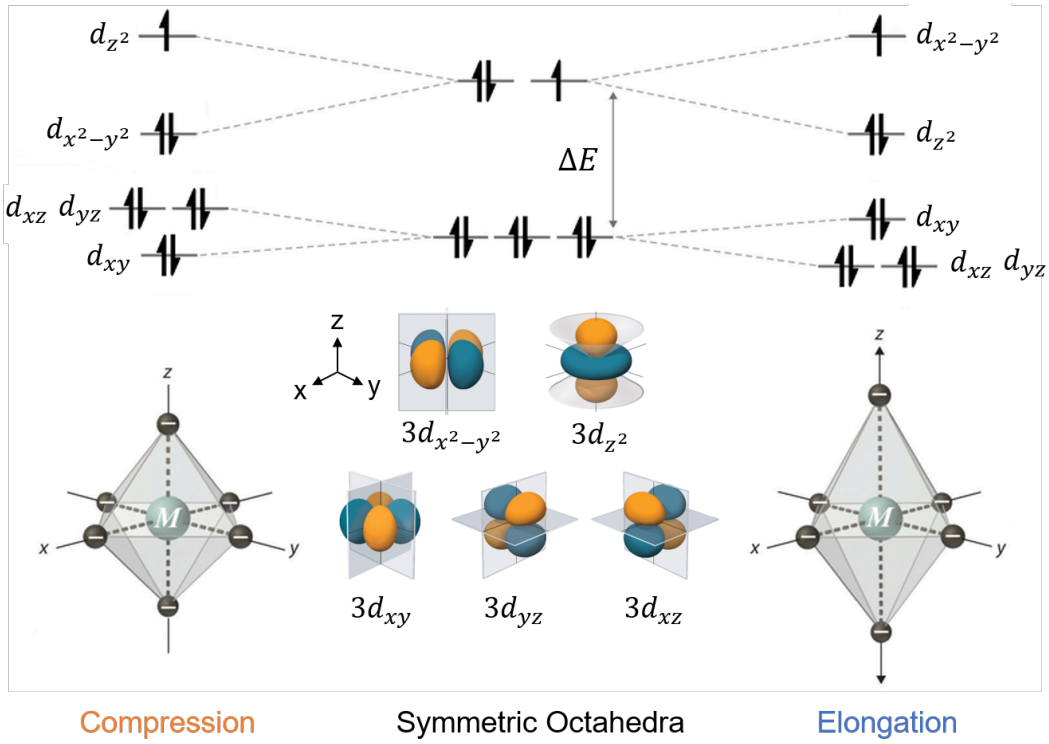

Figure 1.3: *Energy levels of B-site cation 3d orbitals in a octahedral cage. A schematic of shifted energy levels in compressed and elongated octahedra are also given.*

is called e_g orbitals.[2] The degeneracy, however, can be further lifted if one "stretch" or "compress" the octahedra. Under a certain electronic occupancy (d^9 system as an example, **Figure 1.3**), the resulting total energy in a low-symmetry octahedra is lower than that in a high-symmetry octahedra. Therefore, the octahedra are distorted at equilibrium. This type of octahedral distortion is called a Jahn-Teller distortion, proposed by Hermann Jahn and Edward Teller in 1937 [21].

As discussed above, the crystal structure of a perovskite system is strongly coupled with the chemical stoichiometry, cation type/radii, and electronic structure of the compound. Plus, *vice versa*, if one alters the chemistry and electronic structure of the compound, the structure of the material will change accordingly. In turn, at first look, it seems that since the structure of the material is dependent on the other degrees of freedom in the system, the crystal symmetry is determined once the other material parameters are known. This is essentially true in a stand-alone bulk system under no external perturbations. However, in thin films where a thin layer of material (*e.g.*, 2-100 nanometers thick) is epitaxially coupled with the underlying substrate or other epitaxial layers, the crystal structure can

[2]Here the letter *t* and *e* stand for triple and double degeneracy, respectively. Subscription *g* is the abbreviation of *Gerade* and indicates inversion symmetry of the d_{xy}, d_{yz}, d_{xz}, d_{z^2}, and $d_{x^2-y^2}$ orbitals.

indeed be controlled and manipulated independently and arbitrarily. The reason is that in the thin films, the external perturbations (*e.g.*, electrostatic boundary conditions, elastic boundary conditions, point defects and *etc.*) could have a larger energy that dominates the overall energetics of the system and determines the final state of the material. In turn, the coupling between the thin-film material and the external boundary conditions distorts the crystal structure to reach to equilibrium. As such, the manipulation of perovskite structure (namely, the lattice degree of freedom) can be effectively used as a "dialing knob" to engineer the material functionalities. Here, a brief explanation on the perovskite structural features that can be engineered and controlled is given first, while the details of how these structural features are related to the overall crystal symmetry and the engineering routes to manipulate these structural degrees of freedom will be discussed in depth in **Chapter 2**.

Three primary structural features in the lattice are considered in this dissertation: lattice expansion/compression, lattice monoclinic/triclinic tilting, and oxygen octahedral rotation. Briefly, as illustrated in **Figure 1.4**, the *lattice expansion/compression* is the systematic change in lattice parameters along three orthogonal directions. This change in lattice parameters is typically accompanied by a change in unit cell volume. Second, the *lattice monoclinic/triclinic tilting* essentially means that the crystal lattice is undergoing a shear deformation. The tilting is called monoclinic when the deformation takes places along one particular crystallographic axis, while it is triclinic as the lattice shears along three crystallographic directions. And third, *oxygen octahedral rotation* is the systematic displacement of oxygen anions from the face-center of the lattice, and can be visualized as the "rotation" of the rigid octahedral cage. Here, a rigid octahedron suggests that the change in octahedral edge length is negligible compared to the displacement of the oxygen from face-center. The three structural degrees of freedom can be controlled and characterized both individually and collectively, and thus their respective impact on material properties can be analyzed. Again, it is important to reiterate that the discussion on these structural features only applies to thin-film systems. In the bulk material, these structural features

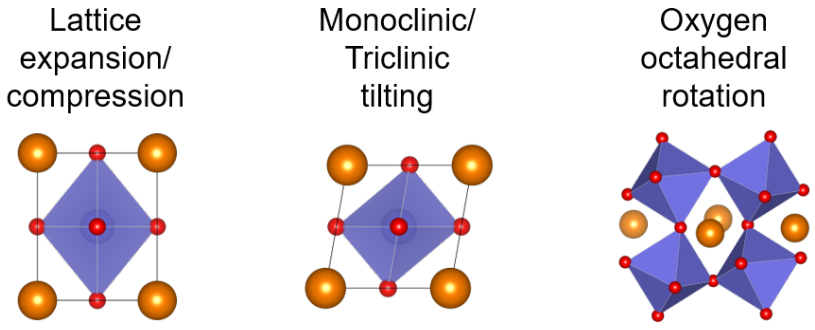

Figure 1.4: *Schematics of the three structural features that can be engineered in thin-film perovskite oxides: lattice expansion&compression, lattice tilting, and octahedral rotations*

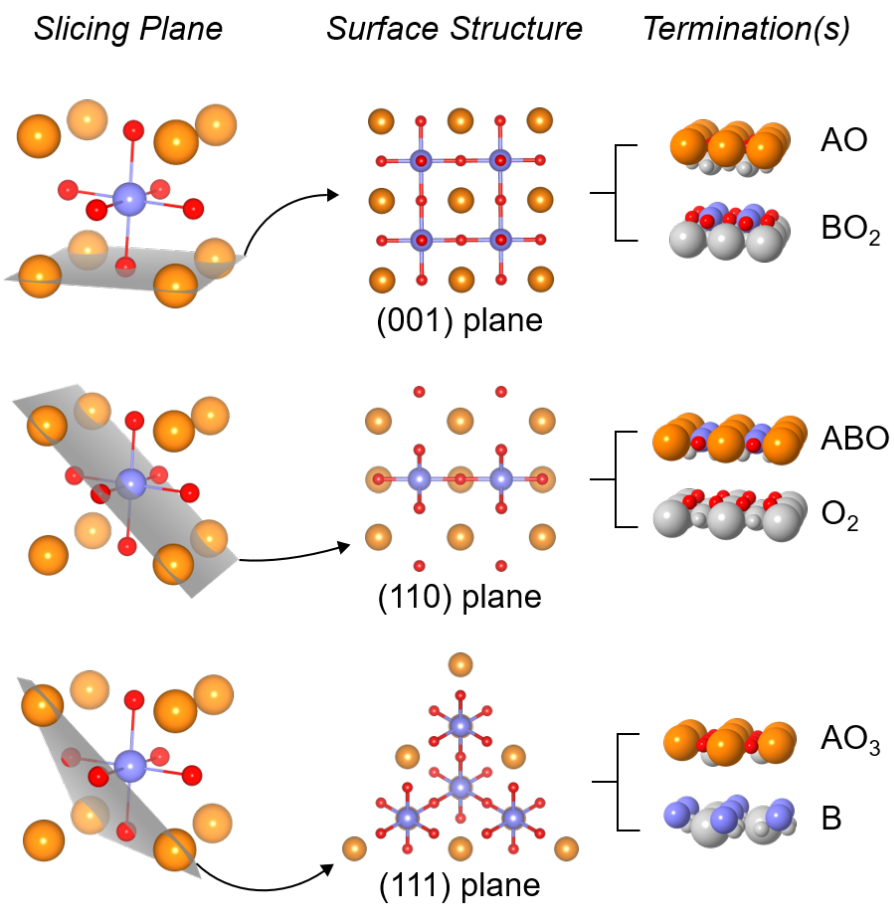

Figure 1.5: *Surface structure of perovskites at solid-gas interface can be effectively engineered by slicing the material along different lattice plane.*

are essentially determined for a given chemical stoichiometry, and the crystallographic symmetry group is a complete description of all the structural features that the material possesses. For instance, high-symmetry $SrTiO_3$ which belongs to group $Pm\bar{3}m$[3] at room temperature does not possess any lattice distortions [22]. $GdFeO_3$ at room temperature is an orthorhombic perovskite of which the crystal symmetry is given by $Pbnm$[4] [23]. This symmetry group contains both lattice monoclinic tilting and octahedral rotation, where the magnitudes of these two structural distortions are correlated.

[3] $Pm\bar{3}m$ is a cubic space group abbreviated from $P4/m\bar{3}2/m$. P stands for primitive lattice, $4/m$ means four-fold rotation symmetry along *x*-, *y*-, and *z*-axis with mirror plane perpendicular to the axes, $\bar{3}$ means three-fold rotoinversion along the body diagonal, the last $2/m$ means two-fold rotation symmetry along the face diagonal with mirror plane perpendicular to the axes.

[4] $Pbnm$ is an orthorhombic space group. P stands for primitive lattice, b means there's a *b-glide* plane perpendicular to *x*-axis, n means there's a *n-glide* plane perpendicular to *y*-axis, and m means there's a mirror plane perpendicular to *z*-axis.

Despite the structural changes that can be imposed in the lattice of perovskite thin films, the surface of the thin film is also subject to structural manipulations. Of the majority cases discussed in this dissertation, the surface is the two-dimension slice of material at the solid-gas interface (typically within a thickness of 1-2 nanometers). This means that the surface can be controlled by slicing the material along a variety of crystallographic planes where the arrangement of atoms on that specific two-dimension plane is fundamentally different from each other (**Figure 1.5**). As it can be seen from the figure that the surface structure can either be cubic lattice, rectangular lattice, or hexagonal lattice if the exposing crystal plane is (001), (110), or (111), respectively. In addition, depending on the exact position of the "slicing plane", the chemical formula of the two-dimension surface can be different. In another word, the termination at the material surface can be controlled. For instance, as indicated in the figure, the (001) surface of $SrTiO_3$ can either be *SrO* terminated or TiO_2 terminated, although both possess the same cubic lattice symmetry. As it pertains to interfacial or surface phenomena, the termination variation of $SrTiO_3$ plays a significant role. For example, if one grows an insulating material on top of $SrTiO_3$ surface with *A*-site and *B*-site cation taking a valence state of 3^+ (*e.g.*, $LaAlO_3$), the two terminations will give rise to drastically different interfacial properties, where the interface is conducting for TiO_2 termination but insulating for *SrO* termination [24].

1.3 Motivation and opportunities

The study on structure-property relationships in perovskite oxides is traditionally accomplished either by the mechanically twist the lattice or a change in the effective tolerance factor by chemical dopants. Due to the high Young's modulus[5] in oxides, applying mechanical stress on bulk perovskites is challenging as the material will crack under moderate mechanical strain. Also, limited types of physical measurements can be applied to the materials as it becomes difficult to reliably measure the properties while maintain the mechanical strain at the same time. On the other hand, although chemical dopants with different atomic sizes can effectively introduce structural distortions in the parent phase, the inclusion of exotic dopants makes the interpretation complicated as the intrinsic structural impact on properties is generally convoluted with secondary effects such as dopant-dopant interactions, dopant-defect interactions, changes in electronic structures, *etc*.

In the past decades, owing to the advances made in material synthesis, epitaxial thin-film heterostructure has emerged as an ideal route to achieve more precise and deterministic control over perovskite structures. Thin-film synthesis techniques such as atomic layer deposition, pulsed laser deposition, molecular beam epitaxy have shown the capability of creating high-quality single crystal thin films with crystallinity similar or better than that

[5]Young's modulus is defined as $E = \sigma/\epsilon$ where σ and ϵ are stress and strain, respectively. High Young's modulus means the material is resistive to deformation but is subject to fracture

of the bulk material [25]. More importantly, the strong epitaxial coupling (*i.e.*, epitaxial strain, epitaxial orientation, *etc*.) between film and substrate can significantly modify the structure of the film where the degree of modification on the structure is controllable by properly choosing the lattice mismatch between the film and the substrates [26, 27]. For instance, a wide range of domain structures can be controlled and achieved in ferroelectric $PbZr_xTi_{1-x}O_3$ or multiferroic $BiFeO_3$ thin films by epitaxially strain the film from compressive to tensile strain [11, 28–30]. At the same time, the polarization and lattice symmetry of these two ferroic materials can also be effectively modified if growing the material along either (001), (110), or (111) crystallographic direction [9, 31]. Moreover, a more aggressive modification of the crystal structure can be achieved near the interfacial region of the epitaxial layer where the crystal symmetry can be drastically different from the bulk materials [32–34]. Thus, compared to conventional chemical or mechanical routes, the epitaxial techniques allows for structural modification in pristine model system without the introduction of unwanted contributions from chemical variants, strain inhomogeneity/gradient, dislocations, *etc*, which allows for quantitative analysis of the structure-property coupling effects.

Adding to this is the advances in modern thin-film characterization techniques that allows for precise quantification of the structural changes in the materials. On the one hand, diffraction techniques such as high-resolution transmission electron microscopy and phase-retrieval X-ray diffraction are shown to resolve the position of atoms at a precision level of tens of picometers [35–37], and the positions of cations and anions in the perovskite lattice can both be determined. Recent studies utilizing these techniques have successfully demonstrated the capability of quantifying structural changes at atomic level in thin-film heterostructures, and have also suggested the richness and complex nature of structural changes that can take place in perovksite oxides under specific boundary conditions. For example, the surface atomic structure of highly catalytic $La_{1-x}Sr_xCoO_3$ has recently been revealed via X-ray diffraction techniques and the enrichment of strontium cation at surface is suggested to be critical to the electrocatalytic properties of the material [38]. The octahedral rotation tilts in nickelates can be clearly resolved by high-resolution transmission electron microscopy, and have been used to engineer the metal-insulator-transition behaviors [14]. These insights, which are typically difficult to extract in traditional studies, shed light on the structure-property relationship in perovskites and lay the foundation for engineering superior functionalities in these materials.

In turn, in recent years, there has been a growing interest in the fundamental understanding of the structure-property correlations in a number of perovskite oxide materials with simple chemistry and lattice symmetry. These initial studies have provided vital insights for understanding the material behaviors in strongly-correlated systems, and have suggested new routes to better control the structure and the corresponding physical properties. Additionally, the universality of strong structure-property coupling discovered in these studies further indicates the necessity of perform a systematic study on a broader spectrum of materials, especially those with great technological importance but a more complex stoichiometry or lattice structures.

1.4 Statement and organization of the dissertation

Driven by the above motivations, the goal of the dissertation is to understand and unravel the structure-property relationships in a number of representative perovskite systems. To do that, I establish the detailed and quantitative correlation between the perovskite structural features and the physical properties by leveraging the modern thin-film synthesis techniques and a range of state-of-the-art characterization approaches. A systematic study approach is adopted which embraces thin-film material synthesis, structural engineering, structural characterization, and the measurement of corresponding physical properties. Motivated by the technological importance, I focus on four model perovskite systems with characteristic physical properties including magnetism ($SrRuO_3$), ferroelectricity ($PbZrO_3$), charge transport ($La_{0.9}Sr_{0.1}Ga_{0.95}Mg_{0.05}O_{3-\delta}$, LSGM), and electrochemistry ($La_{0.8}Sr_{0.2}Co_{0.2}Fe_{0.8}O_{3-\delta}$, LSCF).

Specifically speaking, $SrRuO_3$ is a widely-studied ferromagnetic conductor that can be epitaxially grown very well as a bottom electrode for other functional layers. The simplicity of its crystal structure and the moderate correlation of its electrons make $SrRuO_3$ a first choice to examine the efficacy of various structural engineering routes and the impacts of structural changes on physical properties. The demonstrated structural engineering approaches can be used to control the magnetic/electronic transport properties of $SrRuO_3$ and to be utilized in the engineering of other material systems. Second, $PbZrO_3$ is chosen as an example to illustrate the control of ground-state lattice symmetries and the electrical switching properties. A drastically different switching behavior can be achieved via the engineering of the lattice symmetry by growth-mediated antisite defects. Third, owing to the high ionic conduction for applications in the energy-conversion devices, LSGM is chosen as a model ion-conducting perovskite to reveal the detailed impacts of structural distortions on ionic transport properties. With atomic-scale structural control and characterization, transport measurements, and theoretical modeling, this study presents the first systematic and quantitative study of the structure-property relationships in a ion-conducting perovksite oxide. And lastly, LSCF is picked as a model electrochemically active perovksite to reveal the correlation between surface structures as mediated by growth-orientations and gas-exchange kinetics. The significant enhancement of gas-exchange kinetics on the (111) surface reveals the strong surface-structure dependency of electrochemical activities, and the potential surface-engineering routes towards better device efficiency.

This dissertation is organized as the following. **Chapter 2** and **Chapter 3** are introductory chapters that details the general experimental techniques that will be applied to control and characterize the material properties. **Chapter 2** focuses on a brief introduction to the control of perovskite structures using epitaxial techniques. Pulsed-laser deposition is discussed as the major route of material synthesis throughout this dissertation. Next, a range of engineering routes such as epitaxial strain, interfacial structural coupling, growth-mediated defects, and orientational growth control are introduced. In **Chapter 3**, I first discuss how to quantify the structural features in the materials using X-ray diffraction

techniques, and will also include discussions on the measurement techniques for reliable extraction of physical quantities.

Chapter 4 focuses on the structural control of a model itinerant ferromagnetic material $SrRuO_3$ and the corresponding impact on its magnetic and electrical transport properties. I will apply interfacial structural coupling as a novel route to engineer the perovksite lattice structure beyond epitaxial strain, and I have found that the symmetry of $SrRuO_3$ can be readily manipulated. With the established structural engineering and characterization, the magnetic and electrical transport properties of $SrRuO_3$ are examined and found to be controllable via interfacial structural coupling.

Chapter 5 details structural engineering via growth-mediated antisite defects in ferroic material systems. Antiferroelectric $PbZrO_3$ thin films are synthesized with a slight variation in cation ratio, and it is revealed that an excess in lead content changes the lattice symmetry from orthorhombic to rhombohedral. Such lattice symmetry change is a result of the induced lead antisite defects, which stabilize a ferroelectric rhombohedral phase in an antiferroelectric material.

Chapter 6 is the culmination of the study where I apply a systematic structural control on a ion-conducting perovksite material (LSGM), and have managed to deterministically design a structure to achieve superior ionic conductivity. This study reveals that there exists a strong structure-transport coupling in the oxygen vacancy migration in perovskite lattice, and the optimal design of the structure is to simultaneously obtain a large lattice volume and large octahedral rotation magnitudes.

Chapter 7 takes a different approach from lattice control in perovskites and primarily focuses on the correlation between electrochemical activity and surface structures (varied epitaxial orientations) in a model electrocatalytic perovksite LSCF. A new device structure is designed to perform a series of electrochemical characterizations, and the results have shown that polar (111) surface has the best electrochemical activity.

Chapter 2

The control and manipulation of perovskite structures

This chapter focuses on the manipulation of structural degrees of freedom in perovskite oxides using thin-film epitaxy. First, pulsed-laser deposition is introduced as a thin-film growth technique for the synthesis of high-crystallinity materials. Next, epitaxial-strain engineering is discussed as a route to control the perovskite structures and the effects of epitaxial strain on structural evolution are discussed. An alternative route to control the structures via growth-mediated antisite defects is introduced, which indicates the importance of stoichiometry control in the study of structure-property coupling effects. Beyond strain engineering, additional structural manipulation can be achieved near the heterostructure interface, and the interfacial structural coupling effects will be developed as an emerging route to engineer thin-film properties. Finally, the control of perovskite surfaces is achieved via epitaxial growths along different crystallographic orientations.

2.1 An epitaxial thin-film approach

As indicated by the name,[1] epitaxial thin films are synthesized by growing a crystallized material on top of the substrate material which possesses a similar crystal structure. There's a variety of ways to establish the epitaxial relations. If the epitaxial layer has the exact same chemical composition and lattice structure compared to the underlying substrate, such epitaxial relation is termed *homoepitaxy*. While if the epitaxial layer has a different lattice parameter, the epitaxial relation is called heteroepitaxy (**Figure 2.1**). In heteroepitaxy, the lattice mismatch between the epitaxial film and the substrate is given by

$$f = \frac{a_s - a_f}{a_f} \tag{2.1}$$

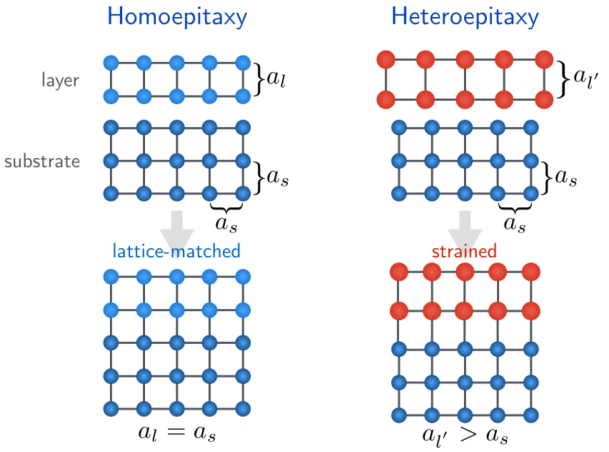

Figure 2.1: *An illustration of homoepitaxy and heteroepitaxy in perovskite thin-films. Note that compressive strain is shown in the heteroepitaxy.*

where a_s and a_f refer to the substrate lattice constant and film lattice constant, respectively. Due to such lattice mismatch a mechanical deformation is induced in the epitaxial layer either in the form of tensile ($a_s > a_f$) or the compressive ($a_s < a_f$) stress which induces strain. Such mechanical deformation from bulk lattice, so-called *epitaxial strain*, can be as large as 2-3% (6% compressive as a record high in $BiFeO_3$ thin films [29, 39, 40]) and introduces a significant structural change in the epitaxial layer. These strains are an order of magnitude higher than where these materials would typically crack in the bulk form [41, 42]. Additionally, although the schematic gives an example of epitaxial growth along [001], the substrate material can be sliced along various crystallographic planes. Consequently the epitaxial layer will also grow along the specific plane where the surface structure can be modified. At the same time some specific physical properties that are strongly correlated with the crystal axes (e.g., magnetism and ferroelectricity) can be engineered effectively [9, 10, 43–45]. Beyond the structural deformation induced by epitaxial strain, near the interfacial region the interfacial structural coupling introduces an additional set of structural distortions in the lattice [32, 46], which can be utilized to further engineer the properties of ultra-thin epitaxial films and will be discussed more in detail later in this chapter.

There are a number of ways to synthesize epitaxial structures in modern materials science. In general, the methodology is categorized into chemical vapor deposition (CVD)

[1]The word *epitaxy* can be decomposed into "*epi*" which means above, and "*taxis*" which means in an ordered manner.

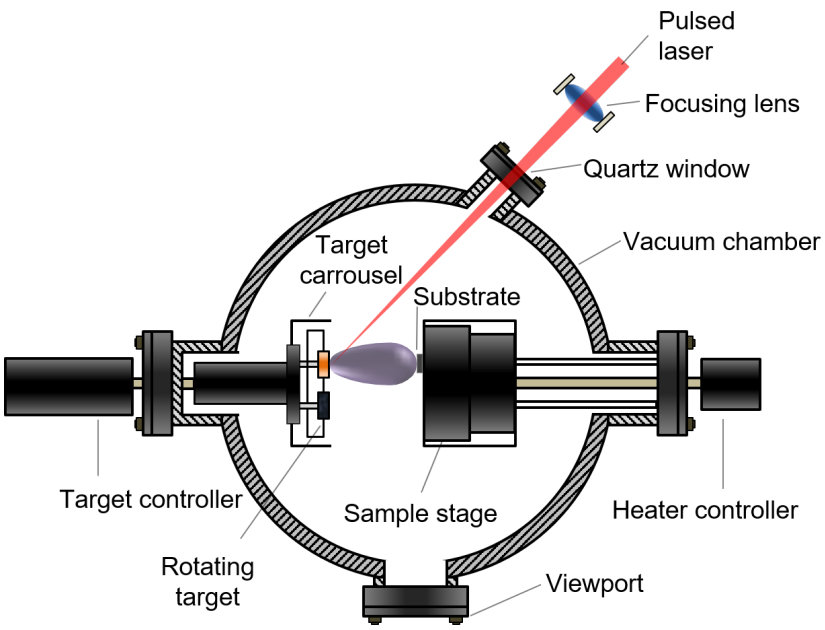

Figure 2.2: *The setup of pulsed-laser deposition.*

and physical vapor deposition (PVD). In the CVD approaches, vaporized chemical precursors react and form crystallized solid phase on top of the heated substrate surface. CVD has the advantage of high growth rate, uniformity, and is typically capable of synthesizing a wide range of compounds [47]. While PVD approach is to evaporate the solid-phase compound and deposit the material onto heated substrates. PVD has the advantage of using a relatively simpler operational process, lower processing temperature, and the capability of achieving atomic level control of chemical composition [48]. Both approaches are able to produce high-quality crystallized thin films while the choice is typically based the specific target material and requirements. For perovskite oxide materials, the most widely applied techniques for laboratory studies are PVD-based molecular beam epitaxy (MBE) and pulsed-laser deposition (PLD), and PLD is the main focus of this dissertation [49, 50].

Pulsed-laser deposition of thin-film perovskite oxides

PLD is a thin-film growth technique that has a wide-spread implementation in laboratory work which requires precise chemical/structural control and rapid prototyping of materials [51]. Briefly, PLD is a process where a pulsed high-energy ultra-violent laser beam is focused onto the target material inside a vacuum chamber, and the evaporated plume reaches to the heated substrate to form solid-phase compounds (**Figure 2.2**). PLD is able to synthesize materials with either exact stoichiometric transfer from target to substrate, or materials with deviated stoichiometry depending on the growth parameters used

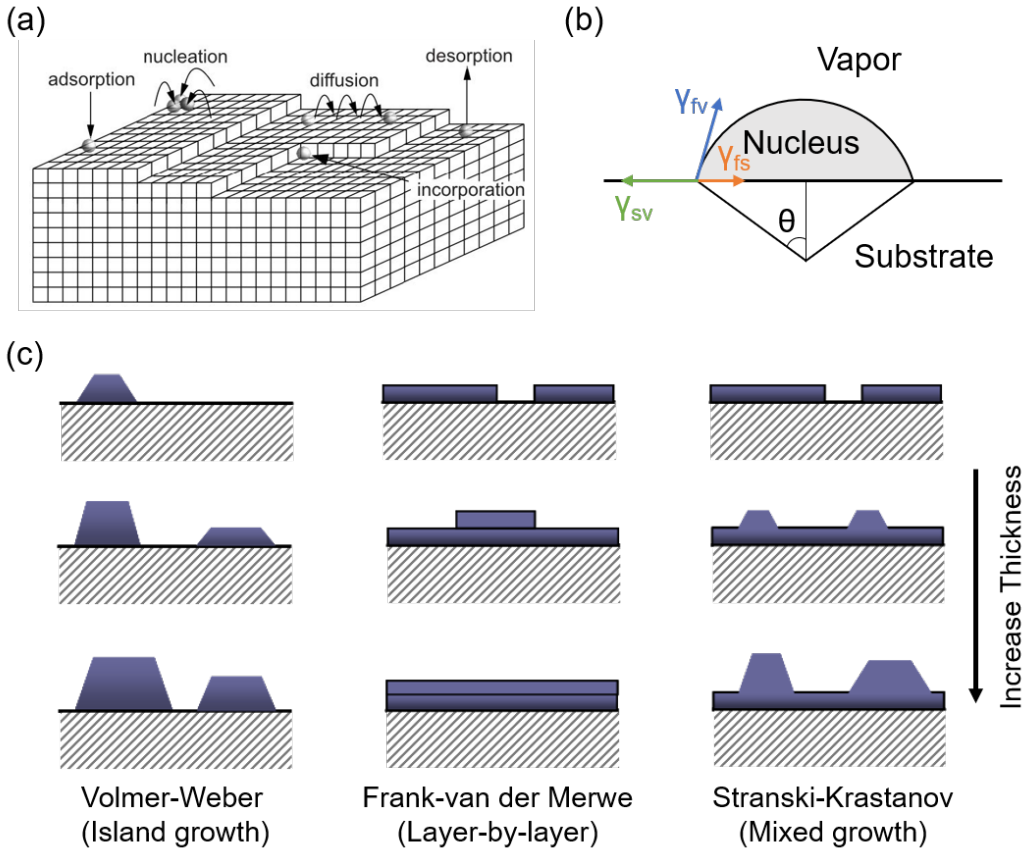

Figure 2.3: *(a)The microscopic steps during the growth of perovskite oxides. (b)Schematic of atomic nucleation process during film growth. (c)Illustration of the three thin-film growth modes at near-equilibrium conditions*

in a specific synthesis. The sensitivity to the growth parameters varies depending on specific materials to be synthesized, while, in general, there are few key growth parameters but not limited to that affect the stoichiometry and quality of the products: *a*. substrate temperature; *b*. gas partial pressure (typically oxygen and sometimes argon or vacuum); *c*. laser fluence on target (energy per area); *d*. substrate-target distance; *e*. offset of the substrate from the center of the plume.

One of the major efforts in the synthesis of desired epitaxial thin films is the systematic optimization of the growth parameters as each material system has its specific combination of optimal growth conditions. variations in material-growth conditions are rooted in the fact that PLD is a kinetic-growth process where each step of the process is strongly depending on the energetics of the ionized species. The formation of solid phases includes the adsorption of atoms, diffusion of atoms to the nucleation sites, formation of new growth nuclei, and also the desorption of adatoms (**Figure 2.3**(a)). Depending on the growth parameters, the rate of each step is varied and thus the resulting stoichiometry, surface rough-

ness, crystallinity and chemical ordering in the film are drastically affected. For instance, although a stoichiometric growth is desired and achievable in the synthesis of $NdNiO_3$ thin films, a slight change in the laser fluence from the optimal value can give rise to a 15% change in the cation ratio ([Nd]:[Ni]), and the resulting metal-insulator-transition behaviors in the material is completely different from stoichiometric films [15]. On the other hand, a smoother surface and better crystallinity can be achieved in the $NdNiO_3$ thin films if a so-called interval growth is used where a sequence of high-frequency laser bursts is fired, and a small waiting time is given in between each burst to let the surface reconstruct [13]. The number of pulses per burst is determined such that each burst will give rise to the growth of exact one monolayer of material. Here, I will briefly discuss the thin-film growth kinetics in a PVD process, and the technique to monitor the growth dynamics. The readers are guided to a number of papers that take a deep dive into the growth control in a variety of perovskite materials [52–56].

With the purpose of achieving efficient structural control, a smooth and high-quality epitaxial film surface is required. Under conditions close to thermodynamic equilibrium, the surface smoothness and film quality are strongly affected by the nucleation process during the growth. Three different growth modes are typically observed in thin-film material growth depending on the thermodynamic surface energies in materials and interfaces. The mechanical equilibrium among the horizontal components of the interfacial tensions between constitutive phases is described by *Young*'s equation

$$\gamma_{sv} = \gamma_{fs} + \gamma_{fv}\cos(\theta) \tag{2.2}$$

$$\cos(\theta) = \frac{\gamma_{sv} - \gamma_{fs}}{\gamma_{fv}} \tag{2.3}$$

where γ_{sv}, γ_{fs}, γ_{fv}, and θ refer to the surface tension at the substrate-vapor, film-substrate, and film-vapor interfaces, and the wetting angle, respectively (**Figure 2.3**(b)). With the purpose of depositing a smooth and coherent surface, the wetting angle should ideally be zero. In this scenario where $\gamma_{sv} \geq \gamma_{fv} + \gamma_{fs}$, the atoms are more likely attached to the substrate surface than to themselves and the growth is categorized as Frank-van der Merwe growth mode, or layer-by-layer growth mode (**Figure 2.3**(c)). To get high-quality layer-by-layer deposition one needs a film and substrate with small differences in surface energies and the film material is better to have smaller surface energy compared to substrate material. These energies, however, are extremely sensitive to the growth parameters. In turn, if such ideal energetics of materials are not satisfied, a rough film surface can be formed where the growth mode is essentially Volmer-Weber, or island growth mode. In island growth mode, the wetting angle $\theta < 0$ and thus $\gamma_{sv} < \gamma_{fv} + \gamma_{fs}$. In some cases where the lattice mismatch between the film and substrate is large, the layer-by-layer growth is initially happening for a few mono-layers and subsequently taken over by island growth mode. Such mixed growth mode is called Stranski-Krastranov growth mode.

The three growth modes discussed above apply for situations where the growth process is essentially close to thermodynamic equilibrium (*i.e.*, high substrate temperature and

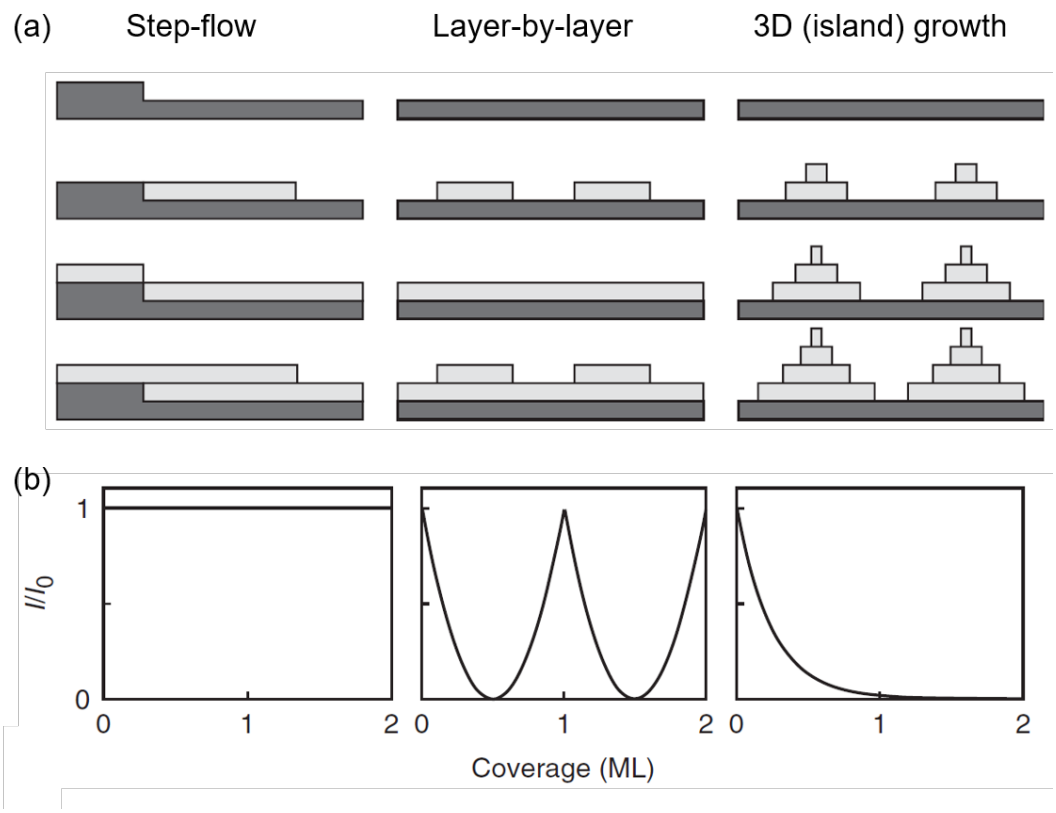

Figure 2.4: *(a)Microscopic illustration of the growth kinetics under varied conditions. (b)The theoretical surface roughness as function of time (surface coverage) under three different growth kinetics (Figure adapted from [57]).*

low vapor flux). However, such conditions are not always satisfied. Quite in contrary, PLD growth is typically away from equilibrium, where the resulting morphology of the films is more influenced by the growth kinetics rather than thermodynamics. In another word, the final morphology of the film is determined by the hierarchy of diffusivity of adatoms on the exposing surface as compared to the deposition rate which is controlled by a number of growth parameters such as laser spot size, laser fluence, gas pressure, and *etc*. Thus, the detailed kinetics and mechanism is far from trivial and is above the scope of the dissertation. Nevertheless, there are some general rules that one should keep in mind while performing controlled PLD growth.

At a given growth temperature, the diffusivity of adatoms (four possible jumps to the nearest neighbors) on the 2D surface is given by

$$D = \frac{d_{nn}^2 v_0}{4} e^{-\frac{E_m}{k_B T}} \tag{2.4}$$

where d_{nn} is distance of the nearest neighbor site that equals to the jump length. v_0 is the jumping frequency on the order of 10^{13}Hz [57], and E_m is the activation energy barrier

for the adatoms to migrate from one site to another. In the kinetic regime, assuming that there are n_x nuclei on the surface under a fix deposition flux F_{dep}, the density of the nuclei can be derived and is given by [58]:

$$n_x = \frac{1}{4}(\frac{D}{F_{dep}})^{-\frac{1}{3}} \tag{2.5}$$

Now assuming that the adatoms travel an averaged distance of λ to reach to another nucleation site, then if we draw a circle with radius λ at each nucleation site, the ensemble of the circles should fully cover the substrate surface. Thus, if the density of the nucleation sites is normalized, the relationship is given by:

$$n_x \pi \lambda^2 \approx 1 \tag{2.6}$$

and thus,

$$\lambda \approx \sqrt{\frac{1}{\pi n_x}} \approx (\frac{D}{F_{dep}})^{\frac{1}{6}} \tag{2.7}$$

On a substrate with a fixed terrace width[2] d, if λ is larger than d, the adatoms can easily reach to the terrace edge and no islands will form as all atoms are flowing along the ascending substrate steps. This growth kinetic is called step-flow growth (left panel in **Figure 2.4**(a)) where the roughness of the film surface is not changing over time. If one probe the surface roughness *in situ* by diffraction techniques using electrons, X-ray, or Helium atoms, the intensity of the diffracted spot remains constant throughout the growth (left panel in **Figure 2.4**(b)). On the other hand, if λ is smaller than d but the adatoms on top of the nucleation island can descend, the roughness of the film will go through a periodic change over time where the maximum roughness is reached when half of the surface area is covered with nuclei (middle panel in **Figure 2.4**(a-b)). In this layer-by-layer growth kinetic, the thickness of the film can be precisely monitored and the detailed monitoring technique will be discussed in the following section. Lastly, if λ is smaller than d but the adatoms experience a high energy barrier to mobile away from the top of the nucleation site, the resulting film morphology is rough and such growth kinetic is called 3D growth (right panel in **Figure 2.4**(a-b)). In some material systems such as $SrRuO_3$ [59] or $PbZrO_3$ [60], the growth dynamic can transit from one to another depending on the thickness of the film.

As one can notice from Equation 2.7 that growth kinetic of the material is manipulable by varying the deposition rate and diffusivity of the adatoms. In most of the cases in this dissertation, we specifically grow under the layer-by-layer growth kinetics under the

[2]If a crystallized material is cleaved along a specific lattice plane and forms a vicinal surface, terraces are typically observed with a fixed terrace height of one unit cell but a varied terrace width depending on the polishing angle. The origin of the terraces is from the fact that the polishing angle is practically difficult to be exactly parallel to the lattice plane. The higher difference between the polishing surface and the lattice plane (so-called mis-cut angle), the narrower the terrace width would be.

circumstances that the thickness of the material and surface quality are to be precisely controlled. To do that, we use reflection high-energy electron diffraction (RHEED) to perform *in situ* surface roughness/structure monitoring. The technical details and operation of RHEED will be discussed in the following section.

RHEED-assisted thin-film growth

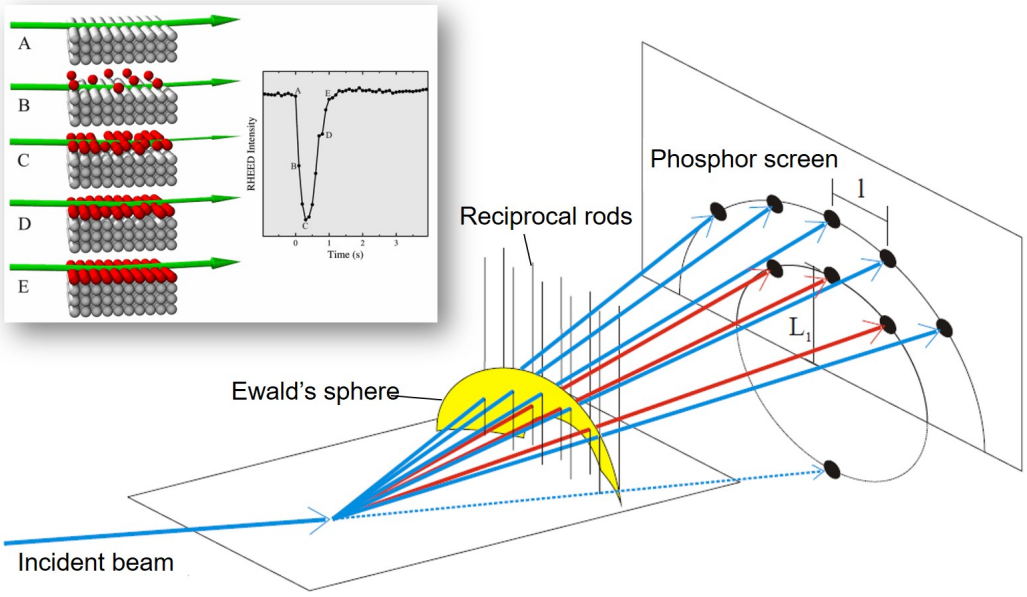

Figure 2.5: *Schematic of reflection high-energy electron diffraction (Figure adapted from [61]). The inset gives an example of the intensity oscillation of the diffraction spot during the growth of one monolayer.*

RHEED is a powerful tool to examine the surface structure during the thin-film growth and to deterministically control the synthesis process. The name is based on the fact that the incident angle of the electron beam is typically around 1°-3° such that only the surface portion of the film is measured, and the incident electron beam energy is on the order of 10k*eV* to 60k*eV* depending on users' specifications. Here I will give a brief introduction to the operation principle of RHEED and how to interpret the diffraction data.

Due to the fact that the electron beam will only examine the very top layers of the crystallized material, the reciprocal space seen by the electron beam is no longer single spots. Taking simple cubic lattice as an example, the reciprocal lattice vector in the z-axis (out-of-plane) is given by

$$\mathbf{c}^* = \frac{2\pi}{c}\hat{\mathbf{z}} \tag{2.8}$$

where c is the out-of-plane lattice constant and $\hat{\mathbf{z}}$ is the unit vector in the reciprocal space. Since the lattice is essentially a 2D plane ($c = 0$), the reciprocal lattice becomes infinitely long rods that are aligned in the out-of-plane direction. For non-cubic lattices, the arrangement of the rods is more complicated compared to cubic lattice. If the Ewald's sphere is drawn on the reciprocal surface, the intersects between the Ewald's sphere and the reciprocal rods satisfy the diffraction condition

$$\mathbf{G} = \mathbf{k}_i - \mathbf{k}_o \tag{2.9}$$

and a diffraction spot can be seen on the phosphor screen. Here, k_o is the wavevector of incident beam while k_i is the wavevector at any intersects between the Ewald's sphere and the reciprocal rods. During the operation, the diffraction spot intensity is monitored. As given in **Figure 2.5**, the diffraction intensity is maximized when the surface is smooth and will start to drop as nucleation starts to form and disrupts the width and sharpness of the reciprocal rods. Once the surface is fully covered with a smooth monolayer of deposited material, the diffraction intensity is back to maximum, giving rise to intensity oscillation during the growth. Therefore, the exact thickness and termination of the deposited thin film can be deterministically controlled. For instance, in the growth of $SrRuO_3$ on $SrTiO_3$ (001) substrates, the surface reconstruction process is termination-dependent and can be monitored by RHEED. If the $SrTiO_3$ is *SrO* terminated, the growth of $SrRuO_3$ starts with layer-by-layer immediately and the RHEED oscillation has a constant periodicity. However, if the $SrTiO_3$ is *TiO_2* terminated, RHEED oscillation will not start till 1-2 unit cells of $SrRuO_3$ are deposited. The reason is that *RuO_2* is not a stable termination and slowly decomposes until the surface is fully *SrO* terminated for continuous layer-by-layer growth [62]. Additionally, surface morphology, surface crystal structure, and growth mode can be obtained by analysing RHEED diffraction patterns. For instance, the surface structure of single crystal $SrTiO_3$ can be examined by RHEED [63]. An realistic iron oxide growth mode analysis using RHEED is also given in **Figure 2.6** where different growth conditions results in a rich spectrum of growth kinetics.

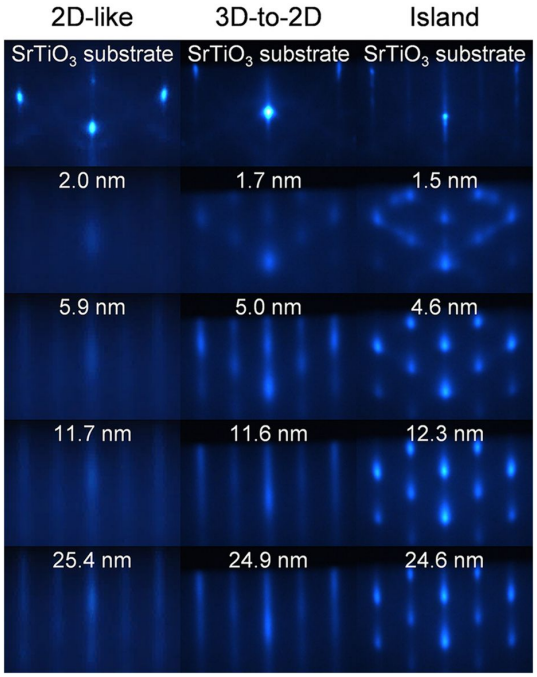

Figure 2.6: *A collection of realistic RHEED patterns of Fe_3O_4 thin films grown under various growth modes (Figure adapted from [52]).*

2.2 Control of lattice structures in perovksite thin films

Lattice symmetry and octahedral rotation

Crystal materials are solid phase materials with highly-ordered arrangement of constituent atoms, where the ordering can be decomposed into crystal lattice and lattice basis (**Figure 2.7**(a-b)). The crystal lattice is a three-dimensional pattern that describe the periodicity in the space and each lattice point is given by

$$\mathbf{R} = n_1\mathbf{a}_1 + n_2\mathbf{a}_2 + n_3\mathbf{a}_3 \tag{2.10}$$

where n_i are integers and $\mathbf{a}_i$ are primitive vectors in different directions and span across the entire space. Such infinite array of discrete points generated by sets of discrete translation operations is termed *Bravais lattice*. Depending on the magnitudes of n_i and the spacial alignment of between a_i vectors, there are in total 7 lattice systems which is further divided into 14 Bravais lattices. In addition to the 14 Bravais lattices, the basis also possesses a set of symmetry operations which can be described by 32 *point groups*. Point groups are discrete symmetry groups of Euclidean space that leaves the origin (lattice point) fixed. If one needs to describe the symmetry of the crystal symmetry as a whole, the Bravais lattice and point groups are combined, which generates crystal *space groups* that does not have a fixed origin and include symmetry operations such as translation, glide, and screw.

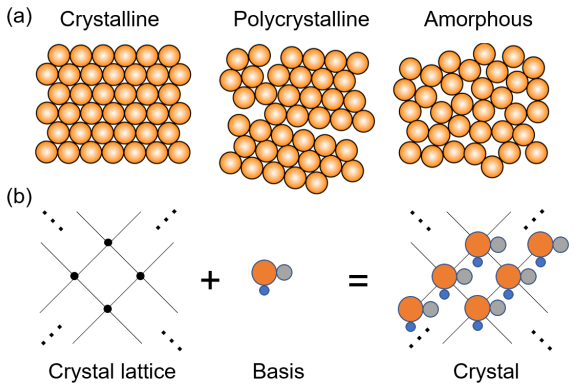

Figure 2.7: *(a)Illustration of crystalline, polycrystalline, and amorphous materials. (b)A schematic of the structure of a crystalline material. The structure of a crystal material can be described by crystal lattice plus basis.*

Knowing the exact space group of a crystalline material requires the fitting of a complete set of diffraction data. While in epitaxial thin-film systems, due to the practical difficulty in accessing all diffraction planes in the epitaxial systems (films are grown along a specific crystal plane with limited thickness), a more simplified approach is taken where some structural features are measured to compare with bulk structure and infer the change in crystal symmetries. As discussed in **Chapter 1**, three major structural features, *i.e.*, lattice expansion/compression, lattice tilting, and octahedral rotations, are typically measured in perovskite thin-film systems to examine the structural evolution (**Figure 1.4**). As the crystal symmetry of the material is changed, such change can be directly reflected on the change in magnitudes of the three structural features that can be easily quantified using either laboratory-based or more advanced synchrotron-based diffraction techniques.

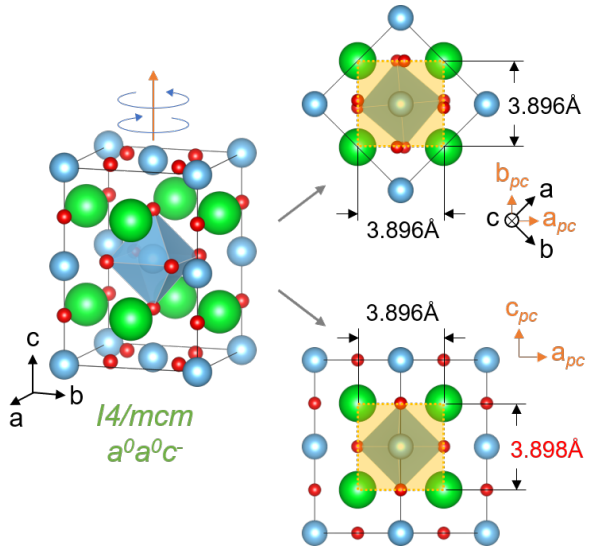

Figure 2.8: *Tetragonal $SrTiO_3$ at low temperature. The crystal symmetry transition from $Pm\hat{3}m$ to $I4/mcm$ can be represented by a expansion of the c-axis in pseudo-cubic unit cell plus out-of-phase octahedral rotation along the c-axis.*

The characterization of these structural features will be discussed later in **Chapter 3**. Here, the correlation between crystal symmetry and structural features is explained first.

Two representative space groups are given as an example. First, at low temperature (T<105K) the structure of $SrTiO_3$ evolves to tetragonal with space group $I4/mcm$ [22]. If one focuses on the pseudo-cubic unit cell of $SrTiO_3$ (**Figure 2.8**), the tetragonal symmetry can actually be represented by a expansion of the lattice along *c*-axis from 3.896Å to 3.898Å, and a systematic out-of-phase octahedral rotation along the *c*-axis. Here, out-of-phase octahedral rotation means that the two neighboring octahedra along a specific direction rotate towards different directions (*i.e.*, if one rotates clockwise the neighboring one rotates counterclockwise). Since the octahedra do not rotate along *a*-axis and *b*-axis, this particular rotation pattern can be described via Glazer notation system [64, 65] as $a^0a^0c^-$.[3]

A second example is given for $DyScO_3$, which is an orthorhombic crystal system at room temperature with space group $Pnma$ [66]. This crystal structure is common for most of the transition-metal perovskite systems where the *A*-site cation is relatively small and the tolerance factor is less than 0.9. For such orthorhombic system, the conversion between orthorhombic lattice and pseudo-cubic lattice is detailed in **Appendix A** and the structural features that can be used to describe the orthorhombic lattice is also illustrated (**Figure 2.9**). First of all, the pseudo-cubic lattice of $DyScO_3$ has low symmetry that it has monoclinic tilting with a tilting plane perpendicular to the *b*-axis. Plus, the lattice constant along *b*-axis is 3.951Å, slightly larger than that along the other two edges (3.947Å). Additionally, the octahedral rotation pattern in $DyScO_3$ is given by $a^-a^+c^-$,[4] where the in-phase rotation axis is aligned with the *b*-axis.

[3]In Glazer notation, the three letter indicates the rotation magnitudes along *a*-, *b*-, and *c*-axis, respectively. Same letters means that that the rotation magnitudes are the same. Superscript represents the phase relation between the neighboring octahedra where + means in-phase, - means out-of-phase, and 0 means no rotation. In this case, $a^0a^0c^-$ means that there is no rotation along *a*- and *b*-axes but has out-of-phase rotation along *c*-axis.

[4]This notion means there is out-of-phase octahedral rotation along *a*- and *c*-axis with different magnitudes while the rotation along *b*-axis is in-phase, same magnitude as that along *a*-axis.

Again, although the three structural features are listed separately, they are dependent in bulk system. For example, in the orthorhombic system, the larger tilt of a pseudo-cubic lattice, the stronger octahedral rotation plus larger anisotropy in lattice parameters. The reason is that in orthorhombic symmetry where the *A*-site cation is relatively too small to completely fill the interstitial site, once the *A*-site cations displace a certain distance from the ideal position in an aristotype cubic structure, the oxygen at the face center will also displace to maintain an equilibrium bonding environment. This systematic displacement of *A*-site cations is essentially the tilting and distortion in pseudo-cubic lattice, and the systematic displacement of oxygen anions is simply the rotation of the octahedra cage. In thin-film systems, nevertheless, these features can be controlled and the interrelationship can be broken under external perturbations. Three engineering routes to control the structural degrees of freedom will be introduced in the following.

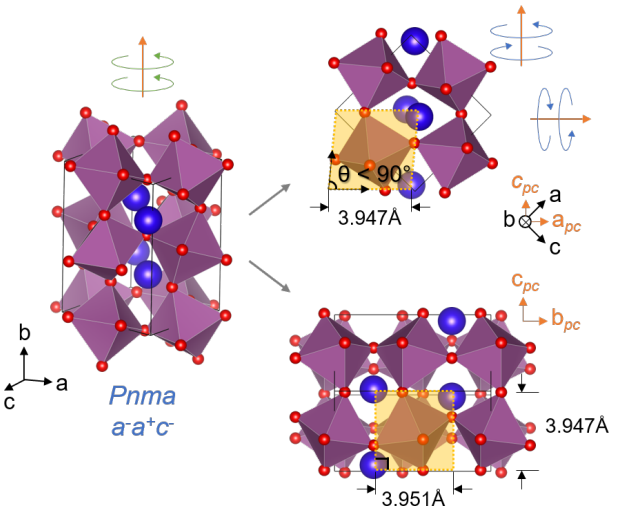

Figure 2.9: *Orthorhombic $DyScO_3$ belongs to space group $Pnma$. The pseudo-cubic lattice (indicated by yellow dashed line) possesses lattice tilting, anisotropic lattice parameters, and octahedral rotation with Glazer pattern $a^-a^+c^-$.*

Route I — Epitaxial strain engineering

No other engineering route has had as flexible and effective control over the structural features as epitaxial strain engineering. Strain measures the deformation of material from its original form under external perturbations. For different materials, one way to describe the mechanical behavior and sensitivity to external perturbation is by measuring the stress(σ)-strain(ϵ) curve experimentally.[5] Ceramic materials are brittle and there will be an enormous amount of stress built up in the material under relatively small deformation. For instance, sapphire (Al_2O_3) is a material with high toughness and the Young's Modulus is around 470 GPa. This means that to induce 1% deformation in sapphire, one needs to apply a hydrostatic pressure of 4.7 GPa, which is not a trivial effort in most laboratories. Alternatively, using thin-film epitaxy one can easily induce 1-3% coherent strain in the material by properly choosing the lattice-mismatch between the film and the substrates. Note that, here, thin film indicates that the thickness of the epitaxial material needs to

[5]In elastic regime the relation between stress (σ) and strain (ϵ) is given by $\sigma = E\epsilon$, where E is the Young's Modulus of the material.

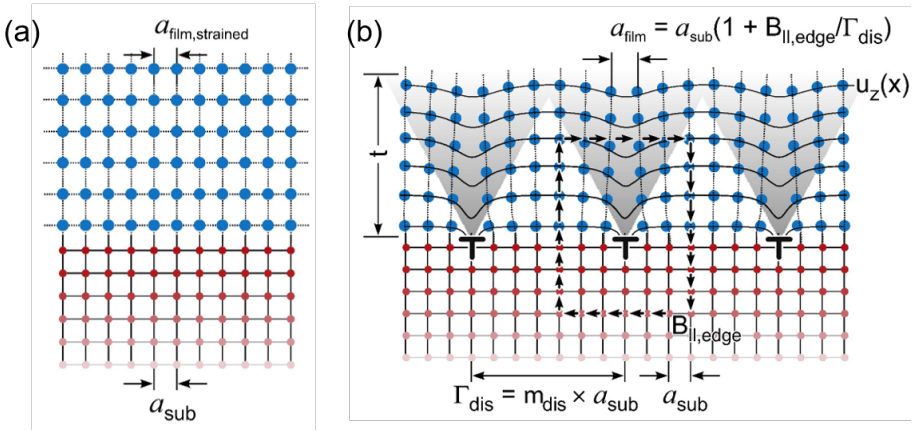

Figure 2.10: *(a) Coherently strained film on substrate. (b) Partially relaxed film on substrate that has larger lattice mismatch. The strain is relaxed by forming dislocations at the interface (Figure adapted from [67]).*

be controlled under the critical thickness above which the strain relaxation will take place by forming dislocations (both coherently strained and partially relaxed cases are given in **Figure 2.10**(b)).

In the epitaxial growth of perovskite thin films on a perovskite substrate, the in-plane lattice parameters of the film material is forced to be the same as the underlying substrate lattice. Under biaxial strain conditions, the mechanical relations in the film are given by

$$\epsilon_\perp = \frac{1}{E}(\sigma_\perp - \nu\sigma_x - \nu\sigma_y) = -\frac{2\nu}{E}\sigma_\parallel \tag{2.11}$$

$$\epsilon_\parallel = \frac{1}{E}(\sigma_x - \nu\sigma_y - \nu\sigma_\perp) = \frac{1-\nu}{E}\sigma_\parallel \tag{2.12}$$

where ν is the Poisson's ratio,[6] $\epsilon_\parallel$ is the biaxial strain defined as $(a_\parallel - a_f)/a_f$, $\sigma_\parallel (= \sigma_x = \sigma_y)$ is the in-plane stress assuming there's negligible in-plane anisotropy, and $\sigma_\perp$ is the out-of-plane stress which equals to zero. With the above relations, the out-of-plane lattice parameter of the film is derived as

$$a_\perp = a_f[1 - \frac{2\nu}{1-\nu}\epsilon_\parallel] \tag{2.13}$$

Such change in lattice parameters in the film immediately suggests that the structure and symmetry of the epitaxial layer is different from the bulk form. First, the substrate imposed an expansion of the epitaxial-film lattice under tensile strain, or a compression of the lattice under compressive strain. In addition to the expansion/compression of the

[6]Poisson's ratio is the measure of material's elastic deformation along the axis perpendicular to the uniaxial-stress axis or the biaxial-stress plane.

lattice, the lattice tiling is strongly dependent on the sign and magnitude of the strain, and the specific material system. In orthorhombic $La_{0.7}Sr_{0.3}MnO_3$ for instance, the pseudo-cubic lattice is originally monoclinic but becomes more tetragonal under tensile strain. While under compressive strain, the pseudo-cubic lattice is still monoclinic but the tilting angle is dependent on the strain magnitude [68]. In rhombohedral $BiFeO_3$, epitaxial strain gives rise to an extremely rich spectrum of structural variants including rhombohedral phase, tetragonal phase, and monoclinic phase. Even within the monoclinic phase, the degree of lattice tilting and tilting direction is dependent on the magnitude of strain [69].

Beyond the lattice change, epitaxial strain can also be accommodated by the deformation of oxygen octahedral network. One way to respond to the elastic energy in the material is to stretch/compress the octahedral cage. This involves the change in *B-O* bonding length and strength. Another possibility is the change in rotation angles of the rigid octahedral cages, which is essentially the change in *B-O-B* bonding angles along different directions but the bonding length remains the same. Theoretical computation has suggested that the realistic scenario is a mixture of the two [32, 33], while experimentally the later case is more frequently observed. Note that these changes in octahedral network have long been predicted by computation but remained difficult to be extracted in experiments till recent years, and the details regarding the extraction of octahedral rotation will be discussed in **Chapter 3**. A computational example is given for $LaAlO_3$ here. In $LaAlO_3$ under biaxial strain, the octahedral rotation pattern and magnitudes are highly sensitive to epitaxial strain and the complex evolution of rotation and pattern has been predicted [33, 70]. At zero-strain, the structure of $LaAlO_3$ is rhombohedral and the rotation pattern is given by $a^-a^-c^-$ in Glazer notation system. At tensile strain, the out-of-plane rotation is dramatically quenched and approaches zero at relatively small strain magnitude. The in-plane tilting, on the contrary, increases and thus the rotation pattern becomes $a^-a^-c^0$. While on the compressive side, the out-of-plane rotation is enhanced accompanied by a quenching of in-plane rotation, giving rise to a rotation pattern of $a^0a^0c^-$ in a tetragonal lattice.

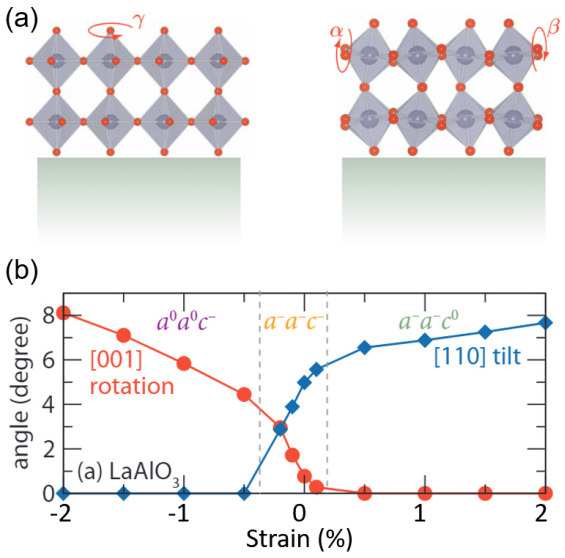

Figure 2.11: *(a)Illustration of the accommodation of epitaxial strain by a change in the rotation magnitudes along three orthogonal directions. (b)The evolution of octahedral rotation patterns of $LaAlO_3$ under strain (Figure adapted from [33]).*

Route II — Cation stoichiometry and ordering

Modern thin-film synthesis techniques provides an opportunity for researchers to deterministically control the cation stoichiometry, doping level, local ordering of cation species, and *etc*. A variation in cation type or cation stoichiometry in the material results in a different tolerance factor, and thus a varied structural features in the lattice. In $LnNiO_3$ systems (*Ln* stands for lanthanides), as the cation changes from *La* to *Gd*, the *B-O-B* bonding angle decreases from approximately 165° to 151° and the lattice symmetry goes from rhombohedral to orthorhombic (**Figure 2.12**(a)). Such change in structure comes with a shifting in magnetic and electronic properties where the $LaNiO_3$ is a paramagnetic metal while $GdNiO_3$ is antiferromagnetic insulator at low temperature [71]. In some off-stoichiometry occasions where the *A*-site cations have multiple valence states and similar size to the *B*-site cations, *A*-site cations can go into *B*-site as anti-site defects, which has been found to exhibit great impact on lattice symmetry and electronic properties in oxide materials. As given in Figure, the anti-site defect concentration in Sr_2FeMoO_6 can be controlled by doping and affects the magnetic susceptibility and magnetoresistance (**Figure 2.12**(b)) [72].

In addition to cation stoichiometry, cation ordering has been proposed as a promising route to engineer the octahedral rotation pattern plus the inversion symmetry of the crystal. For instance, it has been shown that in cation ordered $PbTiO_3/SrTiO_3$ structure where the *Pb* and *Sr* cations are alternating by each unit cell, an overall enhanced polarization is obtained and the phase transition order parameter becomes the octahedral rotation tilting pattern instead of the polarization. Such material is called improper ferroelectrics and people have suggested to produce such novel phase of matter by creating the arbitrary cation-ordered superlattices using RHEED-assisted growth techniques [74–76]. Moreover, a more general route to break inversion symmetry in material and induce ferroelectricity is to create perovskite superlattices or layered-perovskites with *A*-site cation ordering where

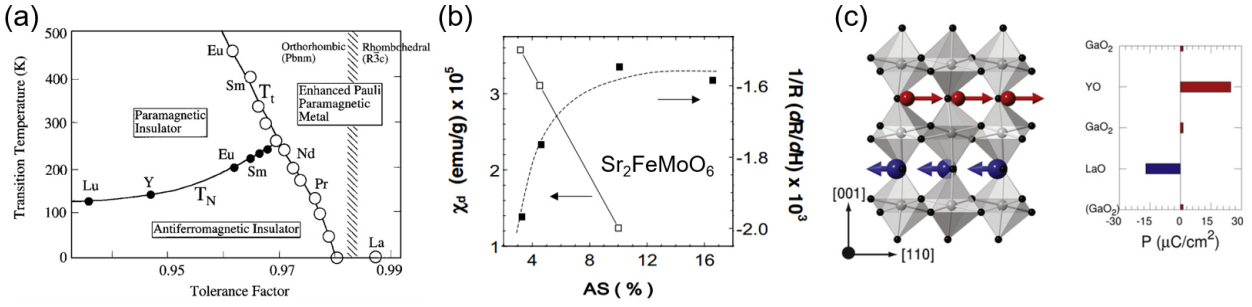

Figure 2.12: *(a)Cation size effect on the lattice and electronic structure of nicklates (Figure adapted from [71]). (b)Change in magnetic susceptibility and magnetoresistance in Sr_2FeMoO_6 induced by cation anti-site defects (Figure adapted from [72]). (c)Illustration of the breaking of inversion symmetry via cation ordering in perovskite structure (Figure adapted from [73]).*

the two types of *A*-site cations have different ionic radii (**Figure 2.12**(c)) [73, 77, 78]. Such ordering breaks the inversion symmetry of the crystal lattice and induces polarization due to the uncompensated displacement of *A*-site cations at different layers.

Route III — Interfacial structural coupling

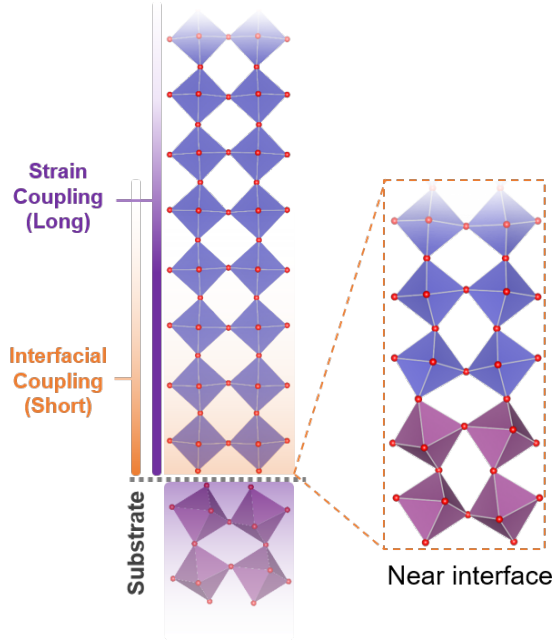

Figure 2.13: *Illustration of interfacial structural coupling between a high-symmetry film and low-symmetry substrate. The structural features such as octahedral rotation pattern from the substrate propagates into the epitaxial film.*

Study on the physical properties at the interfacial region of a perovskite heterostructure is one of the most attractive research topics for both materials scientists and physicists. In general, the physical properties at the interface can be fundamentally different from those in the bulk, and many phenomena that are absent in the bulk or even in a relatively thick epitaxial film are observed near the interface. These phenomena, at times, are termed as emergent phenomena or emergent phases. For example, high-mobility electron gas is observed at the interface of $LaAlO_3/SrTiO_3$ heterostructure [79], emergent ferromagnetism is detected at the interfacial region of an antiferromagnet $LaMnO_3$ grown on $SrTiO_3$ [80], super-ionic conduction is observed at the interface between two bad ionic conductors CaF_2 and BaF_2 [81], metallic material that has spontaneous polarization has been discovered at heterostructure interface [82, 83], and so on. In many cases, the origin of the phenomena is from the strong structural coupling between the ultra-thin epitaxial layer and the substrate. In another word, the structural features in the substrate material is very different from the epitaxial layer, and such structural mismatch drives additional structural distortions in the epitaxial layer in addition to those induced by epitaxial strain (an example of the interfacial coupling of a high-symmetry film grown on low-symmetry substrate is given, **Figure 2.13**). Typically the critical thickness of strain relaxation is around 100 nm depending on the material system and therefore the strain coupling is a relatively long-range effect. On the other hand, the interfacial coupling effect is short-range and the coupling distance is around 4-6 unit cells above in the epitaxial film from the interface [32, 84]. In turn, the strong structural coupling gives a more radical change in the epitaxial film near the interfacial region if the symmetry mismatch is large, and such engineering route

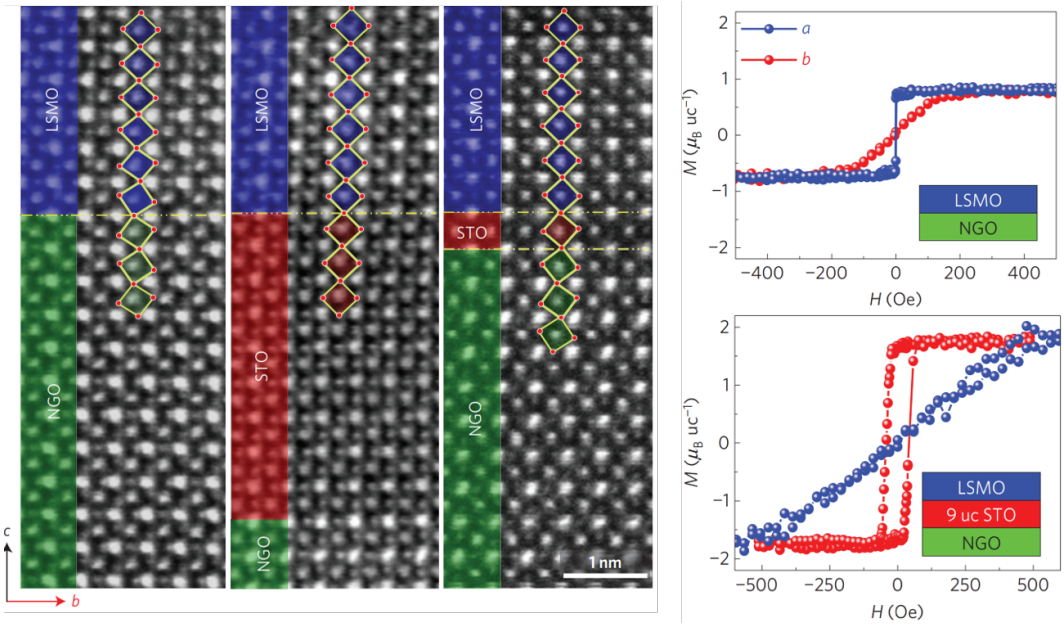

Figure 2.14: *The octahedral rotation pattern of $La_{0.7}Sr_{0.3}MnO_3$ thin film can be engineered by substrate surface symmetry and the magnetic easy axis is able to turn 90° depending on the thickness of the high-symmetry buffer layer (Figure adapted from [7]).*

gives another dimension for researchers to manipulate the structure at ultra-thin epitaxial layers.

Not only does the interfacial coupling affect the structures near the interfacial region, the crystal symmetry of the substrate at the interface can also dictate the crystal symmetry and domain structure of the entire epitaxial film in some cases. Namely, the structure of the epitaxial layer can be controlled using two substrates with exact same lattice constants but different surface symmetry. For instance, the domain structure of $BiFeO_3$ is different for the film growing directly on a $DyScO_3$ substrate and a $DyScO_3$ substrate with a ultra-thin $SrTiO_3$ buffer layer [85]. The role of the ultra-thin $SrTiO_3$ layer is to change the pseudo-cubic lattice symmetry of the substrate surface from monoclinic to tetragonal, while the lattice constant of $DyScO_3$ is maintained as the $SrTiO_3$ is coherently strained. Moreover, the octahedral rotation and magnetic easy-axis of $La_{0.7}Sr_{0.3}MnO_3$ can be engineered if a high-symmetry buffer layer is inserted in between the film and the low-symmetry substrate [7]. As illustrated in **Figure 2.14** where the high-resolution transmission electron microscopy images are given, the octahedral rotation pattern in $La_{0.7}Sr_{0.3}MnO_3$ is different with or without a high-symmetry buffer layer, and thus the magnetic easy-axis is rotated in-plane by 90° since the electronic structure is highly sensitive to the crystal field generated by the octahedra. Similarly in $SrRuO_3$, it was shown that the symmetry of the film can be altered if the crystal symmetry at the film-substrate interface is modified by the insertion of a buffer layer [86].

2.3 Control of surface structures in perovskite thin films

Orientation control in thin-film growth

One major advantage of performing epitaxial thin-film growth is the ability to control the growth orientation by using a particular substrate pre-cut along a specific crystallographic orientation. Epitaxially growth along various crystallographic orientations (typically (001)-, (110)-, or (111)-orientated substrates) can have a range of impacts on the thin films regarding both lattice and surface structure. For instance, in ferroic materials, thin-film growth on (001)- or (111)-substrates can results in drastically different saturated polarization [31], mesoscopic domain structures [10], lattice symmetry [9], *etc*. Such phenomena are essentially due to the asymmetric strain imposed on the lattice. Owing to such changes in the film structures, the corresponding ferroelectric switching kinetics can be properly engineered via orientation control, which effectively provides an additional route to achieve novel functionalities.

In addition, as discussed in **Chapter 1**, the atomic arrangement and the electronic structure of the exposing perovskite solid-gas interface can also be fundamentally changed in orientation-controlled growth. For instance, depending on the specific valence-states of the *A*- and *B*-site cations, Tasker [89] has suggested that both polar and nonpolar surfaces can be created in the ideal perovskite structure where the charge density at different types of surfaces are varied. Taking $SrTiO_3$ as an example, the (001) surface is nonpolar as either *SrO* or TiO_2 termination is fully charge compensated [90]. While (110) and (111) surfaces of $SrTiO_3$ are polar surfaces [91], the electronic structure of which has been revealed to be drastically different [92]. Alternatively, the (001) surface of $LaAlO_3$ is polar due to the

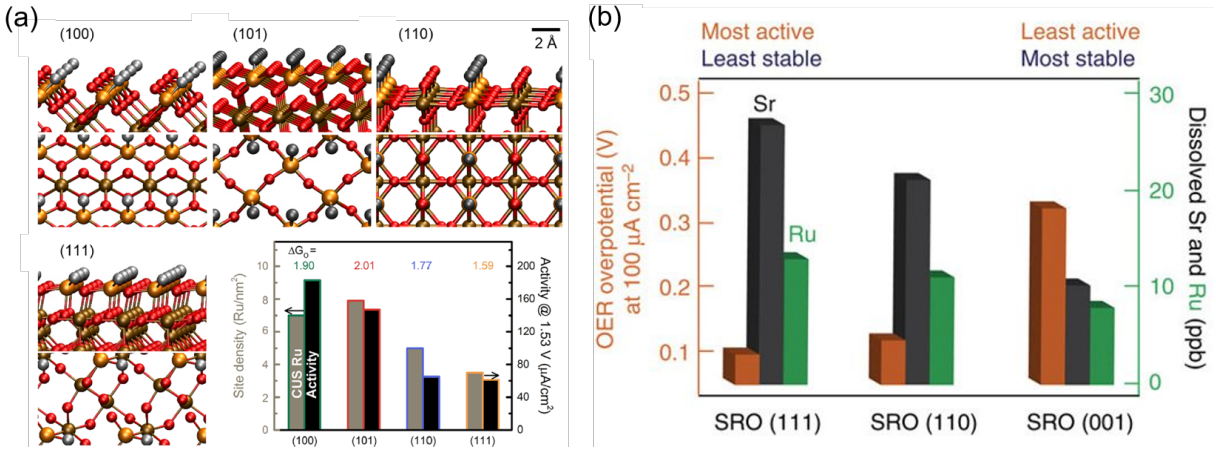

Figure 2.15: *(a) Surface-orientation dependency of surface activity in RuO_2 (Figure adapted from [87]). (b) Correlation between surface stability and electrochemical activity in $SrRuO_3$ grown along (001), (110), and (111) (Figure adapted from [88]).*

fact that *La* and *Al* are both 3^+ in valence state and the ionic charges are not compensated in either *LaO* or AlO_2 layers [79]. In reality, the surface structure can be much more complicated compared to the ideal scenario. For example, various surface reconstructions can take place at the surface to compensate extra charges [93, 94]. Different surface terminations and reconstruction can be created depending on the growth sequence and the growth conditions [79, 95–97]. Cation redistribution near the surface is also widely observed in a number of perovskite systems with aliovalent dopants [98, 99]. These effects require extra attention in the analysis of the data acquired from different perovskite surfaces.

In practice, orientation-control in perovskite thin-film growth could be extremely important in the engineering of electrochemical activities. In water-splitting or fuel-cell applications, there have been extensive studies on orientation-dependent adsorption, surface energy, and electrocatalytic activities on elemental or alloyed metallic catalysts with varied exposed surface orientations [100–106]. Some particular crystallographic orientations result in different surface electronic structures and atomic arrangement in the catalysts. For instance, the (111) surface of Pt_3Ni nanoparticles has been found to exhibit high electrocatalytic activity due to the structural variation near the outermost (111) surface [102, 104]. In binary-dioxide catalysts, it has been experimentally demonstrated that there also exists a strong orientation dependency on gas kinetics [87] **Figure 2.15**(a). The origin of such dependency is attributed to the different density of under-coordinated ruthenium sites at different exposed surfaces. In perovskite $SrRuO_3$ thin films, it has been shown that there is a strong correlation between the surface stability and electrochemical activity along various orientations [88] **Figure 2.15**(b). As perovskite oxides have increasingly shown the superior properties in electrochemistry as compared to metallic electrocatalysts, using epitaxial techniques to synthesize oriented perovskite heterostructures is highly beneficial for the fundamental understanding of the correlation between surface structure and electrocatalytic activities, plus discovering the further engineering routes for perovksite geometries with superior performance.

Chapter 3

Characterization of perovskite heterostructures

This chapter focuses on the characterization techniques of structural and physical properties in perovskite heterostructures. The structural features in perovskites are primarily characterized by X-ray diffraction techniques, and several analysis approaches are introduced for the extraction of lattice symmetry, octahedral rotation patterns, and atomic positions. Next, a number of physical property measurement methods important for this work are presented. For the measurement of magnetic, electrical transport and ferroelectric properties, the working principles of the instrumentation are briefly explained. The characterization of ionic-charge transport and surface-electrochemical reaction in perovskite heterostructures is based on a custom measurement setup of which the structure and technical details are included.

3.1 Structural characterization of perovskite oxides

X-ray diffraction is the most efficient and powerful non-destructive technique to examine the lattice structure of a highly-ordered crystal material. The diffraction process is essentially a Fourier transformation of the crystal lattice where the periodicity in the real-space lattice along various orientations is manifested as diffraction spots with specific spacing and intensity in the reciprocal space. Thus, the change in lattice or structural features is measured as a change in the X-ray diffraction peak position, intensity, and relative phase relationships. Depending on specific needs, the X-ray diffraction setup can be as compact as a desk-top instrument, or as enormous as ten soccer fields. The choice of X-ray diffractometer size and setup determines the resolution of the characterization results and the types of structural features that can be efficiently and effectively detected. For instance, for lattice parameters and lattice distortions, using a laboratory-based X-ray diffractometer is sufficient to extract accurate results. While for more delicate features such as octahedral rotations or displacement of light-weight cation/anions, the extraction of precise atomic position information requires the usage of a high flux X-ray beam which is generated by a synchrotron.[1] Here, three major diffraction pattern analysis techniques, of particular important for this work, are introduced for the extraction of necessary structural features in the perovskite lattice.

Lattice distortion analysis

Changes in lattice parameters arising from compression or expansion the lattice can be analyzed by determining the diffraction peak positions along three orthogonal axes. In addition, symmetry lowering (*e.g.*, from cubic to orthorhombic or rhombohedral) in the crystal lattice is manifested in the pseudo-cubic lattice as monoclinic or triclinic tilts, respectively. Pseudo-cubic lattice monoclinic or triclinic tilting angle can be readily acquired in laboratory-based X-ray diffractometers. In both analysis procedures, X-ray reciprocal space mapping (RSM) is typically used. In single-crystal diffractometer setup, RSM is a 2-axis scan along both ω and 2θ axes in the real space, which at the same time creates a 2D area intensity map in reciprocal space of the corresponding crystal lattice (**Figure 3.1**(a-b)). The defined scan area is represented by two reciprocal lattice vectors, the magnitudes of which are related to the scanning angles in real space by

$$Q_{\parallel} = \frac{2\pi}{\lambda}[\cos(\omega) - \cos(2\theta - \omega)] \tag{3.1}$$

$$Q_{\perp} = \frac{2\pi}{\lambda}[\sin(\omega) + \sin(2\theta - \omega)] \tag{3.2}$$

where $Q_{\parallel}$ and $Q_{\perp}$ correspond to the in-plane and out-of-plane crystallographic directions,

[1] Synchrotron radiation is the generation of electromagnetic flux when charged particles (typically electrons) are accelerated radially. The generation of X-ray beam can be achieved via a range of apparatus including bending magnets, wiggler, and undulator.

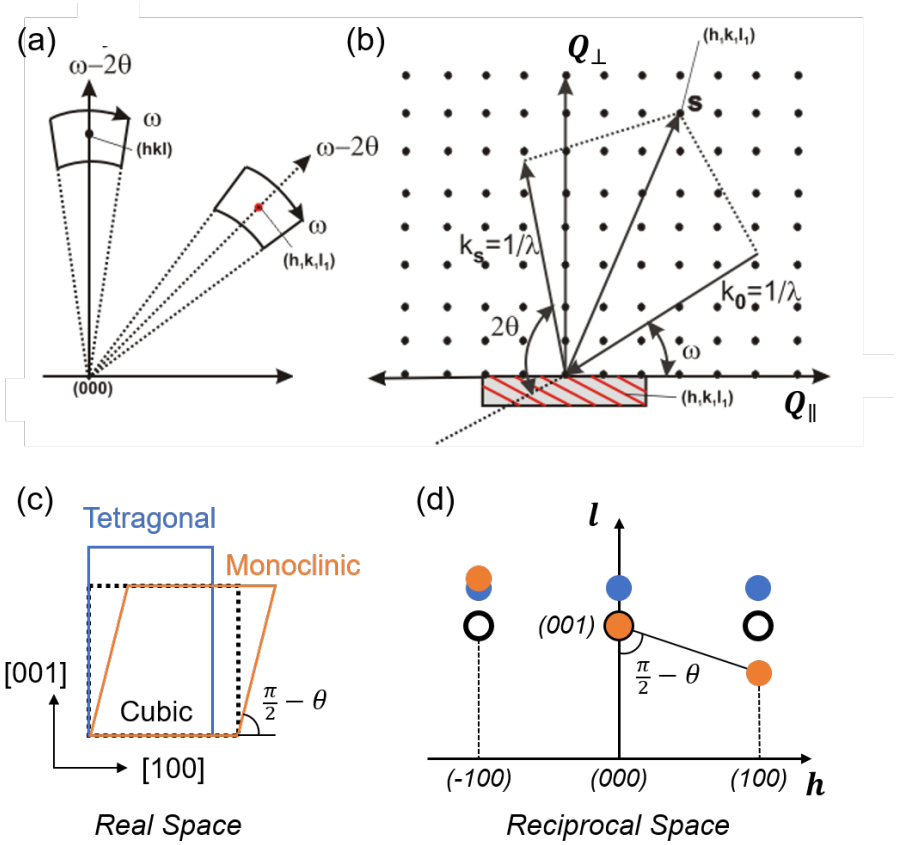

Figure 3.1: *RSM scan in real space (a) and reciprocal space (b). (c)Schematic of lattice distortions in the real space while the corresponding changes in diffraction spots in reciprocal space are illustrated (d).*

respectively. Thus, when a diffraction spot is captured in the RSM scan, based on the peak index, $Q_{\parallel}$, and $Q_{\perp}$ values one can extract the lattice parameters of the film. For instance, if a peak is observed at diffraction condition *h0l*, the lattice parameters of the film corresponding to the *h*-direction ad *l*-direction are given by

$$a_h = h * \frac{1}{Q_{\parallel}} \tag{3.3}$$

$$a_l = l * \frac{1}{Q_{\perp}} \tag{3.4}$$

Therefore, as long as the peak index is properly determined at the diffraction condition and is none zero, the lattice parameters of the unit cell can be extracted. By comparing the lattice parameters of the thin film unit cell with the bulk lattice, the expansion/compression of the lattice (strain state) can also be subsequently evaluated.

To extract the monoclinic lattice tilting angle of the pseudo-cubic unit cell, two diffraction peaks with same *l*-index but opposite *h*-index (or *k*-index) must be scanned. Since

the lattice is tilted towards one axis, the two diffraction peaks will have the same in-plane reciprocal lattice parameter but different out-of-plane reciprocal lattice parameter. And, as illustrated in **Figure 3.1**(d), the tilting angle in the reciprocal space is actually the tilting angle in the pseudo-cubic unit cell lattice, which can be easily calculated using the geometrical relationship between the two diffraction peaks. A practical example of extracting tilting angle in $SrRuO_3$ thin films will be given in detail in **Chapter 4**.

Octahedral rotations — Half-order Bragg peak analysis

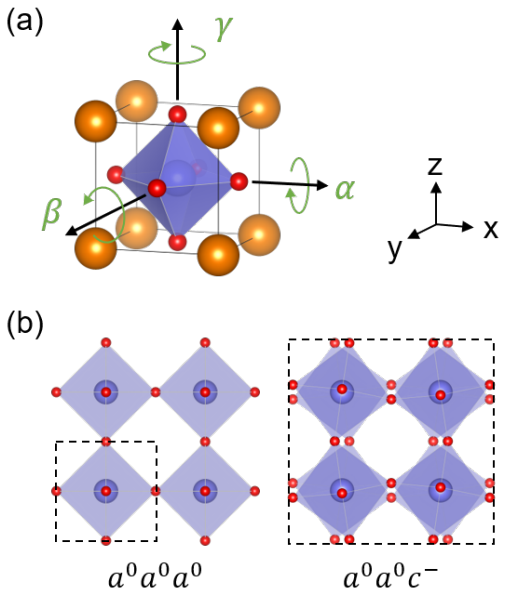

Figure 3.2: *(a)Illustration of octahedral rotation in the perovskite lattice. (b)Once the octahedra rotate out-of-phase along one direction (c-axis as illustrated), the origin of half-order peak can be interpreted as the doubling of pseudo-cubic unit cell.*

Due to the small atomic weight and low scattering factor of oxygen anions, the determination of oxygen position in the perovskite structures has been challenging work in the past for both electron- and X-ray-diffraction techniques. In 2010, S. May [107] proposed an experimental approach that the octahedral rotation pattern and rotation angles in strained perovskite thin films can be extracted in a more straightforward manner compared to other techniques such as X-ray absorption fine structure analysis and truncation rod measurements [108–111]. The idea is that the octahedral rotation pattern can be determined by fitting the intensity of the half-order Bragg peaks of which the intensity is directly related to the displacement (rotation) of the octahedral cages, and such analysis sometimes is termed as *half-order Bragg peak analysis*.

Briefly, the origin of the half-order Bragg peak in the perovksite lattice can be understood as the follows. In the pseudo-cubic notation, the diffraction peaks given by the aristotypical cubic lattice are indexed by *hkl* integers. Once the octahedra start to rotate out-of-phase along a specific crystallographic direction, the pseudo-cubic unit cell cannot represent the full symmetry of the lattice as it cannot span the whole space, and thus the unit cell is doubled along three directions. In turn, if one still applies the same index, the doubled unit cell will give rise to additional peaks in between the integer peaks as half-order diffraction peaks. As the readers might notice, if the octahedra are rotated in-phase along a specific direction, there will be no unit-cell doubling, and thus no half-order peaks will appear along that direction. Therefore, the appearance of specific sets

of half-order peaks can be used to determine the rotation pattern along each orthogonal directions. Nevertheless, the above interpretation is relatively simplified compared to the realistic cases where the rotation along one direction is at the same time affecting the intensities of half-order peaks in the other two directions. Thus, to analyze the full rotation pattern for a low symmetry lattice, one needs to scan multiple peaks with various indexes that span across four quadrants in the reciprocal space. Here, the diffraction conditions corresponding to different types of rotation along three orthogonal axes in the pseudo-cubic lattice are given (**Table 3.1**). As discussed in **Chapter 2**, the three alphabetic letters represent rotation magnitudes along *x*- (or *h*-), *y*- (or *k*-), and *z*- (or *l*-) axis in pseudo-cubic lattice (reciprocal lattice) under Glazer notation and the subscription denotes either the neighboring octahedra are rotating in-phase (+) or out-of-phase (-).

With a known rotation pattern, the rotation angles along each axis can be extracted by comparing the calculated peak intensities and experimental values. The calculated peak intensities are obtained from

$$I = I_0 \frac{1}{\sin\eta} \frac{1}{\sin 2\Theta} (\sum_{j=1}^{4} D_j |F_{hkl}|^2) \tag{3.5}$$

where I_0 is the incident photon flux, $1/\sin\eta$ is the beam footprint correction, $1/\sin 2\Theta$ is the Lorentz polarization factor, F_{hkl} is the structure factor for the oxygen anions, and D_j is the volume fraction of the four possible structural domains which will be discussed in detail in **Chapter 4**. The rotation angle information is encoded in the structure factor of each type of Bragg peak and the structure factor is given by

$$F_{hkl} = f_O^{2-} \sum_{n=1}^{24} \exp[2\pi i(hu_n + kv_n + lw_n)] \tag{3.6}$$

where f_O^{2-} is the atomic scattering factor of O^{2-} and for *n*th oxygen anion the lattice position is given by (u, v, w). Thus, with the determined positions of the oxygen anions in the

Table 3.1: *Correlation between the octahedral rotation tilting pattern and corresponding half-order peak conditions [65, 112]*

Type of tilt	Half-order peak	Restrictions
$\mathbf{a}^+$	int-half-half	$k \neq l$
$\mathbf{b}^+$	half-int-half	$h \neq l$
$\mathbf{c}^+$	half-half-int	$h \neq k$
$\mathbf{a}^-$	half-half-half	$k \neq l$
$\mathbf{b}^-$	half-half-half	$h \neq l$
$\mathbf{c}^-$	half-half-half	$h \neq k$

pseudo-cubic lattice, the octahedral rotation angles can be calculated and projected onto each rotational axis.

Crystal truncation rod measurements and coherent Bragg rod analysis

The two types of structural analysis approaches introduced above are useful in the extraction of partial structural information such as lattice symmetry and octahedral rotations. This is because only the intensity of the Bragg diffraction peaks are utilized in the analysis process. However, in a coherently-strained heterostructure, the complex scattering factor along the substrate-defined truncation rods contains all the information of the film structure, and is a direct Fourier transform of a well-defined real-space electron density. The scattering factor along the truncation rods is given by

$$T_{\eta,\zeta} \propto \int_V d^2r dx \, \exp\{i[\boldsymbol{r} \cdot \boldsymbol{k}_{\eta,\zeta} + kx]\} \sum_{i,j} \rho(x, \boldsymbol{R}_{i,j} + \boldsymbol{r}) \tag{3.7}$$

where $T_{\eta,\zeta}$ is the complex scattering factor along the Bragg rod, subscripts (i, j) and (η, ζ) denotes the 2D unit cell and reciprocal-space lattice, respectively. Thus, once the complex scattering factor is measured for the film, one can perform a Fourier transform of the scattering factor and acquire a 3D reconstruction of the electron density $\rho(x, \boldsymbol{R}_{i,j} + \boldsymbol{r})$. The electron density essentially gives the atomic position of the unit cells since all the electrons in the atom scatter the electromagnetic waves, and the center of the electron cloud is where the center of the corresponding atom is located. This entire approach consists of the crystal truncation rod measurements and a phase-sensitive analysis method called coherent Bragg rod analysis (COBRA) [37, 38, 110, 113, 114]. As a surface sensitive technique, COBRA is capable of extracting structural information from the surface down to approximately 20 nm into the heterostructure.

As illustrated in **Figure 3.3**(a), the truncation rod measurements basically measure the scattering intensity of a specific set of diffraction conditions along the out-of-plane direction. Due to the finite thickness of the sample and structural distortion away from ideal cubic geometry, the scattering intensity between the Bragg rods oscillates and encodes atomic position information. Thus, to perform such measurements, synchrotron-based diffraction with a high coherence X-ray beam and high beam flux is needed to improve the signal-to-noise ratio and resolve the fine features along the truncation rods (**Figure 3.3**(b)). For a low-symmetry system with structural variants such as octahedral-rotation domains, truncation rods in all four-quadrants, as defined by the 2D surface lattice, need to be included to reveal the necessary structural information. During COBRA analysis, the procedure starts with an initial structural model that contains the substrate plus the pseudomorphic epitaxial film. The complex scattering factor of the initial model (surface layers) is acquired by first comparing the calculated intensity with the measured intensity as given in the equation below

$$|\mathbf{S}_0 + \mathbf{U}_0|^2 = \mathbf{T}^2 \tag{3.8}$$

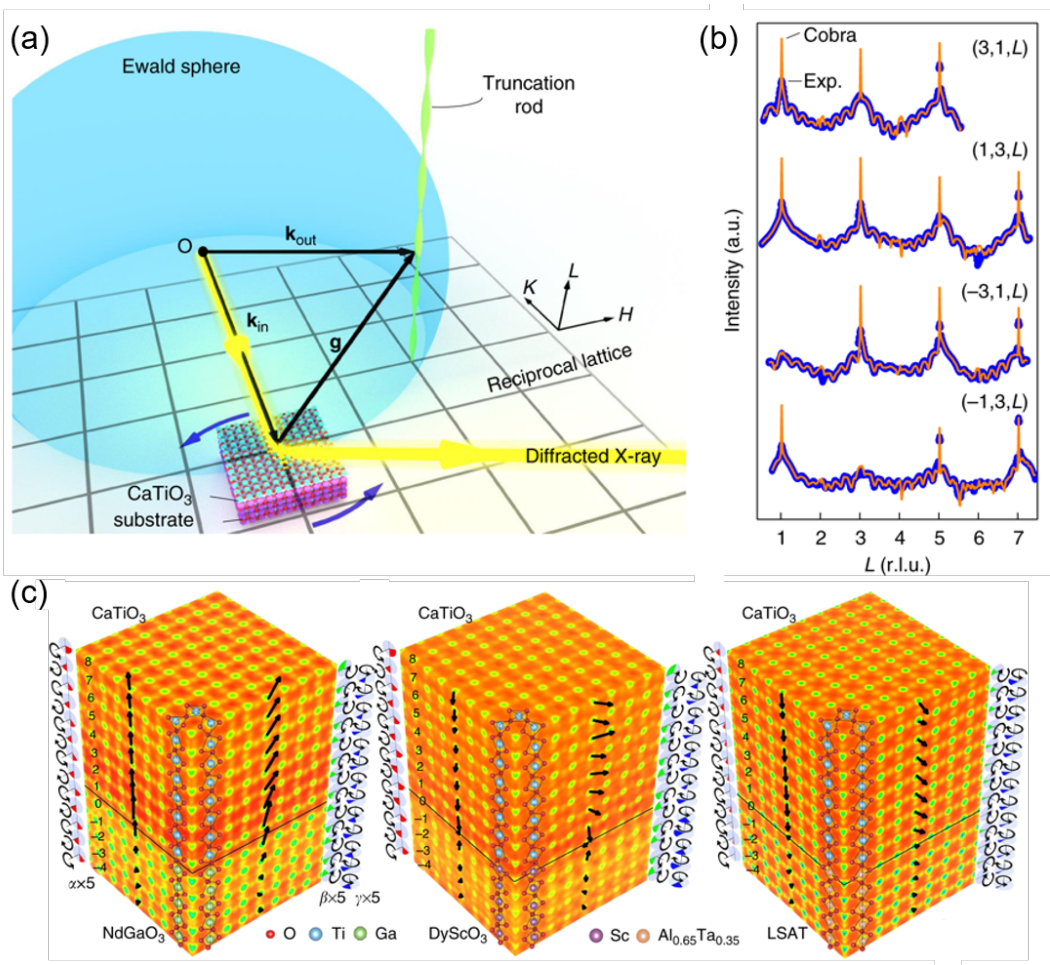

Figure 3.3: *(a)Schematic setup of the synchrotron-based crystal truncation rod measurements. (b)Representative truncation rod measurements data where the fine intensity variation in between the Bragg's rods contains necessary information for electron density map reconstruction. (c)3D electron density map (atomic position) of $CaTiO_3$ grown under various strain states (Figure adapted from [37]).*

where $\mathbf{S}_0$, $\mathbf{T}_0$ are the complex scattering factor of the model and measured diffraction intensity, respectively. The yield unknown part $\mathbf{U}_0$ can be solved by assuming it varies slowly compared to the other two factors. Then the solved unknown part, with amplitude and phase, is added to the initial model while a new iteration starts until $|S_n|^2$ is equal to the measured intensity $\mathbf{T}_0$. In turn, with the known $\mathbf{S}$ of the thin layer (also plus few layers from the substrate as is typically the case), the electron density map can be extracted (**Figure 3.3**(c)).

COBRA analysis can extract the complete crystal structural information in the lattice compared to the two analysis approaches discussed before. However, due to the difficulty of performing the measurement and stringent sample requirement, the three approaches

are all used in a complementary fashion and as required throughout this dissertation depending on the specific material system and scientific needs. It is also worth mentioning that X-ray diffraction is a powerful technique to extract structural information but not the only one for similar purpose. The position and the displacement of the cations/anions can be quantitatively determined from electron-diffraction based techniques such as transmission electron microscopy (TEM), scanning transmission electron microscopy (STEM), and coherent diffraction imaging (CDI). A comparison of these techniques is summarized by Yuan *et al.* [37] and is reproduced in **Table 3.2** below.

Table 3.2: *A comparison of the crystal structure analysis techniques*

	CDI	**TEM/STEM**	**COBRA**
Probe beam	X-ray/Electron	Electron	X-ray
Beam coherency requirement	Fully coherent	No	Axial coherence
Sample type	Objects with clear boundaries	Require delicate preparation	Epitaxial thin films
Sample size	Hundreds nm to microns	Sample <100 nm	Film <20 nm
Sample environment	Non-destructive; in-situ/operando	Destructive; in-situ/operando	Non-destructive; in situ/operando
Beam stability	High stability	High stability	Normal
Best resolution achieved	∼5.5 nm in 3D	∼40 pm in 2D	∼40 pm in 3D
Data processing method	Phase retrieval	Image processing	Phase retrieval
Data acquisition time	∼2 hours	∼2 min per image	∼6 hours

3.2 Physical properties and characterization

Again, in this dissertation, four representative perovskite systems (*i.e.*, $SrRuO_3$, $PbZrO_3$, LSGM, and LSCF) are investigated and their corresponding characteristic physical properties are studied as a fingerprint of the impact of structural distortions. Specifically, the magnetic and electrical transport are focused on for SRO, anti-/ferroelectricity and dielectric properties are focused for $PbZrO_3$, ionic charge transport is studied for LSGM, and electrochemical gas kinetics are studied for LSCF. For $SrRuO_3$ and $PbZrO_3$, commercially available instrumentation is applied to examine the properties. While for LSGM and LSCF,

the measurements require temperature- and oxygen-partial-pressure-dependent studies in a custom measurement platform designed and setup for such a purpose. Specifically for gas-kinetics studies in LSCF, a device structure is designed to perform the measurement in heterostructure geometries. Here, a brief introduction to the principles and designs of the measurement methods are presented.

Magnetism and electrical transport

Magnetism is the spin polarization of materials. Magnetism measurement on thin-film samples in this dissertation involves the measurement of magnetization as a function of applied field (M-H curve), temperature-dependent magnetization (M-T curve), and magnetic anisotropy measurement. The device used for magnetization measurement is so-called a superconducting quantum interference device (SQUID) as shown in **Figure 3.4**(a). A SQUID device is composed of two Josephson junctions connected in parallel where the subtle changes in the magnetic flux inside the superconducting loop can be reflected as a voltage amplitude/phase change across the SQUID device. The current in a SQUID loop under a small applied magnetic flux (Φ_x) is given by

$$I = 2I_c\left|\cos\left(\frac{1}{2}\cdot\frac{2\pi}{\Phi_0}\Phi_x\right)\right| \tag{3.9}$$

where I_c is the critical current of the Josephson junction below which there's no voltage buildup across the junction, and $\Phi_0 = h/2e$ is the magnetic flux quantum. Based on this fundamental feature of the quantum interference device, an extremely precise magnetization measurement can be accomplished if the magnitude and phase of the current/voltage is measured. Practically, if the SQUID is operated at constant current mode, the voltage across the junction is oscillating and can be expressed as

$$V = \frac{RI}{2}\left[1 - \left(\frac{2I_c}{I}\cos\frac{\pi\Phi_x}{\Phi_0}\right)^2\right]^{1/2} \tag{3.10}$$

Since the sample is sometimes under large magnetic field or itself possesses high magnetization, these magnetic flux from the sample needs to be isolated from the SQUID circuit. Typically, the sample is surrounded by a set of pick-up coils which filter out the magnetic flux from the externally applied field, isolate the magnetic moment from the sample, and deliver such magnetic flux signal to the SQUID device to convert it into electrical signal. For the measurement of magnetic anisotropy, the sample is either mounted perpendicular or parallel to the applied magnetic field in the non-magnetic drinking straw as illustrated (**Figure 3.4**(b)).

Regarding resistivity measurement of the thin-film samples, a traditional van der Pauw geometry is used and is illustrated in **Figure 3.4**(c). The van der Pauw method is a measurement approach that is not limited by the sample geometry. As illustrated, the resistance of the two wire-bonding geometries is first measured at a specific temperature and

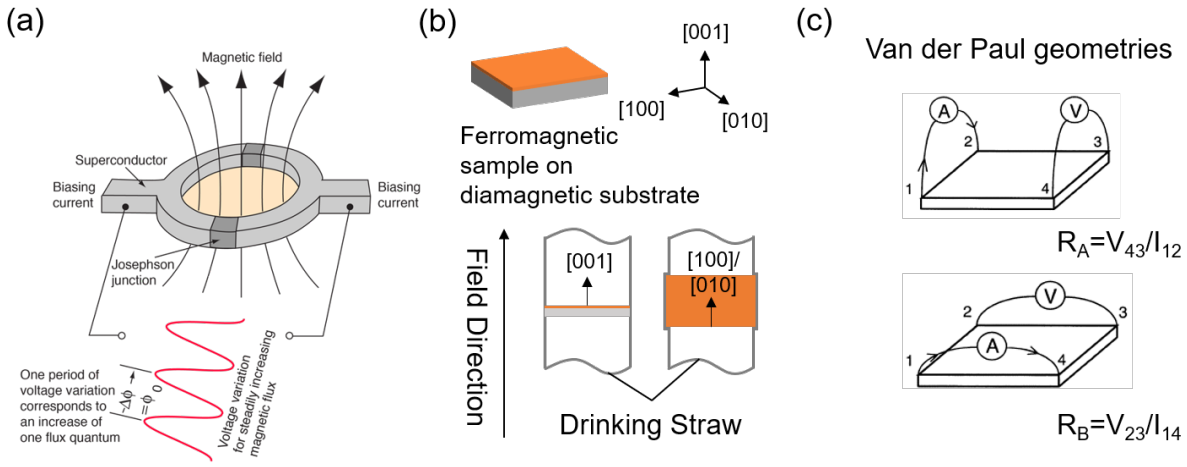

Figure 3.4: *(a)The SQUID measurement unit and an illustration of the oscillating voltage under external magnetic flux. (b)The sample holder for thin film heterostructures. (c)Resistivity measurement on thin-film samples using van der Paul method*

the resistance is denoted as R_A and R_B. As it has been shown by van der Pauw [115], the resistivity of the film is givn by

$$\rho = \frac{\pi d}{\ln 2} \frac{R_A + R_B}{2} f\left(\frac{R_A}{R_B}\right) \tag{3.11}$$

where $f(\frac{R_A}{R_B})$ is a function that satisfies the following relation which can be solved numerically.

$$\frac{R_A - R_B}{R_A + R_B} = f \operatorname{arccosh}\left[\frac{\exp\left(\frac{\ln 2}{f}\right)}{2}\right] \tag{3.12}$$

The requirement for using the van der Pauw method is to make sure that the average diameters of the contacts, and sample thickness must be much smaller than the distance between the contacts.

Dielectric, ferroelectric, and antiferroelectric properties

A dielectric material is a broad category of insulating materials that can develop a certain amount of polarization under applied electric field. The response of a dielectric material to external field can be either linear (**Figure 3.5**(a)) or non-linear. Ferroelectricity refers to the electrically switchable spontaneous polarization in non-centrosymmetric materials. If an external bias is applied across such a material, the polarization in the material is manifested as a ferroelectric hysteresis loop (**Figure 3.5**(b)). Antiferroelectrics, on the other hand, are those dielectric materials which do not have spontaneous polarization at ground state but the centrosymmetry can be broken under certain applied electric field,

above which the materials become ferroelectric. In turn, the electrical hysteresis loop has two sub-ferroelectric-loops at higher fields (**Figure 3.5**(c)).

To measure the polarization hysteresis loops in (anti)ferroelectric thin-film materials, a sandwich device structure with two electrodes on the top and bottom surfaces of the (anti)ferroelectric thin films is typically used. To fabricate such device structure, a series of established microfabrication procedures are used (**Figure 3.5**(d)). Briefly, a heterostructure with a bottom electrode material (∼20 nm) and a (anti)ferroelectric layer (∼50-150 nm) is grown in sequence in the deposition chamber. After the growth, lithography is used to pattern circular photoresist pads on the heterostructure with diameter ranging from 12.5 μm to 100 μm. The small diameter of the circular capacitor ensures limited electrical leakage in the film during the measurement. Afterwards, a MgO layer of 200 nm thickness is deposited at room temperature on the pattern heterostructure to form a "hard-mask". The photoresist is then removed by acetone and the heterostructure with patterned hard-mask is loaded in the chamber for top-electrode growth. Finally, after the growth the hard-mask is etched off using dilute phosphorous acid and the stand-alone arrays of circular electrodes are fabricated.

During the electrical measurement, the corner of the sample is scratched with a dia-

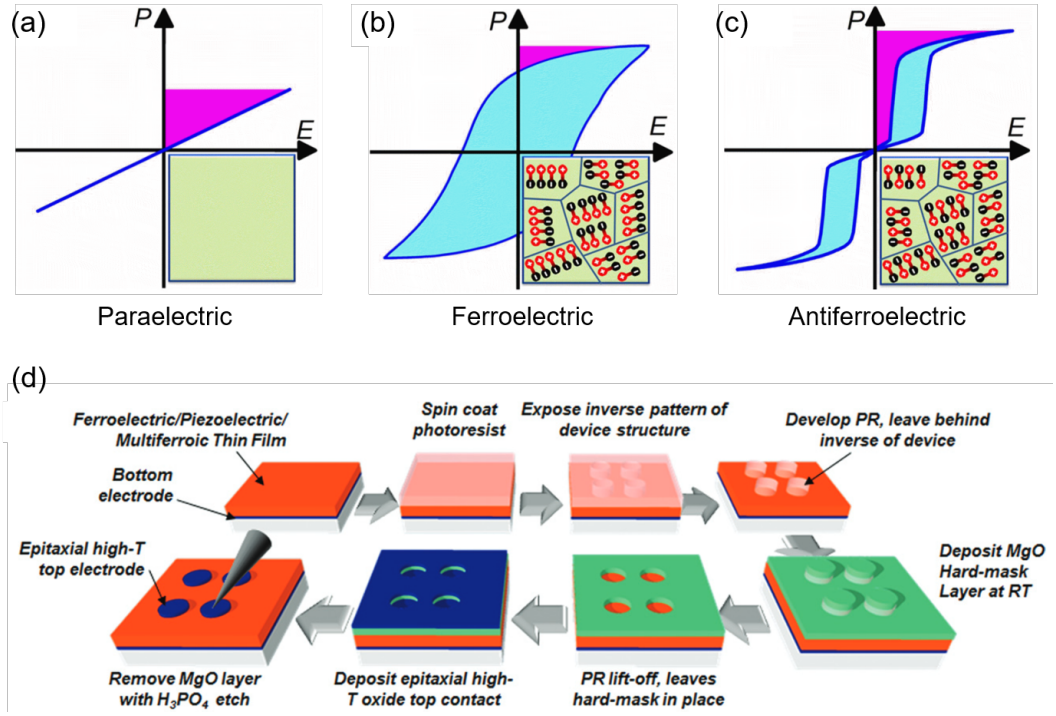

Figure 3.5: *The electrical hysteresis loops of paraelectric (a), ferroelectric (b), and antiferroelectric (c) materials. The corresponding dipole alignment and domain structures are illustrated in the insets. (d)Microfabrication process of top circular electrodes using a MgO hard-mask (Figure adapted from [116]).*

mond scribe to expose the bottom electrode. Two probe tips mounted on micro-manipulators are then contacted with the bottom electrode and the top circular electrode to establish a complete circuit. For ferroelectricity/antiferroelectricity measurements, a ferroelectricity tester (Radiant Technology Inc.) is used which applies voltage pulses in a triangular waveform and the current response from the sample is measured. The integration of the current at different voltage magnitude gives the electrical hysteresis behavior of the material. The ferroelectric tester can also perform tasks such as leakage, PUND (positive-up-negative-down), fatigue, DLTS (deep-level transient spectroscopy), FORC (first-order reversal curve), *etc*. These measurements are frequently used on related materials but are beyond the scope of this dissertation. Readers are guided to a number of publications regarding these ferroelectric analysis techniques [10, 12, 117–120].

Dielectric properties of ferroelectric/antiferroelectric materials also provide significant indication of material behaviors. Dielectric measurements are performed on the same device structure while an AC bias from the impedance analyzer is applied to the sample to extract the magnitude and the phase of the current. The magnitude of the current gives the strength of capacitance, namely, the dielectric constant (relative permittivity) can be extracted ($C = \frac{\epsilon_r \epsilon_0 A}{d}$). The phase of the current provides information regarding the capacitive or the resistive features of the sample. Ideally, the ferroelectric/antiferroelectric material should be a good insulator, thus a capacitive behavior ($i = C\frac{dv}{dt}$) where the current leads the voltage by 90° is expected. For a non-ideal dielectric material with a certain amount of electronic conduction, the dielectric loss tangent is defined as

$$\tan\delta = \frac{\omega\epsilon^{''} + \sigma}{\omega\epsilon^{'}} \tag{3.13}$$

where $\epsilon^{''}$ and $\epsilon^{'}$ are the imaginary and real component of the dielectric permittivity, σ is the electronic conductivity. For reliable dielectric measurement, the contribution from σ should be as small as possible.

Ionic transport and electrochemical properties

Perovskite oxides with high ionic conductivity or surface electrochemical reactivity are promising to be used in solid-oxide fuel cells — devices that efficiently convert chemical energy into electrical energy. The ionic transport property is essentially the diffusion of charged ionic particles in the material, while the electrochemical reactivity is how fast the material can exchange charged ionic particles with the gaseous environment. To extract these properties, a number of experimental techniques can be used such as tracer diffusion and secondary ion mass spectroscopy [121–123], the Hebb-Wagner method [124–126], electrochemical impedance spectroscopy [127, 128], and electrical conductivity relaxation [129–132]. Among those techniques, electrochemical impedance spectroscopy (EIS) is very promising for the study of thin-film heterostructures. The EIS method applies a small sinusoidal AC perturbation to the thin-film samples and the current response contains important information regarding the behavior of the charged particles. The principles

and data analysis of the EIS method are detailed in **Appendix C**. The EIS measurement has to be conducted in the form of a series of temperature- and gas-partial-pressure-dependent studies to further extract the rate constant of a specific reaction process. Such measurements require precise environmental temperature/gas-pressure control but most commercially available measurement setups are designed for bulk samples. Thus, to perform a quantifiable and controllable measurement on thin-film heterostructures, a custom-built measurement setup and measurement procedures were developed.

Both ionic-transport and electrochemical gas kinetic measurements can be performed in the setup. The setup is essentially a sealed tube furnace with feedthroughs to perform temperature monitoring, gas flow control, and electrical connections. As illustrated (**Figure 3.6**), a 2" alumina tube is sustained in the center of a tube furnace. One end of the tube is connected to the vacuum pump and the outlet gas pressure is monitored by either a Pirani gauge or a full-range gauge. The other end of tube is sealed with a customized the KF-type flange which serves the purpose of sample connection, gas inlet, and temperature monitoring. The detailed flange design is given in the figure — four BNC feedthroughs plus a *K*-type thermocouple feedthrough are located around the gas inlet port. An alumina bar is inserted into the alumina bar mount and is fixed by two screws. A gap is maintained between the end of the alumina bar and the flange surface to ensure the gas flow from the gas inlet port. The other end of the alumina bar is mounted with a ceramic chip carrier (CERDIP, Topline Corp.) which is tightened onto the alumina bar using tungsten wires. The electrical pins of the CERDIP is connected to the BNC feedthrough via silver

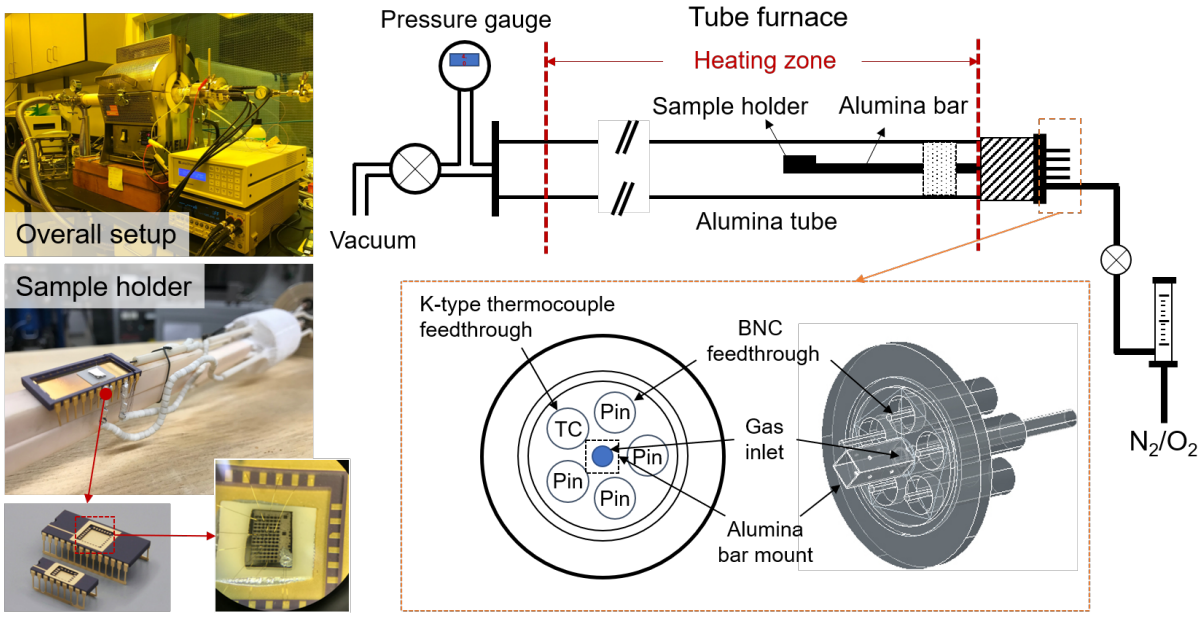

Figure 3.6: *The schematic of the tube-furnace based measurement setup for temperature dependent and gas-pressure dependent studies for thin-film heterostructures*

wires insulated by ceramic beads. A thermal block, which is visible in the figure, is used to hold four thin alumina tube (insulate and protect the silver wires) and to block the heat from reaching the BNC connectors. The thin-film samples are glued via silver paint onto the CERDIP with an AlN substrate, and the connections to the CERDIP are made through gold-wire bonding. Note that the silver paint on the sample corner shown in the figure is for connection to counter electrode in electrochemical gas kinetic measurement.

During the measurement, the temperature is monitored via the internal thermocouple mounted in proximity to the chip carrier and the PID setting of the heater is properly tuned for such sample geometry. The oxygen partial pressure control is achieved in two approaches. The first approach is to maintain the total gas pressure in the tube at atmospheric pressure while change the N_2/O_2 gas mixing ratio. After the tube is pumped to vacuum, the vacuum pump is disconnected and the gas mixture is introduced into the tube with a constant gas flow at atmospheric pressure. This approach is used for qualitative studies where a drastic change in oxygen partial pressure is needed. The other approach is to use oxygen gas only but pump the tube simultaneously to reach to desired pressure. The second approach is used for more quantitative studies where the the oxygen partial pressure is controlled from 100 mtorr to 760 torr. As the desired temperature and gas pressure is achieved and stabilized in the tube, electrochemical impedance spectroscopy measurement is performed using a electrochemical potentiostat (PARSTAT 3000, Princeton Applied Research). The measurement can be performed in either four-probe geometry or two-probe geometry depending on the specific needs of the experiments. In this dissertation, two-probe geometry is typically used for both transport and electrochemical measurement.

Chapter 4

Structure control, magnetism, and transport in $SrRuO_3$

In this chapter, the control of lattice symmetry and octahedral-rotation patterns in $SrRuO_3$ and the corresponding impacts on the magnetic and electrical properties are studied. The structure of $SrRuO_3$ is engineered via the use of octahedral-rotation mismatch at the heterointerfaces. The evolution of the structural features (*i.e.*, lattice parameters, symmetry, and octahedral rotations) of $SrRuO_3$ are examined for films grown on substrates engineered to have the same lattice parameters, but different octahedral-rotation patterns. $SrRuO_3$ films grown on $SrTiO_3$ (001) (no octahedral rotations) and $GdScO_3$-buffered $SrTiO_3$ (001) (with octahedral rotations) substrates are found to exhibit monoclinic and tetragonal symmetry, respectively. Electrical transport and magnetic measurements reveal that the tetragonal films exhibit higher resistivity, lower magnetic Curie temperatures, and more isotropic magnetism as compared to those with monoclinic structure. Synchrotron-based half-order Bragg peak analysis reveals that the tilting pattern in both film variants is the same (albeit with slightly different magnitudes of in-plane rotation angles). The abnormal rotation pattern observed in tetragonal $SrRuO_3$ indicates a possible decoupling between the internal octahedral rotation and lattice symmetry, which could provide new opportunities to engineer thin-film structure and properties.

4.1 Introduction

$SrRuO_3$ is among one of the most extensively studied perovskite systems in the past few decades. It is a member of the larger class of ruthenates with formula $Sr_{n+1}Ru_nO_{3n+1}$ where n=∞ as in the case of $SrRuO_3$. In the bulk form, $SrRuO_3$ is a strong itinerant ferromagnetic material below $\sim$160K primarily due to the more localized electrons with ruthenium 4*d* character. The electrical transport of bulk $SrRuO_3$ shows Fermi-liquid behavior at low temperatures, while it exhibits bad-metal behavior at higher temperature [2, 133, 134]. These properties have driven continuous attention from researchers, and it has the appealing feature that many phenomena are present in the undoped parent phase such that complications from chemical disorder or local strain can be avoided. In recent years, epitaxial thin-film versions of $SrRuO_3$ have become the more widely adapted approach in the study of strong electron correlation phenomena. Beyond the interests in strain engineering, orientation-dependent, or thickness-dependent properties in epitaxial $SrRuO_3$ thin films, the epitaxial $SrRuO_3$ is simultaneously the most popular epitaxial electrode for studies on complex oxide heterostructures.

Structurally speaking, $SrRuO_3$ has orthorhombic symmetry with lattice parameters a_o=5.567 Å, b_o=5.530 Å, and c_o=7.854 Å, where the subscript o denotes an orthorhombic unit cell [135]. The pseudo-cubic lattice has a averaged lattice parameter of a=3.93 Å with octahedral-rotation pattern $a^-a^-c^+$. Early studies have suggested strong coupling between the crystal structure in $SrRuO_3$ and the physical properties. For instance, the magnetic properties are shown to be strongly correlated to the distortion of the octahedral cages where the change of octahedral patterns and angles can suppress or quench the magnetization in $SrRuO_3$ [136]. There is also an intrinsic uniaxial magnetocrystalline anisotropy in the single crystal or thin-film $SrRuO_3$ [137, 138]. Thus, with the advances in thin-film epitaxial techniques, strain engineering has become a dominant approach to enable the direct manipulation of the lattice degree of freedom and study its corresponding impact on magnetism and transport behaviors in $SrRuO_3$. For example, the ferromagnetism can be quenched under application of epitaxial strain due to a suppression of the octahedral rotations that fundamentally changes the density of states of spin-up and -down electrons at the Fermi level [136, 139, 140]. Additionally, the orthorhombic lattice can be driven, under relatively large tensile or compressive strains, to exhibit tetragonal symmetry [141, 142].

However, the pervasive approach in the study of epitaxial strain has been to consider only the role of lattice mismatch-induced strain while neglecting or downplaying the role of octahedral-rotation mismatch (which is hard to quantify and investigate) [32, 36, 46]. As it has been discussed in **Chapter 2**, the interfacial structural coupling has recently been demonstrated as another approach to control the structural degrees of freedom in the perovskites, but at the same time, a complete physical picture of such interactions and understanding of the length scales over which such effects can extend are still being developed. Nonetheless, it is becoming clear that in order to exert deterministic control over such

heterostructures, knowledge of both the lattice and octahedral-rotation mismatch effects are needed. This is particularly important when one considers that at room temperature most commercially-available substrates used for perovskite possess orthorhombic $a^-a^-c^+$ or rhombohedral $a^-a^-a^-$ symmetry with robust octahedral rotations [23, 66, 143, 144]. Thus, the effects of lattice mismatch could be convoluted by additional contributions from the interfacial octahedral-rotation mismatch. Finally, with the increasing study of ultrathin heterostructures and superlattices, where interfacial octahedral rotation coupling could potentially play a more dominant role in controlling film properties, such understanding is essential. Hence, in this chapter, $SrRuO_3$ is used as a model system to examine how interfacial octahedral-rotation mismatch contributes to the micro/macroscopic structural and physical properties.

4.2 Sample design and thin-film synthesis

In order to examine the effects of octahedral-rotation mismatch alone, 10 nm $SrRuO_3$ films are grown directly on bare cubic substrates and on orthorhombic-layer-buffered cubic substrates which leverage strategies to control lattice parameter and octahedral rotations simultaneously. I focused on 10-nm-thick films of $SrRuO_3$ grown on $SrTiO_3$ (001) substrates (cubic, a=3.905 Å); henceforth referred to as non-buffered $SrRuO_3$, and 4 nm $GdScO_3$-buffered (bulk $GdScO_3$ is orthorhombic with a_o=5.745 Å, b_o=5.481 Å, and c_o=7.929 Å [66]) $SrTiO_3$ (001) substrates; henceforth referred to as buffered $SrRuO_3$. A schematic view of the heterostructures is provided (**Figure 4.1**(a)). The design algorithm is based on the fact that there is expected to be much faster relaxation of octahedral rotation distortion at the heterointerface than lattice mismatch strain [35, 46] and thus the presence of the $GdScO_3$-buffer layer allows for one to produce the same lattice constants (as determined by the underlying substrate), but different octahedral-rotation patterns and magnitudes.

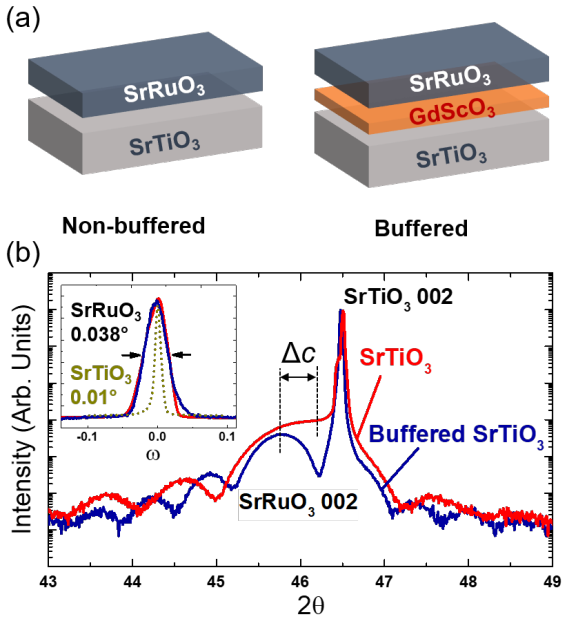

Figure 4.1: *(a)Illustration of the two sample geometries used in this study (b)X-Ray θ-2θ scans about the 002-diffraction conditions for a 10 nm $SrRuO_3$ film grown on both a non-buffered and buffered $SrTiO_3$ substrate. Rocking curves are shown in the insets.*

All films were grown via PLD. Prior to growth, the $SrTiO_3$ substrates were treated by chemical etching and annealing following standard procedures [96]. The $GdScO_3$-buffer layer was grown at 680°C in 7.5 mTorr of oxygen with a laser fluence of 1.5 J/cm^2 at a repetition rate of 5 Hz (a total of 140 pulses yielded 4 nm thick films). The $SrRuO_3$ films were grown at 680°C in 100 mTorr of oxygen with a laser fluence of 1.5 J/cm^2 and a repetition rate of 5 Hz (a total of 750 pulses yielded 10 nm thick films). Following growth, the heterostructures were cooled at 5°C/min. in a static oxygen pressure of 760 Torr. Furthermore, to rule out the effects of varying vicinality in the $SrTiO_3$ substrates [145], $SrRuO_3$ films with or without the $GdScO_3$-buffer layer were grown on multiple pieces of the same substrate wafer. X-ray diffraction studies reveal that all $SrRuO_3$ films are fully-epitaxial and single-phase (**Figure 4.1**(b)). Focusing about the 002-pseudocubic diffraction peak of the $SrRuO_3$, the buffered $SrRuO_3$ exhibits an out-of-plane lattice parameter expansion ($\sim$0.7%) as compared with non-buffered $SrRuO_3$. Rocking curve studies reveal that all $SrRuO_3$ films are uniformly highly crystalline and that the addition of the buffer layer does not diminish the crystalline quality (inset, **Figure 4.1**(b)). Such a lattice expansion suggests a possible structural change of the buffered $SrRuO_3$.

4.3 Structural characterization

RSM studies about the 103- and 013-diffraction peaks of the $SrRuO_3$ and $SrTiO_3$ reveal that all diffraction peaks possess the same Q_x values confirming that the films are coherently strained (**Figure 4.2**(a)). Inspection of the peak positions in the Q_z direction, reveals that the $SrRuO_3$ 103-diffraction peak has a higher Q_z value than the 013-diffraction peak for non-buffered $SrRuO_3$; indicative of a monoclinic version of $SrRuO_3$ with $\beta = 89.5°$ ($\beta = 90° - \arctan(\Delta Q_z/Q_x)$). Inspection of the peak positions in the Q_z direction for the buffered $SrRuO_3$, however, reveals that the 103- and 013-diffraction peaks possess the same Q_z values; indicating a tetragonal version of $SrRuO_3$. The observed structural change suggests that coupling effects between different octahedral-rotation patterns at the heterointerface could be crucial in determining the film crystal symmetry. Such results call for a more comprehensive and detailed structural analysis.

Synchrotron-based half-order Bragg peak analysis has been used to extract octahedral rotation information in perovskite systems [65, 107]. Again, as given in **Table 3.1**, simple rules can be applied to understand the nature of the system: 1) in-phase octahedral rotations (+) will give rise to "even-odd-odd" half-order reflections, while out-of-phase octahedral rotations (-) will produce "odd-odd-odd" reflections; 2) in-phase rotations giving rise to "even-odd-odd" reflections with $k \neq l$ are an indication of an a^+-type rotation and those with $h \neq l$ and $h \neq k$ are indicative of b^+- and c^+-type rotations, respectively, and 3) out-of-phase rotations giving rise to "odd-odd-odd" reflections with $k \neq l$ are an indication of a^--type rotations and those with $h \neq l$ and $h \neq k$ are indicative of b^-- and c^--type rotations, respectively. Additionally, by comparing the measured and simulated intensities of certain half-order Bragg peaks, one is able to quantitatively determine the rotation

angles in the pattern. Note that due to the biaxial strain exerted on the $SrRuO_3$ by the $SrTiO_3$, the octahedra in $SrRuO_3$ will have an elongation along the c axis. Such effects are considered in our calculation by using appropriate lattice constants for the pseudocubic $SrRuO_3$ unit cells. Furthermore, due to the orthorhombic nature of the $SrRuO_3$ unit cell, it is possible to have four different structural domains if the material is grown on an (001) cubic substrate [145], which are denoted as structural domains D_X, D_Y, $D_{X'}$, and $D_{Y'}$, respectively (**Figure 4.2**(b)). When the fittings of the intensities of the half-order Bragg peaks are completed, no *a priori* assumption is made about the make-up of the film as it pertains to these structural domains; thus, one can also extract the volumetric ratio of the different structural domains from these analyses.

Although over 100 *hkl* scans were performed to get accurate rotation angles and domain structures, four representative scans for each heterostructure type are shown here which are sufficient to determine the octahedral-rotation patterns in the $SrRuO_3$ films (**Figure 4.3**). The octahedral-rotation patterns of the monoclinic, non-buffered $SrRuO_3$ (**Figure 4.3**(a)) are first analyzed.[1] Based on the rules discussed above, the appearance of $1\frac{1}{2}\frac{3}{2}$-diffraction peaks from the $SrRuO_3$ indicates that the in-phase (+) rotation is along the [100] or [010] of the $SrTiO_3$ substrate while the peak intensity difference suggests that one structural domains is dominant. In addition, $\frac{1}{2}\frac{1}{2}\frac{3}{2}$-, $\frac{1}{2}\frac{1}{2}\frac{3}{2}$-, and $\frac{1}{2}\frac{3}{2}\frac{1}{2}$-diffraction peaks are also observed, which reveal that there are two, out-of-phase rotation (-) axes that lie either in-plane or out-of-plane, but perpendicular to the (+) axis. Therefore, we can determine that the octahedra cage in the monoclinic variant of $SrRuO_3$ is rotated along all three orthogonal directions and that the (+) axis of the rotated octahedra is aligned along either the [100] or [010] of the $SrTiO_3$ substrate resulting in two structural domains (D_X and D_Y), albeit with

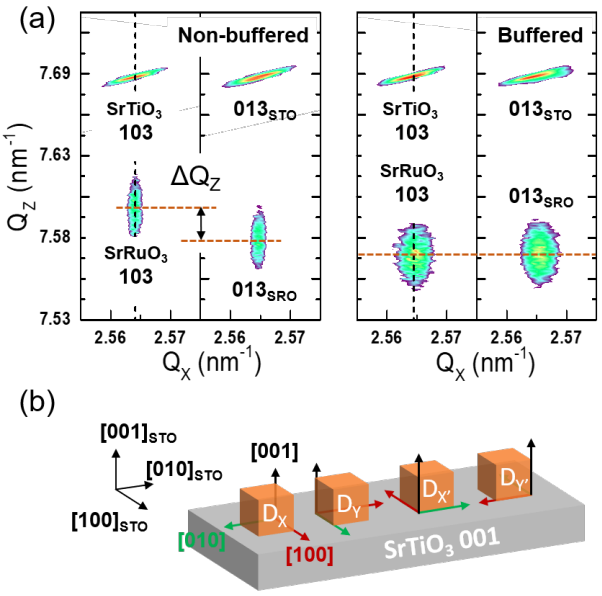

Figure 4.2: *(a)Reciprocal space mapping about 103- and 013-diffraction conditions of the $SrRuO_3$ and $SrTiO_3$ for films grown on non-buffered and buffered substrates. (b)Four structural domains (D_X, D_Y, $D_{X'}$, and $D_{Y'}$) of $SrRuO_3$ on $SrTiO_3$ substrates. D_Y, $D_{X'}$, and $D_{Y'}$ domains can be thought of rotating domain D_X by 90°, 180°, and 270° about [001] direction. Note that [100] direction is aligned with in-phase (+) rotation axis.*

[1]The half-order Bragg peak analysis were accomplished in collaboration with Mr. Y. Dong, Dr. H. Zhou, and Dr. D. D. Fong at Advanced Photon Source, Argonne National Laboratory, IL, USA.

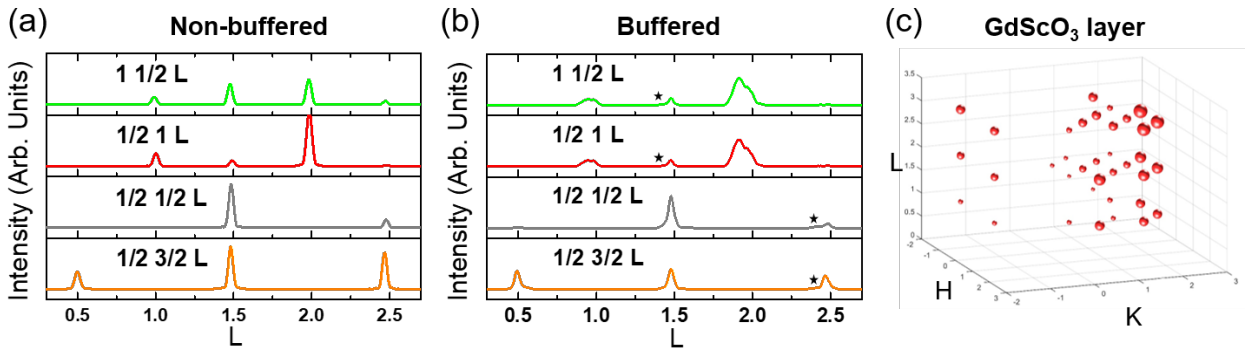

Figure 4.3: *Four representative half-order Bragg peak patterns for 10 nm thick SrRuO$_3$ films grown on (a) non-buffered and (b) buffered SrTiO$_3$. (c)Difference in l of corresponding hkl diffractions from GdScO$_3$ buffer layer and tetragonal SrRuO$_3$ films. Higher index gives bigger difference, which is indicating that GdScO$_3$ has a monoclinic structure.*

one of those domains dominating. Such a preference for forming one type of domain is expected due to the miscut of the $SrTiO_3$ substrate which will tend to drive the orthorhombic *c*-axis of the $SrRuO_3$ to be aligned with the step edges of the substrates.

Similar analysis can be applied to the tetragonal, buffered $SrRuO_3$. First, the appearance of half-order Bragg peaks from the $GdScO_3$-buffer layer next to those from the $SrRuO_3$ (marked with stars, **Figure 4.3**(b)) suggests that both layers possess a similar octahedral-rotation pattern and domain structure. Further analysis of the $GdScO_3$-buffer layer reveals that it exhibits bulk-like monoclinic lattice symmetry as suggested by the increasing out-of-plane diffraction peak position difference as compared to the tetragonal $SrRuO_3$ as one moves to higher *hkl* indices (**Figure 4.3**(c)). In other words, the octahedral-rotation pattern of the substrate is different when the 4 nm $GdScO_3$-buffer layer is included in the heterostructure. Upon turning our attention to the half-order Bragg peaks arising from the $SrRuO_3$, however, the fitting suggests that the octahedral-rotation pattern in this tetragonal variant of $SrRuO_3$ is same as that in the monoclinic variant of non-buffered $SrRuO_3$. At the same time, the structural domain pattern of the tetragonal, buffered $SrRuO_3$ is changed as indicated by nearly equivalent peak intensities for the $1\frac{1}{2}\frac{3}{2}$- and $\frac{1}{2}1\frac{3}{2}$-diffraction peaks; indicating that the D_X and D_Y structural domains have a similar volumetric ratio. To summarize, using the buffer-layer approach, the nature of the octahedral-rotation pattern of the substrate can be effectively tuned, while the same in-plane lattice parameters are maintained. In turn, this results in a change in the lattice symmetry of the $SrRuO_3$ and the structural-domain fractions, but does not change the octahedral-rotation patterns. From here, we can further extract quantitative values for the nature of these octahedral rotations.

As noted above, comparison of the calculated peak intensities of a full range of half-order *hkl* scans with the experimental data provides a route to extract the octahedral rotation angles and structural-domain fractions for the system as given in (3.5) and (3.6) [84, 107]. The fitting results for $SrRuO_3$ on non-buffered- and buffered-$SrTiO_3$ substrates

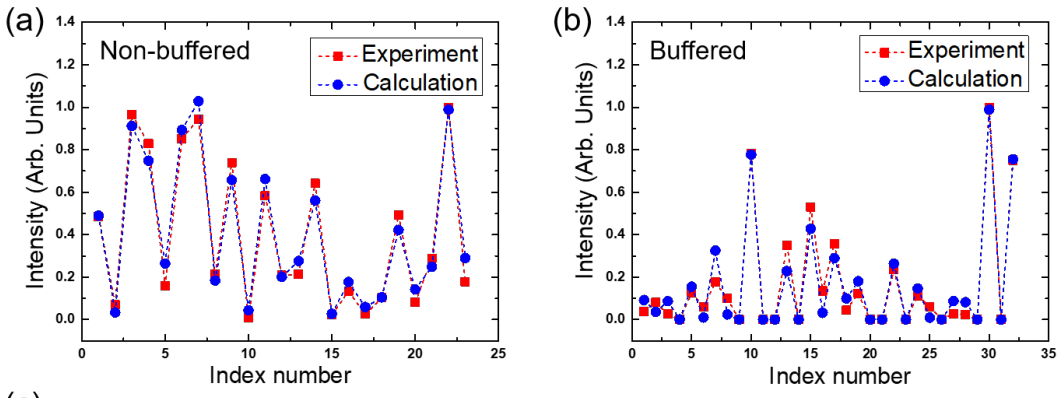

(c)

	Octahedral Rotation Angle (°)			Variant Ratio (%)			
	α	β	γ	X	Y	X'	Y'
Non-Buffered	6.2 ± 1.3	6.8 ± 1.4	7.4 ± 1.5	33.2	12.5	35.7	18.6
$GdScO_3$-Buffered	5.7 ± 1.6	5.9 ± 1.9	7.2 ± 1.4	20.8	23.2	30.6	25.4
Bulk	6.19	5.97	5.97	-	-	-	-

Figure 4.4: *Half-order Bragg peak analysis results of non-buffered $SrRuO_3$ films grown on non-buffered $SrTiO_3$ substrates (a) and $GdScO_3$-buffered $SrTiO_3$ substrates (b). Red data are acquired from experiments and blue data are calculated intensities. (c)The experimentally measure and extracted octahedral rotation angles and domain variant fractions as obtained from the half-order Bragg peaks analysis.*

are shown (**Figure 4.4**(a) and (b), respectively). In each figure set, the figure plots the measured/calculated peaks with respect to peak indices. The blue data is the calculated peak intensities and the red data is from the experimental results. For the monoclinic variant of $SrRuO_3$, the best fitting results give the coefficient of determination R^2=0.917 with a variance χ=0.082. For the tetragonal variant of $SrRuO_3$, the best fitting results give the coefficient of determination R^2=0.969 with a variance χ=0.151. Thus, fitting results for both samples provide reasonable accuracy in determining rotation angles and domain structures.

The extracted rotation angles and structural-domain fractions are given (**Figure 4.4**(c)). For monoclinic, non-buffered $SrRuO_3$, the rotation angles along the three orthogonal axes are extracted to be $\alpha = 6.2° \pm 1.3°$ (in-plane (+) axis), $\beta = 6.8° \pm 1.4°$ (in-plane (-) axis), and $\gamma = 7.4° \pm 1.5°$ (out-of-plane (-) axis). Two majority structural variants (D_X and $D_{X'}$) occupying ~70% of the volume are observed. Therefore, the octahedral-rotation patterns can be determined to be $a^+b^-c^-$ or $a^-b^+c^-$. For comparison, in bulk $SrRuO_3$ the rotation pattern is $a^+c^-c^-$ with $\alpha_{bulk} = 6.19°$ and $\beta_{bulk} = \gamma_{bulk} = 5.97°$ [2]. Thus, in monoclinic, non-buffered $SrRuO_3$, the octahedral rotation angle in the in-plane (+) axis is similar to the bulk value, but the rotations in the two (-) axes, especially the one along the [001] of

$SrTiO_3$, are considerably larger and the down-selection of structural domains is consistent with prior work [145].

Similarly, for tetragonal, buffered $SrRuO_3$, the rotation angles are extracted to be $\alpha = 5.7° \pm 1.6°$, $\beta = 5.9° \pm 1.9°$, and $\gamma = 7.2° \pm 1.4°$, which are slightly smaller than those in the monoclinic, non-buffered variant. Surprisingly, four structural domains (D_X, D_Y, $D_{X'}$, and $D_{Y'}$) are found to occupy similar volumetric fractions in the films. Based on the discussion above, the octahedral-rotation pattern of tetragonal $SrRuO_3$ can also be represented as $a^+b^-c^-$ or $a^-b^+c^-$. As compared to monoclinic, non-buffered $SrRuO_3$, however, in the tetragonal variant the out-of-plane (-) axis octahedral rotation remains the same, but the two in-plane rotation angles are slightly reduced. Such a decrease in the in-plane octahedral rotation angles results in an out-of-plane lattice expansion, while the unchanged γ angle suggests that the octahedral rotation along the out-of-plane axis is mainly controlled by lattice mismatch.

4.4 Octahedra rotational domains

What is more surprising is the observation of four structural domains in the tetragonal variant. As the lattice possesses four-fold symmetry about the [001], only one structural variant should be allowed. One potential explanation that could be considered, is that instead of having a tetragonal variant of $SrRuO_3$, the buffered sample has an equal volumetric fraction of four different structural nanodomains of a monoclinic structure with an expanded out-of-plane lattice parameter. Such a structure could potentially give rise to a similar set of RSM diffraction patterns to that observed for a tetragonal structure. In assessing this possibility, however, we believe that our proposed tetragonal structure is more likely for a number of reasons.

- First, as noted above, the shape of the RSM diffraction peaks are consistent with a tetragonal structure due to the lack of broadening in the Q_Z direction (*i.e.*, suggesting only a single structural variant is present).

- Second, a highly-distorted monoclinic structure, with lattice expansion along the out-of-plane direction, cannot be easily rationalized considering that the strain state is unchanged and that the octahedral-rotation pattern and angles are nearly the same in the two observed structures.

- Third, we have also observed "even-even-odd" half-order Bragg diffraction peaks arising from *A*-site cation displacement in films grown on both non-buffered and buffered $SrTiO_3$. Variations in the intensity of the "even-even-odd" half-order Bragg peaks provide an indication of the change in the monoclinic angle in the structures. From our data (taken from samples of the same size, thickness, substrate, exposure times, *etc*.) the intensity of the "even-even-odd" peaks from the films grown on the buffered $SrTiO_3$ (*i.e.*, the suspected tetragonal variant of $SrRuO_3$) are much lower than for

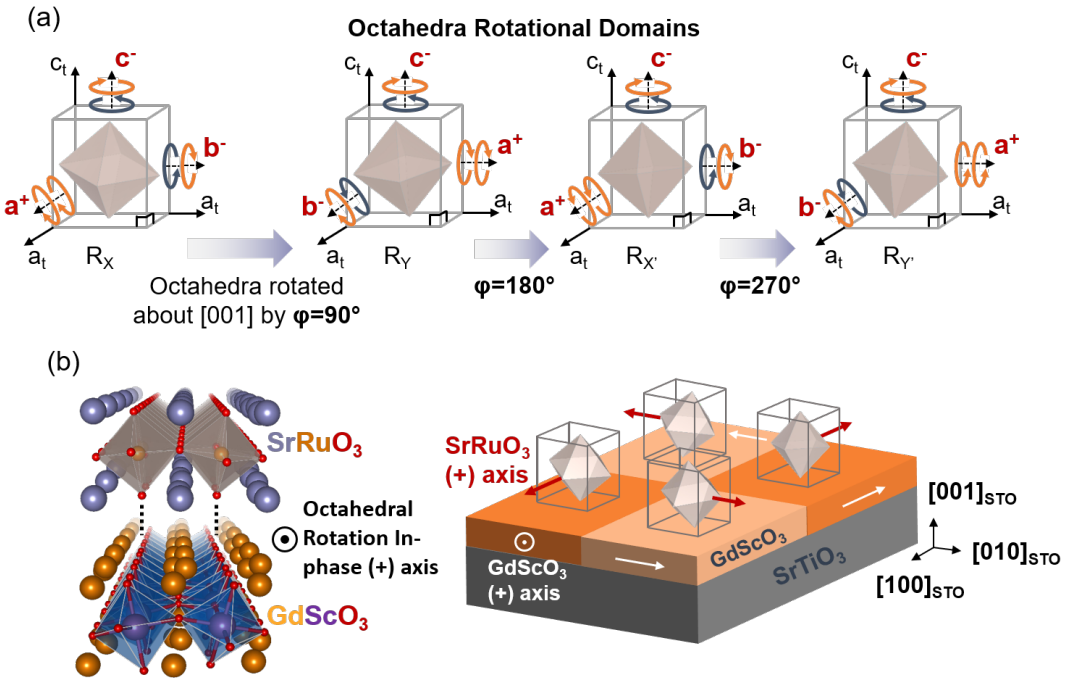

Figure 4.5: *(a)Schematic illustration of the four "rotational" domains (R_X, R_Y, $R_{X'}$, and $R_{Y'}$) possible in the tetragonal variant of $SrRuO_3$ where the various rotational domains can be thought of rotating the octahedra within the lattice about the [001] by 0°, 90°, 180°, or 270°. (b) Illustration of the tendency of the $SrRuO_3$ to align its in-phase (+) rotation axis with the $GdScO_3$ (+) rotation axis during growth and the corresponding coupling between $GdScO_3$ structural domains and $SrRuO_3$ rotational domains. Arrows show the direction of in-phase (+) octahedral rotation axis.*

films grown on non-buffered $SrTiO_3$ (*i.e.*, the monoclinic variant of $SrRuO_3$); thus suggesting that the monoclinic angle has been reduced in the tetragonal variant.

- Finally, examination of the RHEED data taken during the growth of the $SrRuO_3$ on the buffered $SrTiO_3$ reveals a step-flow growth mode as the diffraction intensity was found to increase with time and flatten out (continued film growth) showing no indication of intensity oscillations. In step-flow growth, it is likely that the $SrRuO_3$ will down-select to a single dominant structural variant; suggesting that the presence of four different structural domains of a distorted monoclinic structure is unlikely.

With these being said, however, fitting of the half-order Bragg peaks suggests the presence of four different "structural" domains within the tetragonal lattice. These "structural" domains are the result of different octahedral-rotation patterns in the films which, in turn, give rise to a number of half-order diffraction peaks. From the fit, we observe four uniquely different octahedral-rotation patterns where the octahedra can rotate about the [001] by

0°, 90°, 180°, or 270°, thus giving rise to what we will refer to as "rotational" domains R_X, R_Y, $R_{X'}$, and $R_{Y'}$ (**Figure 4.5**(a)). In other words, the combination of RSM and half-order Bragg peak analyses suggest that in tetragonal $SrRuO_3$, it is possible to rotate the nature of the octahedral rotation independently within the lattice. The fits also reveal a nearly equivalent volume fraction of the different rotational domains (**Figure 4.4**(c)). We propose that this arises due to the presence of a number of rotational domains in the $GdScO_3$-buffer layer. As is common, when an orthorhombic material is grown on a cubic substrate, multiple structural variants are formed. In this case, although the results suggest that the $GdScO_3$ has a similar octahedral-rotation pattern to the $SrRuO_3$, exact fitting of this pattern is difficult because of large changes in the rotation pattern in the $GdScO_3$ which is confined between non-rotated ($SrTiO_3$) and rotated ($SrRuO_3$) materials. In turn, we hypothesize that the presence of various rotational domains in the $GdScO_3$ results in uniform epitaxial growth of the tetragonal variant of $SrRuO_3$, but separation of the $SrRuO_3$ in four different rotational domains as dictated by the local octahedral rotation alignment in the $GdScO_3$-buffer layer which tends to drive the in-phase (+) rotation axis in the $GdScO_3$ and $SrRuO_3$ to be aligned (**Figure 4.5**(b)).

In the theory proposed by Glazer [64] that relates the octahedral rotation network and the lattice symmetry, a three-tilt system is expected to have lower lattice symmetry (*e.g.*, triclinic or orthorhombic). For a high-symmetry lattice (*e.g.*, tetragonal), however, it is thought that the octahedra is only allowed to rotate along one axis (*i.e.*, $a^0a^0c^-$) [68, 146, 147]. In the tetragonal, buffered $SrRuO_3$, however, we observe the presence of a three-tilting octahedral-rotation pattern suggesting that the internal octahedral-rotation pattern could be decoupled from the symmetry of the lattice. Similar structural changes in tensile-strained $SrRuO_3$ have been reported before, but the results suggest no/limited decoupling between oxygen octahedra and lattice symmetry [86]. Moreover, due to such a decoupling of the lattice symmetry and octahedral-rotation pattern, we are able to observe multiple rotational domains in a tetragonal lattice. It is important to note that such decoupling is fundamentally allowed because, within the calculation framework of Glazer, the displacement of cations are not considered, and thus the symmetry given by the octahedral network and the symmetry given by cations could potentially be considered separately. Such decoupling is likely to be a generic feature of perovskite oxide thin films, but the magnitude of this effect could vary depending on the extent of hybridization of the states arising from the *A*-site cation and those of the *B*-site and anion lattice. For instance, similar results have been reported for $SrTiO_3$ thin films grown on tensile substrates wherein the lattice appears to be tetragonal while the internal octahedral-rotation pattern belongs to orthorhombic symmetry group *Cmcm* [148]. Likewise, for $BiFeO_3$ films on $(LaAlO_3)_{0.3}(Sr_2AlTaO_6)_{0.7}$ substrates, the tetragonal lattice as probed by synchrotron radiation contains a monoclinic, polar symmetry [149]. Such findings deserve further studies and could be potentially useful in designing novel ultrathin/superlattice perovskite systems.

4.5 Impact on physical properties of $SrRuO_3$

Armed with this detailed understanding of the lattice symmetry and octahedral rotations, we proceeded to explore how such effects could drive changes in the physical properties of $SrRuO_3$. Temperature-dependent resistivity measurements from 25-250 K in the van der Pauw geometry (**Figure 4.6**) [115] reveal the high-quality of the $SrRuO_3$ heterostructures as indicated by the overall low resistivity ($10^{-5} - 10^{-4}$ Ω-cm) and the relative large ratio (4-6) between high- and low-temperature resistivity (ρ_{250K}/ρ_{25K}) [2]. In general, it has been argued that epitaxial strain [136], film thickness [146, 150], and stoichiometry [151] can significantly affect the film structure (*i.e.*, Ru-O-Ru bond angle) thereby giving rise to changes in hybridization between the ruthenium *4d* orbitals and the O *2p* orbitals which will manifest in marked changes in the macroscopic electrical transport. From this work, however, in a situation where we have controlled film thickness, stoichiometry, crystallinity, and strain state to be the same, the mere insertion of the $GdScO_3$-buffer layer (and the subsequent changes the lattice symmetry and in-plane octahedral rotation angles of $SrRuO_3$) results in an increase in T_C by $\sim$5 K and gives rise to a large increase in the overall film resistivity (over 100% at low temperature).

We additionally studied the magnetic properties of buffered and non-buffered $SrRuO_3$ heterostructures. Hysteresis loops for the monoclinic, non-buffered $SrRuO_3$ (**Figure 4.7**(a)) reveal that the $SrRuO_3$ films have an out-of-plane easy axis that gives a saturated magnetization of $\sim$1.46 μ_B/Ru ($\sim$225 emu/cc) and projects anisotropically onto the [100] and [010]. Additionally, a sharp magnetic phase transition was observed in the temperature-dependence of the non-buffered $SrRuO_3$ and the T_C was determined to be $\sim$148 K (**Figure 4.7**(b)). Upon insertion of the $GdScO_3$-buffer layer and transformation of the $SrRuO_3$ film to tetragonal symmetry, the films still exhibit an out-of-plane easy axis, but with nearly isotropic in-plane magnetic response (**Figure 4.7**(c)). Also, the out-of-plane magnetization was also found to be decreased to $\sim$1.06 μ_B/Ru ($\sim$165 emu/cc). In $SrRuO_3$, the magnetization is strongly coupled with the orthorhombicity of the unit cell and, as has been calculated [152], increasing the unit-cell symmetry from orthorhombic to cubic will lower the ground-state magnetic moments. Thus,

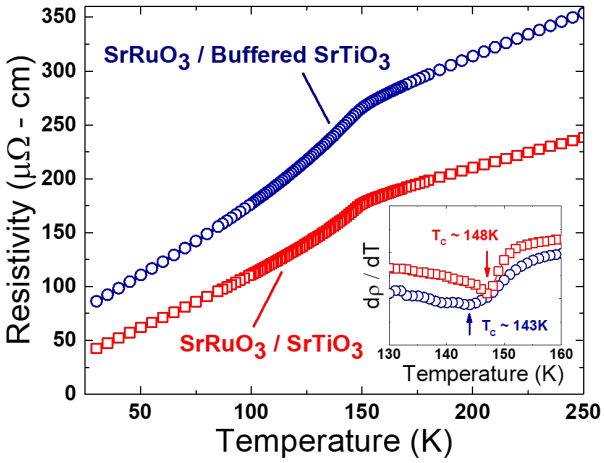

Figure 4.6: *Temperature-dependent electrical resistivity behavior for 10 nm $SrRuO_3$ films grown on non-buffered and buffered $SrTiO_3$. The inset shows $d\rho/dT$ vs. T curves and demarcates the T_C.*

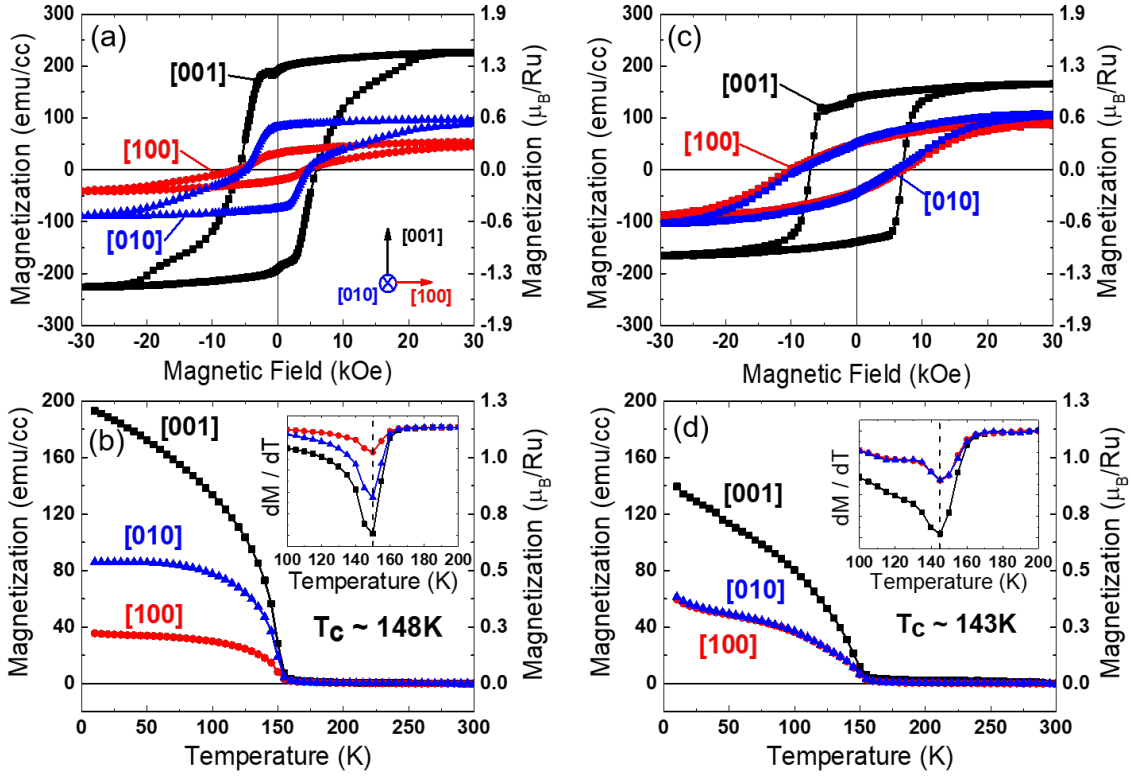

Figure 4.7: *Magnetization-magnetic field and magnetization-temperature results for 10 nm $SrRuO_3$ films grown on (a),(b) non-buffered and (c),(d) buffered $SrTiO_3$. All sample are cooled at 1 T field from room temperature to 5 K prior to study.*

the smaller saturated magnetic moments that we observed in the $SrRuO_3$ films grown on buffered $SrTiO_3$ are consistent with an increase in the symmetry of the film. Likewise, in the tetragonal variant of $SrRuO_3$, a reduction of the T_C to ~143 K was observed (**Figure 4.7**(d)); consistent with the observations from the electronic transport.

4.6 Conclusions

In summary, it is demonstrated that for buffered and non-buffered $SrRuO_3$ films, even under the same lattice mismatch strain, one is able to change the film lattice symmetry and corresponding electrical and magnetic behavior by changing the interfacial octahedral-rotation patterns. Detailed structural studies via half-order Bragg peak analysis have revealed that the octahedral-rotation pattern of buffered and non-buffered $SrRuO_3$ are both $a^+b^-c^-$, while the in-plane octahedral rotation angles are reduced in those grown on non-buffered substrates and nearly equal fractions of "rotational" domain are observed. The observed $a^+b^-c^-$ octahedral-rotation pattern in tetragonal variants of $SrRuO_3$ suggests that

the symmetry of the octahedral rotation network as described by Glazer can actually be decoupled from the symmetry of the overall lattice. These results, in turn, provide new insights into novel ways of engineering structure and physical properties of perovskite thin films, and lead to better understand the interaction between strain, octahedral behavior and crystal symmetry in perovskite oxide thin films.

Chapter 5

Control of antiferro-/ferroelectricity in $PbZrO_3$

Antiferroelectric $PbZrO_3$ is being considered for a wide range of applications where the competition between centrosymmetric and non-centrosymmetric phases is important to the response. In this chapter, the evolution of crystal structure in $PbZrO_3$ is studied under the impact of caion nonstoichiometry. The epitaxial growth of $PbZrO_3$ thin films in layer-by-layer growth mode using pulsed laser deposition are achieved and the chemistry-structure coupling in $Pb_{1+\delta}ZrO_3$ (δ= 0, 0.1, 0.2) is explored. Although no significant lattice parameter change is observed in X-ray studies, electrical characterization reveals that while the $PbZrO_3$ and $Pb_{1.1}ZrO_3$ heterostructures remain intrinsically antiferroelectric, the $Pb_{1.2}ZrO_3$ heterostructures exhibit a hysteresis loop indicative of ferroelectric response. Further X-ray scattering studies reveal strong quarter-order diffraction peaks in $PbZrO_3$ and $Pb_{1.1}ZrO_3$ heterostructures indicative of antiferroelectricity, while no such peaks are observed for $Pb_{1.2}ZrO_3$ heterostructures. Density functional theory calculations suggest the large cation nonstoichiometry is accommodated by incorporation of antisite Pb_{Zr} defects, which drives the $Pb_{1.2}ZrO_3$ heterostructures to a ferroelectric phase with *R*3*c* symmetry. In the end, stabilization of metastable phases in materials via chemical nonstoichiometry and defect engineering enables a novel route to manipulate the energy of the ground state of materials and the corresponding material properties.

5.1 Introduction

Antiferroelectricity is the condensation of a nonpolar lattice mode that "exhibits large dielectric anomalies near the transition temperature and that can be transformed to an induced ferroelectric phase by application of an electric field" [153]. It is an close analogy to the definition of ferroelectricity that a ferroelectric phase is obtained by the condensation of a polar lattice mode and can be switched between more symmetry-related modes via applied field. The competition between a ferroelectric polar phase and an antiferroelectric nonpolar phase is the intrinsic feature of antiferroelectric materials. The macroscopic electrical behavior of antiferroelectric material is manifested by a double-hysteresis loop of polarization under applied electric field (**Figure 5.1**(a)). Energetically speaking, a phenomenological description of an antiferroelectric system is proposed by Kittel [154] and the Helmholtz free energy is given by

$$A(P_a, P_b, T) = A_0 + f(P_a^2 + P_b^2) + gP_aP_b + h(P_a^4 + P_b^4) - E(P_a + P_b) \tag{5.1}$$

where P_a and $P_b$are the polarization of two interpenetrating sublattices a and b. f, g, h are coefficients and E is the electric field. Coupling term g>0 indicates the favored antiparallel alignment of dipole moments. The Kittel model can be converted into a Landau functional [155] given by

$$G(P_F, P_A, T) = \frac{1}{2}(f + \frac{g}{2})P_F^2 + \frac{1}{2}(f - \frac{g}{2})P_A^2 + \frac{h}{8}(P_F^4 + 6P_A^2P_F^2 + P_A^4) - EP_F \tag{5.2}$$

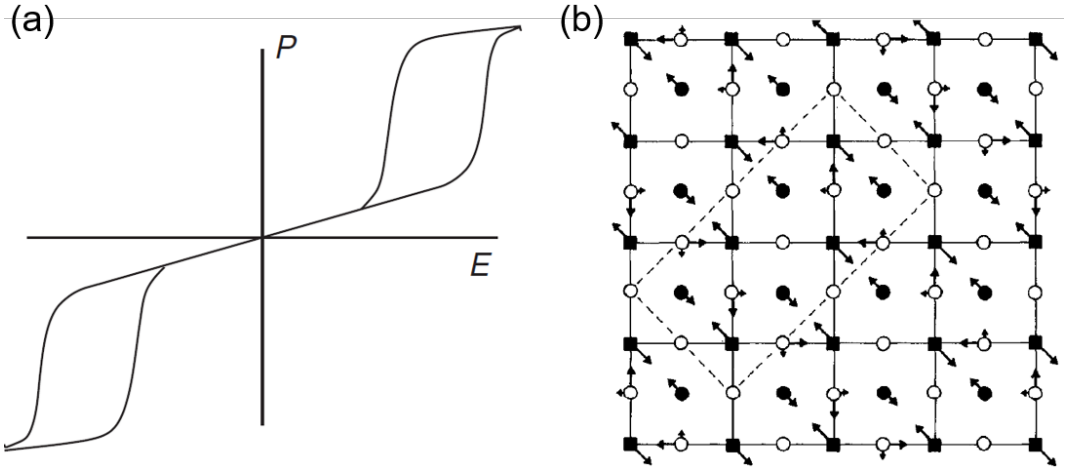

Figure 5.1: *(a) A representative polarization hysteresis loop of antiferroelectrics. (b) Projection of atomic displacements associated with the Σ_2 mode at $q = \frac{2\pi}{a}(1/4, 1/4, 0)$ onto the ab-plane. Squares and circles indicate lead and oxygen ions, respectively. Filled and open circles show ions on the lead cation layer and ions on the zirconium cation layer, respectively [153].*

where $P_F = P_a + P_b$ represents ferroelectric polarization and $P_A = P_a - P_b$ represents the antiferroelectric polarization. The polarization behavior of antiferroelectric materials under electric field can be calculated by minimizing the Gibbs free energy such that

$$\frac{\partial G}{\partial P_F} = 0, \tag{5.3}$$

and

$$\frac{\partial G}{\partial P_A} = 0. \tag{5.4}$$

By solving this phenomenological model the double hysteresis loop under applied field can be achieved.

While from a structural point of view, the antiferroelectric ground state of the material typically involves a low-symmetry unit cell with antiparallel displacement of the cations. It's important to note that although some materials also possess antiparallel displacement of cations such as $GdFeO_3$-type perovskites, the antiferroelectric materials are distinguished from those by a breaking of centrosymmetry under applied electric field. Taking the canonical antiferroelectric $PbZrO_3$ as an example, the main features of the orthorhombic *Pbam* structure can be described by two dominant phonon modes. The first is the Σ_2 mode at $q = \frac{2\pi}{a}(1/4, 1/4, 0)$ which describes the antiparallel displacement of the lead ions along [110]. Another dominant phonon mode is the antidistortive octahedral rotation mode R_5^- with rotation about the [110]. These two modes generate the space group *Pbam* with a $\sqrt{2}a \times 2\sqrt{2}a \times 2a$ unit cell (a as the lattice parameter of the pseudocubic unit cell) which consists of eight pseudocubic unit cells [156–159]. An illustration of the atomic displacement corresponding to the two modes projected on the *ab*-plane of $PbZrO_3$ is given (**Figure 5.1**(b)). In the bulk, $PbZrO_3$ is able to undergo an electric-field-induced, first-order phase transition from a non-polar ground state to a metastable polar state. The antiferroelectric features of $PbZrO_3$ makes it a promising candidate for applications in energy storage [160], electro-thermal energy conversion [161, 162], and transducers [163, 164]. Alternatively, because of the small free energy difference between the phases, the system is highly susceptible to perturbations including electric fields [165, 166], point defects [167, 168], lattice distortions [169, 170], and electrostatic boundary conditions [171–173], which can tip the balance of the ground state energy competition.

Thus, it is important to understand the effect of these perturbations to better control and engineer $PbZrO_3$ for future applications, and to synthesize the material in a controllable way such that the desired properties are achieved. In the past decades, although various routes, such as chemical substitution [174], epitaxial strain [175–178], and size effects [173, 179], have been studied to modify and control the ground state of $PbZrO_3$, the impact of cation nonstoichiometry has rarely been explored. There is growing evidence that cation nonstoichiometry can play a significant role in the evolution of material properties as has been highlighted in, for example, $SrTiO_3$ [180–182], $BaTiO_3$ [183, 184], and $BiFeO_3$ [185]. This is particularly important in perovskite systems where the polarization and lattice modes are strongly coupled and, thus, local nonstoichiometry and lattice imperfection

can distort the structure and drive the material into exotic ground states. For instance, in nonstoichiometric $Sr_{1-\delta}TiO_3$ thin films, the local strontium-deficiency is thought to perturb the lattice and give rise to relaxor-like behavior [182, 186]. It has also been reported that in ferroelectric $BaTiO_3$ thin films, local lattice imperfection and aligned defect dipoles can induce dramatic changes in the ferroelectric-to-paraelectric phase transition temperature [187]. Thus, the effect of cation nonstoichiometry where local cation excess or deficiency and lattice distortions are expected, could have a significant impact on antiferroelectric $PbZrO_3$ where multiple lattice instabilities are involved in determining the final ground state. Additionally, in $PbZrO_3$, previous work has already found that the system is prone to antisite defects (*i.e.*, lead ions replacing zirconium ions) [188–191]. This tendency for antisite defects and the fact that, to acquire high-quality lead-based compounds, excess lead is typically added to the precursors to compensate for the evaporation of lead at high temperature [192–194], motivates the need for a systematic study of the impact of cation nonstoichiometry on the structure and properties of $PbZrO_3$. In this spirit, this chapter focuses on the effects of cation stoichiometry on the antiferroelectric-ferroelectric phase stability, structural distortions, and field-dependent polarization behavior of $Pb_{1+\delta}ZrO_3$ thin films.

5.2 $PbZrO_3$ thin-film growth dynamics

In this study, $Pb_{1+\delta}ZrO_3$ thin films were grown on 10 nm $SrRuO_3$-buffered $DyScO_3$ (110) substrates (CrysTec GmBH) via RHEED-assisted PLD from ceramic targets of nominal stoichiometries of $PbZrO_3$, $Pb_{1.1}ZrO_3$, and $Pb_{1.2}ZrO_3$. The $SrRuO_3$ was grown at a heater temperature of 680°C in a dynamic oxygen pressure of 100 mTorr and with a laser fluence and repetition rate of 1.0 J/cm^2 and 5 Hz, respectively. For the various $Pb_{1+\delta}ZrO_3$ films, growth was completed at a heater temperature of 630°C in a dynamic oxygen pressure of 80 mTorr and with a laser fluence and repetition rate of 1.8 J/cm^2 and 5 Hz, respectively. All films were grown in an on-axis geometry with a target-to-substrate distance of 5.2 cm. Following growth, the films were cooled to room temperature at a rate of 10°C/min. in a static oxygen pressure of 700 Torr.

To illustrate the growth dynamics, I use the RHEED intensity and pattern acquired during the growth a $Pb_{1.2}ZrO_3$ heterostructure as an example as it clearly illustrated the typical oscillation pattern observed (**Figure 5.2**(a)). The intensity vs. time and the diffraction patterns reveal an initially high intensity specular reflection corresponding to the smooth $SrRuO_3$ bottom electrode grown prior to the $Pb_{1+\delta}ZrO_3$ heterostructures. As the laser begins to fire and deposit material, an initial rapid decrease in intensity is followed by 2-3 oscillations in the first $\sim$10 seconds of growth of the $Pb_{1+\delta}ZrO_3$ (**Figure 5.2**(b)). After these initial oscillations, the specular reflection intensity drops to a nearly constant value and the diffraction pattern becomes indicative of a 3D-like structure (**Figure 5.2**(a), inset with orange arrow). Such growth dynamics are consistent with a *Stranski-Krastanov*-like (*S-K*) growth mode where several smooth mono-layers are followed by 3D island growth

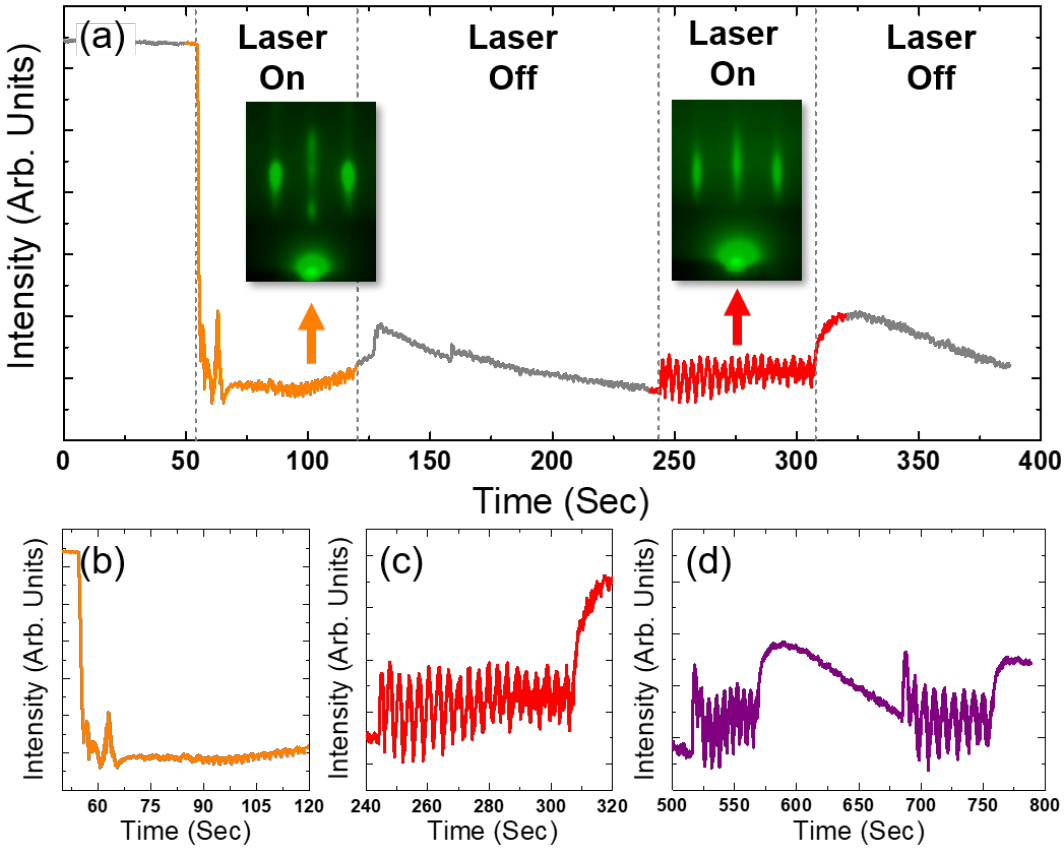

Figure 5.2: *(a) Monitored main diffraction peak intensity in RHEED for $Pb_{1.2}ZrO_3$ heterostructure growth. The insets show 3D and 2D diffraction patterns under S-K growth mode at different growth stages. (b) Initial 2-3 unit cells of $Pb_{1.2}ZrO_3$ under layer-by-layer growth mode. (c) Layer-by-layer growth after surface reconstruction during laser-off time period. (d) Continuous layer-by-layer growth which can be sustained by intermittently stopping the laser to have film surface reconstructed.*

after a critical thickness is reached (**Figure 2.3**(c)). In our case, 2-3 unit cells are deposited initially via a layer-by-layer growth mode and are believed to be the strained $Pb_{1+\delta}ZrO_3$. Later I will show this portion of the film can be observed in synchrotron X-ray diffraction studies where a weak peak can be observed with the same L value as substrate but much smaller $(H+K)/2$ value. After the growth of the initial 2-3 strained $Pb_{1+\delta}ZrO_3$ layers, due to the large lattice mismatch between film and substrate (up to -5.2% compressive strain) and the growing strain energy of the film, the remaining $Pb_{1+\delta}ZrO_3$ transitions to an island-growth mode. The 3D-like growth was, in this example, continued for another $\sim$45 seconds, and then the deposition is stopped for $\sim$1 minute to allow the film to recover. During this period, one is able to observe the 3D-like RHEED pattern transition back into a 2D-like streaky pattern (**Figure 5.2**(a), inset with red arrow). The streaky

RHEED pattern indicates a 2D surface of the film with a certain amount of roughness that increases with time (as indicated by the gradual decrease in diffraction intensity during laser-off time) and likely corresponding to the evaporation of lead from the surface. Upon commencing the deposition again and turning the laser back on after the recovery period, continuous layer-by-layer growth can be obtained for the $Pb_{1+\delta}ZrO_3$ films (**Figure 5.2**(c)). Such 2D layer-by-layer growth can be sustain for a reasonably long time, even up to a total thickness of 80-100 nm. I note that to maintain a robust layer-by-layer growth mode, intermittent laser-off/recovery periods must be provided (**Figure 5.2**(d)). It also appears that any evaporation of lead during the dwell periods is fixed by the first 2-3 pulses of next cycle as the diffraction intensity is observed to recover quickly. This also help explain the fact that using lead-excess targets can achieve better layer-by-layer growth since the excess lead will dynamically and continuously compensate for lead-loss at the film surface.

5.3 Structural and chemistry characterization

$PbZrO_3$ has an orthorhombic unit cell with lattice parameters a=5.882 Å, b=8.228 Å, and c=11.783 Å [158, 159]. X-ray line-scans indicate that the films are $(120)_O$-oriented (*i.e.*, the film $[120]_O$ is parallel to the substrate normal $[110]_O$ where subscript "O" denotes orthorhombic indices) for all three target chemistries (**Figure 5.3**(a)) [195, 196]. Further examination of the X-ray RSMs (**Figure 5.3**(b-d)) for all three heterostructure variants reveals that all $Pb_{1+\delta}ZrO_3$ films are single phase and exhibit essentially identical lattice parameters regardless of the target chemistry. Note that the coexistence of 90° structural domains in $PbZrO_3$, which has been observed previously [197, 198], should correspond to 440_O- and 280_O-diffraction peaks in the RSM scans. Despite no clear separation between these peaks in the laboratory-based RSM studies, later synchrotron-based studies show both are present, but likely unresolvable due to the small lattice distortion in $PbZrO_3$. Additionally, the three heterostructure variants have essentially equal crystalline quality as indicated by the presence of strong Laue fringes and nearly identical rocking-curve full-width-at-half-maximum (FWHM $\approx$ 0.025°) values (**Figure 5.3**(e-g)). Initial analysis of the structural data suggests that all three heterostructure variants, despite being grown from different target compositions, have the same structure.

The film chemistry was probed *ex situ* using Rutherford back-scattering spectrometry (RBS) with an incident helium-ion energy of 3,040 keV, incident angle α = 22.5°, exit angle β = 25.35°, and scattering angle θ = 168°). Detailed principles and operations of RBS can be found in **Appendix B**. The resulting spectra were fitted using the RBS analysis software SIMNRA. Studies of the film chemistry using RBS (**Figure 5.4**(a-c)) reveal that the resulting films are, in fact, stoichiometric replications of the targets with nominally chemistries of $PbZrO_3$, $Pb_{1.1}ZrO_3$, and $Pb_{1.2}ZrO_3$. The latter implies that at least 20% lead-excess can be accommodated in the lattice without a significant change in the lattice or deterioration of the film crystallinity. Such a finding is, at face value, intriguing and suggests a need for careful analysis of $PbZrO_3$ materials produced from lead-rich starting

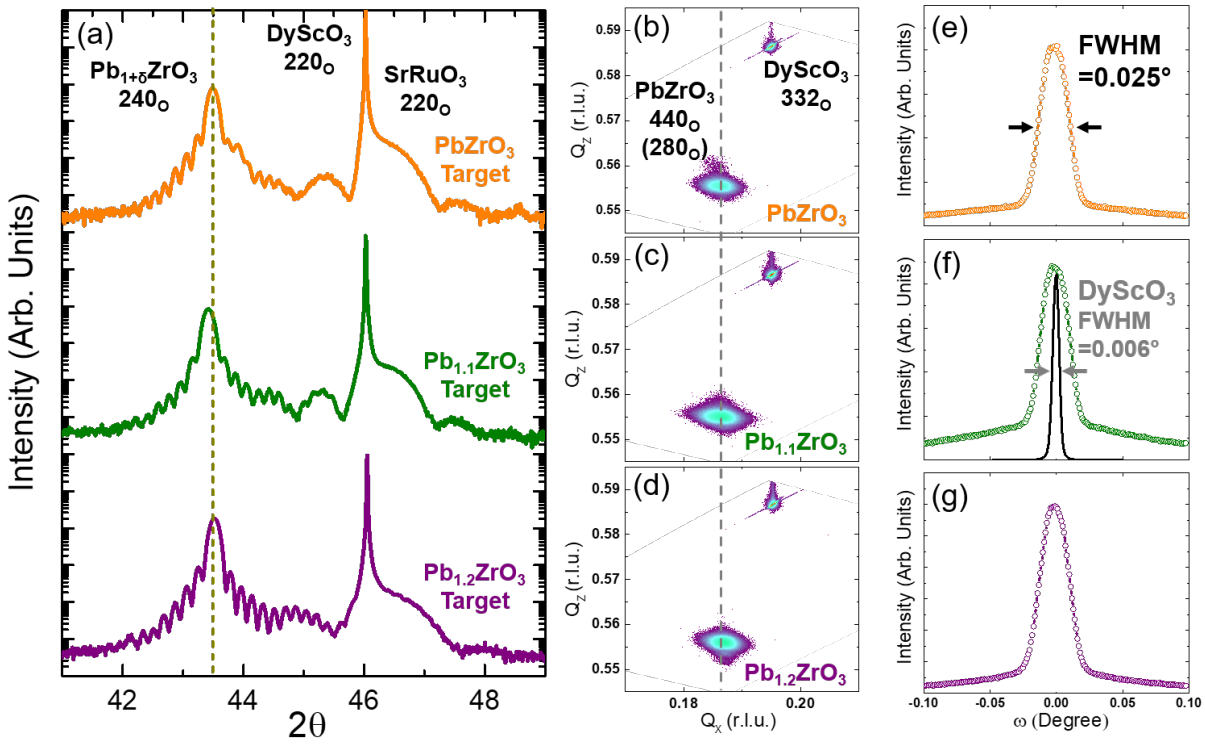

Figure 5.3: *(a) X-ray θ-2θ line scans reveal high-quality $(120)_O$-oriented 50 nm $Pb_{1+\delta}ZrO_3$ films on 10 nm $SrRuO_3/DyScO_3$ 220 grown with different (non)stoichiometric lead zirconate targets. (b)-(d) Reciprocal space mapping of three heterostructures confirms fully relaxed epitaxial $Pb_{1+\delta}ZrO_3$ films with similar lattice parameters. (e)-(g) Rocking curves of three $Pb_{1+\delta}ZrO_3$ heterostructures show consistent and high crystallinity as indicated by a film FWHM of 0.025° as compared with FWHM of 0.006° for $DyScO_3$ substrates.*

chemistries since basic structural characterization may not directly reflect these variations. In addition, the introduction of defects in ferroic material typically results in a significant lattice changes, while such invariant lattice in 20% lead-excess films do suggest necessary investigation into the defect structures in such materials.

5.4 Electrical characterization

Before exploring a more thorough analysis of the defect structures of these films, I first examine how the cation nonstoichiometry in $Pb_{1+\delta}ZrO_3$ affects the electrical properties. Symmetric capacitor structures were fabricated by *ex situ* deposition of 100 nm thick, 25 μm diameter, circular $SrRuO_3$ top electrodes defined using an MgO hard-mask process. Deposition of top electrodes was done at 500°C and in a dynamic oxygen pressure of 100 mTorr to avoid significant lead loss. Other than temperature, the same growth conditions were used for the top $SrRuO_3$ growth as for the bottom electrodes. Ferroelectric

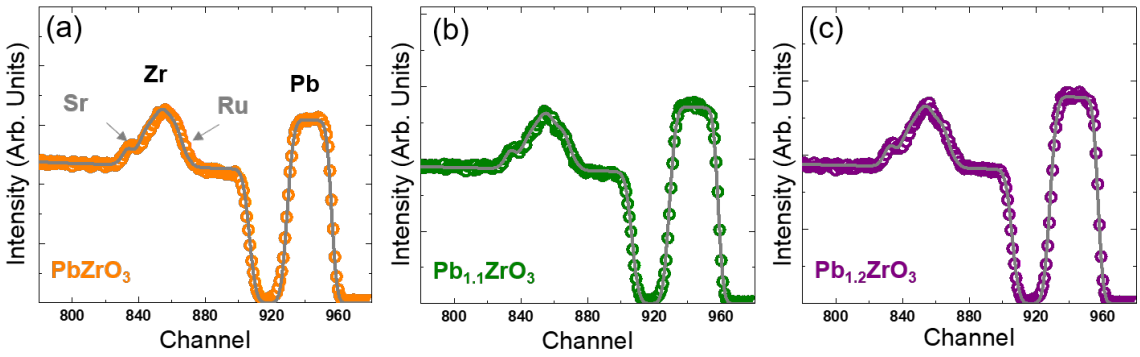

Figure 5.4: *Rutherford back-scattering spectrometry studies on three $Pb_{1+\delta}ZrO_3$ films reveal nominal chemistries of (a) $PbZrO_3$, (b) $Pb_{1.1}ZrO_3$, and (c) $Pb_{1.2}ZrO_3$.*

polarization hysteresis loops were measured using a Precision Multiferroic Tester (Radiant Technologies), and dielectric and loss tangent measurements were performed using an E4890 LCR meter (Agilent/Keysight).

Polarization-electric field hysteresis loops and dielectric permittivity as a function of frequency and temperature were measured for the three different $Pb_{1+\delta}ZrO_3$ heterostructure variants (**Figure 5.5**). For the $PbZrO_3$ (**Figure 5.5**(a)) and $Pb_{1.1}ZrO_3$ (**Figure 5.5**(b)) heterostructures, double-hysteresis loops (here shown for frequencies from 0.1-10 kHz), typical for an antiferroelectric, are observed for both stoichiometries with a saturated polarization of $\sim$50 $\mu C/cm^2$ and similar switching forward field values (380 kV/cm and 390 kV/cm, respectively). Studies of the $Pb_{1.2}ZrO_3$ heterostructures (**Figure 5.5**(c)), however, reveal the presence of a single hysteresis loop indicative of ferroelectric-like response. The coercive field for the ferroelectric-like $Pb_{1.2}ZrO_3$ heterostructures is $\sim$100 kV/cm and the saturation polarization is $\sim$40 $\mu C/cm^2$; slightly smaller than the antiferroelectric samples. Different from antiferroelectric $PbZrO_3$ where the remnant polarization is close to zero at zero field, the $Pb_{1.2}ZrO_3$ heterostructures exhibit remnant polarization of $\sim$10 $\mu C/cm^2$. Further study of the dielectric permittivity as a function of temperature reveals that both the antiferroelectric $PbZrO_3$ and $Pb_{1.1}ZrO_3$ heterostructures (**Figure 5.5**(d-e)) exhibit a relatively sharp anomaly at $\sim$290°C and that the loss tangent remains low for frequencies ranging from 0.5-100 kHz. Similar studies of the ferroelectric-like $Pb_{1.2}ZrO_3$ heterostructures (**Figure 5.5**(f)) reveal considerably broaden temperature-dependence of the permittivity (which gradually peaks around $\sim$260°C) and essentially flat loss tangent at all temperatures measured (except at the highest temperatures, likely due to increased conduction of the sample). Furthermore, no obvious change in the frequency dispersion of the dielectric permittivity or permittivity peak shifts as a function of frequency were observed for all heterostructures across the temperature range studied.

Current-voltage (I-V) leakage studies reveal that all three $Pb_{1+\delta}ZrO_3$ heterostructure variants exhibit insulating response with a maximum leakage current $< 10^{-4}$ A/cm^2 at

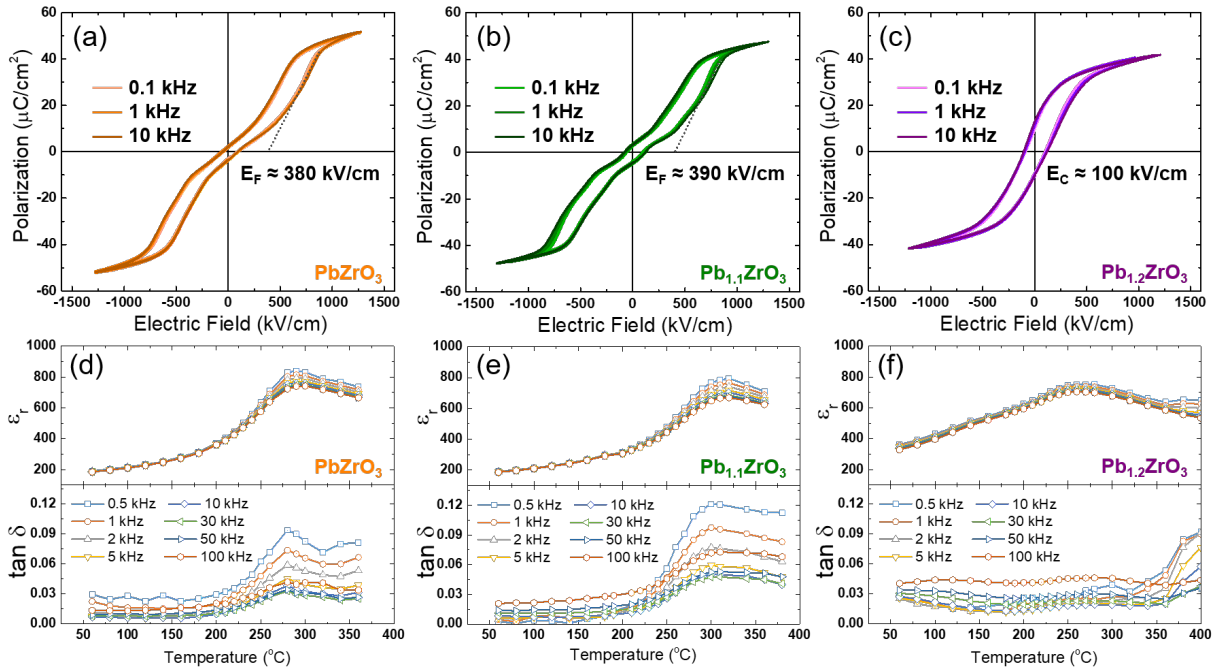

Figure 5.5: *Antiferroelectric double-hysteresis loops are observed for $PbZrO_3$ and $Pb_{1.1}ZrO_3$ variants (a) (b), while single hysteresis loops are shown in $Pb_{1.2}ZrO_3$ films (c). Temperature-dependent dielectric responses under various probed frequencies reveal sharp dielectric anomalies for antiferroelectric (d) $PbZrO_3$ and (e) $Pb_{1.1}ZrO_3$ films, while (f) a broader phase transition with no frequency-dispersion change across transition temperature is observed in ferroelectric $Pb_{1.2}ZrO_3$ heterostructures.*

the highest electric field of 1400 kV/cm (**Figure 5.6**(a)). Despite systematic variations in the film chemistry, no clear trend in leakage behavior is observed; and all variants were found to be considerably more resistive than similarly produced $PbZr_{0.2}Ti_{0.8}O_3$ thin films. Note that some of the fine features of the I-V curves in the $PbZrO_3$ and $Pb_{1.1}ZrO_3$ heterostructures are the result of switching currents since antiferroelectric samples cannot be pre-poled. Room temperature dielectric permittivity reveals a 1 kHz permittivity value of $\sim$188 for both the $PbZrO_3$ and $Pb_{1.1}ZrO_3$ heterostructures, and a permittivity value of $\sim$387 for the $Pb_{1.2}ZrO_3$ (**Figure 5.6**(b)). Low loss tangents (< 0.05) are observed for all heterostructure variants (consistent with the highly resistive nature of the films). Ferroelectric polarization hysteresis loops for a $Pb_{1.2}ZrO_3$ heterostructure across a wide frequency range are also provided (**Figure 5.6**(c)), where the coercive field of the $Pb_{1.2}ZrO_3$ is found to increase as the measurement frequency increases. Also, the concave feature of the polarization curve, as well as the saturation of polarization at all frequencies, are similar and this strongly indicates the ferroelectric nature of the $Pb_{1.2}ZrO_3$ heterostructures.

From these measurements, I can conclude that cation nonstoichiometry can dramati-

cally change the electrical properties of $Pb_{1+\delta}ZrO_3$ such that antiferroelectricity is no longer manifested in the $Pb_{1.2}ZrO_3$ heterostructures. I further propose that the electrical behavior of the $Pb_{1.2}ZrO_3$ heterostructures is indicative of true ferroelectricity, not spurious effects arising from leakage or otherwise. This is consistent with current-voltage studies as well as the low loss tangent (as a function of frequency) at room temperature for all three heterostructure variants which shows that the samples are quite insulating and should have minimal leakage-related contributions to the ferroelectric hysteresis loops. Also, the ferroelectric nature of the $Pb_{1.2}ZrO_3$ heterostructures is further supported by frequency-dependent hysteresis loops at room temperature which show that the coercive field increases systematically with frequency and that polarization saturates to the same level, and in with the same profile, indicating that the effects likely arise from switched polarization [199]. Furthermore, the nature of the temperature- and frequency-dependent dielectric response of the $Pb_{1.2}ZrO_3$ heterostructures suggests a homogeneous bulk response, instead of inhomogeneously polarized nano-regions where strong frequency-dependent dispersion in dielectric permittivity would be expected in the low-temperature regime [200, 201]. Taken together, the data suggest that the $Pb_{1.2}ZrO_3$ heterostructures are intrinsically ferroelectric, which implies that the structure of the film must be different from the antiferroelectric $PbZrO_3$ and $Pb_{1.1}ZrO_3$ heterostructures.

5.5 Lattice symmetry determination

As discussed in the previous section, the electrical characteristics of the $Pb_{1.2}ZrO_3$ variants indicate ferroelectric response, and the symmetry of the lattice is expected to by higher compared to antiferroelectric versions. To confirm this point, synchrotron-based X-ray RSM studies were performed. In antiferroelectric $PbZrO_3$, the frozen Σ mode that gives rise to the antiparallel displacement of the lead cations also gives rise to $\frac{2\pi}{a}(1/4, 0, 1/4)$ quarter-

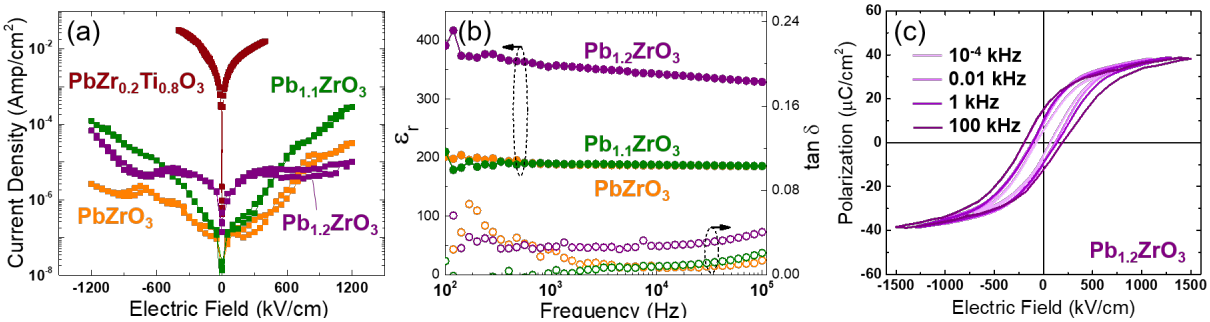

Figure 5.6: *(a) I-V studies on three $Pb_{1+\delta}ZrO_3$ heterostructures show good insulation and low leakage currents as compared with ferroelectric PZT films. (b) Room temperature dielectric responses. (c) Hysteresis loops for $Pb_{1.2}ZrO_3$ taken at frequencies from 0.1 Hz to 100 kHz at room temperature reveals characteristic ferroelectric response in the sample.*

order diffraction peaks, in a pseudocubic unit cell where a is the pseudocubic unit cell lattice constant [158, 159, 202]. Such diffraction peaks would not be observed in a ferroelectric phase. In turn, RSM studies about the $DyScO_3$ 332_O-diffraction condition were undertaken (**Figure 5.7**(a-c)). These RSM studies reveal a number of interesting points.

First, the scans show evidence of a predominantly relaxed film, but with a small fraction of coherently strained material. Both the relaxed and strained peaks (labeled as "R" and "S", respectively) can be observed for all heterostructures. This finding is consistent with the growth mode observed by RHEED (**Figure 5.1**). Again, the RHEED analysis reveals a *Stranski-Krastanov*-like growth mode wherein the film relaxes and transitions form 2D to 3D growth after 2-3 unit cells as evidenced by 2-3 oscillations of the RHEED intensity followed by an intensity drop and corresponding transition from streaks to dots in the diffraction pattern. The strained layer observed by the synchrotron-based X-ray RSM likely corresponds to those initial 2-3 unit cells. Second, the scans show marked variations in the intensity of the quarter-order diffraction peaks. The main $Pb_{1+\delta}ZrO_3$ diffraction conditions are indexed as 440_O and 280_O, while the quarter-order Bragg diffraction conditions from the antiparallel displaced lead cations are indexed as 450_O and 290_O. Examination of the RSMs for the $PbZrO_3$ and $Pb_{1.1}ZrO_3$ heterostructures, reveals the presence of both the main and quarter-order diffraction peaks, clearly revealing antiferroelectric order and the coexistence of 90° antiferroelectric domains (**Figure 5.7**(a-b)). Similar examination of the RSMs for the $Pb_{1.2}ZrO_3$ heterostructures, however, reveals considerably reduced intensity of the quarter-order Bragg peaks (**Figure 5.7**(c)). Plotting the dominant 450_O-diffraction condition intensity, normalized with respect to the substrate intensities, further reveals that for both the $PbZrO_3$ and $Pb_{1.1}ZrO_3$ heterostructures, a sharp Bragg peak can be observed and that the $Pb_{1.2}ZrO_3$ heterostructures exhibit a peak two orders of magnitude lower in diffraction intensity (**Figure 5.7**(d)). I note that the 450_O-diffraction condition from the $Pb_{1.2}ZrO_3$ heterostructures does not disappear completely, but becomes diffusive and elongated along the $[\bar{1}10]_{pc}$ (dashed square, **Figure 5.7**(c)). Here, "pc" denotes the pseudo-cubic lattice. The narrow and elongated peak profile suggests a limited fraction of a strongly anisotropic antiferroelectrically-ordered phase is present [203].

Analysis of the diffuse diffraction peak intensity is specifically focused on the $Pb_{1.2}ZrO_3$ heterostructures where, about the 450_O-diffraction condition location, the strong Bragg diffraction peak is replaced by an elongated and weak diffusive peak (**Figure 5.8**(a)), suggesting weak and strongly anisotropic antiferroelectric ordering [204]. Diffuse scattering analysis for correlated displacement of atoms is typically applied in the study of relaxor ferroelectrics such that the correlation length of displaced atoms can be extracted via Lorentzian fitting of the diffusive peak. Although slightly different from the case of relaxor ferroelectrics where the correlation comes from a region of static and oriented displacement of atoms embedded in a random non-polar network, our analysis deals with groups of atoms with antiparallel displacement which are separated from the polar background state with parallel displacement. The analysis was performed by fitting the diffusive scattering peak along two orthogonal directions ($[\bar{1}10]_{pc}$ and $[110]_{pc}$) with a Lorentzian function

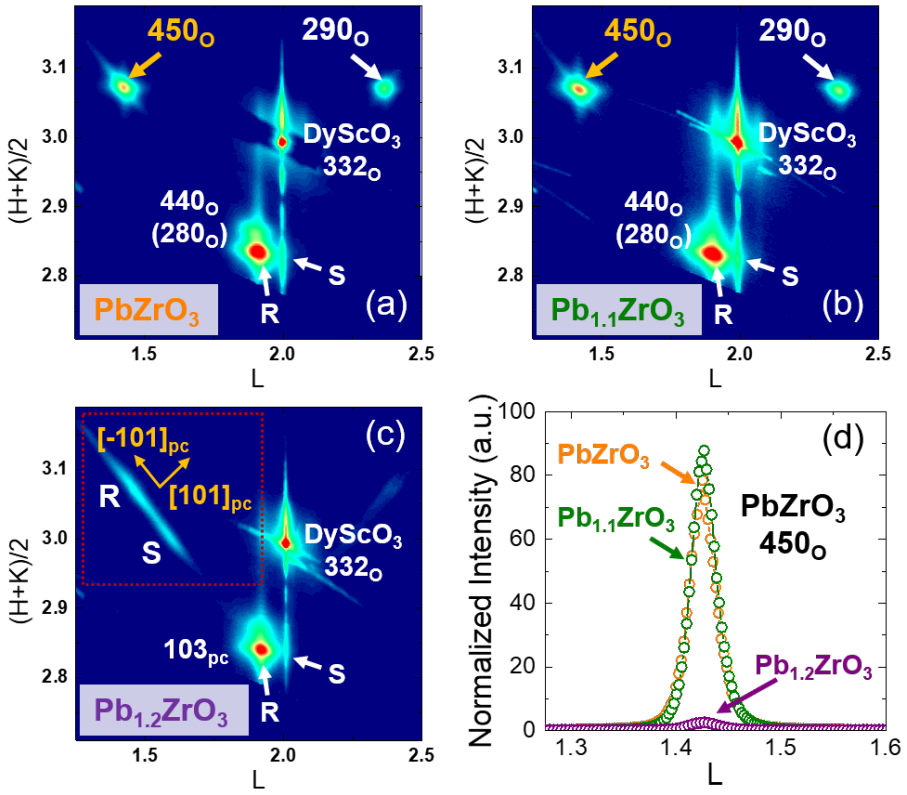

Figure 5.7: *Synchrotron-based X-ray reciprocal space mapping around $DyScO_3$ 332_O-diffraction conditions are taken for all three heterostructures. Data is plotted in reciprocal HKL vector space with respect to $DyScO_3$ orthorhombic lattice such that [0 0 L] is the in-plane axis and [H K 0] is the out-of-plane axis. Relaxed and strained peaks from $Pb_{1+\delta}ZrO_3$ are labeled as "R" and "S", respectively. Quarter-order Bragg peaks (450_O and 290_O in orthorhombic lattice) are labeled for (a) $PbZrO_3$ and (b) $Pb_{1.1}ZrO_3$ heterostructures, while diffused patterns along $[\bar{1}01]_{pc}$ are observed in (c) $Pb_{1.2}ZrO_3$. (d) Plotting normalized 450_O peak intensity with respect to substrate along L-direction reveals strong Bragg diffraction for antiferroelectric $PbZrO_3$ and $Pb_{1.1}ZrO_3$ heterostructures. However, antiferroelectric quarter-order peak intensity is two orders lower in magnitude for ferroelectric $Pb_{1.2}ZrO_3$ heterostructures.*

[204] given by

$$I_{diff} = A\left|F_{diff}(\boldsymbol{G})\right|^2 \sum_i \left|\boldsymbol{Q}\cdot\boldsymbol{\epsilon}_i\right|^2 \frac{\Gamma}{\boldsymbol{q}^2+\Gamma^2} \tag{5.5}$$

Note that I have intentionally eliminated the diffusive peak coming from the strained part of the film (only the bottom 2-3 unit cells) and focus on the diffusive profile with higher intensity that comes from the relaxed portion. I set the coefficient in Equation 5.5 before $\frac{\Gamma}{\boldsymbol{q}^2+\Gamma^2}$ as constant for a pseudo-quantitative analysis and for simplicity. Here, $\boldsymbol{q}$ is

the reciprocal space vector that points along the $[101]_{pc}$ or $[\bar{1}01]_{pc}$ away from the Bragg diffraction point (450_O in this case). Γ gives the reciprocal correlation length along $\boldsymbol{q}$. After the Lorentzian fitting of the diffusive peak (**Figure 5.8**(b)), I acquire $\Gamma_{[\bar{1}01]}$=0.132 and $\Gamma_{[101]}$=0.019. Since the reciprocal space mapping is plotted in vector space with *hkl* notation designated with respect to the $DyScO_3$ substrate, Γ will be unit-less and the value of correlation length can be calculated by using $\lambda = \frac{1}{2}\Gamma_{c_{DSO}}$, where λ is the correlation length with units of Å and c_{DSO} is the lattice parameter along the *c*-axis of the orthorhombic $DyScO_3$ [66]. It is important to note that typically the correlation along the $[101]_{pc}$ will not be specifically calculated due to the fact that the correlation is long-range and the diffusive peak profile might be affected by non-displacement-induced diffuse intensities such as crystallinity, chemical inhomogeneity, defect scattering, *etc* [203]. Thus, the correlation length of $Pb_{1.2}ZrO_3$ films will be, pseudo-quantitatively: $\lambda_{[\bar{1}01]} \approx$3 nm;$\lambda_{[101]} >$ 30 nm. In addition, there is weak, diffuse intensity about the 290_O-diffraction condition as well, suggesting four variants of this scattering may be present. This means that the small fraction of antiferroelectrically-ordered phase would be shaped as thin "discs" or "sheet" with the normal of the flat surface pointing along the $\langle\bar{1}01\rangle_{pc}$. To summarize, both the electrical and structural characterization point to the fact that excess-lead content in $PbZrO_3$ drives the material away from the antiferroelectric ground state, towards a ferroelectric state. The presence of what appears to be a residual antiferroelectric minority phase in the $Pb_{1.2}ZrO_3$ heterostructures further suggests that this transition is gradual in nature and is consistent with the nearly energy-degenerate nature of the two possible phases in $PbZrO_3$.

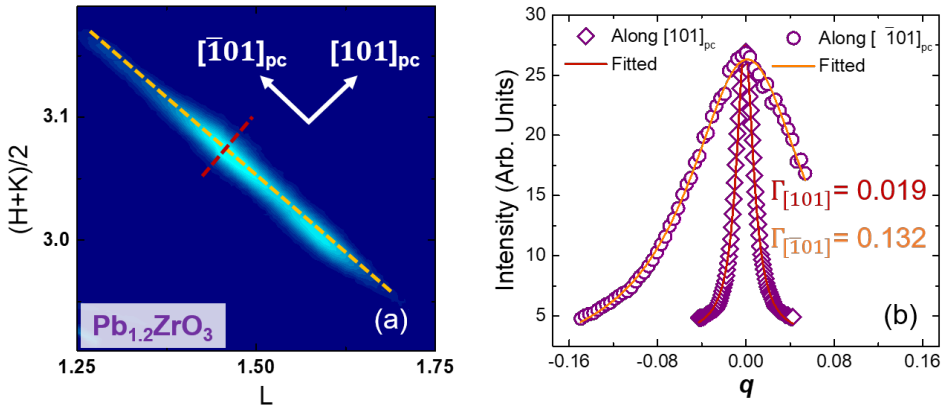

Figure 5.8: *(a) Diffused pattern observed around 450_O-diffraction condition in $Pb_{1.2}ZrO_3$ indicates weak antiferroelectric ordering along $[\bar{1}01]_{pc}$ axis while stronger antiferroelectric ordering along $[101]_{pc}$. (b) Fitted Lorentzian profiles along orange line ($[\bar{1}01]_{pc}$ and red line ($[101]_{pc}$) are given.*

5.6 Energy ground states in lead-excess $PbZrO_3$

To better understand this evolution and competition, density functional theory (DFT) was employed to explore the nature of the defects and the effects of cation nonstoichiometry on the energy competition between the antiferroelectric and ferroelectric phases.[1] The technical details and bench-marking calculations of this DFT work can be found here [60]. Based on the observed lead excess from RBS and the high-quality nature of the films observed via X-ray diffraction, the primary defect types corresponding to point defects are hypothesized to be a few possibilities: zirconium vacancies ($V_{Zr}^{''''}$) or lead antisite defects ($Pb_{Zr}^{''}$ or $Pb_{Zr}^{\times}$). Because the lattice does not show dramatic expansion with the increasing lead nonstoichiometry, one might expect that there is not a large concentration of either the $V_{Zr}^{''''}$ or $Pb_{Zr}^{''}$ defects; both of which would drive a change in the lattice parameters of the material and potentially a corresponding large concentration of compensating anion defects. These initial observations were supported by the results of the DFT calculations, which showed good agreement (<1% difference) between the computed and experimental lattice constants for pristine $PbZrO_3$ and a negligible increase of the lattice parameters of 0.1%, 0.3% and 0.5% for one, two, and three lead antisite substitution. In addition, calculations of the formation energy of the various defects showed that lead antisite defects have a much smaller formation energy than that for the zirconium vacancies (**Figure 5.9**(a)). In fact, the formation energy calculations suggested that creating $PbZrO_3$ with even a small amount of lead-excess — accommodated by lead antisites — is more energetically favorable than creating stoichiometric $PbZrO_3$. These results are consistent with previously reported defect studies on $PbZrO_3$ [188–191]. In addition, examination of the Born effective charge showed that the valence state of the lead cations increases from +3.2 to +4.8 when they are located at the lead antisite, which indicates that lead is in a higher valence state on the zirconium site; in this manner, the system achieves charge neutrality in the system without the need to introduce additional point defects or charge carriers, consistent with our experimental findings that all three lead-excess samples remain electrically insulating. Also, the transition to a higher valence state for the lead antisite defect is accompanied by a decrease in ionic radius (the Shannon-Prewitt ionic radii for Pb^{2+}, Pb^{4+}, and Zr^{4+} in 6-fold coordination are 1.19 Å, 0.775 Å, and 0.72 Å, respectively) [205] such that very little lattice distortion is expected for the system including significant lead antisite defects.

With this understanding of the nature of defects in the system, their effect on the relative stability of the antiferroelectric and ferroelectric phases were examined next. To do this, the relative energy stability of several polar structures with respect to the orthorhombic *Pbam* ground state were considered. The competing polar structures of $PbZrO_3$ are obtained by freezing in the unstable zone-center polar mode along different crystallographic directions, in combination with different oxygen octahedral patterns. In agreement with

[1]The DFT calculations were accomplished in collaboration with Dr. S. E. Reyes-Lillo and Prof. J. B. Neaton from Physics Department at University of California, Berkeley, CA, USA.

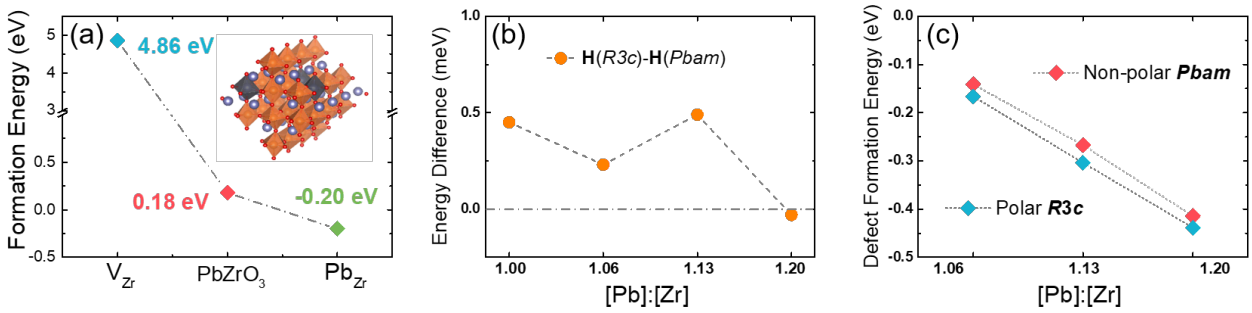

Figure 5.9: *(a) Formation energies at T=0 K of stoichiometric $PbZrO_3$, zirconium vacancies ($V_{Zr}^{''''}$) and antisite defects ($Pb_{Zr}^{\times}$) in Pbam $PbZrO_3$ lattice are given. Stoichiometric $PbZrO_3$ is suggested to be metastable at low temperature while antisite defect formation in $PbZrO_3$ lattice is unavoidable. (b) The energy difference between R3c and Pbam phases in nonstoichiometric $Pb_{1+\delta}ZrO_3$ is small and remains <1 meV. (c) Antisite defects ($Pb_{Zr}^{\times}$) can both form in Pbam and R3c $Pb_{1+\delta}ZrO_3$ films, while it is more favored in R3c phase as suggested by the lower defect formation energy across whole doping range.*

previous results [177], the first-principles calculations show that the lowest energy structures correspond to the orthorhombic *Pbam* and rhombohedral *R*3*c* structures. These results confirm the *Pbam* structure as the lowest-energy antiferroelectric phase and suggest that the nearly energetically-degenerate *R*3*c* polar structure most likely corresponds to the field-induced ferroelectric phase observed here for $PbZrO_3$. A small volume difference was found between *Pbam* and *R*3*c* of +0.5%. The computed macroscopic polarization is found to be 59 μC/cm^2, in good agreement with the saturated polarization for pristine $PbZrO_3$.

Focusing on the *Pbam* and *R*3*c* structures, the energy evolution was explored as a function of the lead antisite content by computing the energy difference between the *Pbam* and *R*3*c* structures with [Pb]:[Zr] = 1.00, 1.06, 1.13, and 1.20 cation ratios, where all the lead excess is accommodated by antisite defects (**Figure 5.9**(b)). Across this range of cation ratios, the calculations revealed that the energy difference between the *Pbam* and *R*3*c* structures remains small, approximately ∼1 meV per formula unit, with increasing lead content (purple data, right axis, **Figure 5.9**(b)). While the exact energy difference between the *Pbam* and *R*3*c* structures depends on the choice of functional, similar qualitative results for other functionals used in the calculation are still expected. For comparison, the energy difference between the *Pbam* and *R*3*c* structure was found to be ∼4 meV per formula unit across the range of cations rations using the local density approximation (LDA) [206]. The latter suggests that the structures remain nearly energetically degenerate as the lead content increases, and that the ferroelectric order arises due to the energetic cost of defect formation rather than a coherent structural phase transition. To understand this better, the defect formation energies were calculated across the same range of cation ratios for the *Pbam* and *R*3*c* structures. The calculations reveal that as the lead content is increased the energy gain to create such defects in the *R*3*c* structure is always larger than that for the *Pbam* structure (**Figure 5.9**(c)). Thus, I propose that since the energy dif-

ference between the *Pbam* and *R*3*c* structures remains small across the entire cation ratio range studied herein, incorporation of lead excess in the form of lead antisite defects tips the energy balance in favor of the *R*3*c* structure as the cost of producing those defects is smaller in this structure and this, in turn, gives rise to the ferroelectric order.

5.7 Conclusions

To summarize, the effects of cation nonstoichiometry on the evolution of lattice structure, and the corresponding impact on electrical and dielectric properties, and (anti-)ferroelectric order in $PbZrO_3$ thin films were explored. High-quality $PbZrO_3$, $Pb_{1.1}ZrO_3$, and $Pb_{1.2}ZrO_3$ thin films showing negligible differences in the lattice parameters have been produced. Subsequent studies reveal that the $PbZrO_3$ and $Pb_{1.1}ZrO_3$ heterostructures exhibit the expected antiferroelectric behavior and structure along with a relative sharp phase transition at $\sim$290°C. $Pb_{1.2}ZrO_3$ heterostructures, however, likely exhibit rhombohedral symmetry and ferroelectric response along with a broader phase transition that peaks at $\sim$260°C. In turn, synchrotron-based RSMs of the $Pb_{1.2}ZrO_3$ heterostructures reveal dramatically suppressed peak intensities for quarter-order Bragg peaks expected for the orthorhombic, antiferroelectric phase — confirming the likely rhombohedral and ferroelectric nature of the nonstoichiometric samples. DFT calculations suggest that excess lead in the system is incorporated in the form of lead antisites, that the cost to form those defects is lower in the rhombohedral phase, and, since the energy difference between the orthorhombic (antiferroelectric) and rhombohedral (ferroelectric) structures remains small across the entire cation ratio range studied herein, incorporation of lead excess in the form of lead antisite defects tips the energy balance in favor of the *R*3*c* structure and results in the ferroelectric order. These results reveal the important role of cation stoichiometry in governing the competition between phases in complex materials such as the $PbZrO_3$ system and provides a potential pathway by which one can control the lattice structure and properties of such materials.

Chapter 6

Designing optimal ion-conducting perovskite structure

Solid-oxide fuel/electrolyzer cells are limited by a dearth of electrolyte materials with low Ohmic loss and an incomplete understanding of the structure-property relationships that would enable the rational design of better materials. Driven by such motivation, this chapter focuses on the detailed correlation between ionic transport and lattice structure in a model perovskite ionic conductor. Using epitaxial thin-film growth, synchrotron-based X-ray diffraction, impedance spectroscopy, and density-functional theory, I delineate the impact of structural parameters (*i.e.*, unit-cell volume and octahedral rotations) on ionic conductivity in the electrolyte $La_{0.9}Sr_{0.1}Ga_{0.95}Mg_{0.05}O_{3-\delta}$ (LSGM). As compared to the zero-strain (or bulk-like) state, compressive strain reduces the unit-cell volume while maintaining large octahedral rotations, resulting in a strong reduction of ionic conductivity, while tensile strain increases the unit-cell volume while quenching octahedral rotations, resulting in a negligible effect on the ionic conductivity. Calculations reveal that larger unit-cell volumes and octahedral rotations decrease migration barriers and create low-energy migration pathways, respectively. The desired combination of large unit-cell volume and octahedral rotations is normally contraindicated, but through the creation of superlattice structures I experimentally realize both expanded unit-cell volume and strong octahedral rotations which result in an enhancement of the ionic conductivity. All told, the potential to tune ionic conductivity with structure alone by a factor of 2.5 at around 600°C is observed. These findings provide a deeper understanding of the structure-transport relationships in perovskite electrolytes and shed new light on the rational design of ion-conducting perovskite oxides.

6.1 Introduction

Ion-conducting oxide is a good electrolyte candidate in the application of solid-oxide fuel cells where it transports charged anions (oxygen vacancies) from one electrode to the other. Ionic conduction in the material is a diffusion process that higher temperature results in lower impedance for the transport of the charged species. Using a higher operation temperature, in turn, has become the dominant strategy to reduce Ohmic loss in the operation of high-power solid-oxide fuel cell stations. However, such need for high operation temperatures (>800°) for electrolyte-supported solid-oxide fuel/electrolyzer cells has been one of the major limitations for commercialization [207–209]. In an effort to push the operating temperature down to a more cost-effective range (<500°C), considerable research activities have been undertaken on the development of electrolytes with improved low-temperature ionic conductivity [210, 211]. In this regard, doped-perovskite systems (*i.e.*, $A_{1-x}A'_xB_{1-y}B'_yO_{3-\delta}$ where A' and B' are aliovalent dopants) have emerged as promising candidates for oxygen-ion conductors [212]. For example, strontium and magnesium co-doped $LaGaO_3$ has been identified as an excellent alternative to yttria-stabilized zirconia due to its competitive ionic conductivity (>0.01 $S.cm^{-1}$ at 600°C)[1] and chemical stability [212–214]. But, despite these attractive properties, few high-performance alternatives have been discovered[215–217] and a systematic approach to the design of such materials has yet to be established. This is made more difficult by the fact that most research has focused on polycrystalline and mesostructured ceramics wherein complexity arising from grain boundaries, twinning structures, secondary phases, etc. can make interpretation of results more challenging [215, 218–221]. In turn, many of the advances have come from the chemical and physical intuitions of researchers in the field and time-consuming trial-and-error experimental iterations.

In order to advance a rational-design approach for ionic-conducting materials, it is vital to gain a thorough understanding of the impact of systematic changes to the structure and chemistry on property evolution. In this spirit, researchers have undertaken a range of studies on thin-film versions of various ionic-conducting systems where lattice symmetry, microstructure, and material stoichiometry can be deterministically controlled and studied [222–226]. These studies have marked significant progress in the understanding of the fundamental material behaviors. At the same time, advances in theoretical understanding of these systems have provided suggestions as to how to manipulate the structure to improve transport properties [16, 227, 228]. For instance, strain engineering has been proposed to further enhance the conductivity of the fluorite yttria-stabilized zirconia (YSZ) ion conductor. But at the same time, many of these studies, however, have provided conflicting recommendations and outcomes. Such incongruous results are potentially related to incomplete or limited structural characterization of the systems under study and from confounding contributions arising from sample geometry/structure (*e.g.*, microstructure

[1] This is a reference conductivity for electrolyte which has a thickness of 15 μm and contributes less than 0.15 $\Omega.cm^2$ to the total cell area-specific resistivity.

[221, 225], substrate contributions to conductivity [226, 229], *etc*.). More importantly, most studies have focused on fluorite structures while the more complex perovskite systems remain understudied. Thus, one key to developing a rational-design approach for high ion-conducting perovskites is to quantitatively and deterministically control the structural variables and build up a systematic correlation between these variables and transport properties without convolution from such confounding effects. Thus, this chapter focuses on a model perovskite ion-conducting system LSGM using thin-film epitaxy where chemical inhomogeneity, grain boundaries, and secondary phases are absent. This multi-faceted experimental and theoretical study delineates the impact of structural parameters (namely, unit-cell volume and octahedral rotations) on ionic conductivity in LSGM.

6.2 Strain engineering and quantification of structural features

A ceramic target of $La_{0.9}Sr_{0.1}Ga_{0.9}Mg_{0.1}O_{3-\delta}$, with 95% theoretical density, was used for film growth. 100 nm LSGM thin films were grown via PLD on $NdGaO_3$ (110), $SrTiO_3$ (001), and $DyScO_3$ (110) substrates (CrysTec, GmBH), corresponding to lattice mismatches of -1.12%, +0.05%, and +1.10%, respectively (where "-" and "+" indicate compressive and tensile strain, respectively). The LSGM films was grown at a heater temperature of 800°C in a dynamic oxygen pressure of 40 mTorr and with a laser fluence and repetition rate of 1.8 J/cm^2 and 5 Hz, respectively. All films were grown in an on-axis geometry with a target-to-substrate distance of 5.2 cm. Following growth, the films were cooled to room temperature at a rate of 10°C/min. in a static oxygen pressure of 700 Torr. The resulting $(001)_{pc}$-oriented heterostructures (where "pc" refers to pseudocubic indices) are found to be single-phase and highly-crystalline (**Figure 6.1**(a)). Reciprocal space mapping studies of the LSGM heterostructures along two orthogonal in-plane directions reveal that the films are coherently strained on all substrates (a representative RSM scan is given for LSGM/$DyScO_3$ heterostructure, **Figure 6.1**(b)), and thus the lattice parameter of the LSGM films can be extracted. The film chemistry was probed *ex situ* using RBS with an incident-ion energy of 3.3 MeV, an incident angle α=22.5°, an exit angle β=25.35°, and a scattering angle θ=168°. The spectra were fitted using the RBS analysis software SIMNRA (**Figure 6.1**(c)). The beam energy was specifically tuned to the magnesium resonance to maximize the scattering cross section from this light element [230]. The fitted results yield a nominal stoichiometry of $La_{0.9}Sr_{0.1}Ga_{0.95}Mg_{0.05}O_{3-\delta}$ (henceforth, LSGM). Given that the target stoichiometry used for PLD growth is $La_{0.9}Sr_{0.1}Ga_{0.9}Mg_{0.1}O_{3-\delta}$, there does appear to be some magnesium-loss during the growth process.

Synchrotron-based half-order Bragg peak analysis is applied to further examine the octahedral rotation evolution under epitaxial constraint.[2] The fitting process specifically

[2]The half-order Bragg peak analysis were accomplished in collaboration with Mr. Y. Dong at Advanced Photon Source, Argonne National Laboratory, IL, USA.

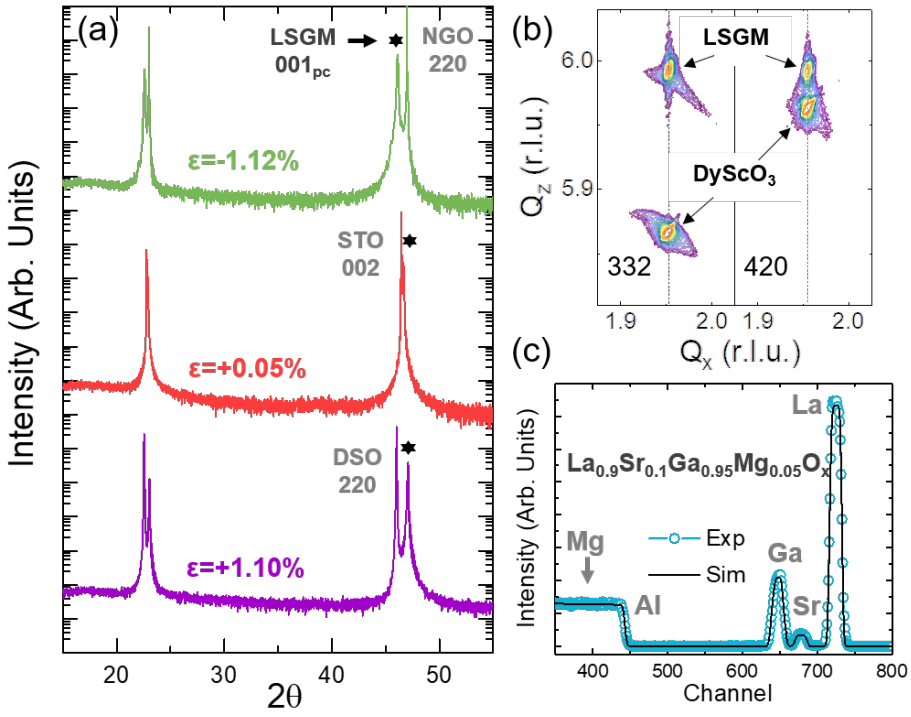

Figure 6.1: *(a) X-ray line scans for all heterostructures reveal high quality, single phase, epitaxial LSGM thin films from biaxial compressive strain to tensile strain. (b) A representative RSM of LSGM/$DyScO_3$ heterostructure along two orthogonal directions is given, suggesting that the film is coherently strained onto the substrate. (c) RBS studies of LSGM thin films grown on sapphire substrate under the same growth conditions reveal nominal chemistry of $La_{0.9}Sr_{0.1}Ga_{0.95}Mg_{0.05}O_{3-\delta}$.*

considered the *A*-site displacement in orthorhombic lattice, and thus five parameters were optimized to minimize least-squares error of calculated and measured peak intensity including α, β, and γ which describe the octahedral rotation angles along three orthogonal axes, and d_1, d_2 which describe the *A*-site cation displacement [107, 231]. Here, it is assumed that the existence of oxygen vacancies does not significantly affect the atomic-scattering factor of the oxygen anions due to the low vacancy concentration (∼7.5%) and that the atomic-scattering factor of *A*- and *B*-site cations can be taken to be the averaged value of the mixed cations on both atomic sites. The scans taken at room temperature are used for quantitative analysis. Bulk structural characterization has suggested robust orthorhombic symmetry of LSGM from room temperature to around 800°C [232]. To confirm this point, a few representative half-order peaks are measured at 650°C which is the high-end of the temperature range in transport measurement. The similar peak intensities reveal essentially the same rotation magnitude of LSGM from room temperature to high temperature (**Figure 6.2**(a)).

The comparison of calculated peak intensities and experimental intensities are given

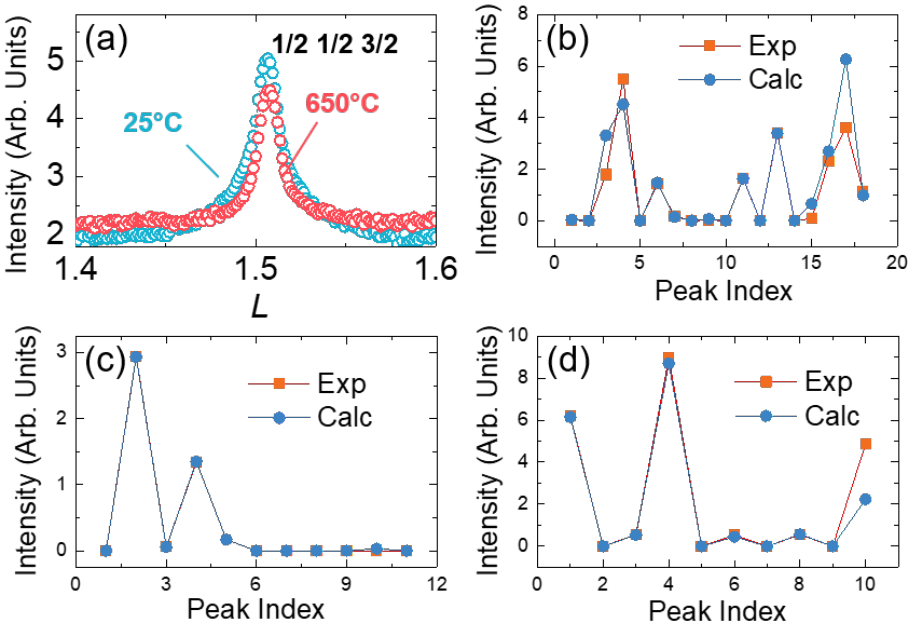

Figure 6.2: *(a) The similar peak intensities of (1/2 1/2 3/2) scans at 25°C and 650°C suggest that the octahedral rotation pattern remains essentially the same within the measurement temperatures. Comparison of calculated half-order peak intensities and experimental values for all heterostructures (b) LSGM/$NdGaO_3$, (c) LSGM/$SrTiO_3$, and (d) LSGM/$DyScO_3$ are given.*

(**Figure 6.2**(b-d)) and excellent agreement is achieved for all heterostructures. From there, the final results including lattice parameters extracted from RSM scans are tabulated (**Table 6.1**). Note that the unit of *A*-site cation displacement is given by percentage, which is the relative displacement compared to the overall lattice parameter of the unit cell. It is also worth noting that the structural parameters for the LSGM/$SrTiO_3$ heterostructures are in excellent agreement with bulk LSGM, except for a small deviation of the α and γ angles [232–234]. Recall that LSGM is under +0.05% tensile strain when grown on $SrTiO_3$ substrates; thus the deviation of octahedral rotation is expected and this suggests that the rotation is extremely sensitive to epitaxial strain. Additionally, the assumption of unchanged scattering factor of oxygen in the slightly dilute system is valid. For simplicity of presentation, in later discussions an effective octahedral rotation magnitude is defined as $\sqrt{\alpha^2+\beta^2+\gamma^2}$, assuming that the rotations along three orthogonal axes all have impact on the ionic conduction. To summarize the observations, in comparison to the zero-strain state (*i.e.*, on $SrTiO_3$ substrates, where the extracted structural parameters are in agreement with bulk LSGM), as it is progressing from compressive to tensile strain, the unit-cell volume of LSGM increases monotonically. Additionally, while the octahedral rotations are found to be the largest near the zero-strain state, they are slightly quenched under compressive strain, and almost fully suppressed under tensile strain (**Figure 6.3**(a), and a projection of the structure along the $[001]_{pc}$ is shown (**Figure 6.3**(b)). These results,

Table 6.1: *Extracted structural parameters from X-ray diffraction studies for all heterostructures. Structural parameters for bulk LSGM are also included.*

	Bulk	**-1.12%**	**+0.05%**	**+1.10%**
a (Å)	3.907	3.863	3.905	3.947
b (Å)	3.904	3.854	3.905	3.952
c (Å)	3.907	3.934	3.889	3.854
Volume ($Å^3$)	59.6	58.5	59.7	60.1
Alpha (°)	7.1	5.3±1.6	3.5±0.7	2.3±0.6
Beta (°)	0	1.1±1.9	0±1.8	0.5±0.8
Gamma (°)	7.1	6.1±1.9	8.5±1.1	0.4±1.4
$\mathbf{d_1}$ (%)	N/A	0.342±0.27	0.00±0.18	0.00±0.1
$\mathbf{d_2}$ (%)	N/A	0.05±0.37	0.11±0.12	0.15±0.06

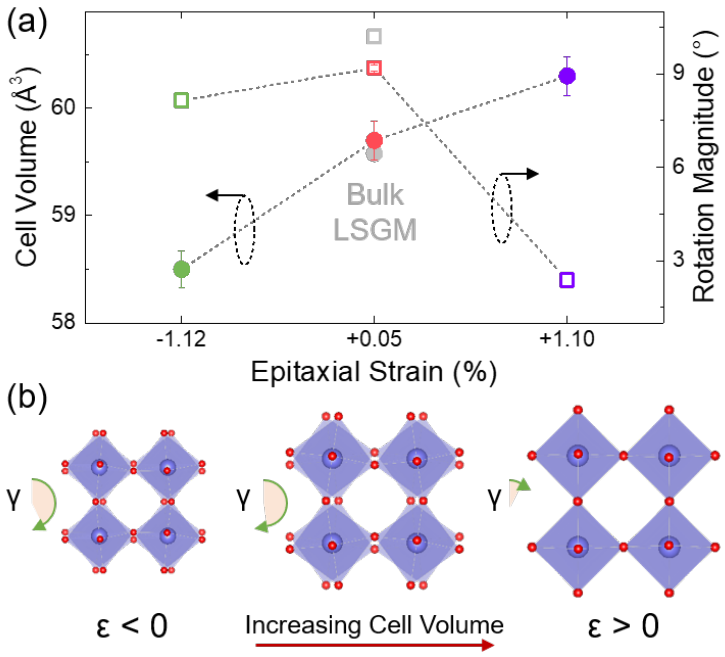

Figure 6.3: *(a) Structural parameters of LSGM under various strain states are given and schematics of these evolution are illustrated (b). Note that the oxygen positions are extracted from X-ray studies while the rotation magnitude indicator is exaggerated for better representation.*

again, suggest that strain engineering is an effective approach to manipulate the lattice structure of perovskite oxides.

6.3 Ion-transport measurement

With this understanding of the structural evolution, I proceed to correlate these structural changes with the ion transport. To characterize ion-transport properties in the films, in-plane AC-impedance spectroscopy measurements (10 mV from 10 kHz to 0.1 Hz) are performed on all heterostructures from 500°C to 650°C under high (pure O_2) and low (pure N_2) oxygen-partial pressures (**Figure 6.4** and **Figure 6.5**). The measurement is performed in a custom experimental setup based on a Mellen tube furnace and the technical details of the setup are discussed in **Chapter 3**. The ionic-conductivity measurement is conducted by sputtering 120 nm platinum interdigitated electrodes[3] (IDEs) on the heterostructure surface, which is subsequently wire-bonded to a CERDIP chip carrier and hooked up to the potentiostat. It is also important to note that, empirically, the IDE structure will give rise to a field penetration depth of $\lambda/4$ to $\lambda/3$, where λ is the spacing of the electrode fingers [235]. In this study, since the film thickness is 100 nm, the electric field will penetrate through the entire film and collect response from part of the substrate. Thus, specific cares are taken to ensure that signal from the substrate is not affecting the measurement of the LSGM layer.

First, the temperature range was purposely chosen to eliminate the contribution from mixed ionic and electronic conducting $SrTiO_3$ substrates. $SrTiO_3$ is reported to be ionically conducting at and below 400°C while it becomes predominantly an electronic conductor at and above 500°C [236], consistent with the measurement on bare $SrTiO_3$ substrates where dominant electronic conduction is found (**Figure 6.5**(b)). Since ionic charge and electronic charge can be treated in two separate conducting channels during fitting, the electronic conduction from the $SrTiO_3$ substrates will not affect the extracted ionic conductivity in LSGM layer. As for $NdGaO_3$ (**Figure 6.5**(a)) and $DyScO_3$ substrates (**Figure 6.5**(c)), the impedance from the substrates are measured to be at least one order of magnitude higher compared to the overall impedance from the heterostructure, and thus the substrate contribution can be neglected. Second, oxygen partial pressure dependent measurements are performed on all heterostructures and bare substrates. The substrates all have shown strong oxygen partial pressure dependency in impedance spectra, suggesting a pressure-dependent oxygen vacancy concentration. However, all heterostructures show one dominant "waterdrop-like" feature, characteristic of a mixed ionic and electronic conductor with ionic blocking boundary conditions (**Figure 6.4**). Thus, the high-frequency intercept gives the total resistance ($R_{total} = R_i + R_e$, where R_i and R_e are the ionic and electronic resistance, respectively), while the low-frequency intercept gives the electronic resistance [237,

[3]The IDE geometry used in this study has a finger length of 500 μm, finger width of 6 μm, and finger spacing of 6 μm. There are 20 fingers on each parent finger, thus the circuit is effectively composed of 39 resistors in parallel.

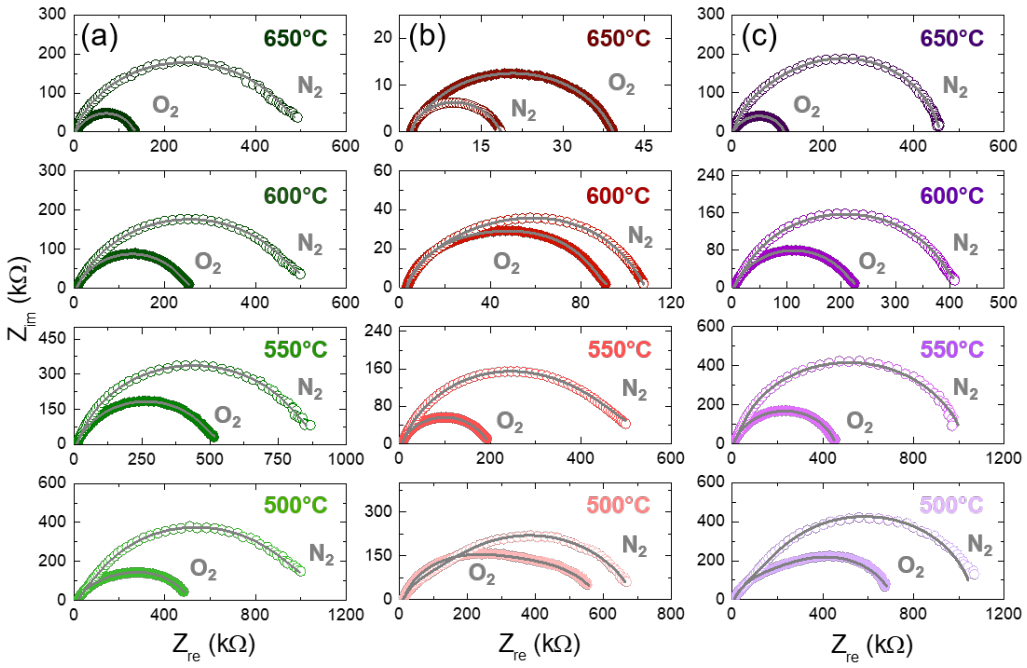

Figure 6.4: *Impedance spectra for all heterostructures under both O_2 and N_2 environment (a) LSGM/$NdGaO_3$, (b) LSGM/$SrTiO_3$, and (c) LSGM/$DyScO_3$.*

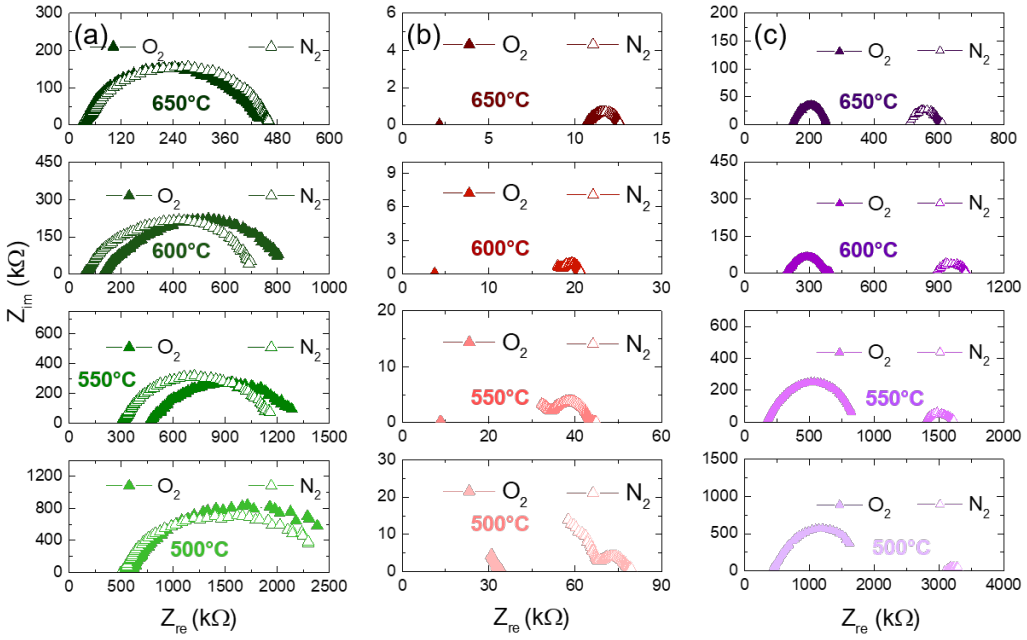

Figure 6.5: *Impedance spectra for all bare substrates under both O_2 and N_2 environment (a) $NdGaO_3$, (b) $SrTiO_3$, and (c) $DyScO_3$.*

238]. Since the low-frequency resistance increases at lower oxygen-partial pressures, this suggests that there is limited p-type electronic conduction. The invariant high-frequency resistance under different oxygen-partial pressures suggests that the ionic-charge concentration is independent of gas environment and is fixed by extrinsic dopants. This, again, confirms that the conduction in the heterostructures predominantly arises from the LSGM films, not the substrates.

Ionic conductivity of LSGM is extracted by fitting the impedance spectra using established transmission-line models (**Figure 6.6**(a)) [237]. More details regarding the measurements and fitting can be found in **Appendix C**. As shown in the model, R_{ion} is the ionic impedance of the heterostructure, R_{eon} is the electronic impedance of the heterostructure, and CPE_{chem} is the chemical capacitance (wherein an imperfect capacitor is described by a constant-phase element $CPE = Ti\omega^{-p}$, where p takes value from 0 to 1) of the heterostructure. The platinum contact is first assumed to be perfectly blocking to ionic charges and that no electrochemical reaction is taking place at the triple-phase-boundaries due to the low electrochemical activity of the LSGM (which is reasonable considering it possesses a fully occupied *d*-orbital at the *B*-site). Thus, the electronic impedance at the Pt/LSGM interface will be first set to zero ($R^{\perp}_{eon}$ and $CPE^{\perp}_{eon}$ equal to zero) while the ionic impedance at the Pt/LSGM interface will be set to infinite ($R^{\perp}_{ion}$ and $CPE^{\perp}_{ion}$ set to infinity). Three parameters (R_{ion}, R_{eon}, and CPE_{chem}) were used in the initial fitting iterations and more elements ($R^{\perp}_{eon}$, $CPE^{\perp}_{eon}$, and $CPE^{\perp}_{ion}$) would be added onto the circuit later if discrepancy within the low-frequency regime is found. Discrepancies in the low-frequency

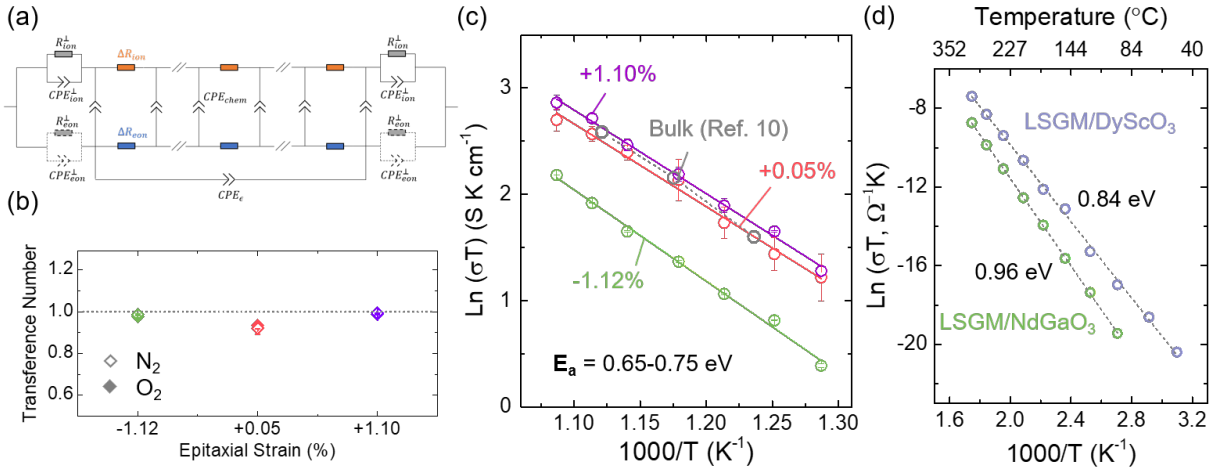

Figure 6.6: *(a) Transmission line model used for fitting mixed ionic and electronic conductors. (b) Extracted ionic charge transference numbers are in good agreement with bulk single crystal and further supports that the ionic conduction is given by LSGM films in all heterostructures. (c) Arrhenius plot of LSGM conductivity as function of strain and temperature. Activation energies of oxygen vacancy migration for all heterostructures are ∼0.65-0.75 eV. (d) Ionic conduction measurement at low temperature region. A clearer difference in activation energy is noted.*

regime are possible, for example, if there is imperfect contact between the electrode and film surface, or there is negligible gas reaction at elevated temperatures. Nevertheless, impedance spectra of all heterostructures can be well fit by applying this approach, and typically only 3 to 4 elements are needed due to the inert and stable nature of LSGM. With the extracted impedance, the conductivity of the heterostructures was calculated as

$$\sigma = \frac{w}{R_{ion} \times t \times L} \tag{6.1}$$

where w is the IDE finger spacing (6 μm), t is the film thickness (100 nm), and L is the IDE finger length (500 μm).

Fitting reveals a high transference number

$$t_{trans} = \frac{\sigma_T - \sigma_e}{\sigma_T} \tag{6.2}$$

where σ_T and σ_e are the total and electronic conductivity, respectively, of 0.94-0.98 across all heterostructures (**Figure 6.6**(b)), consistent with results for LSGM single crystals [214]. The smaller transference number in the LSGM/$SrTiO_3$ heterostructures is expected due to the relatively high electronic conduction from the substrates. In turn, the strain- and temperature-dependent evolution of the ionic conductivity and the migration-energy barrier for all heterostructures are extracted (**Figure 6.6**(c)). Examination of the conductivity and the structural parameters reveals several key findings. First, the activation energy of conduction is found to be within the range of E_a=0.65-0.75 eV for all heterostructures. It should be noted, that due to the relatively small temperature window used to extract the activation energy of conduction (which was intended to limit the substrate contributions to overall conductivity), one cannot resolve a difference in the activation energy of conduction smaller than $\sim$0.1 eV. This is further compounded by the nonlinear nature of activation energy in LSGM around 500°C [214]. Wider-temperature-range measurements, excluding LSGM/$SrTiO_3$ heterostructures wherein the substrate contributes too much to ionic conduction to allow for reliable extraction of the real conductivity of the LSGM, were completed for the LSGM/$NdGaO_3$ and $DyScO_3$ heterostructures and reveals a change of the activation energy of conduction of $\sim$0.12 eV from compressive to tensile strains (**Figure 6.6**(d)). Second, the conductivity of the near-zero strain state heterostructures matches well with values measured for bulk single-crystal samples (*e.g.*, the conductivity at 600°C for the films and bulk samples are 0.0126 S/cm and 0.0128 S/cm [214], respectively). Third, the structural changes in LSGM are revealed to have a significant impact on the ion-transport properties. In particular, from compressive strain to near-zero strain, as the LSGM unit-cell volume increases by $\sim$1% and the octahedral-rotation magnitude remains almost invariant, the conductivity of the LSGM is increased by $\sim$100%, indicating that a larger unit-cell volume is preferred to achieve high ionic conductivity. Moreover, as the unit-cell volume is further increased by another $\sim$1% under tensile strain, while simultaneously quenching the octahedral rotations, the observed conductivity is negligibly affected (increases by $<$5%, within the error bars of the measurement). This suggests that

quenching the octahedral rotations also strongly affects the overall transport properties, thus counterbalancing the effect of the expanded unit cell under tensile strain. In other words, this suggests that to achieve high ionic conduction in perovskite structures, the material should be controlled to have both larger unit-cell volume and octahedral rotations.

6.4 First-principle calculations

To understand why these structural features impact ionic conductivity in this manner, DFT calculations coupled with a Green's function method [239] were applied to probe the local effect of structure on ion transport.[4] This method requires the vacancy jump network, the site energies for all unique sites in the network, the migration barriers, and pre-factors for all unique jumps within the network as input parameters and computes the diffusivity at a given temperature. For both the strained and unstrained geometries, the site energies, migration barriers, and pre-factors are obtained from DFT calculations which consider single-vacancy hops in an undoped $LaGaO_3$ supercell. The final diffusivity has contributions from all rates, however, each transition rate has the Arrhenius form of Ae^{-E/k_BT}. $LaGaO_3$ was first constructed via DFT and the structure is shown (**Figure 6.7**(a)). $a^-b^+a^-$-type octahedral tilting in the $LaGaO_3$ geometry is obtained from DFT, and it is shown that

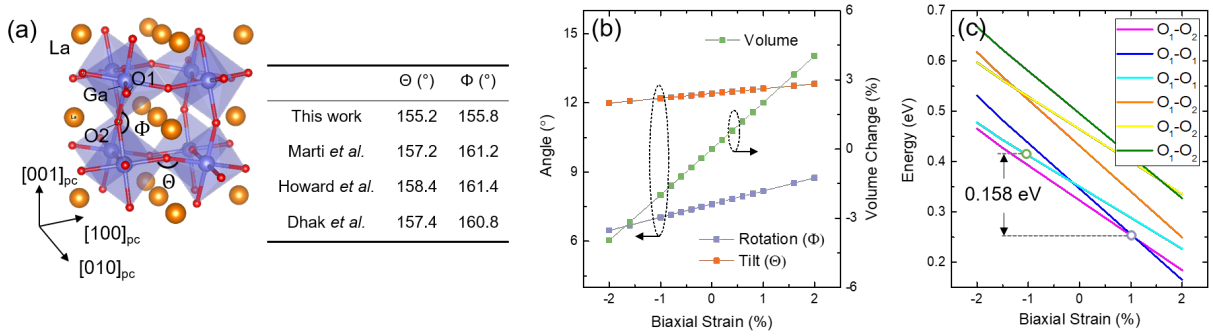

	Θ (°)	Φ (°)
This work	155.2	155.8
Marti *et al.*	157.2	161.2
Howard *et al.*	158.4	161.4
Dhak *et al.*	157.4	160.8

Figure 6.7: *(a) Geometry of the $LaGaO_3$ unit cell relaxed from DFT. The La atoms are orange, Ga atoms are light purple and the O atoms are red. The O atoms in the Ga plane perpendicular to $[010]$ are O1 and the ones in La plane are O2. The O1-O1-O1 bond angle (Θ) and the Ga-O2-Ga bond angle (Φ) measure the in-plane octahedral rotation and out-of-plane octahedral tilt angle, respectively. The in-plane rotation $\theta = (90 - \Theta)/2$, and the out-of-plane tilt angle $\phi = (180 - \Phi)/2$. Comparison of experimental values are also given. (b) Strain effects on unit cell volume and octahedral rotation and tilt in $LaGaO_3$. (c) Oxygen vacancy migration energy versus strain. Tensile strain reduces migration energy barrier of all types of jumps.*

[4]The DFT calculations were accomplished in collaboration with Mr. A. Jain and Prof. D. R. Trinkle from Materials Science and Engineering Department at University of Illinois at Urbana-Champaign, IL, USA.

the DFT accurately reproduces the experimentally-observed geometry and tilt angles in $LaGaO_3$ [240, 241]. The structure of $LaGaO_3$ corresponds to the *Pnma* space group. The smallest cell required to capture this structure contains 4 lanthanum, 4 gallium, and 12 oxygen atoms. All lanthanum and gallium sites are individually equivalent, but there are two types of oxygen sites, which will be further discussed in detail. The octahedral-rotation pattern and unit-cell volume evolution as a function of strain in the undoped $LaGaO_3$ system are computed (**Figure 6.7**(b)). Note that the in-plane rotation $\theta = (90 - \Theta)/2$ and the out-of-plane tilt angle $\phi = (180 - \Phi)/2$. The calculation reveals that by increasing strain from -2% to +2%, the unit-cell volume of $LaGaO_3$ is monotonically increased by $\sim$8%; a trend consistent with experimental observations. It is interesting to note that, in the undoped $LaGaO_3$ system the octahedral rotation has negligible strain dependence and the rotation pattern and angles remain almost unchanged across the applied strain states. Thus, the effect from unit volume change on diffusivity can be isolated.

I will first discuss the effect of octahedral rotations on ionic transport and then address the impact of volume change. The undoped $LaGaO_3$ parent phase was examined to study the impact of octahedral rotations on ion-migration pathways, and at the same time to eliminate dopant-strain effects. As discussed above, because of the distorted octahedra in $LaGaO_3$, there are two distinct oxygen sites located either in the LaO or GaO_2 planes; denoted as *O1* and *O2*, respectively. Calculations further support this difference in that the energy of a vacancy at an *O1* site is 15 meV lower than that for a vacancy at an *O2* site. Furthermore, due to the octahedral rotations, it is found that there are two *O1-O1*-type and four *O1-O2*-type symmetry-unique vacancy jumps with distinct migration-energy barriers (noted in various colors, **Figure 6.8**(a)). Since there are no allowed *O2-O2*-type jumps, vacancy migration along the three orthogonal axes (*i.e.*, in-plane $[001]$ and $[1\bar{1}0]$, and out-of-plane $[110]$) is achieved by either a series of *O1-O1*-type or a combination of *O1-O1* and *O1-O2*-type jumps. As a result, compared to a cubic system with no octahedral rotations, the presence of octahedral rotations creates different energy barriers to ion migration along each direction and, in turn, anisotropic jump phenomena. Thus, ion conduction preferentially occurs along a sub-set of low-energy jumps thereby resulting in two types of fast ion-conducting pathways: The first is via a series of *O1-O1*-type jumps (two equivalent pathways along different directions are shown, **Figure 6.8**(b)) and the second is via a series of *O1-O1* and *O1-O2*-type jumps (**Figure 6.8**(c)). In general, the *O1-O1*-type jump with the highest energy (0.35 eV) determines the overall migration-energy barrier. It is noted that this value is smaller than that extracted from the experiments ($\sim$0.70 eV) and this discrepancy will be addressed later.

Having established the effect of octahedral rotations on ionic migration, biaxial strain (compressive -2% to tensile +2%) was subsequently applied to examine the impact of unit-cell volume change. In undoped $LaGaO_3$, the unit-cell volume is shown to expand by $\sim$8% from compressive to tensile strain while the octahedral rotations remain almost unchanged ($<2^\circ$ change in angles across this entire range of strain, **Figure 6.7**(b)), and therefore, the impact of unit-cell volume can be isolated. Diffusivity calculations reveal that, from compressive to tensile strain, the vacancy diffusivity is nearly isotropic and

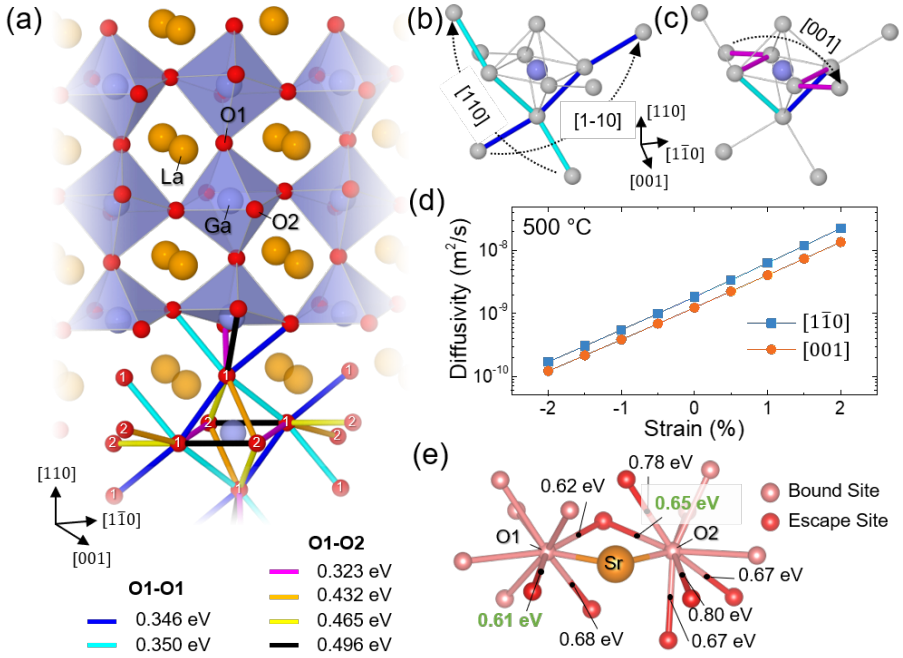

Figure 6.8: *(a) Illustration of the undoped $LaGaO_3$ crystal from the DFT calculations (top). Calculations further reveal six unique energy barriers for different oxygen vacancy jumps (each jump is labeled with different color, bottom). The values of migration barriers are given relative to the O1 site and there are two O1-O1- and four O1-O2-type jumps. Schematic illustration of various fast ion-conducting oxygen vacancy migration pathways including ones based on (b) a series of O1-O1-type jumps (two equivalent pathways along different directions are shown) and one based on (c) a series of O1-O1 and O1-O2-type jumps. (d) DFT calculated vacancy diffusivity as a function of strain for undoped $LaGaO_3$. e, Migration energies for oxygen vacancies when $LaGaO_3$ is doped with strontium at lanthanum-sites where, vacancies are found to either jump between bound sites (i.e., circle around the strontium trap) through low-energy barrier jumps (0.20-0.45 eV) or jump towards unbound sites (i.e., escape from the strontium trap) through high-energy barrier jumps (0.61-0.80 eV).*

increases almost linearly across the experimentally probed regime from -1% to 1% strain (Figure 3d). This enhancement of the diffusivity is a direct consequence of a reduction all the migration energy barrier across that strain regime (**Figure 6.7**(c)). It is worth noting that although the exact computation of diffusivity in LSGM is not a trivial matter and requires mesoscopic modeling [227, 242, 243], the DFT results support the trends of the experimental findings wherein a larger unit-cell volume is preferred for higher ionic conduction [17].

For a better representation of the experimental scenario, strontium- and magnesium-doped versions of $LaGaO_3$ were also examined by DFT. Doping lanthanum with strontium

and gallium with magnesium creates multiple unique vacancy sites, but only the binding energies with oxygen vacancies at the dopant sites within the first neighbor shell are shown. There are four lanthanum sites within the first neighbor shell of both *O1* and *O2* sites, and octahedral tilting causes each of these sites to have different vacancy-dopant binding energies. Similarly, the first neighbor shell of *O1* has two unique gallium sites and that of *O2* has one unique gallium site. These configurations are represented as $V_i X_j^k$, where i represents an *O1*- or *O2*-type oxygen vacancy, X is the nearest dopant atom, j is the neighbor shell of the oxygen site, and k identifies the symmetry unique dopant sites within each shell. These studies reveal that the nearest strontium-on-lanthanum sites (*Sr1*) have attractive binding with both vacancy sites (*O1* and *O2*) while the nearest magnesium-on-gallium sites (*Mg1*) have negligible repulsive binding with the vacancies (**Figure 6.9**(a-b)). In contrary to previous studies which suggested magnesium as trapping center [244], the results from this study and recent studies [245, 246] reveal that it is the strontium that attracts vacancies while magnesium does not. In turn, to examine the rate-limiting steps for vacancy diffusion, the oxygen-vacancy-migration barriers out of the most strongly bounded *O1-Sr1* and *O2-Sr1* vacancy configurations were calculated (Figure 3e). Vacancies are found to either jump between bound sites (*i.e.*, circle around the strontium trap) through low-energy barrier jumps (0.20-0.45 eV) or jump towards unbound sites (*i.e.*, escape the strontium trap) through high-energy barrier jumps (0.61-0.80 eV). Therefore,

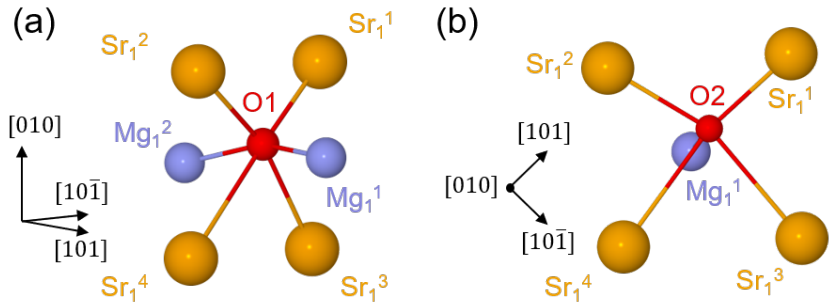

Config.	Binding (eV)
$V_{O1}Sr_1^1$	-0.24
$V_{O1}Sr_1^2$	-0.13
$V_{O1}Sr_1^3$	-0.02
$V_{O1}Sr_1^4$	0.00
$V_{O1}Mg_1^1$	0.05

Config.	Binding (eV)
$V_{O1}Sr_1^1$	-0.30
$V_{O1}Sr_1^2$	-0.11
$V_{O1}Sr_1^3$	-0.09
$V_{O1}Sr_1^4$	-0.02
$V_{O1}Mg_1^1$	0.06
$V_{O1}Mg_1^2$	0.03

Figure 6.9: *The binding energy of O vacancy at (a) O1 and (b) O2 sites with dopant atoms at sites within the first neighbor shell. The O-Sr pair has a strong attractive binding while O-Mg pair has a weakly repulsive binding.*

vacancies are trapped inside a superbasin surrounding the Sr atom. The energies required for the vacancy to escape out of the superbasin, therefore, is likely to control the diffusion behavior in doped systems. With the inclusion of dopant effects, the escape energies from *O1* and *O2* sites (0.61 eV and 0.65 eV) agree well with the experimentally observed activation barriers (∼0.70 eV).

6.5 Experimental realization of the optimal structure

As such, I now turn the attention to creating such an optimal structure wherein the efficacy of this design process can be demonstrated. To do this, an approach leveraging both strain and interfacial engineering is adopted [7, 34]. Although a particular rotation pattern of an epitaxial film is energetically fixed under a given strain state [32, 68], it has been shown that utilization of perovskite substrates with large octahedral rotations can drive an increase in the rotation magnitude in the film near the heterointerface (**Figure 6.10**) [34, 36, 84]. Thus, in order to achieve both large unit-cell volume and octahedral rotations in the LSGM, I turn to superlattice $(DyScO_3)_m/(LSGM)_n$ (where *m* and *n* refer to the number of unit cells (UC) of $DyScO_3$ and LSGM, respectively) structures grown on $DyScO_3$ substrates. The superlattice structure is chosen for a number of reasons. First, $DyScO_3$ is an insulating material with large octahedral rotations (the *Sc-O-Sc* bonding angle is ∼140°) [66, 247] such that the rotation pattern from the $DyScO_3$ interlayers can propagate into the LSGM layers. Second, $DyScO_3$ substrates are chosen to maintain the desired tensile strain to expand the unit-cell volume of the LSGM. Finally, multiple LSGM layers give rise to higher total conductance to limit the substrate contribution to the measured conductance and facilitate easier measurement of the ion-transport properties.

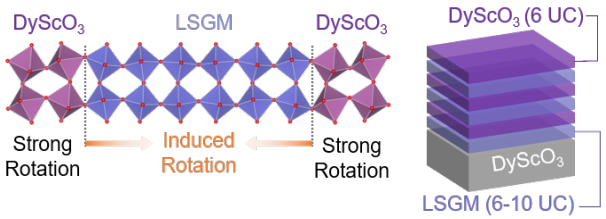

Figure 6.10: *Illustration of introduction of octahedral rotation via interfacial engineering.*

RHEED-assisted PLD was used to synthesize a series of superlattice structures with a composition of $(DyScO_3)_m/(LSGM)_n$ superlattices (m = 6 UC, n = 6-10 UC) . The same growth conditions were used for both the LSGM and $DyScO_3$ layers except that the laser repetition rate was adjusted to 2 and 3 Hz, respectively, for better visualization of the RHEED oscillations (**Figure 6.11**(a)). X-ray diffraction studies reveal strong superlattice peaks with clear Laue fringes, indicating high crystallinity and sharp interfaces (**Figure 6.11**(b)); features further validated by sharp *in situ* RHEED patterns during growth (insets, **Figure 6.11**(a)). The superlattices are found to be coherently strained to the substrate via reciprocal space mapping studies (**Figure 6.11**(c)) and structurally and chemically robust during ∼24 hours of high-temperature measurement (**Figure 6.11**(d)).

To confirm the realization of the desired large unit-cell volume and octahedral rotations in the LSGM, synchrotron-based X-ray crystal truncation rod measurements accompanied by COBRA were performed on a 6 UC $DyScO_3$/6 UC LSGM/$DyScO_3$ (110) heterostructure emulating a single repeat of the superlattices.[5] COBRA allows for the extraction of atomic positions for each layer near the surface (top ~20 nm) [37]. COBRA studies were completed at the Advanced Photon Source, Argonne National Laboratory, Sector 12-ID-D. Crystal truncation rods (CTRs) were measured using a surface X-ray diffraction χ-geometry with a five-circle diffractometer under X-ray photon energy of 20 keV with a total flux of $\sim 2.0 \times 10^{12}$ photons/sec. A large set of CTRs in the reciprocal lattice coordinate were measured at room temperature with $H_{max} = \pm 4$ *r.l.u.*, $K_{max} = \pm 4$ *r.l.u.*, and $L_{max} = \pm 9$ *r.l.u.* under $2 \times 2 \times 2$ pseudo-cubic notation (*r.l.u.* as reciprocal space units). This CTR data set includes all relevant superstructure Bragg rods due to the oxygen octahedral rotation and *A*-site cation displacement off the symmetric point. Experimental CTR data were first background subtracted, and then properly corrected for geometric and polarization factors. Initial atomic structural model was constructed based on bulk $DyScO_3$ structures with fitted *c* lattice constant using *GenX* software [248]. Within each COBRA iteration, real space and reciprocal space constraints are alternatively applied to reconstruct phase

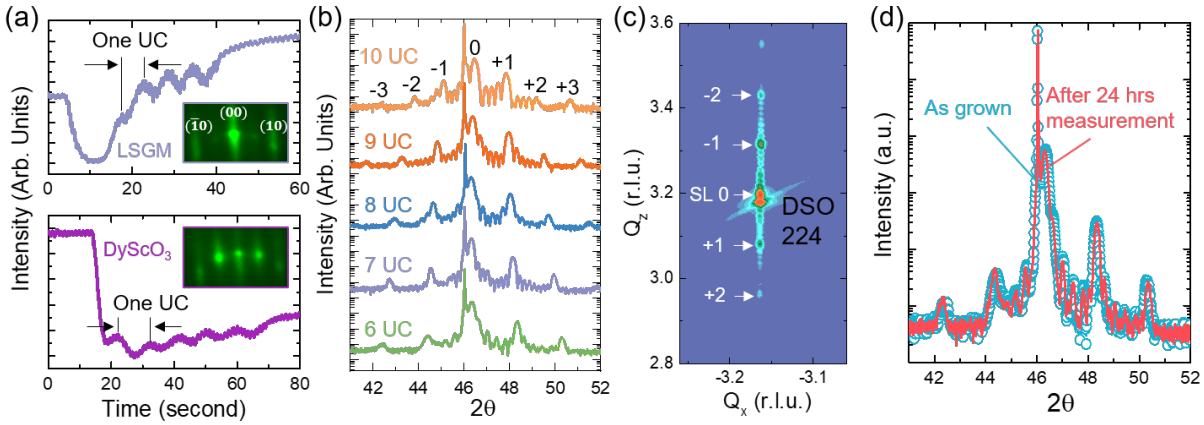

Figure 6.11: *(a) RHEED spectra of LSGM and $DyScO_3$ growth on $DyScO_3$ substrates. All films reveal layer-by-layer growth mode and the exact monolayer numbers can be deterministically controlled. Sharp electron diffraction patterns reveal high surface quality and crystallinity (figure insets). (b) X-ray line scans of all superlattice structures reveal clear Laue thickness fringes and superlattice peaks, indicating good crystallinity and sharp interfaces. (c) Synchrotron X-ray RSM show clear strained superlattice peaks. (d) X-ray line scans before and after high temperature measurement (24 hours at above 500°C under O_2 and N_2 environment) show now changes in line-scan profile, suggesting robustness of sample during measurement hours.*

[5]COBRA analysis were accomplished in collaboration with Dr. H. Zhou at Advanced Photon Source, Argonne National Laboratory, IL, USA., Dr. Y. Yuan and Prof. G. Venkatraman from Materials Science and Engineering Department at Pennsylvania State University, PA, USA.

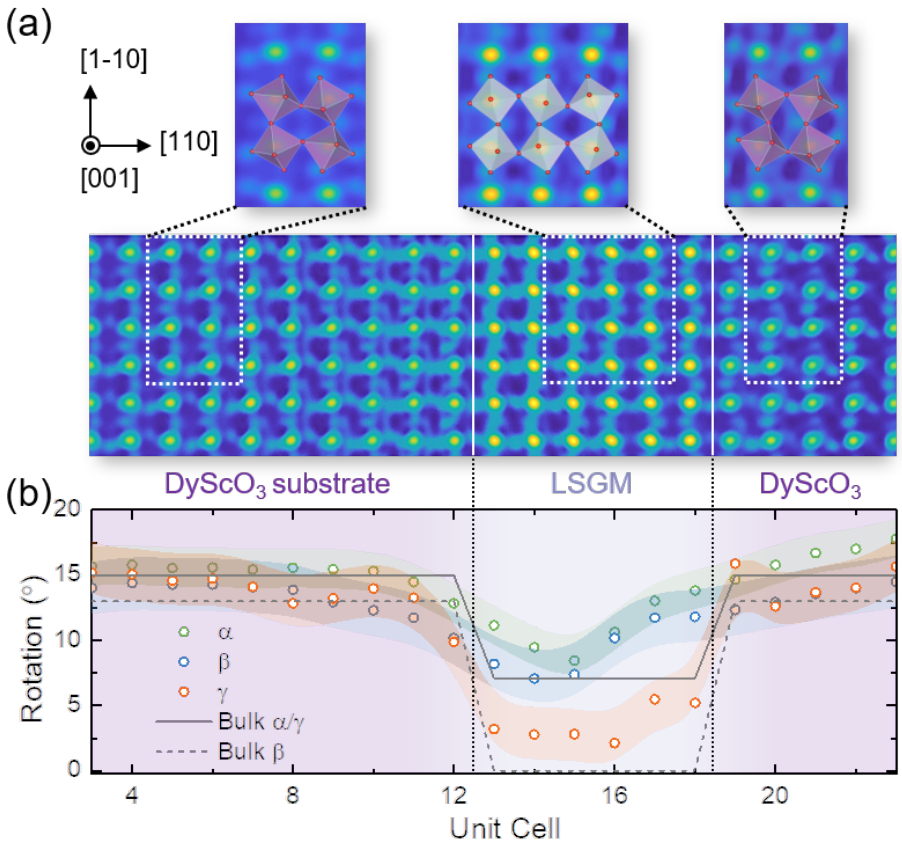

Figure 6.12: *(a) Electron density map for a $(DyScO_3)_6/(LSGM)_6/DyScO_3$ heterostructure from the COBRA analysis. The map reveals large octahedral rotations extending from the $DyScO_3$ into the ultrathin LSGM. (b) Extracted octahedral rotation angles as a function of unit cell through the thickness of the heterostructure confirming the large octahedral rotation of both the bottom and top $DyScO_3$ layers and the formation of large in-plane rotations (α and β angles) in the LSGM that are markedly different from bulk values (solid and dashed lines).*

information for measured CTRs, until a final convergence is achieved. All atomic positions are determined by fitting the electron density at corresponding atomic sites with three-dimensional Gaussian function. The α and β angles of oxygen octahedral tilts were calculated using apical oxygen atoms. The γ rotation angles were calculated using equatorial oxygen atoms.

Although the rotation magnitude of thicker LSGM films under tensile strain is nearly zero, the electron density maps projected along the [001] reveal large tilts of the octahedra in the embedded LSGM layer (**Figure 6.12**(a)). Both $DyScO_3$ layers also show large and rigid octahedral rotation patterns, with rotation angles in good agreement with bulk [66, 247]. The extracted octahedral rotations for the LSGM layer are, however, drastically different from bulk [232] (**Figure 6.12**(b)). Namely, the two in-plane rotation angles (α

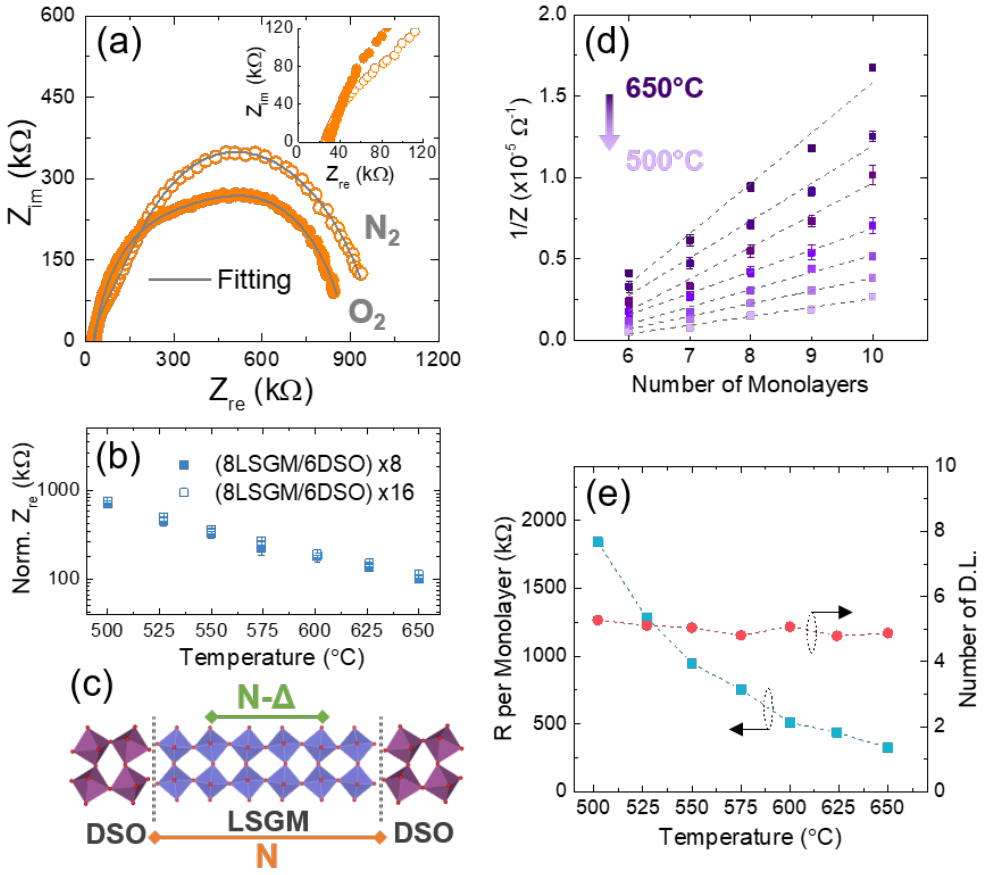

Figure 6.13: *(a) Representative impedance spectra for a superlattice sample at 500°C. (b) Same normalized impedance per LSGM layer of $(LSGM)_6/(DyScO_3)_6$ superlattices with different repetition (i.e., 8 and 16 repetitions) suggests that all LSGM layers are effectively conducting. (c) Illustration of hypothesized conducting and non-conducting part of LSGM ultrathin films. The conductivity and thickness of non-conducting part of LSGM can be extracted via linear fitting of superlattice samples with different LSGM thickness (d), and the impedance of LSGM and number of non-conducting "dead layers" in LSGM are given (e) Note that for all superlattice geometries, there are consistently 5UC of LSGM that are not conducting. In other words, when calculating the conductivity of LSGM I use the thickness of conducting LSGM unit cells instead of the total thickness*

and β) are increased due to the coupling with the $DyScO_3$ layers while the out-of-plane rotation angle (γ) is quenched as a result of the tensile strain. Overall, compared to the 100-nm-thick LSGM grown directly on $DyScO_3$ substrates where the octahedral rotations are significantly quenched, the effective octahedral rotation magnitude for the ultrathin LSGM in the superlattice structures has been dramatically increased from $\sim$2.3° to $\sim$13.7°.

6.6 Conductivity measurement in superlattice structures

The in-plane transport measurements on the superlattice structures were performed in a similar manner and a representative Nyquist plot taken at 500°C is given (**Figure 6.13**(a)). It is revealed that the superlattice structures exhibit an oxygen partial pressure dependency of the resistance in the low-frequency regime, while in the high-frequency regime the intercepts are invariant. The weaker oxygen-partial pressure dependency of low-frequency resistance is possibly due to the presence of the $DyScO_3$ such that the interaction between the LSGM and the gas environment is blocked. To accurately extract the ionic conductivity of this optimal structure in the superlattice geometry, there are two challenges: First, is to assure that all LSGM layers are similarly conducting and, second, is to have accurate values of the thickness of the conducting layers. To accomplish this, a series of superlattice structures with varying periodicity are grown to apply standard scaling laws to the analysis. To confirm that all LSGM layers were conducting, multiple heterostructures built from a single representative $(DyScO_3)_6/(LSGM)_6$ superlattice unit with different total film thickness (specifically in structures with 8 and 16 total repetitions) were examined and it was found that the normalized resistance per LSGM layer was the same (**Figure 6.13**(b)). As it pertains to understanding the thickness of the conducting layers, because there is a lack of complete understanding about the nature of ionic conduction at and near interfaces, no assumption is made that each of the LSGM unit cells is conducting in the same fashion. In turn, the average resistance of each conducting LSGM unit cell is assumed to be R_{UC}. And, recalling that the total number of LSGM unit cells is n, the number of conducting LSGM unit cells will be $n - \Delta$, where Δ denotes potentially non-conducting unit cells at or near interfaces (**Figure 6.13**(c)). As such, a linear relationship between the resistance per layer R_L and n is expected and given by

$$R_L^{-1} = R_{UC}^{-1}(n - \Delta). \tag{6.3}$$

Fitting this relation across the temperature region of interest (500°C to 650°C) by merely varying n, yields R_{UC} and subsequently the conductivity of the conducting unit cells of LSGM can be extracted (**Figure 6.13**(d-e)). This fitting shows that there is an invariant number of non-conducting LSGM "dead layers" ($\Delta \approx 5$) within the temperature range and is independent of the total thickness n of each LSGM layer (**Figure 6.13**(e)). Thus, to get the accurate conductivity of LSGM, only the conducting layers of LSGM instead of the total thickness of LSGM layers are counted.

To understand the origin of the "dead layer", low-energy ion scattering (LEIS) spectrometry[6] is used to qualitatively examine the near-surface La:Sr ratio for the ultrathin LSGM films (technical details of LEIS can be found in **Appendix B**). 5 UC LSGM/$DyScO_3$ heterostructures were used for this study. LEIS dynamic depth profiling was performed with a sputtering argon source (500 eV, 90 nA, 4 mm^2) to constantly remove the top layer of

[6]LEIS measurements are performed in collaboration with Dr. V. Thoréton, Prof. J. Kilner, and Prof. T. Ishihara from Kyushu University, Japan.

LSGM, while a more focused neon source (6000 eV, 1 nA, 1 mm^2) was used to analyze the heavier cation concentration of the exposed surface. The summation of all acquired signals yields a La:Sr ratio of ∼11:1 (using integrated peak area as qualitative analysis), which is close to that probed via RBS in thicker films (**Figure 6.14**(a)). The dynamic depth profile of the 5 UC LSGM/$DyScO_3$ heterostructures reveals a very clear strontium redistribution across the film thickness, and around 50%-60% strontium occupation at the *A*-site is observed at film surface layer (**Figure 6.14**(b)). Such strontium redistribution/segregation towards the surface has been observed in various alkaline-doped perovskite systems and results in dramatic changes in the physical properties. For instance, strontium redistribution has also been observed in ultrathin $La_{1-x}Sr_xMnO_3$ (LSMO) and has been proposed as a possible cause for the magnetic "dead layer" in LSMO [249]. It is further hypothesized that the observed strontium redistribution and enrichment at the surfaces in the ultrathin LSGM films is potentially the origin of the 5 UC of insulating (non-conducting) behavior as the enriched strontrium could disturb the local strain, exacerbate trapping, and impede migration [215, 250]; although a more thorough study is required to unequivocally make this conclusion. With this noted, I extracted the conductivity of the optimized perovskite structure and find that it is increased by a factor of 2.5 as compared to the non-optimal, compressively-strain heterostructures and nearly 70% as compared to the bulk-like state around 600°C (**Figure 6.15**). This result suggests that the design algorithm revealed by this work can provide a pathway to enhance the ionic-transport properties.

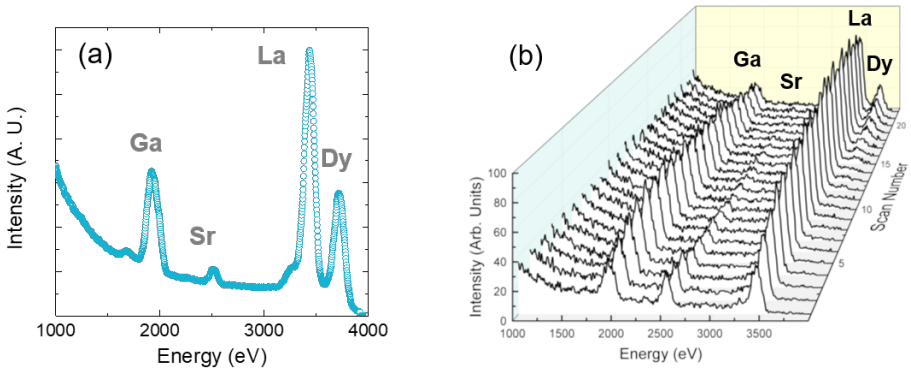

Figure 6.14: *LEIS studies on 5UC LSGM/$DyScO_3$ sample is subsequently performed to better understand the origin of "dead layer" in LSGM. The total yield reveals that 5UC LSGM has the same nominal chemistry compared with thicker films (a), while the depth profile of LSGM suggests that there is significant Sr redistribution along the out-of-plane direction of the film (b). The redistribution (segregation) of Sr is likely to be the cause of transport "dead layer" in ultrathin LSGM.*

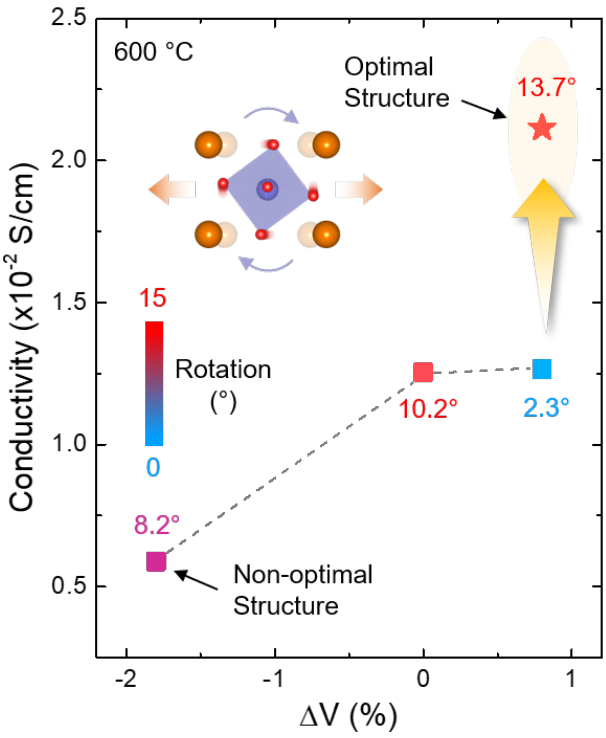

Figure 6.15: *Conductivity of LSGM at 600°C as function of unit cell volume and octahedral rotation magnitudes. The optimal structure of LSGM achieves an enhancement of conductivity by a factor of 2.5 compared with non-optimal heterostructures at compressive strain state*

6.7 Conclusions

In summary, the correlation between structural features (*i.e.*, unit-cell volume and octahedral rotations) and ionic conductivity in perovskite oxides has been investigated in this chapter. Quantifiable control over unit-cell volume and octahedral rotations in LSGM was achieved via strain engineering. It was found that unit-cell volume and octahedral rotations both have significant impact on ionic migration in the perovskite structure and the optimal design is to have both large unit-cell volume and octahedral rotations. DFT calculations of vacancy diffusion further reveal that larger unit-cell volume reduces migration-energy barriers while large octahedral rotations create low-energy migration pathways. Subsequent superlattice structuring enables the creation of both large unit-cell volume and octahedral rotations which results in an enhancement of the conductivity. Again, the work in this chapter reveals the detailed relationships between structural parameters and transport evolution in perovskite ion-conducting systems and provides insights towards a rational-design approach of electrolyte materials for intermediate-temperature energy conversion applications.

Chapter 7

Correlating surface orientations and electrochemistry

In this chapter, I focus on studying the effects of perovskite surface structure on gas-exchange kinetics via epitaxial surface-orientation control. $La_{0.8}Sr_{0.2}Co_{0.2}Fe_{0.8}O_{3-\delta}$ (LSCF) is chosen as the model electrode, and the gas-exchange kinetics are characterized by developing an epitaxial half-cell geometry where three surface variants are created [*i.e.*, LSCF/LSGM/$SrRuO_3$/$SrTiO_3$ (001), (110), and (111)]. AFM, LEIS, and XPS are applied to study the various surface variants and the results reveal that they possess similar roughness and surface chemistry in the as-grown state. Subsequent electrochemical measurement at 350°C in both air and dry oxygen, however, reveal a strong surface-orientation dependency of the gas-exchange kinetics, where the (111)-oriented surface variants exhibit an activity 3-times higher compared to the (001)-oriented surface variant. ECR studies on LSCF/$SrTiO_3$ (001), (110), and (111) heterostructures further confirmed such differences. Oxygen-partial-pressure dependent studies from 760 torr to 0.1 torr are performed to further understand the reaction mechanisms and show that the three surface variants have similar rate-limiting steps across this pressure regime. Specifically, the adsorption of oxygen molecules is suggested to be the rate-limiting step at lower pressures ($P_{O_2} \lesssim 1$ torr), while the charge-transfer process could be the rate-limiting step at higher pressure regime ($P_{O_2} \gtrsim 1$ torr). These results suggest that the LSCF (111) surface is energetically favorable for the reaction to take place and shed light on the engineering of high-efficiency electrode structures for solid-oxide fuel cells.

7.1 Introduction

The strong interaction with gas molecules at the solid-gas interface has made perovskite oxides a promising electrode candidate for intermediate-temperature solid-oxide fuel cells [251–254]. Nevertheless, the rate of oxygen electrocatalysis at the electrode surface is still one of the major factors that limits the efficiency of such devices. Extensive research has been performed to understand the surface gas kinetics of perovskite electrodes and its correlation with specific material properties such that better electrodes can be more efficiently designed. In the past, engineering the electronic structure of perovskite electrodes has been the prevailing route to improve the gas-exchange kinetics. For instance, the electron occupancy of the e_g orbitals of the B-site cation has been identified as a descriptor for electrode chemistry design [6, 255, 256]. It has been empirically observed that the occupancy needs to be optimized to $\sim$1.2 via appropriate aliovalent doping to reach the optimal performance. In addition, the position of oxygen 2p band center is also proposed as an important factor that governs the gas exchange rate [257, 258]. Similarly, the control of the band structure can be accomplished via doping or defect engineering on oxygen vacancies.

Despite the significant progress made in the understanding of the correlation between perovskite electronic structure and surface-gas kinetics using dopant species and level, alternatively, advances in thin-film synthesis now enable researchers to study the surface reaction on an orientated single-crystal facet where the structure-property coupling can be better understood. For instance, epitaxial tensile strain is found to promote the surface-gas kinetics of perovskites [17]. The *B*-O-*B* bonding strength and angle have been identified theoretically as important factors that affect the surface reactions [259, 260]. Other studies have revealed that the surface termination of (001) surfaces is also strongly correlated to the rate of electrocatalytic reactions [97, 99, 261]. Few experimental studies, however, have focused on the correlation between perovskite-surface orientation and surface-electrocatalytic properties. In fact, contradictory results have been reported thus limiting our fundamental understanding of gas reactions on differently surfaces [88, 262]. In this spirit, this chapter specifically focuses on the effects of surface orientations on the gas kinetics of perovskite electrodes.

The examination of the impact of surface orientations on gas-exchange kinetics requires the construction of well-defined electrode surfaces and a reliable probe of the gas-exchange kinetics. Previously, electrochemical AC-impedance studies on thin-film epitaxial cells composed of yttria-stabilized zirconia (YSZ) electrolytes and perovskite micro-electrodes have proved to be a useful platform to isolate the surface-exchange reaction and examine the gas-exchange kinetics [263, 264]. Thin-film heterostructures have been further utilized to control the structure of the electrode material such that a fundamental structure-property correlation can be studied [265–267]. Nevertheless, due to the structure-mismatch between the perovskite and the fluorite structures, the fact that YSZ is the only electrolyte used in such cell designs greatly limits the communities ability to quantifiably and deter-

ministically control the perovskite-electrode structures. These limitations arise because the structural mismatch between the perovskite and fluorite make it challenging to quantitatively alter the strain state or surface orientations in the perovskite electrode. This structural mismatch further results in the creation of polycrystalline electrodes and/or the formation of defective (*i.e.*, high densities of dislocations) heterointerfaces, both of which can potentially complicate the interpretation of results [264, 266, 268]. On the other hand, prior studies on quantitative strain effects and surface-orientation effects on gas-exchange kinetics of perovskite electrodes were accomplished by epitaxially growing a single layer of perovskite electrode on a perovskite substrate. Although coherent epitaxial strain can be achieved in such cases, the measurements were typically based on techniques such as isotope-tracer diffusion and solution-based electrochemical cells [17, 87, 269], and hence, some of the advantages of using a full- or half-cell geometry (*e.g.*, high operating temperature, variable gas/pressure environment, measurement simplicity) are not fully utilized. Here, to address these challenges, I design and utilize a fully epitaxial all-perovskite half-cell geometry to study the correlation between electrode-surface orientations and surface-gas-exchange kinetics.

7.2 Epitaxial all-perovskite, half-cell structures

A brief discussion will first be given on the design and operation of the half-cell structure for surface-gas-kinetics measurements. Conventionally, half cells refer to electrochemical cells that only have one type of reaction (*i.e.*, either reduction or oxidation), happening at the electrode. Here, the growth of highly-controlled, epitaxial materials places some geometric restrictions on the design of the half-cells. They still has the two reaction pathways because an AC bias will be applied onto the cell; however, only the working electrode will be primarily responsible for the electrochemical reactions and the counter electrode is

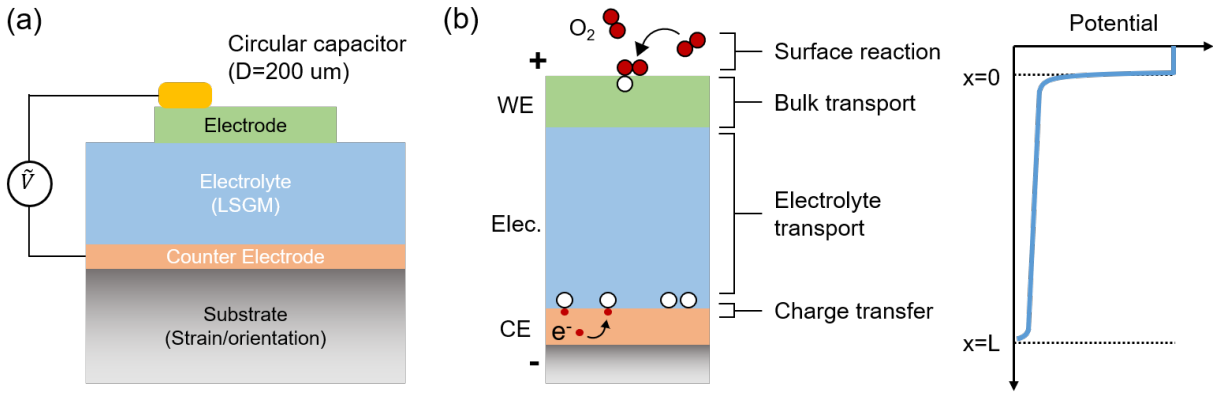

Figure 7.1: *(a) The schematic of a half cell for thin-film gas kinetic measurement. (b) The transport process involved in one voltage cycle and the hypothesized potential profile across the heterostructure if provided.*

designed to have negligible impedance compared to the working electrode, and merely serves to complete the circuit. Thus, only "half" of the cell structure is contributing to the overall potential drop across the cell.

The half cell (**Figure 7.1**(a)) a layer of electronically conducting counter electrode, a layer of ionically conducting electrolyte, and a patterned top working electrode. Since the electrolyte used in the geometry is an epitaxial layer of the perovskite LSGM (details in **Chapter 6**), the key advantage of using such geometry is that the whole stack can be fully epitaxial such that strain engineering and orientation control can be applied by choosing a proper perovskite substrate. Adding to this, is that such epitaxial heterostructures greatly reduce the confounding effects from dislocations or grain boundaries in the perovskite electrodes and provides an opportunity to quantitatively study the correlation between surface structure and electrochemical properties. During the operation of the cell, a small AC bias (10 mV) is applied. Assuming a positive bias is applied to the working electrode, as an example, the ionic charges will first go through a surface-reaction process, being transferred through the electrode and electrolyte, and getting compensated at the electrolyte-counter-electrode interface (**Figure 7.1**(b)). Since the top working electrode has a diameter of 200 μm while the total thickness of the heterostructure is less than two hundred nanometers, the transport impedance is on the order of tens of Ohms and can be negligible based on the ionic conductivity for LSGM and LSCF [213, 270]; meaning the ionic transport impedance can be neglected. As such, the operation of the half-cell can be assumed to be surface-reaction-limited and the potential profile across the half-cell can be simplified (**Figure 7.1**(c)).

7.3 Heterostructure synthesis and characterization of the half-cells

Trilayer heterostructures with 30 nm LSCF as the working electrode, 100 nm LSGM as the electrolyte, and 20 nm $SrRuO_3$ as counter electrode are epitaxially grown on $SrTiO_3$ (001), (110), (111)) substrates where the epitaxial relationship is maintained throughout the heterostructures. The specific stoichiometry of LSCF is picked due to the fact that the lattice parameters of LSCF and $SrTiO_3$ are essentially the same [271], which minimizes the strain energy in the heterostructures. First, 20 nm $SrRuO_3$ counter electrode was grown at 700°C in 100 mTorr of oxygen with a laser fluence of 1.5 J/cm^2 and a repetition rate of 5 Hz (a total of 1500 pulses yielded 20-nm-thick films). Next, 100 nm LSGM electrolyte was grown at a heater temperature of 800°C in a dynamic oxygen pressure of 40 mTorr and with a laser fluence and repetition rate of 1.8 J/cm^2 and 5 Hz, respectively. Finally, 30 nm LSCF working electrode was grown at 700°C in 150 mTorr of oxygen with a laser fluence of 1.5 J/cm^2 and a repetition rate of 5 Hz. All films were grown in an on-axis geometry with a target-to-substrate distance of 5.2 cm. Following growth, the films were cooled to room temperature at a rate of 10°C/min. in a static oxygen pressure of 700 Torr.

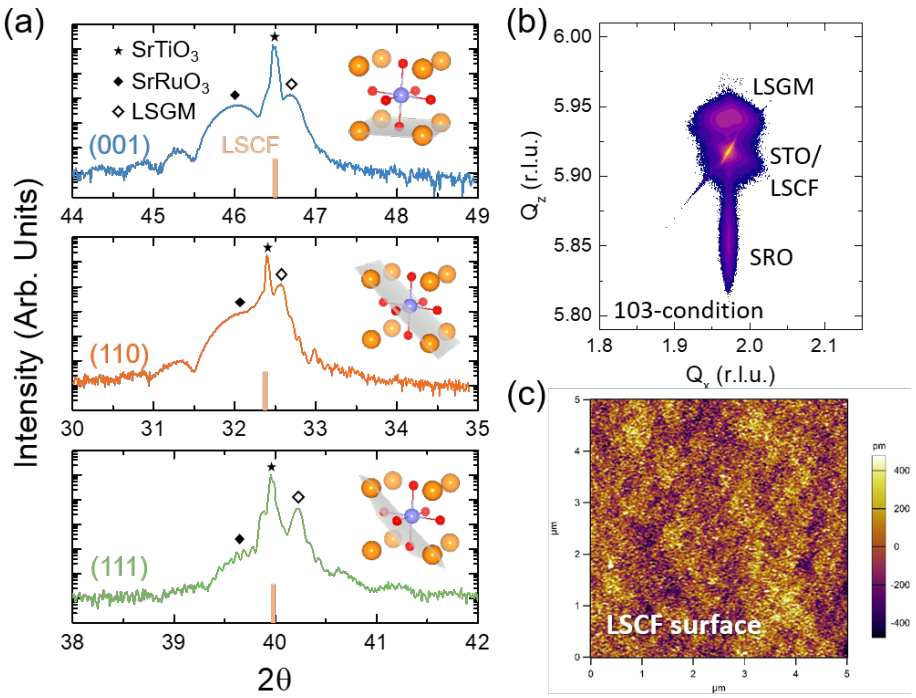

Figure 7.2: *(a) X-ray line scan of the heterostructures grown on $SrTiO_3$ (001), (110), and (111) substrates. (b) RSM around 103-diffraction condition for the heterostructure on $SrTiO_3$ (001) substrates. (c) AFM image of LSCF surface.*

X-ray line scans reveal that all heterostructures are composed of single-phase, high-quality layers epitaxially grown along the substrate-defined orientations (**Figure 7.2**(a)). In the line scans, the $SrRuO_3$ and LSGM peaks are distinguishable and labeled. The LSCF peak is not visible due to the lattice matching with substrate (*i.e.*, it is hidden under the substrate peak), while the expected peak positions of LSCF are marked in the plots. RSM scans reveal that all layers in the heterostructures are coherently strained to the substrates and a representative RSM about the 103-diffraction condition is provided illustrate this point (**Figure 7.2**(b)). Atomic force microscopy (AFM) of the LSCF surfaces was performed and revealed smooth LSCF surfaces with a root mean square of roughness $\sim$500 pm for all orientations (data for a (001)-oriented heterostructure is provided here, **Figure 7.2**(c)).

As it is known that strontium segregation in perovskite electrodes can impact the surface-gas kinetics [267, 272–274], to rule out the possibility that different orientations might have different levels of strontium segregation, X-ray photoelectron spectroscopy (XPS) studies (technical details are found in **Appendix B**) are performed on the as-grown LSCF electrode surfaces to extract the level of strontium segregation. Briefly, if strontium segregation exists near the top surface of the film, the strontium 3*d* doublet peaks will shift to a higher binding energy [273] due to a different binding environment near and at the surface. Thus, two sets of strontium 3*d*peaks, corresponding to strontium near the surface and in the lattice, are expected to be manifested in the spectra. By fitting the

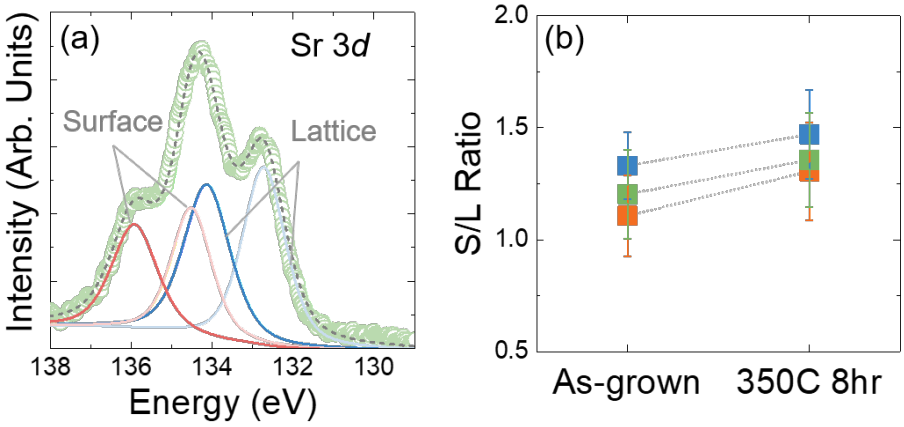

Figure 7.3: *(a) A representative XPS scan around strontium 3d peak. (b) The ratio between surface strontium to lattice strontium for as-grown LSCF films and LSCF annealed for 8 hours in air.*

two strontium 3*d* doublet peaks, one is able to extract the relative concentration of strontium in the lattice and at the surface. A representative XPS scan for LSCF/$SrTiO_3$ (001) heterostructures about the strontium 3*d* peaks is provided (**Figure 7.3**(a)). The doublet from surface strontium, as expected, shifts to higher binding energies and results in three strong peaks in the overall intensity. Fitting the spectra reveals that there is noticeable and consistent strontium segregation in the as-grown LSCF heterostructures regardless of heterostructure orientation (likely arising from segregation during growth or the cooling process) (**Figure 7.3**(b)). It has been argued that the cation segregation in perovskites can be affected by cation-size mismatch, lattice strain, and vacancy concentration [98, 275], and, thus, it is not surprising to observe similar segregation levels among the three different surface variants. Additional XPS studies are conducted on LSCF surfaces after annealing the heterostructures at 350°C for 8 hours, mimicking the subsequent experimental environments used for the EIS studies. This reveals that there is a slightly increased strontium segregation level after annealing, but the segregation level still remains consistent across the three surface variants (**Figure 7.3**(b)).

To further quantify the surface chemistry, LEIS is used to examine the chemical composition of the outermost layer at the LSCF surfaces.[1] The LEIS studies are performed on as-grown LSCF samples using a focused neon beam (6000 eV, 1 nA, 1 mm^2) such that the chemistry of the exposed LSCF surfaces can be quantified. The LEIS results (**Figure 7.4**) reveal that, for all three surface variants, the outermost layer is almost purely *A*-site cation terminated. The only exception is that the (111)-oriented surface variant shows some exposed *B*-site cations, but the concentration is low. This result is in consistent with previous LEIS studies on perovskites which have shown that the outermost layer is purely *A*-site,

[1]LEIS measurements are performed in collaboration with Dr. V. Thoréton, Prof. J. Kilner, and Prof. T. Ishihara from Kyushu University, Japan.

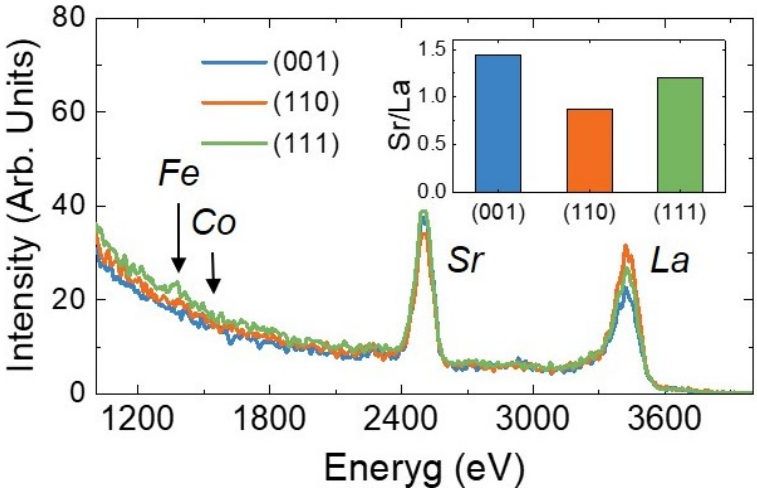

Figure 7.4: *LEIS spectra on LSCF surfaces along different orientations. The outermost layer is purely A-cite terminated. The inset gives the ratio of strontium and lanthanum concentration, which reveals strontium segregation at the surface.*

and *B*-site cations only start to show up at sub-surface layers [99]. Therefore, the (001) and (111) surfaces of LSCF should be *(La,Sr)O* and *$(La,Sr)O_3$* terminated, respectively. For the (110) surface, it is interesting to observe that, although the expected termination is *(La,Sr)(Co,Fe)O*, there is no detectable *B*-site cations. It is possible that some specific reconstruction processes at (110) surface can give rise to the exposure of a predominant concentration of *A*-cite cations; the exact mechanism at work here will be subject to further future study. Additionally, the surface chemistry of the outermost layer across the three different surface variants is essentially the same, suggesting that the difference in electrochemical properties of the three surface variants should likely does not originate from surface chemistry alone. Lastly, while the idealized strontium to lanthanum peak intensity ratio should be 0.2, the ratios extracted for the outermost layers are 1.44, 0.87, and 1.20 for LSCF (001), (110), and (111), respectively, confirming ample strontium segregation (**Figure 7.4**, inset). Based on these results, the LSCF surface variants synthesized for further electrical studies are revealed to be similar in terms of crystallinity, surface quality, and surface chemistry, but only differ in surface orientation.

7.4 The fabrication of the epitaxial half cells

After the detailed structural and chemical characterization, I proceeded to design a measurement strategy and device structure to accurately extract the gas-exchange kinetics for LSCF. It has been demonstrated that EIS measurement on thin-film micro-electrodes is a reliable approach to extract the rate of the surface reactions [263, 264]. The EIS measurements are typically completed on a heater stage where the electrical connections

are made via a platinum tip mounted on a micromanipulator. Such a probe-station based setup, at times, results in noisy data due to unstable contact between the platinum tip and the working electrodes; plus, it also makes it difficult to perform electrochemical studies under different gas environment. Here, I developed a new device structure such that the micro-electrodes can be wire-bonded to a chip carrier for clean signal extraction, and both temperature- and pressure-dependent electrochemical measurements can be readily performed.

The device design (**Figure 7.5**(a)) reveals that the working electrodes are fabricated into circular capacitors and is surrounded by a thick layer (200 nm) of insulating MgO. Next to each circular electrode, a platinum pad is deposited with a extruding thin arm barely connected to the surface of the electrode (**Figure 7.5**(b)). The MgO insulating layer serves to avoid electrical shorting from top electrodes to counter electrodes during the wire-bonding process, and to electrically isolate each micro-electrode. As discussed before (**Chapter 3**), the working electrodes are electrically connected to the impedance spectrometer via wire-bonding the platinum pads to a ceramic chip carrier, which will be subsequently mounted on a tube-furnace-based measurement setup. For such device structures, an equivalent circuit with three characteristic relaxation time constants is used for impedance spectra fitting (**Figure 7.5**(a), **Appendix C**). The elements R_s and Q_s describe the surface reaction process, R_{ion} is the ionic impedance of the cell stack, and the elements

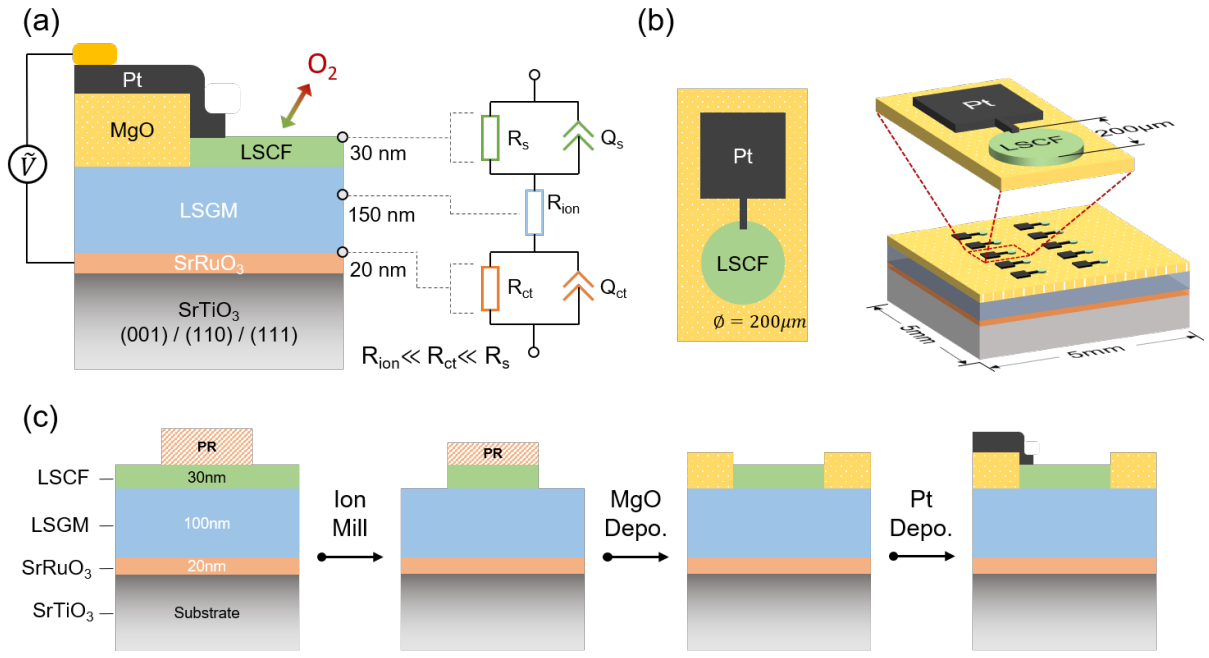

Figure 7.5: *(a) Side view of the half-cell heterostructure. (b) Detailed schematics of the device structure around LSCF working electrodes. (c) Device fabrication process flow involving ion-milling.*

R_{ct} and Q_s describe the charge transfer process near the counter electrode. As discussed above, in a surface process limited reaction, the surface reaction impedance R_s is much larger compared to R_{ion} and R_{ct}, and I will show later that such relationship is valid since the impedance spectra typically have only one dominant "semicircle".

To fabricate the device, two process flows can be used. The first process (**Figure 7.5**(c)) begins after growth of a trilayer heterostructures, wherein a layer of photoresist is spin-coated and then patterned via lithography to a structure with circular openings (200 μm in diameter). The patterned structure is then transferred to an ion-milling chamber which is used to mill away 30 nm of material (LSCF) through the circular openings. After ion-milling step, the heterostructure (with remaining photoresist) is mounted into a deposition chamber and a 200 nm layer of MgO is deposited at room temperature via PLD. After MgO deposition, the photoresist is removed by acetone in a ultrasonicator. Next, another photoresist layer is spin-coated on the heterostructure and patterned for the sputtering of platinum pads with the help of a mask aligner. Lastly, a 100 nm layer of platinum is sputtered on the heterostructure and the remaining photoresist is removed by acetone. Such process has a stringent requirement that the ion-milling step should be relatively precise. If the structure is under-milled, the circular electrodes will be electrically shorted on the surface; while if the structure if over-milled, it is typically found that the LSGM electrolyte starts to become electronically conducting, resulting in a significant measurement inaccuracy regarding the rate of surface reaction. An alternative processing step is suitable in the situation where an accurate ion-milling process is not available. This fabrication flow is similar to the MgO hard-mask process discussed in **Chapter 3** where the top working electrodes are fabricated in an *ex situ* manner after the deposition of a MgO masking layer (**Figure 3.5**(d)). However, the difference is that ZnO is used alternatively as the masking layer so that a base solution (NaOH) can be used for ZnO-etching to avoid potential damages to the underlying LSGM electrolyte if an acid solution is used. After the fabrication of circular working electrodes, a similar step is applied to deposit the MgO insulating layer around the capacitors, and then the platinum contacts are sputtered afterwards.

To quantitatively characterize the surface reaction rate, a gas-exchange-kinetic rate constant (k) is typically used. Under applied bias, the current density of a redox process can be described by the Butler-Volmer equation written as

$$j = j_0 \left[exp\Big(\frac{\alpha|z|F\eta}{RT}\Big) - exp\Big(\frac{-(1-\alpha)|z|F\eta}{RT}\Big) \right] \tag{7.1}$$

where F is the Faraday constant and $|z|$ is the number of charges. When the system is under small AC perturbation with zero DC bias, Taylor expansion of the above equation can be adapted near zero point and is given by

$$\frac{\partial j}{\partial \eta}(\eta \to 0) \approx j_0 \frac{|z|F}{RT} = \frac{|z|^2 F^2 C}{RT} k \tag{7.2}$$

where $j_0 = |z|FCk$ is the exchange current density. Thus, the rate constant k is linearly related to the reciprocal of the surface impedance which can be used as a direct reflection of the reaction rate at the electrode surface.

7.5 Validating the epitaxial half cells

To further confirm the validity of the cell design and the equivalent circuit used for impedance spectra analysis, I used the LSCF/LSGM/SrRuO3/$SrTiO_3$ (111) heterostructures as an example and performed a series experiments to demonstrate that the measurements on gas-exchange kinetics using such epitaxial half-cells are reliable.

First, to examine if the surface reaction is activated at the LSCF electrodes, a control sample was made by capping the LSCF surface with a 100 nm platinum layer as illustrated (**Figure 7.6**(a)). The platinum-capped sample should have limited gas reaction on the surface as the platinum can be essentially treated as a blocking electrode. Although gas adsorption can still happen at the platinum surfaces, the impedance of such a process is expected to be much larger compared to the gas-exchange process on the exposed LSCF surfaces. The comparison reveals that by capping the LSCF surface, the surface reaction impedance is increased by approximately one order of magnitude (**Figure 7.6**(a)), suggesting that the LSCF surface is indeed active during the measurement, and the dominant resistive impedance feature in the Nyquist plots can be assigned to R_s, which describes the rate of the surface-gas-exchange kinetics.

Second, since measuring a leaky thin-film LSGM electrolyte (*i.e.*, that is one that is not electronically insulating) with blocking electrodes (platinum) can also yield a single-semicircle spectrum in a Nyquist plot. As such, I performed experiments on half cells with varying electrolyte thicknesses to rule out such a possibility. Varying the LSGM thickness

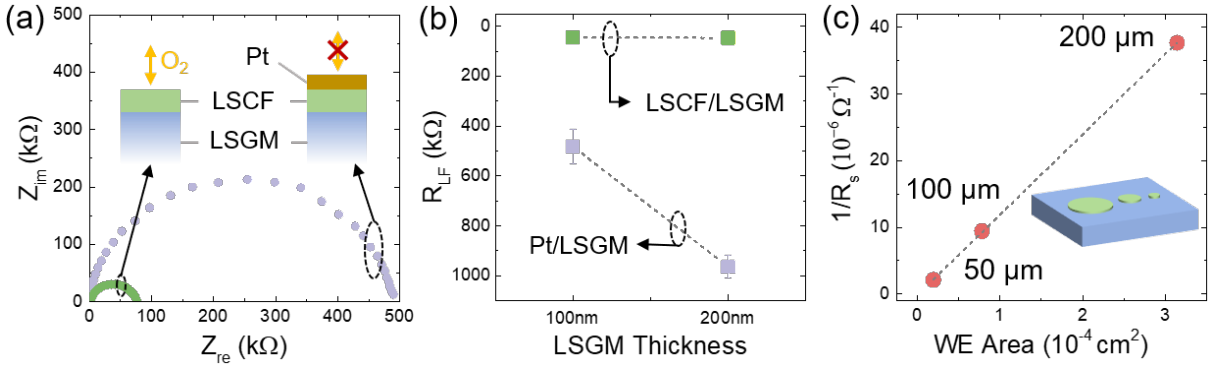

Figure 7.6: *(a) Comparison of impedance spectra of LSCF electrode and LSCF electrode with platinum capping layer. (b) Comparison of impedance spectra of half cells with varied electrolyte (LSGM) thicknesses. (c) Examination of TPB contributions by varying the working-electrode diameters.*

changes the electronic and ionic conduction of the electrolyte at the same time, but the changes in ionic conduction can be neglected due to the extremely small ionic impedance (*i.e.*, just a few Ohms) in such cell design. By comparing half-cells using 100 nm and 200 nm LSGM electrolytes with either LSCF working electrodes (measuring surface reaction) or platinum blocking electrodes (measuring LSGM electrolyte leakage), the half-cells with LSCF working electrodes show no dependency on LSGM thickness while the half-cells with platinum blocking electrodes have strong dependency on LSGM thickness (**Figure 7.6**(b)). These results reveal that the measured responses from the half-cells with LSCF working electrodes are predominantly from surface reactions with limited contribution from electronic leakage of the LSGM electrolyte. It is also worth noting that, at elevated temperatures, the electronic conduction from LSGM increases and will start to affect the accuracy of the surface reaction measurements. Thus, all the measurements are performed around 350°C to reduce the contribution from the electronic conduction of LSGM electrolytes.

Finally, half-cells with different LSCF working electrode areas were examined to rule out the potential contribution from triple-phase boundaries (TPBs). TPBs are regions where the adsorbed gas molecules can get incorporated into the electrolyte lattice much easier. Such phenomena are more significant in cells with porous metallic electrodes where the ionic conductivity of the electrodes is low [276, 277]. However, as given by the results, the linear dependency of the reciprocal of R_s on the electrode areas suggests that the contribution from TPBs in these micro-electrodes can be neglected (**Figure 7.6**(c)), consistent with previous studies using similar electrode geometries [264, 278, 279]. All these preliminary examinations on the epitaxial half cells suggest that, with such measurement geometry, the surface structures can be readily controlled via orientation-controlled growth and the gas exchange kinetics can be reliably extracted.

7.6 Orientation-dependent gas-exchange kinetics

With the validated half-cell geometry, I proceeded to measure the gas-exchange kinetics. The EIS studies on the half-cells with different surface orientations were performed at 350°C in both air and dry oxygen. Representative spectra for three half-cell heterostructures are provided and all three half-cell heterostructures show a single, well-defined semicircle (**Figure 7.7**(a)). This is consistent with the fact that the primary voltage drop takes place at the surface, while the diffusion in the sample is fast. The high-frequency intercepts are on the order of 1 kΩ, likely arising from the contribution of both ionic-transport impedance R_{ion} and the charge transfer impedance R_{ct}. The low-frequency semicircle, as discussed before, reflects the rate of the surface-gas reaction. Fitting the spectra yields R_s and can be further converted into gas-exchange rate constant (k^q) by using

$$k^q = \frac{k_B T}{4e^2 R_s A c_O} \tag{7.3}$$

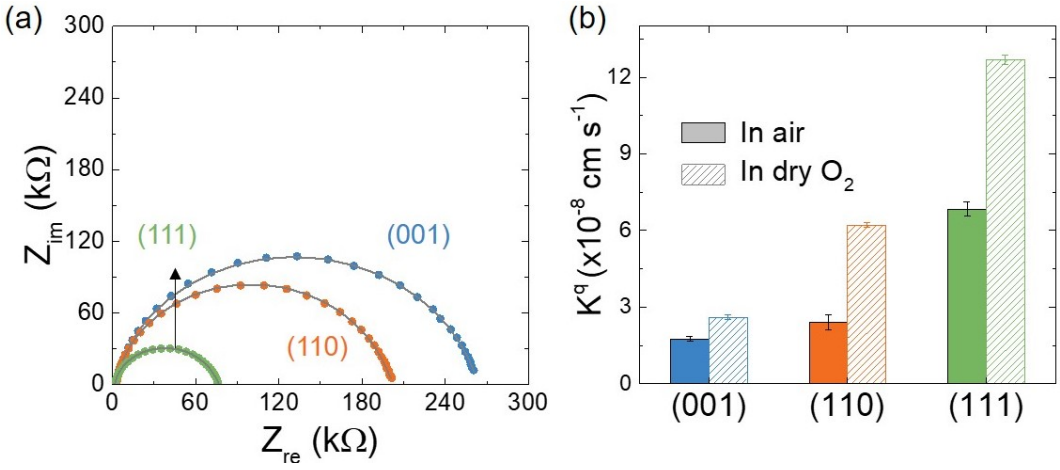

Figure 7.7: *(a) Impedance spectra of the half cells grown along three orientations. (b) The extracted rate constant k^q for three LSCF surfaces.*

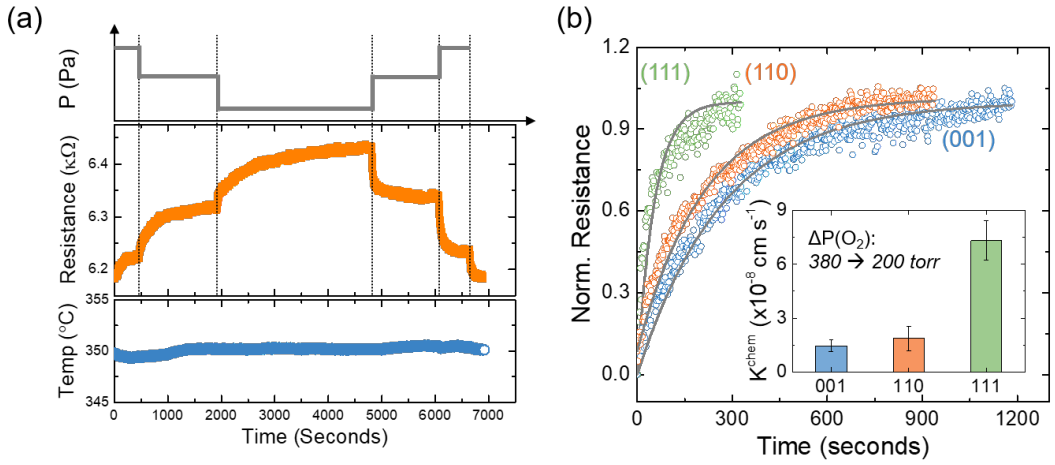

Figure 7.8: *(a) The sequence of a typical electrical conductivity relaxation measurement. (b) Relaxation curve for a pressure change from 380 torr to 200 torr in dry oxygen for LSCF/$SrTiO_3$ (001), (110), and (111).*

where the superscript q indicates such process is under electrical bias, A is the electrode area and c_O is the concentration of oxygen species. The extracted gas-exchange rate constants in air reveal that the (111)-oriented surface variant has a value ∼3-times higher compared to the (001)-oriented surface, with the activity of the (110)-oriented surface in between the two surface variants (**Figure 7.7**(b)). In dry oxygen, the trend holds the same for the three surface variants except for an overall higher reaction rates due to the higher oxygen concentration. The error bars are determined by measuring several devices on two different batches of samples, and the small deviation across samples indicates good consistency and repeatability of the measurements.

In order to further confirm the differences between the gas-reaction kinetics across the three surface variants, electrical conductivity relaxation (ECR) measurements were completed on three 30 nm LSCF/$SrTiO_3$ (001), (110), (111) heterostructures. In a typical ECR measurement setup, the resistance of the sample is constantly monitored at a specific temperature, while the oxygen partial pressure is suddenly changed to induce a chemical potential mismatch at the solid-gas interface [130, 280]. Thus, the gaseous oxygen molecules will exchange with the lattice oxygen, and such exchange induces a stoichiometry change in the material which is directly reflected in the electrical conductivity (**Figure 7.8**(a)). By analyzing the decaying curve of the conductivity (or simply resistance) of the sample, the chemical gas reaction rate constant k^{chem} can be extracted based on

$$\frac{\sigma(t)-\sigma(0)}{\sigma(\infty)-\sigma(0)} = 1 - exp\Big(\frac{k^{chem}t}{a}\Big) \tag{7.4}$$

where a is the sample geometry. This is under the assumption that the surface reaction is the rate limiting step while the bulk diffusion is much faster compared to the surface process. For a sample geometry where a thin layer of LSCF (30 nm) is epitaxially deposited on a $SrTiO_3$ substrate with limited oxygen-vacancy concentration, the oxygen-exchange process in the film can be assumed as a surface-limited process. In addition, since the LSCF is a conductor at high temperature while $SrTiO_3$ substrates are insulating, the measured resistance is mainly from the LSCF layer. The relaxation curves for the three heterostructures are recorded under a sudden oxygen pressure change from 380 torr to 200 torr at 350°C, which is similar to the conditions used in the EIS measurements (**Figure 7.8**(b)). The extracted k^{chem} show a similar trend and magnitude compared to k^q extracted from EIS measurements. With these two measurement results, in turn, we can reach to a conclusion that the surface gas exchange kinetics of perovskite LSCF is strongly correlated with the surface orientations, and (111)-oriented surface variant is the most electrochemically active surface for the oxygen redox reactions.

7.7 Rate-limiting step in the gas exchange reactions

Although a strong surface-orientation dependency is found in gas-exchange kinetics of LSCF, the exact mechanisms giving rise to such correlation are still unclear. Given that the gas reaction is a multi-step process, it is vital to understand what particular rate-limiting steps are in each of the LSCF surface variants. With a known rate-limiting step, one can make further hypotheses regarding the detailed mechanisms that gives rise to the changes in electrochemical activities. Here, I first discuss the potential rate-limiting steps at the solid-gas interface, and then show the experimental approaches to determine the rate-limiting steps in the half-cell heterostructures.

The incorporation of gas-phase oxygen molecules into the solid-phase lattice involves a number of steps (**Figure 7.9**). Briefly, under an applied bias, the gas molecules are attracted to the surface and become adsorbed molecules, then the adsorbed molecules

further dissociate into adsorbed adatoms. In a porous metallic electrode, the adsorbed molecules can diffuse along the surfaces of the electrode and reach to the TPBs for further reactions. In thin-film perovskite electrodes, it is not necessary for the adsorbed atoms to diffuse to the TPBs since perovskites are mixed ionic and electronic conductors with high oxygen-vacancy concentration for reaction to happen, and therefore, such a diffusion process can be neglected in the following discussion. As a neutral adatom is attached to the surface, it can get charged during a charge-transfer process where an electron from the perovskite lattice is transferred to the adatom and attracted to an available vacancy site on the material surface. Eventually, the adatoms diffuse into the vacancy sites and get incorporated into the lattice.

In an electrical measurement, however, the measured impedance is an averaged response from all the reaction steps, and thus it is difficult to know the exact rate of each reaction step. However, if one assumes that one of the reactions is the rate-limiting step and the other steps are relatively fast, the analysis could be greatly simplified, and it becomes possible to derive a quantitative analysis of the reaction pathway. The reason is that, many of the reaction steps are strongly dependent on the thermodynamic activity of the reactants (*i.e.*, oxygen), which can be further correlated to the oxygen-partial pressure near the solid-gas interface. Thus, by examining how the electrical impedance of the half-cells varies as a function of oxygen-partial pressure, it is possible to identify the rate-limiting step in a surface reaction. There have been many proposed rate-limiting steps in literature and a range of oxygen-partial-pressure dependency of gas reaction rate has been calculated and proposed [281–286]. As the derivation and detailed theoretical insights are not the focus of this work, here, I will briefly summarize a few possible rate-limiting steps that could potentially be used to understand our measurement data.

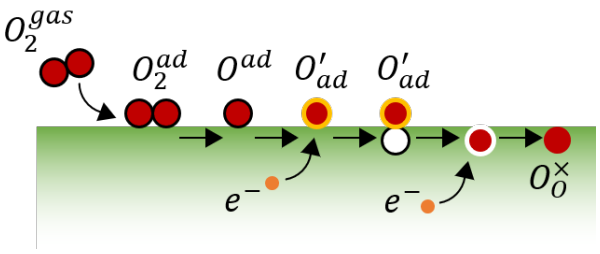

Figure 7.9: *Schematics of the reaction steps in a surface gas exchange process.*

Typically, the relationship between the oxygen partial pressure and the gas reaction rate is described as

$$\frac{1}{R_s} \propto (P_{O_2})^n \tag{7.5}$$

where n is the exponential factor that describe the oxygen-partial-pressure dependency. First, if the oxygen molecules are involved in the rate limiting steps, the reaction can be written as

$$O_2(g) \rightleftharpoons O_{2,ad} \rightleftharpoons 2O_{ad} \tag{7.6}$$

where g refers to gas phase and subscript ad denotes adsorbed atoms. In such scenario, a simple inverse proportionality should be observed, namely $n = 1$. In addition, if only the

atomic oxygen is involved, the exponential factor is expected to be $n = 0.5$. Moreover, if the adsorption of gas molecules is fast, or if the partial pressure is high such that the adsorption is not the rate limiting step, it has been proposed that the charge-transfer step during the incorporation of oxygen adatoms can be the rate-limiting step. In such a process, the reaction after the adsorption can be written as

$$O_{ad} + 2e' + V_O^{\cdot\cdot} \rightleftharpoons O_O^{\times} \tag{7.7}$$

and the exponential factor is calculated to be $n = 0.25$ at high temperature and low pressure, or $n = -0.25$ at low temperature and high pressure. It has also been discussed that if the oxygen vacancy concentration c_{v_O} in the material is not invariant and evolves as the oxygen partial pressure changes, the exponential factor will deviate from 0.25 and is expressed as [287]

$$n = \frac{1}{4} - \frac{1}{2}\frac{\partial \log c_{v_O}}{\partial \log P_{O_2}} \tag{7.8}$$

Now I will turn the focus to perform oxygen-partial-pressure dependent studies on the epitaxial half cells. First, the sheet resistance of 30 nm LSCF/$SrTiO_3$ heterostructures is measured at 350°C from 760 torr to 0.1 torr using a van der Paul four-probe geometry. The results reveal that the sheet resistance of the LSCF films is almost invariant within the pressure region (**Figure 7.10**), indicating that the oxygen-vacancy concentration in the LSCF films is essentially constant. Said another way, within the pressure regime, the available vacancy sites for the reaction to take place hold the same.

Next, the half-cell geometries are mounted in the measurement setup for oxygen-partial-pressure-dependent studies. The pressure control is achieved by a gas regulator while the tube is being constantly pumped via a mechanical pump. Here, the reciprocal of measured Rs and oxygen partial pressure are plotted in logarithmic scale for all three surface variants (**Figure 7.11**). The results reveal a few important observations. First, all the three surface variants show a very similar trend of the surface-reaction impedance as a function of the oxygen-partial pressures. In addition, within the measurement pressure regime, the difference in surface impedance across the three surface variants holds the same. This suggests that the rate-limiting steps for the three surface variants are essentially identical but the rate of the gas-exchange reaction is always faster on the (111)-oriented surface variants. This further indicates that the (111)-oriented surface variants help to reduce the energy barriers for the reactions to move forward. Second, at pressure regime from 760 torr to ∼1 torr, the exponential factor n is fitted to be ∼0.25 for all the three surface variants. As discussed before, this exponential factor value essentially suggests that the charge-transfer process during the incorporation of oxygen adatoms is the rate-limiting step. Such an observation is consistent with the fact that within the higher-pressure regime, the surface coverage of gas molecules is high and will not limit the overall reaction. Moreover, the exponential factor is found to be very close to 0.25, indicating that the oxygen-vacancy concentration should be constant based on Equation 7.8. This agrees well with the observed invariant oxygen vacancy concentration in the LSCF films across

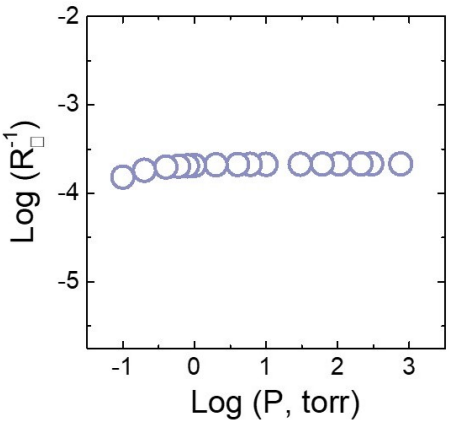

Figure 7.10: *Sheet resistance of 30 nm LSCF films grown on $SrTiO_3$.*

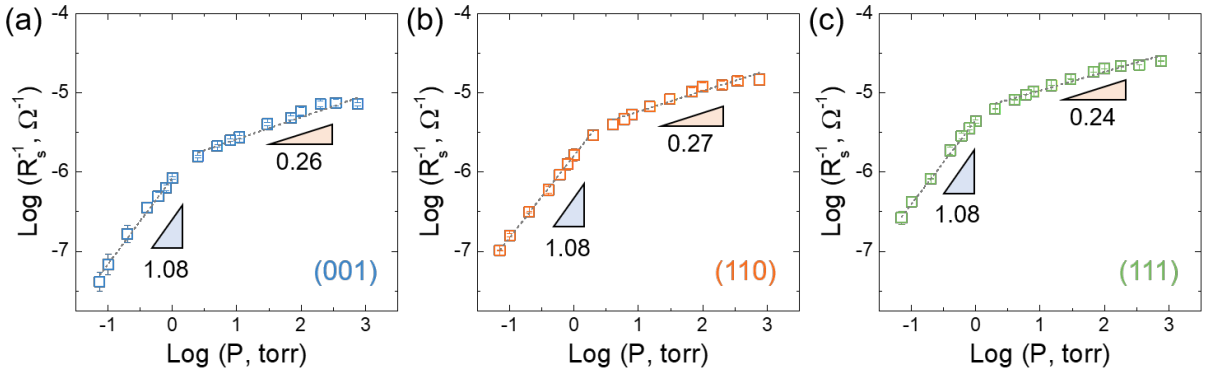

Figure 7.11: *oxygen-partial-pressure dependent studies on three half-cell geometries grown along (a) (001), (b) (110), and (c) (111).*

the entire pressure regime (**Figure 7.10**). And lastly, at pressure regime below $\sim$1 torr, the exponential factor is found to be $n \approx 1$. As discussed above, this is suggesting that the adsorption of the oxygen molecules can be the rate-limiting step in the overall reaction. At low pressure regime, the density of available reaction sites on the surface is higher compared to the coverage of the oxygen molecules, while the (111) surface variant is likely to have higher electron density near the surface such that it is easier for the molecules to get attached to.

7.8 Conclusions and future works

In this chapter, I have examined the effects of surface structures controlled by surface orientation on the electrochemical activity of a model perovskite electrocatalyst LSCF. Three surface variants are achieved by epitaxially growing the LSCF on $SrTiO_3$ (001),

(110), and (111) substrates. Structural and chemical characterization reveal that the three surface variants of LSCF possess similar surface quality and chemistry. To examine the gas exchange kinetics of the three surface variants, an epitaxial half-cell geometry (*i.e.*, LSCF/LSGM/$SrRuO_3$/$SrTiO_3$ (001), (110), and (111)) is developed and validated. The EIS measurements on the half-cell geometries reveal that the (111) surface has an electrochemical activity 3-times higher compared to (001) surface while the (110) surface shows an intermediate activity. By performing the oxygen-partial-pressure dependent studies, the results suggest that the rate-limiting-steps of the surface electrochemical reaction are the adsorption of oxygen molecules (at $P_{O_2} \lesssim 1$ torr) and charge transfer during the incorporation of oxygen adatoms (at $P_{O_2} \gtrsim 1$ torr). This study successfully demonstrated the efficacy of the all-perovskite epitaxial half-cells in the study of surface electrochemical activities, and the advantages of such designs in achieving deterministic structure control for quantifiable structure-property relationship extractions. Moreover, the high electrochemical activity exhibited on the (111) surface provides new insights regarding improving operational efficiency in solid-oxide fuel cells.

Although this study has provided evidences suggesting that the high electrochemical activity on (111) surface is originated from easier adsorption of oxygen molecules and incorporation of oxygen adatoms, the exact mechanism regarding why (111) surface is more energetically favorable for these reactions to happen remains unclear. By the completion of this dissertation, theoretical insights using DFT are still ongoing to examine the electronic structures of the three surface variants, molecule adsorption, and the process of incorporation of oxygen adatoms into the lattice.[2] In addition to the theoretical work, the electronic structure and adsorption of surface species on three LSCF surface variants will also be examined using ambient-pressure XPS at Advanced Light Source, Lawrence Berkeley National Laboratory in the near future.

[2]The ongoing DFT calculations are accomplished in collaboration with Dr. T. Chakraborty and Prof. E. Ertekin at Mechanical Engineering Department at University of Illinois at Urbana-Champaign, IL, USA.

Chapter 8

Summary of findings and suggestions

This chapter serves the purpose of summarizing the key findings and contributions from **Chapter 4** to **Chapter 7** in the understanding of structure-property relationships in perovskite oxide materials. I will also propose a number of future works that can potentially advance our knowledge of such material systems.

8.1 Summary of findings

Chapter 4 — Interfacial octahedral rotation mismatch

Epitaxial strain engineering has long been utilized as an effective approach to control the perovskite structures. Such approach is based on the lattice mismatch between the epitaxial thin films and the underlying substrates. Nevertheless, an additional structural mismatch, so-called octahedral rotation mismatch, can also exist near the film-substrate interface if the epitaxial thin film possesses a different crystal symmetry compared to the substrate. **Chapter 4** focuses on the effects of such octahedral rotation mismatch on properties including lattice symmetry, magnetism, and electrical transport in $SrRuO_3$ thin films. The octahedral mismatch is controlled by the insertion of a low-symmetry $GdScO_3$ buffer layer (*i.e.*, with strong octahedral rotation) between the $SrRuO_3$ films and the $SrTiO_3$ substrates. This study have shown that the octahedral rotation mismatch at the interface can change the lattice symmetry of $SrRuO_3$ from monoclinic to tetragonal under the same epitaxial strain-state. The abnormal rotation pattern observed in tetragonal $SrRuO_3$ indicates a possible decoupling between the internal octahedral rotation and lattice symmetry. And additionally, such symmetry changes are utilized to engineer the magnetic anisotropy and electrical transport properties in $SrRuO_3$.

Chapter 5 — Antisite defects

This chapter primarily explores the control of lattice symmetry and electrical properties in $PbZrO_3$ thin films via growth-mediated antisite defects. The antiferroelectricity in $PbZrO_3$ is originated from the energy competition between the ground-state orthorhombic centrosymmetric phase and the metastable rhombohedral non-centrosymmetric (ferroelectric) phase. Under applied bias, the ferroelectric phase is stabilized, and thus the polarization hysteresis is manifested as a double-ferroelectric loops. In this chapter, I have shown that, such competition between two lattice symmetries can be perturbed and readily controlled via Pb_{Zr} antisite defects. Up to 20% excess lead (could be more, but not covered in this study) can be accommodated by the $PbZrO_3$ lattice as antisite defects without a significant change in lattice parameters. However, the 20%-lead-excess films ($Pb_{1.2}ZrO_3$) have shown robust ferroelectric behavior as revealed by a range of electrical characterization techniques. Lattice symmetry studies via synchrotron-based X-ray and DFT calculations revealed that, with 20%-excess lead as antisite defects, the lattice symmetry can be lifted and the material is stabilized as a ferroelectric rhombohedral *R*3*c* phase.

Chapter 6 — Lattice and octahedral rotation manipulation

The detailed relationships between structural features and ionic transport properties in perovskites are explored in this chapter, and an optimal structure design has been proposed and realized to achieve superior ionic conduction. First, epitaxial strain engineering

is applied on a model perovskite ion-conductor LSGM to control the lattice structure and the corresponding ionic transport properties. It was revealed that, as compared to the zero-strain (or bulk-like) state, compressive strain reduces the unit-cell volume while maintaining large octahedral rotations, resulting in a strong reduction of ionic conductivity, while tensile strain increases the unit-cell volume while quenching octahedral rotations, resulting in a negligible effect on the ionic conductivity. Second, DFT calculation is employed to understand the impacts of different structural features on oxygen vacancy diffusivity. The theoretical studies revealed that, larger unit-cell volumes (lattice expansion) reduce the migration energy barriers, and octahedral rotations serve to create low-energy migration pathways. Thus, an optimal perovskite structure is to contain large unit-cell volume and octahedral rotations at the same time. And lastly, epitaxial strain and interfacial engineering are applied to realize such proposed optimal structure, which resulted in an enhancement of ionic conductivity by a factor or $\sim$2.5. This work presents the first synthesis and characterization of the structural evolution in epitaxially strained LSGM thin films, and the first work to achieve deterministic control over the structural features in perovskite ion conductors using epitaxial strain and interfacial coupling.

Chapter 7 — Surface control via orientation-dependent growth

The previous three chapters mainly focus on the control of lattice structures, while this chapter studies the impacts of surface structure variations on electrochemical properties in perovskites. The model system used for this study is LSCF, which has been widely applied in the solid-oxide fuel cells. The surface structures are controlled by developing a fully epitaxial half-cell geometry where three surface variants are created (*i.e.*, LSCF/LSGM/$SrRuO_3$/$SrTiO_3$ (001), (110), and (111)). Compared to conventional half-cells where fluorite YSZ is used as the electrolyte, the all-perovskite epitaxial half-cells developed in this work has a marked advantage of achieving deterministic control over the electrode structures using epitaxial strain of orientation-control. Characterization on as-grown LSCF surfaces have revealed that all the three surface variants possess similar roughness and surface chemistries. Subsequent electrochemical measurements at 350°C in both air and dry oxygen, however, have revealed a strong surface-orientation dependency of the gas exchange kinetics, where the (111) variants exhibit an electrochemical activity about 3-times higher compared to the (001) variants. The (110) variants have shown an intermediate activity. ECR studies on LSCF/$SrTiO_3$ (001), (110), and (111) heterostructures further confirmed such differences. Oxygen-partial-pressure dependent studies from 760 torr to 0.1 torr are performed to further understand the reaction mechanisms, and have shown that the three surface variants have similar rate-limiting steps across the pressure regime. Specifically, the adsorption of oxygen molecules is suggested to be the rate-limiting step at lower pressure regime ($P_{O_2} \lesssim 1$ torr), while the charge-transfer process could be the rate-limiting step at higher pressure regime ($P_{O_2} \gtrsim 1$ torr). These results have suggested that LSCF (111) surface is energetically favorable for the re-

action to take place and shed light on the engineering of high-efficiency electrode structure on solid-oxide fuel cells.

8.2 Suggestions for future work

Topological magnetic structures in $SrRuO_3$

Recent studies have suggested that novel magnetic skyrmion structures are detected in ultrathin $SrRuO_3$ films by coupling with a ferroelectric layer [288]. The formation of skyrmion structures is indicated by the presence of topological Hall effect features. First, the attribution of the features on Hall measurements to magnetic topological structures is still under debate. It has recently been argued that detailed structural variants in the $SrRuO_3$ films can also give rise to similar features, which cannot be attributed to the formation of magnetic skyrmion [289]. Thus, it is interesting to utilize the learning from **Chapter 4**, control the structural features in $SrRuO_3$ systematically, and examine the contribution of structural variants on the topological features observed in Hall measurements. And second, the proposed mechanism of skyrmion formation is based on Dzyaloshinskii-Moriya interaction (DMI). The required inversion symmetry breaking is achieved via a ferroelectric coupling layer. One may wonder if the ferroelectric layer is the unequivocally needed for the detection of the topological Hall effect features, and what can happen if the crystal symmetry of the coupling layer is changed. And lastly, additional experimental techniques such as X-ray magnetic circular and linear dichroism and Lorentz microscopy can be applied to confirm the magnetic structures in ultrathin $SrRuO_3$.

Explore antisite defects in lead-based relaxors

Lead antisite defects observed in lead-excess $PbZrO_3$ thin films in **Chapter 5** have also been previously suggested to present in ferroic systems such as $Pb(Sc,Ta)O_3$ [191] or $Pb(Zr,Ti)O_3$ [190]. This is largely due to the fact that lead cations have both 2^+ and 4^+ as stable valence states. However, the impact of lead antisite defects on the lattice symmetry, domain structure, switching, dielectric properties in those materials are yet explored. As revealed by synchrotron X-ray diffraction studies (**Figure 5.7**(c)), the introduction of lead antisite defects gave rise to strong diffuse scattering intensities around the quarter-order Bragg peaks. Such diffused intensity is typically a result of the weakly ordered domain structures present in the lattice. This finding is suggesting that, aside from the symmetry change from orthorhombic to rhombohedral, the presence of lead antisite defects also perturbs the long-range ordering and creates nano-size, short-range ordered domain structures. Since the short-range interactions between adjacent nano-domains are critical in determining the switching and dielectric behaviors of a relaxor, it is interesting to study if the incorporation of antisite defects can affect the domain ordering and further engineer the dielectric behaviors in the relaxor ferroelectrics.

Fundamental thickness limit in ionic transport in perovskites

In **Chapter 6** I have studied the correlation between structural features in ionic transport properties in LSGM. To achieve high ionic-conduction, superlattice structures are created by growing ultrathin LSGM coupled with $DyScO_3$ interlayers. Although the goal of understanding the structure-transport coupling is achieved, there still remains a number of open questions. One of the key question to be addressed is the original of an ionic-transport "dead layer" that presents in all superlattice heterostructures. It was found that regardless of the periodicity and repetition of the superlattice structures, there are always 5 unit-cells of LSGM that do not conduct ionic charges. It was hypothesized that such "dead layer" is related to the strontium segregation in the ultrathin LSGM where the high concentration of strontium near the surface greatly impedes the ionic transport. Such hypothesis can be further tested by removing strontium dopants and replace LSGM with $LaGaO_3$ or $La(Ga,Mg)O_3$. If the dead layer still exists, then it will suggest that there is an intrinsic thickness limit for the perovskite structure to transport ionic charges.

In-plane half-cells for electrochemistry studies

To study the surface gas-exchange properties, I developed an epitaxial half-cell geometry in **Chapter 7** for EIS measurements at various temperatures and gas partial pressures. The readers might have noticed that such cell can only be operated at low temperature, namely $\sim$350°C. The reason is that the electrolyte in such geometry is an epitaxial layer of LSGM, which is a mixed ionic and electronic conductor. If the electronic impedance from LSGM is comparable to the surface reaction impedance of LSCF, it will be extremely difficult to differentiate the two contributions based on EIS spectra. Thus, operating the cell at low temperature serves the purpose to reduce and eliminate the contribution from electronic conduction from LSGM. However, since most of the intermediate-temperature solid-oxide fuel cells are operated from 500°C to 700°C, it is necessary to develop a cell geometry that can be used in such temperature regime, while at the same time embraces the advantages of epitaxial control over the electrode surface structures.

One solution to address this problem is to use in-plane half-cell designs. Briefly, one layer of 100-200 nm LSGM is deposited on bare $SrTiO_3$ substrates (or other substrates to introduce epitaxial strain and orientation-control). Working electrodes (*e.g.*, LSCF) are then deposited and patterned into modified IDE geometries. The IDEs should ideally have an optimized finger-spacing that ensures the charge diffusion between the two fingers is fast and negligible compared to the surface reaction process. In addition, compared to regular IDEs that have finger width same as finger spacing, the finger width of the modified IDE is designed to be larger such that sufficient electrode surface area is exposed to gas environment. Since the finger spacing of the in-plane cells is on the order of microns, the electronic leakage from the electrolyte can be significantly reduced.

Studies such as strain effects on surface gas-exchange kinetics can be readily studied in this cell design. And more interestingly, since the electrodes are always exposed to the gas

environment, a DC bias can be applied on the cell to extract more information regarding the electrochemical reactions. Plus, with DC bias, the power out-put of the cell can be extracted and studies such as electrode degradation can be performed.

In situ and *in operando* studies on surface gas kinetics

A custom measurement setup can be designed for *in situ* EIS studies on the well-defined perovskite electrodes with dynamically controlled surface termination, surface structure, surface decoration, and *etc*. The measurement can be setup in a RHEED-assisted PLD chamber, where the growth dynamics and surface structures of the electrodes are constantly monitored by the electron diffraction. The details of the measurements can be described as the following. First, two pieces of electrolyte/substrate (*e.g.*, LSGM/$SrTiO_3$) heterostructures are first synthesized. One piece serves as the monitor sample which will be aligned with RHEED during the measurement, and the other is a measurement sample patterned with MgO mask plus platinum electrodes. The MgO mask defines several in-plane half-cell devices as described in the last section, and the platinum pads (with extruding arms) are used for wire-bonding and to make electrical connections. The MgO mask needs to be sufficiently thick such that the deposition of conducting electrode materials will not short the circuits. In the experiment, two pieces of heterostructures are mounted on a AlN sample holder customized with several defined platinum wire-bonding pads and connection pins for electrical feedthroughs from the chamber wall (careful insulation is required to avoid shorting during the deposition of conducting materials). The measurement sample will be wire-bonded to the sample holder while the monitor sample will be mounted next to the measurement sample for surface characterization. The whole sample holder is mounted on the PLD heater, and routine PLD growth can be performed. By monitoring the RHEED pattern of the monitor sample, EIS spectra can be taken on the measurement sample at the same time to understand how a specific surface structure/chemistry affects the electrochemical reaction.

In operando studies can also be performed for surface XPS studies in the synchrotron-based ambient-pressure XPS setup. The surface electronic structure and surface gas adsorption can be continuously monitored while a DC bias is swept across. The in-plane half-cell geometry can be used for such purpose.

Novel strain engineering of perovskite electrodes

Strain gradient has been shown to have prominent impact on lattice and domain structures on ferroic materials [12], and similar idea can be applied in the engineering of electrochemical properties of perovskite materials. One motivation to perform such study is to explore the possibility of suppressing strontium segregation in the materials and extend the life-time of the cathodes in solid-oxide fuel cells. It has previously been shown that the strontium segregation is largely mediated by epitaxial strain, where tensile strain promotes surface strontium segregation while compressive strain reduces segregation [290]. Thus,

if a sharp strain gradient can be created in the thin-film electrode material where the stain state is tensile at film-substrate interface and compressive at film-gas interface, the strain gradient is expected to drive the strontium away from the surface into the lattice. The strain gradient can be employed by chemically gradient two electrode materials with different lattice parameters, and one potential material combination can be $La_{0.5}Sr_{0.5}CoO_{3-\delta}$ (LSCO, a=3.84Å) and $La_{0.8}Sr_{0.2}Co_{0.2}Fe_{0.8}O_{3-\delta}$ (LSCF, a=3.901Å). If one creates a chemical gradient from LSCO to LSCF on a $SrTiO_3$ substrate (a=3.905Å), a strain gradient from tensile to compressive will simultaneously be induced in the lattice.

References

1. Von Hippel, A., Breckenridge, R. G., Chesley, F. G. & Tisza, L. High dielectric constant ceramics. *Ind. Eng. Chem.* **38,** 1097–1109 (1946).
2. Koster, G. *et al.* Structure, physical properties, and applications of $SrRuO_3$ thin films. *Rev. Mod. Phys.* **84,** 253–298 (2012).
3. Moussa, F. *et al.* Spin waves in the antiferromagnet perovskite $LaMnO_3$: A neutron-scattering study. *Phys. Rev. B* **54,** 15149–15155 (1996).
4. Catalan, G. & Scott, J. F. Physics and applications of bismuth ferrite. *Adv. Mater.* **21,** 2463–2485 (2009).
5. Wu, M. K. *et al.* Superconductivity at 93 K in a new mixed-phase Y-Ba-Cu-O compound system at ambient pressure. *Phys. Rev. Lett.* **58,** 908–910 (1987).
6. Suntivich, J., May, K. J., Gasteiger, H. A., Goodenough, J. B. & Shao-Horn, Y. A perovskite oxide optimized for oxygen evolution catalysis from molecular orbital principles. *Science* **334,** 1383–1385 (2011).
7. Liao, Z. *et al.* Controlled lateral anisotropy in correlated manganite heterostructures by interface-engineered oxygen octahedral coupling. *Nat. Mater.* **15,** 425–431 (2016).
8. Choi, K. J. *et al.* Enhancement of ferroelectricity in strained $BaTiO_3$ thin films. *Science* **306,** 1005–1009 (2004).
9. Xu, R. *et al.* Reducing coercive-field scaling in ferroelectric thin films *via* orientation control. *ACS Nano* **12,** 4736–4743 (2018).
10. Xu, R. *et al.* Kinetic control of tunable multi-state switching in ferroelectric thin films. *Nat. Commun.* **10,** 1282 (2019).
11. Mangalam, R. V. K., Karthik, J., Damodaran, A. R., Agar, J. C. & Martin, L. W. Unexpected crystal and domain structures and properties in compositionally graded $PbZr_{1-x}Ti_xO_3$ thin films. *Adv. Mater.* **25,** 1761–1767 (2013).
12. Agar, J. C. *et al.* Highly mobile ferroelastic domain walls in compositionally graded ferroelectric thin films. *Nat. Mater.* **15,** 549–556 (2016).
13. Liu, J. *et al.* Strain-mediated metal-insulator transition in epitaxial ultrathin films of $NdNiO_3$. *Appl. Phys. Lett.* **96,** 233110 (2010).

14. Liao, Z. *et al.* Metal-insulator-transition engineering by modulation tilt-control in perovskite nickelates for room temperature optical switching. *Proc. Natl. Acad. Sci. U. S. A.* **115,** 9515–9520 (2018).

15. Breckenfeld, E., Chen, Z., Damodaran, A. R. & Martin, L. W. Effects of nonequilibrium growth, nonstoichiometry, and film orientation on the metal-to-insulator transition in $NdNiO_3$ thin films. *ACS Appl. Mater. Interfaces* **6,** 22436–22444 (2014).

16. Kushima, A. & Yildiz, B. Oxygen ion diffusivity in strained yttria stabilized zirconia: where is the fastest strain? *J. Mater. Chem.* **20,** 4809 (2010).

17. Kubicek, M. *et al.* Tensile lattice strain accelerates oxygen surface exchange and diffusion in $La_{1-x}Sr_xCoO_{3-\delta}$ thin films. *ACS Nano* **7,** 3276–3286 (2013).

18. Cohen, R. E. Origin of ferroelectricity in perovskite oxides. *Nature* **358,** 136–138 (1992).

19. Hwang, H. Y. *et al.* Emergent phenomena at oxide interfaces. *Nat. Mater.* **11,** 103–113 (2012).

20. Goldschmidt, V. M. Die gesetze der krystallochemie. *Naturwissenschaften* **14,** 477–485 (1926).

21. Jahn, H. A. & Teller, E. Stability of polyatomic molecules in degenerate electronic states - I — Orbital degeneracy. *Proc. R. Soc. London. Ser. A - Math. Phys. Sci.* **161,** 220–235 (1937).

22. Tsuda, K. & Tanaka, M. Refinement of crystal structure parameters using convergent-beam electron diffraction: the low-temperature phase of $SrTiO_3$. *Acta Crystallogr. Sect. A Found. Crystallogr.* **51,** 7–19 (1995).

23. Vasylechko, L., Matkovskii, A., Savytskii, D., Suchocki, A. & Wallrafen, F. Crystal structure of $GdFeO_3$-type rare earth gallates and aluminates. *J. Alloys Compd.* **291,** 57–65 (Sept. 1999).

24. Huijben, M. *et al.* Structure-property relation of $SrTiO_3/LaAlO_3$ interfaces. *Adv. Mater.* **21,** 1665–1677 (2009).

25. Schlom, D. G. *et al.* Strain tuning of ferroelectric thin films. *Annu. Rev. Mater. Res.* **37,** 589–626 (2007).

26. Schlom, D. G., Chen, L.-Q., Pan, X., Schmehl, A. & Zurbuchen, M. A. A thin film approach to engineering functionality into oxides. *J. Am. Ceram. Soc.* **91,** 2429–2454 (2008).

27. Martin, L. W. *et al.* Multiferroics and magnetoelectrics: thin films and nanostructures. *J. Phys. Condens. Matter* **20,** 434220 (2008).

28. Karthik, J., Damodaran, A. R. & Martin, L. W. Effect of 90° domain walls on the low-field permittivity of $PbZr_{0.2}Ti_{0.8}O_3$ thin films. *Phys. Rev. Lett.* **108,** 167601 (2012).

29. Zeches, R. J. *et al.* A strain-driven morphotropic phase boundary in $BiFeO_3$. *Science* **326,** 977–80 (2009).

30. Damodaran, A. R. *et al.* Nanoscale structure and mechanism for enhanced electromechanical response of highly strained $BiFeO_3$ thin films. *Adv. Mater.* **23,** 3170–3175 (2011).

31. Chu, Y.-H., Martin, L. W., Holcomb, M. B. & Ramesh, R. Controlling magnetism with multiferroics. *Mater. Today* **10,** 16–23 (2007).

32. Rondinelli, J. M. & Spaldin, N. A. Substrate coherency driven octahedral rotations in perovskite oxide films. *Phys. Rev. B - Condens. Matter Mater. Phys.* **82,** 113402 (2010).

33. Rondinelli, J. M. & Spaldin, N. A. Structure and properties of functional oxide thin films: Insights from electronic-structure calculations. *Adv. Mater.* **23,** 3363–3381 (2011).

34. Gao, R. *et al.* Interfacial octahedral rotation mismatch control of the symmetry and properties of $SrRuO_3$. *ACS Appl. Mater. Interfaces* **8,** 14871–14878 (2016).

35. Aso, R., Kan, D., Shimakawa, Y. & Kurata, H. Atomic level observation of octahedral distortions at the perovskite oxide heterointerface. *Sci. Rep.* **3,** 2214 (2013).

36. He, J., Borisevich, A., Kalinin, S. V., Pennycook, S. J. & Pantelides, S. T. Control of octahedral tilts and magnetic properties of perovskite oxide heterostructures by substrate symmetry. *Phys. Rev. Lett.* **105** (2010).

37. Yuan, Y. *et al.* Three-dimensional atomic scale electron density reconstruction of octahedral tilt epitaxy in functional perovskites. *Nat. Commun.* **9,** 5220 (2018).

38. Feng, Z. *et al.* Catalytic ativity and stability of oxides: The role of near-surface atomic structures and compositions. *Acc. Chem. Res.* **49,** 966–973 (2016).

39. Chen, P. *et al.* Optical properties of quasi-tetragonal $BiFeO_3$ thin films. *Appl. Phys. Lett.* **96,** 131907 (2010).

40. Christen, H. M., Nam, J. H., Kim, H. S., Hatt, A. J. & Spaldin, N. A. Stress-induced R-M_A-M_C-T symmetry changes in $BiFeO_3$ films. *Phys. Rev. B* **83,** 144107 (2011).

41. Freund, L. B. & Suresh, S. (*Thin film materials: stress, defect formation, and surface evolution* 750 (Cambridge University Press, 2003).

42. Griffith, A. A. The phenomena of rupture and flow in solids. *Philos. Trans. R. Soc. A Math. Phys. Eng. Sci.* **221,** 163–198 (1921).

43. Gibert, M., Zubko, P., Scherwitzl, R., Íñiguez, J. & Triscone, J.-M. Exchange bias in $LaNiO_3$-$LaMnO_3$ superlattices. *Nat. Mater.* **11,** 195–198 (2012).

44. Hallsteinsen, I. *et al.* Crystalline symmetry controlled magnetic switching in epitaxial (111) $La_{0.7}Sr_{0.3}MnO_3$ thin films. *APL Mater.* **3,** 062501 (2015).

45. Piamonteze, C. *et al.* Interfacial properties of $LaMnO_3/LaNiO_3$ superlattices grown along (001) and (111) orientations. *Phys. Rev. B* **92,** 014426 (2015).

46. Rondinelli, J. M., May, S. J. & Freeland, J. W. Control of octahedral connectivity in perovskite oxide heterostructures: An emerging route to multifunctional materials discovery. *MRS Bull.* **37,** 261–270 (2012).

47. Sherman, A. *Chemical vapor deposition for microelectronics: principles, technology, and applications* 215 (Noyes Publications, 1987).

48. Mahan, J. E. *Physical vapor deposition of thin films* 312 (Wiley, 2000).

49. Martin, L., Chu, Y.-H. & Ramesh, R. Advances in the growth and characterization of magnetic, ferroelectric, and multiferroic oxide thin films. *Mater. Sci. Eng. R Reports* **68,** 89–133 (2010).

50. Martin, L. W. & Schlom, D. G. Advanced synthesis techniques and routes to new single-phase multiferroics. *Curr. Opin. Solid State Mater. Sci.* **16,** 199–215 (2012).

51. Eason, R. *Pulsed laser deposition of thin films: applications-led growth of functional materials* (John Wiley & Sons, Ltd, Hoboken, NJ, USA, 2006).

52. Moyer, J. A., Gao, R., Schiffer, P. & Martin, L. W. Epitaxial growth of highly-crystalline spinel ferrite thin films on perovskite substrates for all-oxide devices. *Sci. Rep.* **5,** 10363 (2015).

53. Zhang, H.-T., Dedon, L. R., Martin, L. W. & Engel-Herbert, R. Self-regulated growth of $LaVO_3$ thin films by hybrid molecular beam epitaxy. *Appl. Phys. Lett.* **106,** 233102 (2015).

54. Breckenfeld, E. *et al.* Effect of growth induced (non)stoichiometry on interfacial conductance in $LaAlO_3/SrTiO_3$. *Phys. Rev. Lett.* **110,** 196804 (2013).

55. Breckenfeld, E., Bronn, N., Mason, N. & Martin, L. W. Tunability of conduction at the $LaAlO_3/SrTiO_3$ heterointerface: Thickness and compositional studies. *Appl. Phys. Lett.* **105,** 121610 (2014).

56. Lee, S. *et al.* A Novel, layered phase in Ti-Rich $SrTiO_3$ epitaxial thin films. *Adv. Mater.* **27,** 861–868 (2015).

57. Brune, H. in *Surf. Interface Sci.* 421–492 (Wiley-VCH Verlag GmbH & Co. KGaA, Weinheim, Germany, 2014).

58. Bales, G. S. & Chrzan, D. C. Dynamics of irreversible island growth during submonolayer epitaxy. *Phys. Rev. B* **50,** 6057–6067 (1994).

59. Choi, J., Eom, C. B., Rijnders, G., Rogalla, H. & Blank, D. H. A. Growth mode transition from layer by layer to step flow during the growth of heteroepitaxial $SrRuO_3$ on (001) $SrTiO_3$. *Appl. Phys. Lett.* **79,** 1447–1449 (2001).

60. Gao, R. *et al.* Ferroelectricity in $Pb_{1+\delta}ZrO_3$ thin films. *Chem. Mater.* **29,** 6544–6551 (2017).

61. Klein, J. *Epitaktische heterostrukturen aus dotierten manganaten* PhD thesis (Universität zu Köln, 2001).

62. Rijnders, G., Blank, D. H. A., Choi, J. & Eom, C.-B. Enhanced surface diffusion through termination conversion during epitaxial $SrRuO_3$ growth. *Appl. Phys. Lett.* **84,** 505–507 (2004).

63. Naito, M. & Sato, H. Reflection high-energy electron diffraction study on the $SrTiO_3$ surface structure. *Phys. C Supercond.* **229,** 1–11 (1994).

64. Glazer, A. M. The classification of tilted octahedra in perovskites. *Acta Crystallogr. Sect. B Struct. Crystallogr. Cryst. Chem.* **28,** 3384–3392 (1972).

65. Glazer, A. M. Simple ways of determining perovskite structures. *Acta Crystallogr. Sect. A* **31,** 756–762 (1975).

66. Veličkov, B., Kahlenberg, V., Bertram, R. & Bernhagen, M. Crystal chemistry of $GdScO_3$, $DyScO_3$ $SmScO_3$ and $NdScO_3$. *Zeitschrift für Krist.* **222,** 466–473 (2007).

67. Hattab, H., Jnawali, G. & Horn-von Hoegen, M. In-situ high-resolution low energy electron diffraction study of strain relaxation in heteroepitaxy of Bi(111) on Si(001): Interplay of strain state, misfit dislocation array and lattice parameter. *Thin Solid Films* **570,** 159–163 (2014).

68. Vailionis, A. *et al.* Misfit strain accommodation in epitaxial ABO_3 perovskites: Lattice rotations and lattice modulations. *Phys. Rev. B - Condens. Matter Mater. Phys.* **83,** 064101 (2011).

69. Chen, Z. *et al.* Low-symmetry monoclinic phases and polarization rotation path mediated by epitaxial strain in multiferroic $BiFeO_3$ thin films. *Adv. Funct. Mater.* **21,** 133–138 (2011).

70. Hatt, A. J. & Spaldin, N. A. Structural phases of strained $LaAlO_3$ driven by octahedral tilt instabilities. *Phys. Rev. B* **82,** 195402 (2010).

71. Torrance, J., Lacorre, P., Nazzal, A., Ansaldo, E. & Niedermayer, C. Systematic study of insulator-metal transitions in perovskites $RNiO_3$ (R=Pr, Nd, Sm, Eu) due to closing of charge-transfer gap. *Phys. Rev. B* **45,** 8209–8212 (1992).

72. Navarro, J. *et al.* Antisite defects and magnetoresistance in Sr_2FeMoO_6 double perovskite. *J. Phys. Condens. Matter* **13,** 8481–8488 (2001).

73. Benedek, N. A., Mulder, A. T. & Fennie, C. J. Polar octahedral rotations: A path to new multifunctional materials. *J. Solid State Chem.* **195,** 11–20 (2012).

74. Dvošák, V. Improper ferroelectrics. *Ferroelectrics* **7,** 1–9 (1974).

75. Bousquet, E. *et al.* Improper ferroelectricity in perovskite oxide artificial superlattices. *Nature* **452,** 732–736 (2008).

76. Stengel, M., Fennie, C. J. & Ghosez, P. Electrical properties of improper ferroelectrics from first principles. *Phys. Rev. B* **86,** 094112 (2012).

77. Rondinelli, J. M. & Fennie, C. J. Octahedral rotation-induced ferroelectricity in cation ordered perovskites. *Adv. Mater.* **24,** 1961–1968 (2012).

78. Oh, Y. S., Luo, X., Huang, F.-T., Wang, Y. & Cheong, S.-W. Experimental demonstration of hybrid improper ferroelectricity and the presence of abundant charged walls in $(Ca,Sr)_3Ti_2O_7$ crystals. *Nat. Mater.* **14,** 407–413 (2015).

79. Ohtomo, A. & Hwang, H. Y. A high-mobility electron gas at the $LaAlO_3/SrTiO_3$ heterointerface. *Nature* **427,** 423–426 (2004).

80. Chen, Z. *et al.* Electron accumulation and emergent magnetism in $LaMnO_3/SrTiO_3$ heterostructures. *Phys. Rev. Lett.* **119,** 156801 (2017).

81. Sata, N., Eberman, K., Eberl, K. & Maier, J. Mesoscopic fast ion conduction in nanometre-scale planar heterostructures. *Nature* **408,** 946–949 (2000).

82. Kim, T. H. *et al.* Polar metals by geometric design. *Nature* **533,** 68–72 (2016).

83. Cao, Y. *et al.* Artificial two-dimensional polar metal at room temperature. *Nat. Commun.* **9,** 1547 (2018).

84. May, S. J. *et al.* Control of octahedral rotations in $(LaNiO_3)_n/(SrMnO_3)_m$ superlattices. *Phys. Rev. B - Condens. Matter Mater. Phys.* **83,** 153411 (2011).

85. Chen, Z. H., Damodaran, A. R., Xu, R., Lee, S. & Martin, L. W. Effect of "symmetry mismatch" on the domain structure of rhombohedral $BiFeO_3$ thin films. *Appl. Phys. Lett.* **104,** 182908 (2014).

86. Aso, R., Kan, D., Shimakawa, Y. & Kurata, H. Control of structural distortions in transition-metal oxide films through oxygen displacement at the heterointerface. *Adv. Funct. Mater.* **24,** 5177–5184 (2014).

87. Stoerzinger, K. A., Qiao, L., Biegalski, M. D. & Shao-Horn, Y. Orientation-dependent oxygen evolution activities of rutile IrO_2 and RuO_2. *J. Phys. Chem. Lett.* **5,** 1636–1641 (2014).

88. Chang, S. H. *et al.* Functional links between stability and reactivity of strontium ruthenate single crystals during oxygen evolution. *Nat. Commun.* **5,** 4191 (2014).

89. Tasker, P. W. The stability of ionic crystal surfaces. *J. Phys. C Solid State Phys.* **12,** 4977–4984 (1979).

90. Goniakowski, J., Finocchi, F. & Noguera, C. Polarity of oxide surfaces and nanostructures. *Reports Prog. Phys.* **71,** 016501 (2008).

91. Pojani, A., Finocchi, F. & Noguera, C. Polarity on the $SrTiO_3$ (111) and (110) surfaces. *Surf. Sci.* **442,** 179–198 (1999).

92. Rödel, T. C. *et al.* Orientational tuning of the Fermi sea of confined electrons at the $SrTiO_3$ (110) and (111) surfaces. *Phys. Rev. Appl.* **1,** 051002 (2014).

93. Kubo, T. & Nozoye, H. Surface structure of $SrTiO_3$ (100). *Surf. Sci.* **542,** 177–191 (2003).

94. Jiang, Q. & Zegenhagen, J. c(6×2) and c(4×2) reconstruction of $SrTiO_3$ (001). *Surf. Sci.* **425,** 343–354 (1999).

95. Erdman, N. *et al.* The structure and chemistry of the TiO_2-rich surface of $SrTiO_3$ (001). *Nature* **419,** 55–58 (2002).

96. Kawasaki, M. *et al.* Atomic control of the $SrTiO_3$ crystal surface. *Science* **266,** 1540–2 (1994).

97. Stoerzinger, K. A. *et al.* Influence of $LaFeO_3$ surface termination on water reactivity. *J. Phys. Chem. Lett.* **8,** 1038–1043 (2017).

98. Jung, W. & Tuller, H. L. Investigation of surface Sr segregation in model thin film solid oxidefuel cell perovskite electrodes. *Energy Environ. Sci.* **5,** 5370–5378 (2012).

99. Druce, J. *et al.* Surface termination and subsurface restructuring of perovskite-based solid oxide electrode materials. *Energy Environ. Sci.* **7,** 3593–3599 (2014).

100. Marković, N., Adić, R. & Vešović, V. Structural effects in electrocatalysis: Oxygen reduction on the gold single crystal electrodes with (110) and (111) orientations. *J. Electroanal. Chem. Interfacial Electrochem.* **165,** 121–133 (1984).

101. Marković, N., Grgur, B. N. & Ross, P. N. Temperature-dependent hydrogen electrochemistry on platinum low-index single-crystal surfaces in acid solutions. *J. Phys. Chem. B* **101,** 5405–5413 (1997).

102. Norskov, J. K. *et al.* Toward efficient hydrogen production at surfaces. *Science* **312,** 1322–1323 (2006).

103. Yang, Y.-Y. & Sun, S.-G. Effects of Sb adatoms on kinetics of electrocatalytic oxidation of HCOOH at Sb-modified Pt(100), Pt(111), Pt(110), Pt(320), and Pt(331) surfaces: An energetic modeling and quantitative analysis. *J. Phys. Chem. B* **106,** 12499–12507 (2002).

104. Cui, C., Gan, L., Heggen, M., Rudi, S. & Strasser, P. Compositional segregation in shaped Pt alloy nanoparticles and their structural behaviour during electrocatalysis. *Nat. Mater.* **12,** 765–771 (2013).

105. Gu, Z. & Balbuena, P. B. Absorption of atomic oxygen into subsurfaces of Pt(100) and Pt(111): Density functional theory study. *J. Phys. Chem. C* **111,** 9877–9883 (2007).

106. Miseki, Y., Kato, H. & Kudo, A. Water splitting into H_2 and O_2 over niobate and titanate photocatalysts with (111) plane-type layered perovskite structure. *Energy Environ. Sci.* **2,** 306 (2009).

107. May, S. J. *et al.* Quantifying octahedral rotations in strained perovskite oxide films. *Phys. Rev. B - Condens. Matter Mater. Phys.* **82,** 014110 (2010).

108. Souza-Neto, N. M., Ramos, A. Y., Tolentino, H. C. N., Favre-Nicolin, E. & Ranno, L. Local tetragonal distortion in $La_{0.7}Sr_{0.3}MnO_3$ strained thin films probed by X-ray absorption spectroscopy. *Phys. Rev. B* **70,** 174451 (2004).

109. Miniotas, A., Vailionis, A., Svedberg, E. B. & Karlsson, U. O. Misfit strain induced lattice distortions in heteroepitaxially grown $La_xCa_{1-x}MnO_3$ thin films studied by extended X-ray absorption fine structure and high-resolution X-ray diffraction. *J. Appl. Phys.* **89,** 2134–2137 (2001).

110. Fong, D. D. *et al.* Direct structural determination in ultrathin ferroelectric films by analysis of synchrotron X-ray scattering measurements. *Phys. Rev. B* **71,** 144112 (2005).

111. Herger, R. *et al.* Structure determination of monolayer-by-monolayer grown $La_{1-x}Sr_x$-MnO_3 thin films and the onset of magnetoresistance. *Phys. Rev. B* **77,** 085401 (2008).

112. Woodward, P. M. Octahedral tilting in perovskites. I. Geometrical considerations. *Acta Crystallogr. Sect. B Struct. Sci.* **53,** 32–43 (1997).

113. Yacoby, Y. *et al.* Direct determination of epitaxial film and interface structure: Gd_2O_3 on GaAs (100). *Phys. B Condens. Matter* **336,** 39–45 (2003).

114. Fister, T. T. *et al.* Octahedral rotations in strained $LaAlO_3/SrTiO_3$ (001) heterostructures. *APL Mater.* **2,** 021102 (2014).

115. Van der Pauw, L. J. A method of measuring specific resistivity and Hall effect of discs of aribtrary shape. *Philips Res. Reports* **13,** 1–9 (1958).

116. Karthik, J., Damodaran, A. R. & Martin, L. W. Epitaxial ferroelectric heterostructures fabricated by selective area epitaxy of $SrRuO_3$ Using an MgO mask. *Adv. Mater.* **24,** 1610–1615 (2012).

117. Stancu, A., Ricinschi, D., Mitoseriu, L., Postolache, P. & Okuyama, M. First-order reversal curves diagrams for the characterization of ferroelectric switching. *Appl. Phys. Lett.* **83,** 3767–3769 (2003).

118. Saremi, S. *et al.* Enhanced electrical resistivity and properties via ion bombardment of ferroelectric thin films. *Adv. Mater.* **28,** 10750–10756 (2016).

119. Saremi, S. *et al.* Local control of defects and switching properties in ferroelectric thin films. *Phys. Rev. Mater.* **2,** 084414 (2018).

120. Saremi, S. *et al.* Electronic transport and ferroelectric switching in ion-bombarded, defect-engineered $BiFeO_3$ thin films. *Adv. Mater. Interfaces* **5,** 1700991 (2018).

121. Kilner, J., Steele, B. & Ilkov, L. Oxygen self-diffusion studies using negative-ion secondary ion mass spectrometry (SIMS). *Solid State Ionics* **12,** 89–97 (1984).

122. De Souza, R. & Kilner, J. Oxygen transport in $La_{1-x}Sr_xMn_{1-y}Co_yO_{3\pm\delta}$ perovskites: Part I. Oxygen tracer diffusion. *Solid State Ionics* **106,** 175–187 (1998).

123. Ruiz-Trejo, E., Sirman, J., Baikov, Y. & Kilner, J. Oxygen ion diffusivity, surface exchange and ionic conductivity in single crystal Gadolinia doped Ceria. *Solid State Ionics* **113-115,** 565–569 (1998).

124. Riess, I. Four point Hebb-Wagner polarization method for determining the electronic conductivity in mixed ionic-electronic conductors. *Solid State Ionics* **51,** 219–229 (1992).

125. Riess, I. Review of the limitation of the Hebb-Wagner polarization method for measuring partial conductivities in mixed ionic electronic conductors. *Solid State Ionics* **91,** 221–232 (1996).

126. Shimonosono, T. *et al.* Electronic conductivity measurement of Sm- and La-doped ceria ceramics by Hebb-Wagner method. *Solid State Ionics* **174,** 27–33 (2004).

127. Chang, B.-Y. & Park, S.-M. Electrochemical impedance spectroscopy. *Annu. Rev. Anal. Chem.* **3,** 207–229 (2010).

128. Lasia, A. in *Mod. Asp. Electrochem.* 143–248 (Boston, 2002).

129. Rivera, A., Santamaria, J. & León, C. Electrical conductivity relaxation in thin-film yttria-stabilized zirconia. *Appl. Phys. Lett.* **78,** 610–612 (2001).

130. Lane, J. & Kilner, J. Measuring oxygen diffusion and oxygen surface exchange by conductivity relaxation. *Solid State Ionics* **136-137,** 997–1001 (2000).

131. Li, Y., Gerdes, K., Horita, T. & Liu, X. Surface exchange and bulk diffusivity of LSCF as SOFC cathode: Electrical conductivity relaxation and isotope exchange characterizations. *J. Electrochem. Soc.* **160,** F343–F350 (2013).

132. Gopal, C. B. & Haile, S. M. An electrical conductivity relaxation study of oxygen transport in samarium doped ceria. *J. Mater. Chem. A* **2,** 2405–2417 (2014).

133. Mackenzie, A. P. *et al.* Observation of quantum oscillations in the electrical resistivity of $SrRuO_3$. *Phys. Rev. B* **58,** R13318–R13321 (1998).

134. Klein, L. *et al.* Anomalous spin scattering effects in the badly metallic itinerant ferromagnet $SrRuO_3$. *Phys. Rev. Lett.* **77,** 2774–2777 (1996).

135. Jones, C. W., Battle, P. D., Lightfoot, P. & Harrison, W. T. A. The structure of $SrRuO_3$ by time-of-flight neutron powder diffraction. *Acta Crystallogr. Sect. C Cryst. Struct. Commun.* **45,** 365–367 (1989).

136. Zayak, A. T., Huang, X., Neaton, J. B. & Rabe, K. M. Structural, electronic, and magnetic properties of $SrRuO_3$ under epitaxial strain. *Phys. Rev. B* **74,** 094104 (2006).

137. Kolesnik, S. *et al.* Effect of crystalline quality and substitution on magnetic anisotropy of $SrRuO_3$ thin films. *J. Appl. Phys.* **99,** 08F501 (2006).

138. Yoo, Y. Z. *et al.* Diverse effects of two-dimensional and step flow growth mode induced microstructures on the magnetic anisotropies of $SrRuO_3$ thin films. *Appl. Phys. Lett.* **89,** 124104 (2006).

139. Gan, Q., Rao, R. A., Eom, C. B., Garrett, J. L. & Lee, M. Direct measurement of strain effects on magnetic and electrical properties of epitaxial $SrRuO_3$ thin films. *Appl. Phys. Lett.* **72,** 978–980 (1998).

140. Grutter, A. J. *et al.* Stabilization of spin-zero Ru 4^+ through epitaxial strain in $SrRuO_3$ thin films. *Phys. Rev. B* **88,** 214410 (2013).

141. Kan, D., Aso, R., Kurata, H. & Shimakawa, Y. Epitaxial strain effect in tetragonal $SrRuO_3$ thin films. *J. Appl. Phys.* **113,** 173912 (2013).

142. Vailionis, A., Siemons, W. & Koster, G. Room temperature epitaxial stabilization of a tetragonal phase in $ARuO_3$ (A=Ca and Sr) thin films. *Appl. Phys. Lett.* **93,** 051909 (2008).

143. Chakoumakos, B. C., Schlom, D. G., Urbanik, M. & Luine, J. Thermal expansion of $LaAlO_3$ and (La,Sr)(Al,Ta)O_3, substrate materials for superconducting thin-film device applications. *J. Appl. Phys.* **83,** 1979–1982 (1998).

144. Lytle, F. W. X-ray diffractometry of low-temperature phase transformations in strontium titanate. *J. Appl. Phys.* **35,** 2212–2215 (1964).

145. Jiang, J. C., Tian, W., Pan, X. Q., Gan, Q. & Eom, C. B. Domain structure of epitaxial $SrRuO_3$ thin films on miscut (001) $SrTiO_3$ substrates. *Appl. Phys. Lett.* **72,** 2963–2965 (1998).

146. Chang, S. H. *et al.* Thickness-dependent structural phase transition of strained $SrRuO_3$ ultrathin films: The role of octahedral tilt. *Phys. Rev. B* **84,** 104101 (2011).

147. Lu, W., Yang, P., Song, W. D., Chow, G. M. & Chen, J. S. Control of oxygen octahedral rotations and physical properties in $SrRuO_3$ films. *Phys. Rev. B* **88,** 214115 (2013).

148. He, F., Wells, B. O. & Shapiro, S. M. Strain phase diagram and domain orientation in $SrTiO_3$ thin films. *Phys. Rev. Lett.* **94,** 176101 (2005).

149. Chen, Z. *et al.* Study of strain effect on in-plane polarization in epitaxial $BiFeO_3$ thin films using planar electrodes. *Phys. Rev. B* **86,** 235125 (2012).

150. Chang, Y. J. *et al.* Fundamental thickness limit of itinerant ferromagnetic $SrRuO_3$ thin films. *Phys. Rev. Lett.* **103,** 057201 (2009).

151. Siemons, W. *et al.* Dependence of the electronic structure of $SrRuO_3$ and its degree of correlation on cation off-stoichiometry. *Phys. Rev. B* **76,** 075126 (2007).

152. Singh, D. J. Electronic and magnetic properties of the 4*d* itinerant ferromagnet $SrRuO_3$. *J. Appl. Phys.* **79,** 4818 (Aug. 1996).

153. Rabe, K. M. in *Funct. Met. Oxides* 221–244 (Weinheim, Germany, 2013).

154. Kittel, C. Theory of antiferroelectric crystals. *Phys. Rev.* **82,** 729–732 (1951).

155. Cross, L. Antiferroelectric-ferroelectric switching in a simple "Kittel" antiferroelectric. *J. Phys. Soc. Japan* **23,** 77–82 (1967).

156. Tagantsev, A. K. *et al.* The origin of antiferroelectricity in $PbZrO_3$. *Nat. Commun.* **4,** 2229 (2013).

157. Waghmare, U. V. & Rabe, K. M. Lattice instabilities, anharmonicity and phase transitions in $PbZrO_3$ from first principles. *Ferroelectrics* **194,** 135–147 (1997).

158. Fujishita, H. & Katano, S. Re-examination of the antiferroelectric structure of $PbZrO_3$. *J. Phys. Soc. Japan* **66,** 3484–3488 (1997).

159. Fujishita, H. & Katano, S. Crystal structure of perovskite $PbZrO_3$ re-investigated by high resolution powder neutron diffraction. *Ferroelectrics* **217,** 17–20 (1998).

160. Burn, I. & Smyth, D. M. Energy storage in ceramic dielectrics. *J. Mater. Sci.* **7,** 339–343 (1972).

161. Mischenko, A. S., Zhang, Q., Scott, J. F., Whatmore, R. W. & Mathur, N. D. Giant electrocaloric effect in thin-film $PbZr_{0.95}Ti_{0.05}O_3$. *Science* **311,** 1270–1 (2006).

162. Parui, J. & Krupanidhi, S. B. Electrocaloric effect in antiferroelectric $PbZrO_3$ thin films. *Phys. status solidi - Rapid Res. Lett.* **2,** 230–232 (2008).

163. Berlincourt, D. Transducers using forced transitions between ferroelectric and antiferroelectric states. *IEEE Trans. Sonics Ultrason.* **13,** 116–124 (1966).

164. Uchino, K., Nomura, S., Cross, L. E., Newnham, R. E. & Jang, S. J. Electrostrictive effect in perovskites and its transducer applications. *J. Mater. Sci.* **16,** 569–578 (1981).

165. Liu, H. & Dkhil, B. A brief review on the model antiferroelectric $PbZrO_3$ perovskite-like material. *Zeitschrift für Krist.* **226,** 163–170 (2011).

166. Shirane, G., Sawaguchi, E. & Takagi, Y. Dielectric properties of lead zirconate. *Phys. Rev.* **84,** 476–481 (1951).

167. Hao, X., Zhai, J. & Yao, X. Improved energy storage performance and fatigue endurance of Sr-doped $PbZrO_3$ antiferroelectric thin films. *J. Am. Ceram. Soc.* **92,** 1133–1135 (2009).

168. Shirane, G. Ferroelectricity and antiferroelectricity in ceramic $PbZrO_3$ containing Ba or Sr. *Phys. Rev.* **86,** 219–227 (1952).

169. Cockayne, E. & Rabe, K. Pressure dependence of instabilities in perovskite $PbZrO_3$. *J. Phys. Chem. Solids* **61,** 305–308 (2000).

170. Mani, B. K., Lisenkov, S. & Ponomareva, I. Finite-temperature properties of antiferroelectric $PbZrO_3$ from atomistic simulations. *Phys. Rev. B* **91,** 134112 (2015).

171. Hung, C.-L., Chueh, Y.-L., Wu, T.-B. & Chou, L.-J. Characteristics of constrained ferroelectricity in $PbZrO_3$/$BaZrO_3$ superlattice films. *J. Appl. Phys.* **97,** 034105 (2005).

172. Kanno, I., Hayashi, S., Takayama, R. & Hirao, T. Superlattices of $PbZrO_3$ and $PbTiO_3$ prepared by multi-ion-beam sputtering. *Appl. Phys. Lett.* **68,** 328–330 (1996).

173. Mani, B. K., Chang, C.-M., Lisenkov, S. & Ponomareva, I. Critical thickness for antiferroelectricity in $PbZrO_3$. *Phys. Rev. Lett.* **115,** 097601 (2015).

174. Woodward, D. I., Knudsen, J. & Reaney, I. M. Review of crystal and domain structures in the $PbZr_xTi_{1-x}O_3$ solid solution. *Phys. Rev. B* **72** (2005).

175. Ge, J. *et al.* Enhancement of energy storage in epitaxial $PbZrO_3$ antiferroelectric films using strain engineering. *Appl. Phys. Lett.* **105,** 112908 (2014).

176. Pisarski, M., Ujma, Z. & Hańderek, J. The influence of hydrostatic pressure on phase transitions in $PbZrO_3$ with Pb and O vacancies. *Phase Transitions* **4,** 157–167 (1984).

177. Reyes-Lillo, S. E. & Rabe, K. M. Antiferroelectricity and ferroelectricity in epitaxially strained $PbZrO_3$ from first principles. *Phys. Rev. B* **88,** 180102 (2013).

178. Roy Chaudhuri, A. *et al.* Epitaxial strain stabilization of a ferroelectric phase in $PbZrO_3$ thin films. *Phys. Rev. B* **84,** 054112 (2011).

179. Boldyreva, K. *et al.* Thickness-driven antiferroelectric-to-ferroelectric phase transition of thin $PbZrO_3$ layers in epitaxial $PbZrO_3$/$Pb(Zr_{0.8}Ti_{0.2})O_3$ multilayers. *Appl. Phys. Lett.* **91,** 122915 (2007).

180. Breckenfeld, E. *et al.* Effect of growth induced (non)stoichiometry on the structure, dielectric response, and thermal conductivity of $SrTiO_3$ thin films. *Chem. Mater.* **24,** 331–337 (2012).

181. Brooks, C. M. *et al.* Tuning thermal conductivity in homoepitaxial $SrTiO_3$ films via defects. *Appl. Phys. Lett.* **107,** 051902 (2015).

182. Tenne, D. A. *et al.* Ferroelectricity in nonstoichiometric $SrTiO_3$ films studied by ultraviolet Raman spectroscopy. *Appl. Phys. Lett.* **97,** 142901 (2010).

183. Lee, J.-K., Hong, K.-S. & Jang, J.-W. Roles of Ba/Ti ratios in the dielectric properties of $BaTiO_3$ ceramics. *J. Am. Ceram. Soc.* **84,** 2001–2006 (2001).

184. Lee, S., Liu, Z.-K., Kim, M.-H. & Randall, C. A. Influence of nonstoichiometry on ferroelectric phase transition in $BaTiO_3$. *J. Appl. Phys.* **101,** 054119 (2007).

185. Dedon, L. R. *et al.* Nonstoichiometry, structure, and properties of $BiFeO_3$ films. *Chem. Mater.* **28,** 5952–5961 (2016).

186. Jang, H. W. *et al.* Ferroelectricity in strain-free $SrTiO_3$ thin films. *Phys. Rev. Lett.* **104,** 197601 (2010).

187. Damodaran, A. R., Breckenfeld, E., Chen, Z., Lee, S. & Martin, L. W. Enhancement of ferroelectric Curie temperature in BaTiOc films via strain-induced defect dipole alignment. *Adv. Mater.* **26,** 6341–6347 (2014).

188. Chotsawat, M., Sarasamak, K., Thanomngam, P. & T-Thienprasert, J. First-principles study of antisite defects in orthorhombic $PbZrO_3$. *Integr. Ferroelectr.* **156,** 86–92 (2014).

189. Kagimura, R. & Singh, D. J. *Ab inito* study of Pb antisite defects in $PbZrO_3$ and Pb(Zr, Ti)O_3. *Phys. Rev. B* **78,** 174105 (2008).

190. Suchaneck, G., Deyneka, A., Jastrabik, L., Savinov, M. & Gerlach, G. Lead Excess in Pb(Zr,Ti)O_3 thin films deposited by reactive sputtering at low temperatures. *Ferroelectrics* **318,** 3–10 (2005).

191. Whatmore, R. W., Huang, Z. & Todd, M. Sputtered lead scandium tantalate thin films: Pb^{4+} in B sites in the perovskite structure. *J. Appl. Phys.* **82,** 5686–5694 (1997).

192. Harjuoja, J., Väyrynen, S., Putkonen, M., Niinistö, L. & Rauhala, E. Atomic layer deposition of $PbZrO_3$ thin films. *Appl. Surf. Sci.* **253,** 5228–5232 (2007).

193. Yadav, A. K. *et al.* Observation of polar vortices in oxide superlattices. *Nature* **530,** 198–201 (2016).

194. Zhang, W., Sasaki, K. & Hata, T. Analysis of sputter process on a new ZrTi+PbO target system and its application to low-temperature deposition of ferroelectric Pb(Zr, Ti)O_3 films. *Jpn. J. Appl. Phys.* **35,** 1868–1872 (1996).

195. Boldyreva, K. *et al.* Microstructure and electrical properties of $(120)_O$-oriented and of $(001)_O$-oriented epitaxial antiferroelectric $PbZrO_3$ thin films on (100) $SrTiO_3$ substrates covered with different oxide bottom electrodes. *J. Appl. Phys.* **102,** 044111 (2007).

196. Pintilie, L., Boldyreva, K., Alexe, M. & Hesse, D. Coexistence of ferroelectricity and antiferroelectricity in epitaxial $PbZrO_3$ films with different orientations. *J. Appl. Phys.* **103,** 024101 (2008).

197. Tanaka, M., Saito, R. & Tsuzuki, K. Electron Microscopic Studies on Domain Structure of $PbZrO_3$. *Jpn. J. Appl. Phys.* **21,** 291–299 (1982).

198. Shen, G. J., Lu, C. J., Shen, H. M. & Wang, Y. N. Transmission electron microscopy study of 180° domain structure in $PbZrO_3$. *J. Mater. Sci. Lett.* **16,** 880–882 (1997).

199. Scott, J. F. Ferroelectrics go bananas. *J. Phys. Condens. Matter* **20,** 021001 (2008).

200. Bokov, A. A. & Ye, Z.-G. Recent progress in relaxor ferroelectrics with perovskite structure. *J. Mater. Sci.* **41,** 31–52 (2006).

201. Pokharel, B. P., Ranjan, R., Pandey, D., Siruguri, V. & Paranjpe, S. K. Rhombohedral superlattice structure and relaxor ferroelectric behavior of $(Pb_{0.70}Ba_{0.30})ZrO_3$ ceramics. *Appl. Phys. Lett.* **74,** 756–758 (1999).

202. Shimizu, H. *et al.* Lead-free antiferroelectric: $x$$CaZrO_3$-(1-$x$)$NaNbO_3$ system ($0 \leq x \leq 0.10$). *Dalton Trans.* **44,** 10763–72 (2015).

203. Goossens, D. J. Diffuse scattering from lead-containing ferroelectric perovskite oxides. *ISRN Mater. Sci.* **2013,** 1–17 (2013).

204. Xu, G., Zhong, Z., Hiraka, H. & Shirane, G. Three-dimensional mapping of diffuse scattering in $Pb(Zn_{1/3}Nb_{2/3})O_3$-$x$$PbTiO_3$. *Phys. Rev. B* **70,** 174109 (2004).

205. Shannon, R. D. Revised effective ionic radii and systematic studies of interatomic distances in halides and chalcogenides. *Acta Crystallogr. Sect. A* **32,** 751–767 (1976).

206. Perdew, J. P. & Zunger, A. Self-interaction correction to density-functional approximations for many-electron systems. *Phys. Rev. B* **23,** 5048–5079 (1981).

207. Steele, B. C. H. & Heinzel, A. Materials for fuel-cell technologies. **414,** 345–352 (2001).

208. Scataglini, R. *et al.* A direct manufacturing cost model for solid-oxide fuel Cell stacks. *Fuel Cells* **17,** 825–842 (2017).

209. Yamamoto, O. Solid oxide fuel cells: fundamental aspects and prospects. *Electrochim. Acta* **45,** 2423–2435 (2000).

210. Wachsman, E. D. & Lee, K. T. Lowering the temperature of solid oxide fuel cells. *Science* **334,** 935–939 (2011).

211. Gao, Z., Mogni, L. V., Miller, E. C., Railsback, J. G. & Barnett, S. A. A perspective on low-temperature solid oxide fuel cells. *Energy Environ. Sci.* **9,** 1602–1644 (2016).

212. Ishihara, T. & Bansal, N. P. in *Perovskite Oxide Solid Oxide Fuel Cells* 65–93 (2009). ISBN: 978-0-387-77708-5.

213. Ishihara, T., Matsuda, H. & Takita, Y. Doped $LaGaO_3$ perovskite type oxide as a new oxide ionic conductor. *J. Am. Chem. Soc.* **116,** 3801–3803 (1994).

214. Rupp, G. M., Glowacki, M. & Fleig, J. Electronic and ionic conductivity of $La_{0.95}Sr_{0.05}$-$Ga_{0.95}Mg_{0.05}O_{3-\delta}$ (LSGM) single crystals. *J. Electrochem. Soc.* **163,** F1189–F1197 (2016).

215. Huang, K., Tichy, R. S. & Goodenough, J. B. Superior perovskite oxide-ion conductor; strontium- and magnesium-doped $LaGaO_3$: I, Phase relationships and electrical properties. *J. Am. Ceram. Soc.* **81,** 2565–2575 (2005).

216. Li, M. *et al.* A family of oxide ion conductors based on the ferroelectric perovskite $Na_{0.5}Bi_{0.5}TiO_3$. *Nat. Mater.* **13,** 31–35 (2014).

217. Li, M. *et al.* Dramatic influence of A-site nonstoichiometry on the electrical conductivity and conduction mechanisms in the perovskite oxide $Na_{0.5}Bi_{0.5}TiO_3$. *Chem. Mater.* **27,** 629–634 (2015).

218. Mori, T., Drennan, J., Lee, J. H., Li, J. G. & Ikegami, T. Improving the ionic conductivity of yttria-stabilised zirconia electrolyte materials. *Solid State Ionics* **154-155,** 529–533 (2002).

219. Filal, M., Petot, C., Mokchah, M., Chateau, C. & Carpentier, J. L. Ionic conductivity of yttrium-doped zirconia and the "composite effect". *Solid State Ionics* **80,** 27–35 (1995).

220. Cheikh, A., Madani, A., Touati, A., Boussetta, H. & Monty, C. Ionic conductivity of zirconia based ceramics from single crystals to nanostructured polycrystals. *J. Eur. Ceram. Soc.* **21,** 1837–1841 (2001).

221. Rupp, J. L. Ionic diffusion as a matter of lattice-strain for electroceramic thin films. *Solid State Ionics* **207,** 1–13 (2012).

222. Korte, C., Peters, A., Janek, J., Hesse, D. & Zakharov, N. Ionic conductivity and activation energy for oxygen ion transport in superlattices - the semicoherent multilayer system YSZ (ZrO_2 + 9.5 mol% Y_2O_3)/Y_2O_3. *Phys. Chem. Chem. Phys.* **10,** 4623 (2008).

223. Jiang, J., Hu, X., Shen, W., Ni, C. & Hertz, J. L. Improved ionic conductivity in strained yttria-stabilized zirconia thin films. *Appl. Phys. Lett.* **102,** 143901 (2013).

224. Mohan Kant, K., Esposito, V. & Pryds, N. Strain induced ionic conductivity enhancement in epitaxial $Ce_{0.9}Gd_{0.1}O_{2-\delta}$ thin films. *Appl. Phys. Lett.* **100,** 033105 (2012).

225. Schichtel, N. *et al.* On the influence of strain on ion transport: microstructure and ionic conductivity of nanoscale YSZ vertical bar Sc_2O_3 multilayers. *Phys. Chem. Chem. Phys.* **12,** 14596–14608 (2010).

226. Garcia-Barriocanal, J. *et al.* Colossal ionic conductivity at interfaces of epitaxial ZrO_2: Y_2O_3/$SrTiO_3$ heterostructures. *Science* **321,** 676–680 (2008).

227. Saiful Islam, M. Ionic transport in ABO_3 perovskite oxides: a computer modelling tour. *J. Mater. Chem.* **10,** 1027–1038 (2000).

228. Mayeshiba, T. & Morgan, D. Strain effects on oxygen migration in perovskites. *Phys. Chem. Chem. Phys.* **17,** 2715–2721 (2015).

229. De Souza, R. A. & Ramadan, A. H. H. Ionic conduction in the $SrTiO_3$|YSZ|$SrTiO_3$ heterostructure. *Phys. Chem. Chem. Phys.* **15,** 4505 (2013).

230. Cheng, H.-s., Shen, H., Yang, F. & Tang, J.-y. Cross sections for non-Rutherford backscattering of 4He from five light elements. *Nucl. Instruments Methods Phys. Res. Sect. B Beam Interact. with Mater. Atoms* **85,** 47–50 (1994).

231. Brahlek, M., Choquette, A. K., Smith, C. R., Engel-Herbert, R. & May, S. J. Structural refinement of Pbnm-type perovskite films from analysis of half-order diffraction peaks. *J. Appl. Phys.* **121,** 045303 (2017).

232. Guenter, M. M. *et al.* Combined neutron and synchrotron X-ray diffraction study of Sr/Mg-doped lanthanum gallates up to high temperatures. *J. Phys. Chem. Solids* **67,** 1754–1768 (2006).

233. Slater, P. The structure of the oxide ion conductor $La_{0.9}Sr_{0.1}Ga_{0.8}Mg_{0.2}O_{2.85}$ by powder neutron diffraction. *Solid State Ionics* **107,** 319–323 (1998).

234. Slater, P. R., Irvine, J. T. S., Ishihara, T. & Takita, Y. High-temperature powder neutron diffraction study of the oxide ion conductor $La_{0.9}Sr_{0.1}Ga_{0.8}Mg_{0.2}O_{2.85}$. *J. Solid State Chem.* **139,** 135–143 (1998).

235. Kim, C. U. *et al. Numerical analysis on effective electric field penetration depth for interdigital impedance sensor* in *J. Phys. Conf. Ser.* **418** (2013), 012020.

236. De Souza, R. a. Oxygen diffusion in $SrTiO_3$ and related perovskite oxides. *Adv. Funct. Mater.* **25,** 6326–6342 (2015).

237. Jamnik, J. & Maier, J. Generalised equivalent circuits for mass and charge transport: chemical capacitance and its implications. *Phys. Chem. Chem. Phys.* **3,** 1668–1678 (2001).

238. Lai, W. & Haile, S. M. Impedance spectroscopy as a tool for chemical and electrochemical analysis of mixed conductors: A case study of ceria. *J. Am. Ceram. Soc.* **88,** 2979–2997 (2005).

239. Trinkle, D. R. Diffusivity and derivatives for interstitial solutes: activation energy, volume, and elastodiffusion tensors. *Philos. Mag.* **96,** 2714–2735 (2016).

240. Marti, W., Fischer, P., Altorfer, F., Scheel, H. J. & Tadin, M. Crystal structures and phase transitions of orthorhombic and rhombohedral $RGaO_3$ (R=La,Pr,Nd) investigated by neutron powder diffraction. *J. Phys. Condens. Matter* **6,** 127 (1994).

241. Howard, C. J. & Kennedy, B. J. The orthorhombic and rhombohedral phases of $LaGaO_3$ - A neutron powder diffraction study. *J. Phys. Condens. Matter* **11,** 3229–3236 (1999).

242. Cherry, M., Islam, M. S. & Catlow, C. R. A. Oxygen ion migration in perovskite-type oxides. *J. Solid State Chem.* **118,** 125–132 (1995).

243. Islam, M., Cherry, M. & Catlow, C. Oxygen diffusion in $LaMnO_3$ and $LaCoO_3$ perovskite-type oxides: A molecular dynamics study. *J. Solid State Chem.* **124,** 230–237 (1996).

244. Khan, M. S., Islam, M. S. & Bates, D. R. Dopant substitution and ion migration in the $LaGaO_3$-based oxygen ion conductor. *J. Phys. Chem. B* **102,** 3099–3104 (1998).

245. Blanc, F., Middlemiss, D. S., Gan, Z. & Grey, C. P. Defects in doped $LaGaO_3$ anionic conductors: Linking NMR spectral features, local environments, and defect thermodynamics. *J. Am. Chem. Soc.* **133,** 17662–17672 (2011).

246. Gambino, M. *et al.* Defect interaction and local structural distortions in Mg-doped $LaGaO_3$: A combined experimental and theoretical study. *J. Chem. Phys.* **147,** 144702 (2017).

247. Heeg, T. *et al.* Growth and properties of epitaxial rare-earth scandate thin films. *Appl. Phys. A Mater. Sci. Process.* **83,** 103–106 (2006).

248. Björck, M. & Andersson, G. GenX: An extensible X-ray reflectivity refinement program utilizing differential evolution. *J. Appl. Crystallogr.* **40,** 1174–1178 (2007).

249. Fister, T. T. *et al.* In situ characterization of strontium surface segregation in epitaxial $La_{0.7}Sr_{0.3}MnO_3$ thin films as a function of oxygen partial pressure. *Appl. Phys. Lett.* **93,** 151903–151904 (2008).

250. Li, S. & Bergman, B. Doping effect on secondary phases, microstructure and electrical conductivities of $LaGaO_3$ based perovskites. *J. Eur. Ceram. Soc.* **29,** 1139–1146 (2009).

251. Chen, D., Chen, C., Baiyee, Z. M., Shao, Z. & Ciucci, F. Nonstoichiometric oxides as low-cost and highly-efficient oxygen reduction/evolution catalysts for low-temperature electrochemical devices. *Chem. Rev.* **115,** 9869–9921 (2015).

252. Stambouli, A. & Traversa, E. Solid oxide fuel cells (SOFCs): a review of an environmentally clean and efficient source of energy. *Renew. Sustain. Energy Rev.* **6,** 433–455 (2002).

253. Grimaud, A. *et al.* Double perovskites as a family of highly active catalysts for oxygen evolution in alkaline solution. *Nat. Commun.* **4,** 2439 (2013).

254. Hwang, J. *et al.* Perovskites in catalysis and electrocatalysis. *Science (80-.).* **358,** 751–756 (2017).

255. Suntivich, J. *et al.* Design principles for oxygen-reduction activity on perovskite oxide catalysts for fuel cells and metal-air batteries. *Nat. Chem.* **3,** 546–550 (2011).

256. Hong, W. T. *et al.* Toward the rational design of non-precious transition metal oxides for oxygen electrocatalysis. *Energy Environ. Sci.* **8,** 1404–1427 (2015).

257. Lee, Y.-L., Kleis, J., Rossmeisl, J., Shao-Horn, Y. & Morgan, D. Prediction of solid oxide fuel cell cathode activity with first-principles descriptors. *Energy Environ. Sci.* **4,** 3966 (2011).

258. Jacobs, R., Mayeshiba, T., Booske, J. & Morgan, D. Material discovery and design principles for stable, high activity perovskite cathodes for solid oxide fuel cells. *Adv. Energy Mater.* **8,** 1702708 (2018).

259. Cheng, X. *et al.* Oxygen evolution reaction on $La_{1-x}Sr_xCoO_3$ perovskites: A combined experimental and theoretical study of their structural, electronic, and electrochemical properties. *Chem. Mater.* **27,** 7662–7672 (2015).

260. Hong, W. T., Welsch, R. E. & Shao-Horn, Y. Descriptors of oxygen-evolution activity for oxides: A statistical evaluation. *J. Phys. Chem. C* **120,** 78–86 (2016).

261. Mastrikov, Y. A., Merkle, R., Kotomin, E. A., Kuklja, M. M. & Maier, J. Surface termination effects on the oxygen reduction reaction rate at fuel cell cathodes. *J. Mater. Chem. A* **6,** 11929–11940 (2018).

262. Komo, M., Hagiwara, A., Taminato, S., Hirayama, M. & Kanno, R. Oxygen evolution and reduction reactions on $La_{0.8}Sr_{0.2}CoO_3$ (001), (110), and (111) surfaces in an alkaline solution. *Electrochemistry* **80,** 834–838 (2012).

263. Fleig, J. *et al.* Thin film microelectrodes in SOFC electrode research. *Fuel Cells* **6,** 284–292 (2006).

264. Baumann, F. S., Fleig, J., Habermeier, H.-U. & Maier, J. Impedance spectroscopic study on well-defined (La,Sr)(Co,Fe)$O_{3-\delta}$ model electrodes. *Solid State Ionics* **177,** 1071–1081 (2006).

265. Kubicek, M. *et al.* Electrochemical properties of $La_{0.6}Sr_{0.4}CoO_{3-\delta}$ thin films investigated by complementary impedance spectroscopy and isotope exchange depth profiling. *Solid State Ionics* **256,** 38–44 (2014).

266. Lee, D. *et al.* Strain influence on the oxygen electrocatalysis of the (100)-oriented epitaxial $La_2NiO_{4+\delta}$ thin films at elevated temperatures. *J. Phys. Chem. C* **117,** 18789–18795 (2013).

267. Chen, Y. *et al.* Segregated chemistry and structure on (001) and (100) surfaces of $(La_{1-x}Sr_x)_2CoO_4$ override the crystal anisotropy in oxygen exchange kinetics. *Chem. Mater.* **27,** 5436–5450 (2015).

268. Mori, D. *et al.* Synthesis, structure, and electrochemical properties of epitaxial perovskite $La_{0.8}Sr_{0.2}CoO_3$ film on YSZ substrate. *Solid State Ionics* **177,** 535–540 (2006).

269. Berenov, A., Atkinson, A., Kilner, J., Bucher, E. & Sitte, W. Oxygen tracer diffusion and surface exchange kinetics in $La_{0.6}Sr_{0.4}CoO_{3-\delta}$. *Solid State Ionics* **181,** 819–826 (2010).

270. Petric, A., Huang, P. & Tietz, F. Evaluation of La-Sr-Co-Fe-O perovskites for solid oxide fuel cells and gas separation membranes. *Solid State Ionics* **135,** 719–725 (2000).

271. Readman, J. E., Olafsen, A., Larring, Y. & Blom, R. $La_{0.8}Sr_{0.2}Co_{0.2}Fe_{0.8}O_{3-\delta}$ as a potential oxygen carrier in a chemical looping type reactor, an in-situ powder X-ray diffraction study. *J. Mater. Chem.* **15,** 1931–1937 (2005).

272. Feng, Z. *et al. In situ* studies of the temperature-dependent surface structure and chemistry of single-crystalline (001)-oriented $La_{0.8}Sr_{0.2}CoO_{3-\delta}$ perovskite thin films. *J. Phys. Chem. Lett.* **4,** 1512–1518 (2013).

273. Crumlin, E. J. *et al.* Surface strontium enrichment on highly active perovskites for oxygen electrocatalysis in solid oxide fuel cells. *Energy Environ. Sci.* **5,** 6081–6088 (2012).

274. Druce, J., Téllez, H. & Hyodo, J. Surface segregation and poisoning in materials for low-temperature SOFCs. *MRS Bull.* **39,** 810–815 (2014).

275. Lee, W., Han, J. W., Chen, Y., Cai, Z. & Yildiz, B. Cation size mismatch and charge interactions drive dopant segregation at the surfaces of manganite perovskites. *J. Am. Chem. Soc.* **135,** 7909–7925 (2013).

276. O'Hayre, R., Barnett, D. M. & Prinz, F. B. The triple phase boundary. *J. Electrochem. Soc.* **152,** A439–A444 (2005).

277. Wilson, J. R. *et al.* Three-dimensional reconstruction of a solid-oxide fuel-cell anode. *Nat. Mater.* **5,** 541–544 (2006).

278. Brichzin, V., Fleig, J., Habermeier, H. & Maier, J. Geometry dependence of cathode polarization in solid oxide fuel cells investigated by defined Sr-doped $LaMnO_3$ microelectrodes. *Electrochem. Solid-State Lett.* **3,** 403–406 (1999).

279. Brichzin, V., Fleig, J., Habermeier, H.-U., Cristiani, G. & Maier, J. The geometry dependence of the polarization resistance of Sr-doped $LaMnO_3$ microelectrodes on yttria-stabilized zirconia. *Solid State Ionics* **152-153,** 499–507 (2002).

280. Lane, J. & Kilner, J. Measuring oxygen diffusion and oxygen surface exchange by conductivity relaxation. *Solid State Ionics* **136-137,** 997–1001 (2000).

281. Adler, S. B. Factors governing oxygen reduction in solid oxide fuel cell cathodes (2004).

282. Adler, S., Chen, X. & Wilson, J. Mechanisms and rate laws for oxygen exchange on mixed-conducting oxide surfaces. *J. Catal.* **245,** 91–109 (2007).

283. Chueh, W. C. & Haile, S. M. Electrochemistry of mixed oxygen ion and electron conducting electrodes in solid electrolyte cells. *Annu. Rev. Chem. Biomol. Eng.* **3,** 313–341 (2012).

284. Fleig, J., Merkle, R. & Maier, J. The $p(O_2)$ dependence of oxygen surface coverage and exchange current density of mixed conducting oxide electrodes: model considerations. *Phys. Chem. Chem. Phys.* **9,** 2713 (2007).

285. Wang, D. Y. & Nowick, A. S. Cathodic and anodic polarization phenomena at platinum electrodes with doped CeO_2 as electrolyte. *J. Electrochem. Soc.* **126,** 1155–1165 (1979).

286. Takeda, Y., Kanno, R., Noda, M., Tomida, Y. & Yamamoto, O. Cathodic polarization phenomena of perovskite oxide electrodes with stabilized zirconia. *J. Electrochem. Soc.* **134,** 2656–2661 (1987).

287. De Souza, R. A. A universal empirical expression for the isotope surface exchange coefficients (k*) of acceptor-doped perovskite and fluorite oxides. *Phys. Chem. Chem. Phys.* **8,** 890–897 (2006).

288. Wang, L. *et al.* Ferroelectrically tunable magnetic skyrmions in ultrathin oxide heterostructures. *Nat. Mater.* **17,** 1087–1094 (2018).

289. Ziese, M., Jin, L. & Lindfors-Vrejoiu, I. Unconventional anomalous Hall effect driven by oxygen-octahedra-tailoring of the $SrRuO_3$ structure. *J. Phys. Mater.* doi:10.1088/2515-7639/ab1aef (2019).

290. Yu, Y. *et al.* Effect of Sr content and strain on Sr surface segregation of $La_{1-x}Sr_xCo_{0.2}Fe_{0.8}O_{3-\delta}$ as cathode material for solid oxide fuel cells. *ACS Appl. Mater. Interfaces* **8,** 26704–26711 (2016).

291. Stoerzinger, K. A., Hong, W. T., Crumlin, E. J., Bluhm, H. & Shao-Horn, Y. Insights into electrochemical reactions from ambient pressure photoelectron spectroscopy. *Acc. Chem. Res.* (2015).

Appendix A

Pseudo-cubic lattice notation

The indices for crystal lattice planes or crystallographic directions in this dissertation are primarily indexed in a cubic lattice, unless it is specified for other lattice symmetries (*e.g.*, orthorhombic and rhombohedral). Since it is easier to describe and analyze the lattice symmetry change and octahedral rotation patterns in cubic indices, many lower-symmetry systems are typically converted to a pseudo-cubic lattice for structure analysis. Here, the conversion between orthorhombic lattice and pseudo-cubic lattice will be discussed.

Taking the $GdFeO_3$-type orthorhombic lattice — one of the most common symmetries in transition-metal perovskite systems — as an example, the epitaxial growth of an orthorhombic lattice on a cubic substrate is to align the $[110]_O$ with the [001] of the cubic substrate (**Figure A.1**). Due to epitaxial strain, the angles between the a_O and b_O axis is not necessarily 90°, and is denoted as γ_O. In turn, the conversion between the orthorhombic

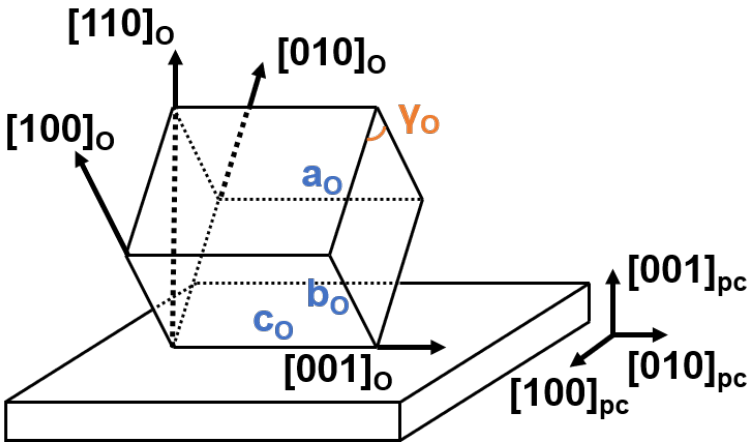

Figure A.1: *The epitaxial relation of $GdFeO_3$-type orthorhombic lattice on cubic substrate. The subscript "O" denotes orthorhombic lattice while "pc" denotes pesudo-cubic lattice.*

lattice and pseudo-cubic lattice is given by

$$\begin{aligned} a_{pc} &= \frac{c_0}{2} \\ b_{pc} &= \frac{\sqrt{a_O^2 + b_O^2 - 2a_O b_O \cos\gamma_O}}{2} \\ c_{pc} &= \sqrt{\frac{a_O^2 + b_O^2 - 2b_{pc}^2}{2}} \\ \alpha_c &= \arccos\left(\frac{b_{pc}^2 + c_{pc}^2 - a_O^2}{2b_{pc}c_{pc}}\right) \end{aligned} \tag{A.1}$$

As one can see, due to the fact that a_O and b_O is not the same, the pseudo-cubic lattice of an orthorhombic material is always monoclinically tilted with an tilting angle α_c defined above. Under epitaxial strain, however, it is possible to control the symmetry of the material and change this tilting angle. In addition, the distorted lattice is generally accompanied with rotated octahedral cages. The octahedral rotation pattern in the bulk $GdFeO_3$-type orthorhombic material is generally taking the form of $a^-a^-c^+$ in Glazer's notation. The in-phase rotation axis is aligned with the pseudo-cubic axis perpendicular to the monoclinic tilting axis. In the strained thin films, such rotation pattern is typically deviated from bulk values, and more discussion regarding such change in rotation pattern can be found in **Chapter 4** and **Chapter 6**.

Another reason to apply the pseudo-cubic notation for low-symmetry lattice is that, near the epitaxial interface between the film and substrate, there typically exists a relaxation of structural distortions. In another word, for instance, if the octahedral rotation is much larger in the substrate than that in the film, the substrate tends to induce large octahedral rotations in the film near the interface. However, such induced distortions gradually relax back to a rotation pattern that is defined by the epitaxial strain state in approximately 4-6 UCs. The larger the symmetry mismatch between the film and substrate, the sharper gradient typically takes place. Thus, for ultrathin films or superlattice structures (see **Chapter 7**), it is difficult to assign one space group for the region near the heterostructure interface, while a description of the structure based on lattice tilt, lattice stretch and octahedral rotations presents a more accurate picture of the structural evolution in the materials.

Appendix B

Characterization of thin-film chemistry

B.1 Rutherford backscattering spectrometry

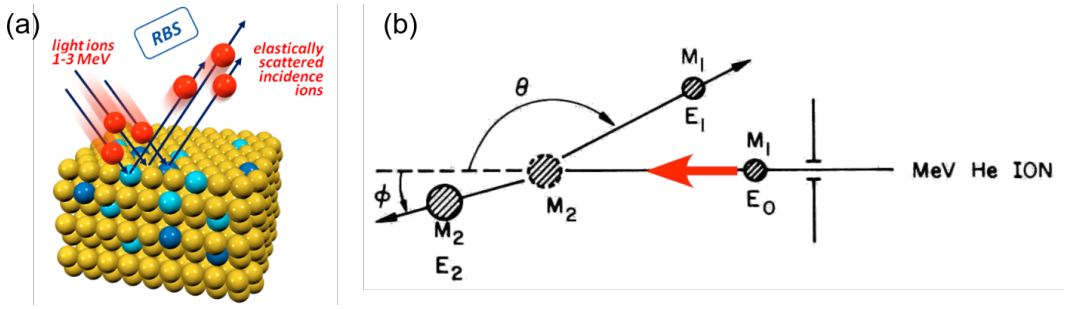

Figure B.1: *(a) Schematic of the operation of RBS measurement. (b) An illustration of the elastic scattering of the incident ion by the immobile nuclei.*

Rutherford backscattering spectrometry (RBS) is a mass spectrometry technique that utilizes the elastic scattering of high-energy helium ion beams to detect the chemical composition of materials. During the operation of the RBS, a beam of focused high-energy helium ions is accelerated to few MeV and incident on the sample surface (**Figure B.1**(a)). The majority of the beam will penetrate through the material due to the small volume fraction of the nuclei in the atom, while some incident ions will hit the nuclei and get backscattered to the detector (**Figure B.1**(b)). The ratio between the energy of the scattered projectile and the initial energy of the incident particle gives the kinematic factor

$$k = \left(\frac{m_1 \cos\theta_1 \pm \sqrt{m_2^2 - m_1^2 (\sin\theta_1)^2}}{m_1 + m_2} \right)^2 \tag{B.1}$$

which can be used to quantitatively determine the target chemical element based on the exiting energy of the scattered particle. In this equation, m_1, m_2, and θ_1 correspond to

mass of projectile particle, mass of target nucleus, and the exiting angle of the scattering particle. In addition, the probability of the backscattering event for a particular type of element can be described by a differential cross-section, which is given by

$$\frac{d\omega}{d\Omega} = \Big(\frac{Z_1 Z_2 e^2}{4E_0}\Big)^2 \frac{1}{(\sin\theta/2)^4} \tag{B.2}$$

where Z_1 and Z_2 are the atomic number of the incident and target nuclei. This equation suggests that it is typically easier to probe heavier atoms in the material, while for lighter elements, it's important to maximize the corresponding cross-section in order to get more accurate analysis.

The energy loss of a backscattered ion is dependent on the energy lost in scattering events with sample nuclei as described above, and an additional energy lost to small-angle scattering from the sample electrons. The first type of energy loss will determine the peak positions in the spectra as different nuclei will produce different exiting energy of the incident ions. These peaks are characteristic of the elements in the material and are used to determine the stoichiometry of the sample. While the second type of energy loss comes from the interaction with the trajectory ions and the electron clouds, which creates a gradual energy loss dependent on the electron density and the distance traversed in the sample. This type of energy loss shifts the peak position by a certain amount but in a continuous manner. Elements which only appear at some depth inside the sample will also have their peak positions shifted by some amount which represents the distance an ion had to traverse to reach those nuclei. In this way, the peak position plus the peak profile provides information of the compositional depth profile of the sample and can be fitted to extract the chemical information.

B.2 X-ray photoelectron spectroscopy

X-ray photoelectron spectroscopy (XPS) is a powerful tool for the analysis of the electronic structure and chemistry at the surface of the material. The probing depth of XPS is typically from outermost surface to few nanometers depending on the kinetic energy of the electrons. During the operation of XPS analysis, as illustrated, the sample surface is exposed to a beam of X-ray, and the kinetic energy of the escaped photoelectrons from the surface will be simultaneously measured (**Figure B.2**(a)). The kinetic energy of the escaped photoelectrons can be converted to the binding energy of the electrons as they were in the material depending on the incident beam energy. The relationship between kinetic energy and binding energy is given by

$$E_B = h\nu - E_k - \Phi \tag{B.3}$$

where $h\nu$ is the energy of the incident X-ray beam, E_k is the measured kinetic energy of the photoelectrons, and Φ is the working function of the material. Such binding energy, in turn, contains useful information including the type of elements, oxidation states,

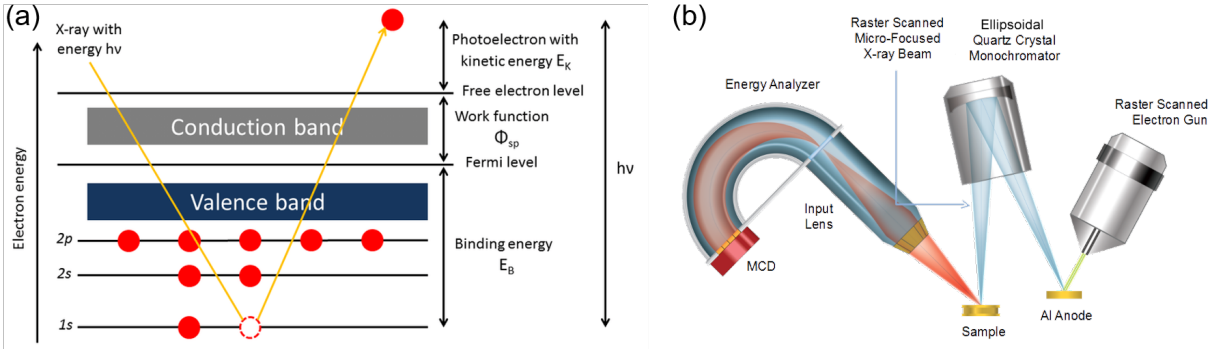

Figure B.2: *(a) The working principle of XPS and the relationship between different energy terms are illustrated. (b) A schematic of the setup of a laboratory-based XPS.*

binding environment, chemical concentration, and *etc*. If the momentum of the photoelectrons can be measured based on the exiting angle, the band structure at the surface of the material in k-space can be reconstructed, and such technique is called angle-resolved photoemission spectroscopy (ARPES) which plays a vital role in the study of strongly correlated materials. Depending on the source of the X-ray beam, XPS can be either installed in the regular laboratory or be part of the beam-line station at a synchrotron beam source. The laboratory-based XPS typically utilizes a aluminum or magnesium X-ray source where a piece of aluminum or magnesium metal is excited by a beam of high-energy electrons and produces X-ray. The X-ray beam is then monochromatized and delivered into the analyze chamber (**Figure B.2**(b)). While for synchrotron-based XPS, the analyze chamber can be located in one branch of the end-station at the synchrotron radiation facility. One key advantage of utilizing synchrotron source are the high flux density of X-ray beam plus the adjustable incident beam energy. Such advantages bring about a good resolution of the analysis due to the high signal-to-noise ratio, and the ability to resolve chemical information at different depth in the sample by tuning the kinetic energy of the exiting photoelectrons.

Typically, XPS is operated at high vacuum (10^{-8} millibar) or ultra-high vacuum (10^{-9} millibar). Recently, there has seen a great progress in the development of a so-called ambient-pressure XPS [291] where the sample is exposed to a range of gas partial pressure (vacuum to $\sim$0.5 millibar). The choice of the reactant gases can be oxygen, argon, carbon dioxide, carbon monoxide, water vapor, and *etc*. And the sample of interest can be probed in a wide temperature range, depending on the specific experimental requirement. The photoelectron detector, on the other hand, is differentially pumped to achieve good resolution of the kinetic energies. Such technique greatly facilitates the understanding of electrochemical reaction at the solid-gas interface as the chemical potential of the reactants can be readily adjusted to reveal useful information.

B.3 Low-energy ion scattering spectroscopy

While RBS is a useful technique to characterize the thin-film lattice chemistry, low-energy ion scattering spectroscopy (LEIS) is extremely sensitive to the surface chemistry of the thin-film samples, especially the outermost layer of the material. Very similar to the working principle of RBS, LEIS utilizes a beam of focused ions to detect the material chemistry based on the exiting energies of the trajectory ions. The scattering process of the trajectory ion is described by Equation B.1.The use of low-energy ions guarantees that the beam is scattered off at the surface and does not penetrate through the sample. This means that the information acquired from the LEIS is essentially from the outermost surface of the material, making LEIS an extremely surface-sensitive technique for the chemistry characterization of thin-film materials. The analysis of the LEIS spectra involves the identification of chemical elements based on the positions of the characteristic peaks, and the peak height which provides information regarding the concentration of the particular element. Moreover, the resolution on the chemical element depends on the masses of the incident ionic particles. For the detection of lighter elements, helium beam is better to be used while for heavier elements, neon beam is a more adopted choice.

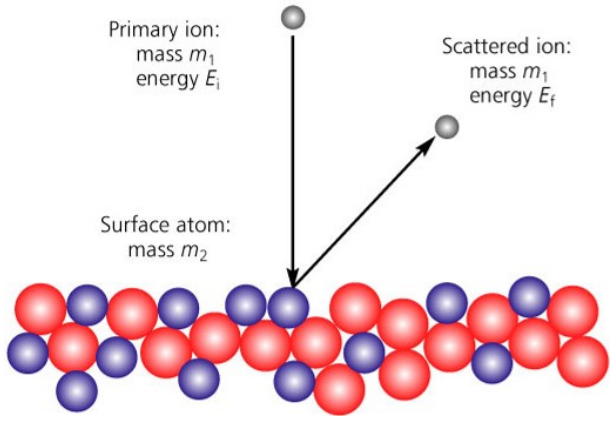

Figure B.3: *Schematics of the scattering of incident ions by the outermost atomic layer in the LEIS measurement.*

Although designed for surface chemistry characterization, LEIS can also provide information of the deeper layer. The chemical information at deeper layer is provided in the backgrounds on the low energy side of the peak and LEIS inherently contains in-depth information up to a maximum of 10 nm. Since the material surface is not damaged significantly during the LEIS analysis, the information in the background signals yields a so-called static depth profile of the sample. The interpretation of these backgrounds is similar to the depth information in RBS where the continuous energy loss comes from the scattering with electron clouds.

In addition, a dynamic depth profile can also be achieved more effectively by the installation of another ion source (argon) in the instrumentation to mill away the material. In

the dynamic depth profile analysis, typically, an argon-ion beam is incident on the sample surface to continuously milling off the surface material, while either the helium- or the neon-ion beam is used to perform surface chemistry analysis. One needs to be careful while performing such measurement due to the possible atomic intermixing during the milling process.

Here I summarize the characteristics of few surface-sensitive material-chemistry characterization techniques.

Table B.1: *Summary of few surface sensitive thin-film chemistry characterization techniques*

	LEIS	XPS	ToF-SIMS
Surface sensitivity	Outermost atomic layer	few nm	few atomic layers
Static depth profile	Inherent	$\sim$10 nm by varying incident-beam energy	No
Dynamic depth profile	Yes with sputter gun	Yes with sputter gun	Yes with sputter gun
Detection limits	0.1-1% for heavier atoms; few % for lighter atoms	0.1-1%	ppm
Quantitative analysis	Excellent	Very good	Average
Electronic structure information	No	Yes	Somewhat, through molecular fragment

Appendix C

Electrochemical impedance spectroscopy

Electrochemical impedance spectroscopy (EIS) has long been a useful tool to investigate the detailed mechanisms of electrochemical reactions, dielectric and transport properties of materials, passive surfaces, and *etc*. The EIS measurement is a linear technique which applies a small perturbation to the physical system, and the response from the system, if measured over an infinite frequency range, contains all of the information of the system and can be interpreted in terms of Linear System Theory. To apply Linear System Theory on the interpretation of the data, the system has to be stable and passive with finite impedance. A few commonly used passive elements are listed below Thus, the application of a small AC perturbation on the system of interest will produce both magnitude and phase information, which can be further modeled by using a series of passive circuit elements. The excitation signal can be written as

$$E(t) = E_0 \sin(\omega t) \tag{C.1}$$

where $E(t)$ is the potential at transient time t, E_0 is the signal amplitude and $\omega = 2\pi f$ is the signal frequency. Now, assuming there's a phase shift in the response current signal

$$I(t) = I_0 \sin(\omega t + \phi) \tag{C.2}$$

then according to Ohm's Law the impedance of the system can be written as

$$Z = \frac{E(t)}{I(t)} = \frac{E_0 \sin(\omega t)}{I_0 \sin(\omega t + \phi)} = Z_0 \frac{\sin(\omega t)}{\sin(\omega t + \phi)} \tag{C.3}$$

which suggests that the impedance can be expressed in terms of magnitude Z_0 and phase shift ϕ. To represent the data, one popular way of plotting is to have the real part plotted on the X-axis and the imaginary part plotted on the Y-axis, yielding a so-called Nyquist plot. Although specific circuits have to be built to get a through idea of the physical process in a particular system, the Nyquist plot is an effective approach to get an intuitive and

Table C.1: *Several commonly used passive electrical circuit element in EIS analysis*

Element	Operational impedance	Fourier impedance
Resistor	R	R
Capacitor	$1/sC$	$1/j\omega C$
Inductor	sL	$j\omega L$
Constant phase element	Q/s^T	$Q/(j\omega)^T$

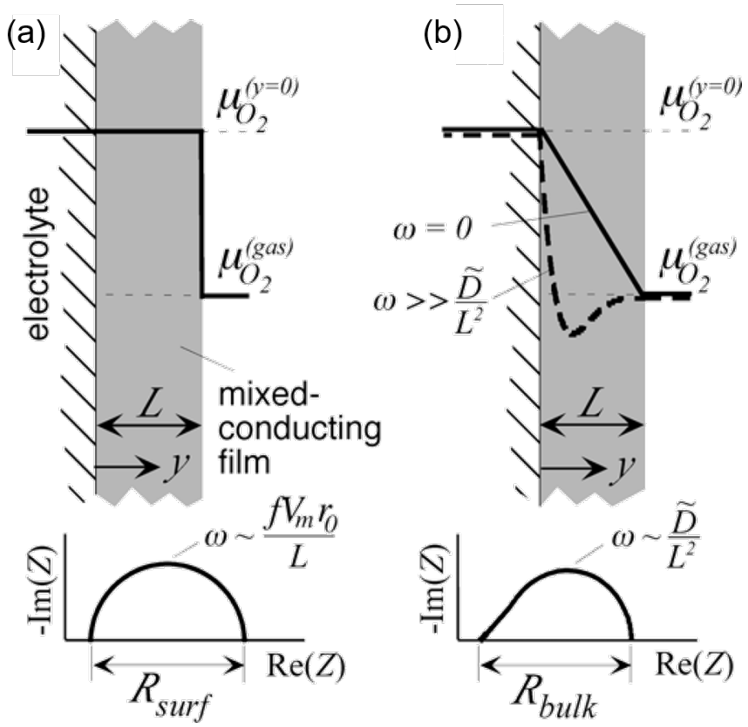

Figure C.1: *Chemical potential profile and Nyquist plot in a (a) surface-reaction-limited process and a (b) diffusion limited process (Figure adapted from [281]).*

preliminary idea of the characteristics of a unknown system. For instance, in a surface reaction process near the solid-gas interface, if the overall process is only limited by surface process, the dominant potential drop happens at the surface and the Nyquist plot is manifested as a well-defined semi-circle (**Figure C.1**(a)). However, if the charge diffusion is the slow process while the surface reaction is fast, the potential will gradually drop across the material and the Nyquist plot is manifested as a distorted semi-circle (**Figure C.1**(b)). The distorted part, typically, can be described by a Warburg diffusion element which can be written as

$$Z_W = \frac{A_W}{\sqrt{\omega}} + \frac{A_W}{j\sqrt{\omega}} \tag{C.4}$$

where A_W is the Warburg coefficient that is given by

$$A_W = \frac{RT}{An^2F^2\Theta C\sqrt{2D}} \tag{C.5}$$

where A is the surface area, n is the valency, F is the Faraday constant, Θ stands for the fraction of the oxidation and reduction species, C gives the concentration, and D is the diffusion coefficient.

To analyze the impedance spectra, an equivalent circuit model is used to analyze the physical process. It is worth noting that multiple equivalent circuits can be fitted to a same impedance spectrum. Thus, one needs to be very cautious when choosing the appropriate fitting model for the data, and supplementary experiments are preferred to be included for a comprehensive rationalization of the hypothesized circuit model. Here, I will briefly introduce two equivalent circuit models that are used in this dissertation. More detailed and in-depth discussion regarding the derivation and application of these models can be found in [237, 238].

C.1 Ionic diffusion in mixed conductors

Mixed conductors refer to materials that conduct both ionic and electronic charges. Assuming the diffusion is one dimensional, the diffusion-drift equation is given by

$$J_i^{mass}(x,t) = -D_i\frac{\partial c_i(x,t)}{\partial x} - \frac{\sigma_i(x,t)}{z_i e}\frac{\partial \phi(x,t)}{\partial x} \tag{C.6}$$

where i denotes the charged species, D_i is the diffusion coefficient for the i^{th} species, c_i is the concentration, σ_i is the conductivity, z is the number of charges carried (*i.e.*, 2 for oxygen vacancies and 1 for electrons or holes), and finally ϕ is the electrical potential. Combining the chemical and electrical potential yields the electrochemical potential which is written as

$$\tilde{\mu}_i(x,t) = \mu_i(x,t) + z_i e\phi(x,t) \tag{C.7}$$

and the diffusion-drift equation can be further written as

$$J_i^{mass}(x,t) = -\frac{\sigma_i(x,t)}{(z_i e)^2}\frac{\partial \tilde{\mu}_i(x,t)}{\partial x} \tag{C.8}$$

A second constraint in the description of the mass flow in the system is given by the continuity equation which basically states that the change in charge concentration with time should be equal to the variation in charge flow along the diffusion direction. The continuity equation is given by

$$\frac{\partial J_i^{mass}(x,t)}{\partial x} = -\frac{\partial c_i(x,t)}{\partial t} \tag{C.9}$$

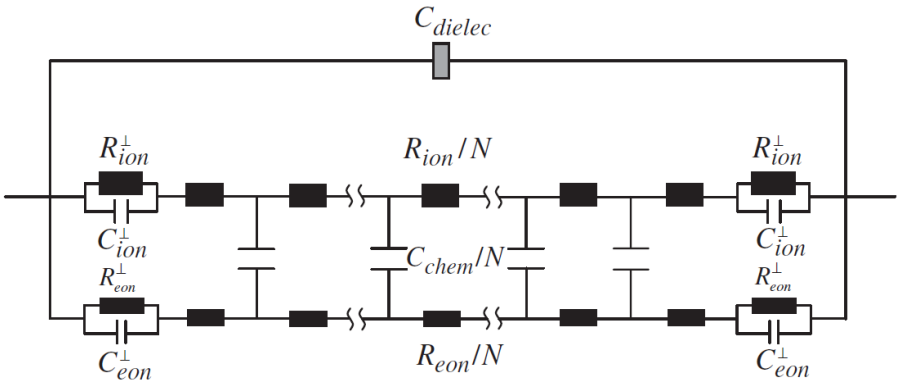

Figure C.2: *Equivalent circuit based on the derived charge flow response under small electrical perturbation (Figure adapted from [238]). Notice that the material is sliced into N slices. For a homogeneous material, position-independent material properties can be used.*

which can be further written as

$$\frac{\partial J_i^{mass}(x,t)}{\partial x} = -\frac{c_i(x,t)}{k_B T}\frac{\partial \mu_i(x,t)}{\partial t} \tag{C.10}$$

And finally, besides the mass flow under a electrochemical potential, a charge displacement current is also generated given by

$$J_{dis}^{charge}(x,t) = -\frac{\partial}{\partial t}\left[\epsilon_r(x,t)\epsilon_0\frac{\partial \phi(x,t)}{\partial x}\right] \tag{C.11}$$

where ϵ_r is the relative permittivity of the material with respect to vacuum permittivity ϵ_0. For now, Equation C.8, Equation C.10, and Equation C.11 fully describe the current flow in the material system. Now, if the perturbation is small, material properties that are time-dependent can be averaged to time-independent values, and the above three equations can be written as

$$\Delta J_i^{charge}(x,t) = -\sigma_i \frac{\partial}{\partial x}\Delta\tilde{\mu}_i^*(x,t) \tag{C.12}$$

$$\frac{\partial}{\partial x}\Delta J_i^{charge}(x,t) = -\frac{(z_i e)^2 c_i}{k_B T}\frac{\partial}{\partial t}\Delta\tilde{\mu}_i^*(x,t) \tag{C.13}$$

$$\Delta J_{dis}^{charge} = -\epsilon_r\epsilon_0\frac{\partial}{\partial x}\frac{\partial}{\partial t}\Delta\phi(x,t) \tag{C.14}$$

where

$$\tilde{\mu}_i^*(x,t) = \frac{\mu_i(x,t)}{z_i e} + \phi(x,t) \tag{C.15}$$

From these three master relations in a mixed conductor, one can realize that only Equation C.12 is time-independent while the other two are time-dependent. This indicates that a resistor can be used to describe the charge behaviors under the relation given by Equation C.12, and capacitors can be used to describe the relations given by Equation C.13 and Equation C.14. Thus, the equivalent circuit can be a direct mapping of the fundamental physical process in the system, and the circuit elements can reflect the material properties directly and are given by

$$R_i = \frac{1}{\sigma_i}\frac{dx}{A} \tag{C.16}$$

$$C_{dis} = \epsilon_r \epsilon_0 \frac{A}{dx} \tag{C.17}$$

$$C_i = \frac{(z_i e)^2 c_i}{k_B T} A dx \tag{C.18}$$

With these quantities, the corresponding equivalent circuit can be derived (**Figure C.2**). In addition, it is worth noting that in the given equivalent circuit, the boundary conditions for both electronic and ionic charges are given by including a resistor $R_i^{\perp}$ and a capacitor $C_i^{\perp}$ connected in parallel. Depending on specific experimental conditions, such boundary conditions can be modified to reflect the realistic cases. For instance, in the transport measurement an ionically blocking electrode is needed to extract accurate ionic conductivity, and thus, the boundary condition for ion-conducting rail can be set to a perfect capacitor only. Nevertheless, if limited charge-exchange still takes place at the TPBs, the perfect capacitor can be modified to an CPE, which represents imperfect capacitive behaviors.

C.2 Surface reaction at solid-gas interface

To model the surface reaction process for a half-cell, the above equivalent circuit can be applied as well. In thin-film electrochemical cells as discussed in this dissertation, the diffusion process in either the electrode material or the electrolyte material is much faster

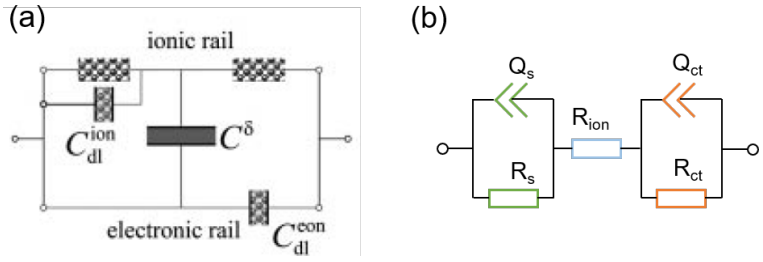

Figure C.3: *(a) Equivalent circuit in half cells with large-area porous counter electrode (Figure adapted from [237]). (b) Equivalent circuit for thin-film epitaxial half cells with embedded counter electrode.*

than the surface reaction process due to the large surface-to-thickness ratio. In this case, the ionic rail in the equivalent circuit can be shorted. Assuming the electrolyte has an infinite large electronic impedance and the electrode is highly electronically conducting, the final equivalent circuit with electrode boundary conditions can be greatly simplified (**Figure C.3**(a)).

For a half cell with an open boundary condition at the counter-electrode side, if the counter electrode area is much larger compared to the working electrode, the counter-electrode impedance can be assumed to be both ionically and electronically shorted. Thus, the measured response is purely from the working electrodes. However, in the epitaxial half cells developed in this dissertation, the counter electrode is embedded in between the electrolyte and the substrate, thus there cannot be continuous ionic-charge exchange with the environment at the counter electrode. Thus, such cells can only be used under AC bias with small perturbations, and the ionic charges are compensated near the electrolyte-counter-electrode interface by either a stoichiometric change in the electrolyte material or by the electronic charges from the counter electrode. In this case, an additional set of capacitor and resistor is included to describe such process (**Figure C.3**(b)). Due to the small diffusion impedance and charge-transfer impedance, nevertheless, the resulting Nyquist plots in the experiments are typically manifested as one semi-circuit, representing the much slower surface-gas-exchange impedance.